Understanding the Akaroa Magmatic System: a multi-method approach to erupted plutonic lithics

---

A thesis

submitted in partial fulfilment of the requirements for the degree

of

Doctor of Philosophy in Geological Sciences

at the

University of Canterbury

by

Elisabeth MacKenzie Bertolett

UNIVERSITY OF CANTERBURY

Te Whare Wānanga o Waitaha

CHRISTCHURCH NEW ZEALAND

UNIVERSITY OF CANTERBURY

2019

Frontispiece

Looking out to Clay Point and Fisherman Bay at sunset.

Abstract

The plutonic-volcanic connection remains one of the main challenges to understanding volcanic eruptions. Past studies have usually approached this using geochemical analysis. Quantitative microstructural analysis is a proven and essential technique for providing context for geochemical data, especially in the formation of cumulates; a necessary process in segregating eruptible melt. This thesis aims to understand the plutonic-volcanic connection by using microstructural analyses in conjunction with geochemical data on erupted plutonic lithics at the Akaroa Volcanic Complex (AVC). There are no exposures of *in situ* plutonic material at the AVC (other than the late-stage Onawe syenite and gabbro), but plutonic lithics within lava flows provide a window in to the crustal magmatic system.

Here, quantitative microstructural analysis (i.e. EBSD) identifies uniaxial compaction crystallographic preferred orientations (CPOs) of plagioclase in cumulates. Rotation axis analysis confirms compaction of the crystal mush both during the settling and organization of crystals in a melt-rich environment as well as near-solidus viscous deformation. The correlation of compaction CPOs of increasing strength with a decrease in glass (from petrographic analysis) and late-stage crystallization of the plagioclase lattice (color-CL) provides some of the first direct evidence of coupled compaction and melt extraction in natural samples, specifically in plutonic lithics which, by definition, have a known volcanic counterpart. Highly luminescent plagioclase grain boundaries are crystallographically the same as the adjacent plagioclase but are compositionally different. These bright CL regions have chemistries that correspond to the evolved lava flows of the AVC, further suggesting that the material represents a residual magmatic melt that was progressively extracted from the crystal framework, evolved, and was potentially able to erupt. Those bright CL compositions that do not match the AVC eruptives are high in FeO and MgO and are likely low-silica immiscible melts. Immiscible melts are used to explain magmatic accumulation and evolution in stacked sill complexes which the AVC crustal magmatic system resembles. The presence of symplectite-style reactive textures supports this interpretation.

This thesis aims to understand the plutonic-volcanic connection at the Akaroa Volcanic Complex (AVC) using erupted plutonic lithics. First, with plutonic lithics from one location,

Goat Rock Dome, and the magmatic processes responsible for cumulate formation and melt extraction. This provides important microstructural and geochemical evidence for compaction, melt extraction, and cumulate formation which, while frequently used to explain magmatic processes, is rarely proven. Finally, these findings are applied to all plutonic lithic-bearing locations at the AVC to better explain crustal magmatism and cone-building on Banks Peninsula.

Acknowledgements

I am a sentimental person; thus, my acknowledgments are long. That being said, I could not name every individual that has helped me during my PhD. I attempt to name a few here and acknowledge all the others that have also contributed along the way.

I acknowledge financial support from the following; a University of Canterbury Doctoral Scholarship, the Mason Trust Fund, a Brian Mason Scientific and Technical Trust Grant (2015/03), and Frontiers Abroad Aotearoa Ltd. Without this support this research would not have been possible.

Firstly, I am grateful for the Frontiers Abroad team for introducing me to New Zealand geology and for the first iterations of this project. I am very thankful for the opportunities to teach on the Frontiers Abroad programme. Indistinguishable from this FA experience is Max Borella who makes so much of this possible – thank you.
As part of Frontiers Abroad and as my senior supervisor, Darren Gravely merits a particular acknowledgment. The ability to create and determine the path of your own research is rare as a student and I am very grateful for the support and encouragement you have always given me in dictating my own research interests. This would have been impossible without your knack for research connections and knowing where to send me to get the expertise I required. Thank you for adapting as an advisor as I grew as a researcher and for five years of support.

Thank you to my co-supervisors:

To Sam Hampton for being my go-to for whenever I got stuck and for supporting me when it felt like no one else was. Thank you for giving me space to develop as an instructor: for acknowledging my strengths while providing an example for how to improve. Thanks for letting me be involved in so many projects and for frequently pulling me out in to the field.
Ben Kennedy – Thanks for being my stand-in advisor when needed and always bringing a much-needed, fresh perspective to my research.
Rachel Beane – You were the first person who expected me to know what I was doing. Thank you for sitting back so I could figure out how to proceed, for teaching me your SEM methodologies, and for all the valuable discussions.
Guil Gualda – Your enthusiasm is both infectious and impossible to keep up with. Your knowledge and commitment to research is inspiring and I am grateful that I got to spend a semester as your PhD student at Vanderbilt as part of this research. Thank you for sharing your invaluable expertise and for many shenanigans.

A special acknowledgment also needs to be made to Dave Prior who directed so much of the early stages of this research and taught me about SEMs, crystals, and being inventive. To Dave: the exact moment at which I understood my research was in a conversation with you in which I could follow what you were saying. Thank you for opening your lab and your calendar to me over the years. You are a well of knowledge and stories, an inspiration.

Thank you to the professors, staff, and postgrads at the University of Canterbury as well as Vanderbilt University. A few are named here:
AJ - For being my beacon of what it means to be an excellent researcher, contentious human, and good friend. Thank you for your mentorship and memes.

Dr. Paul Ashwell - In the moments that I felt ready to walk away from my PhD, you were there to bring me back to reality. Another big thanks for your mentorship as a field teacher. Thank you for being an advocate for me and a good friend.
Lydia Harmon - I wouldn't have had nearly as much fun on this journey without you. I've enjoyed all our bike rides, café work days, and field work across two countries and a handful of years. I aspire to your level of intellect and puns.
Gabby and Astrid - For poorly disguised writing sessions, cake deliveries, and many sarcastic jokes.
The UC tech staff - The first people at UC to make me feel part of the family. I always look forward to tea time with all of you. A particular thank you to Rob Spiers who endured all of my thin section making requirements and let me get away with all kinds of nonsense. And to Sacha, aka Aunty, for always being a motherly figure when I needed one.
Thank you as well to Jim Cole for an early review of this thesis.
And to my undergraduate advisor, Erik Klemetti. In many ways I wouldn't be here if not for your support. First by capturing my nascent interest in geology, then by allowing me to do three years of research with you. I was exposed to people, places, and ideas that still influence me today and for which I am continually grateful.

Finally, a very special thank you to Francis and my family for always supporting and encouraging me.

UNIVERSITY OF CANTERBURY
Te Whare Wānanga o Waitaha
CHRISTCHURCH NEW ZEALAND

Deputy Vice-Chancellor's Office
Postgraduate Office

Co-Authorship Form

Chapter 3: Compacted Cumulates Revealed by Electron Backscatter Diffraction Analysis of Plutonic Lithics

Published in: Geology

The published manuscript was compiled and written by Elisabeth Bertolett, who also conducted field work, laboratory analysis, and interpreted the results. Data collection and interpretation was assisted by David Prior. The concept of the manuscript was developed through discussions between Elisabeth Bertolett, David Prior, and Darren Gravley. David Prior and Darren Gravley contributed to refining the manuscript. All co-authors reviewed draft versions of the manuscript before it was edited for submission by Elisabeth Bertolett

Certification by Co-authors:
If there is more than one co-author then a single co-author can sign on behalf of all

The undersigned certifies that:
- The above statement correctly reflects the nature and extent of the PhD candidate's contribution to this co-authored work
- In cases where the candidate was the lead author of the co-authored work he or she wrote the text

Name: Dr. Darren Gravley

Signature: 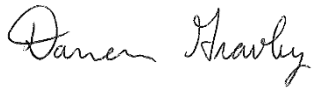

Date: *5/12/2019*

UNIVERSITY OF CANTERBURY
Te Whare Wānanga o Waitaha
CHRISTCHURCH NEW ZEALAND

Deputy Vice-Chancellor's Office
Postgraduate Office

Co-Authorship Form

Chapter 4: Progressive magmatic compaction and melt extraction revealed by a multi-method approach to plutonic lithics

Submitted to: Contributions to Mineralogy and Petrology

The submitted manuscript was compiled and written by Elisabeth Bertolett, who also conducted field work, laboratory analysis, and interpreted the results. Data collection was assisted by Rachel Beane. The concept of the manuscript was developed through discussions between Elisabeth Bertolett, Darren Gravley, Rachel Beane, and David Prior. Rachel Beane, Darren Gravley, David Prior, and Guilherme Gualda contributed to refining and developing the manuscript. Guilherme Gualda assisted with preliminary laboratory analysis. Elizabeth Teeter collected preliminary data as part of a pilot study which contributed to this manuscript. All co-authors reviewed draft versions of the manuscript before it was edited for submission by Elisabeth Bertolett

Certification by Co-authors:
If there is more than one co-author then a single co-author can sign on behalf of all

The undersigned certifies that:
- The above statement correctly reflects the nature and extent of the PhD candidate's contribution to this co-authored work
- In cases where the candidate was the lead author of the co-authored work he or she wrote the text

Name: Dr. Darren Gravley

Signature: Darren Gravley

Date: *5/12/2019*

Table of Contents

Abstract iii
Acknowledgements v
Chapter One – Introduction 1
1.1. Context of Study 1
1.2. Research Framework 3
Aims and Objectives 5
Thesis Layout 6
Chapter Two – Background and Context 9
2.1. The Plutonic-Volcanic Connection 9
2.1.1. Crustal Magmatic Architecture 10
2.1.1.1. Mush Model 10
2.1.1.2. Dike and Sill Complexes 11
2.2. Cumulates 13
2.2.1. Definitions 13
2.2.2. Crystal Accumulation and Cumulate Formation 14
2.2.3. Melt Segregation and Compaction 17
2.2.3.1. Reactive Flow and Immiscible Melts 18
2.3. Deformation and Strain Indicators 20
2.3.1. Electron Backscatter Diffraction 21
2.3.1.1. Application to Igneous Petrology 21
2.3.1.2. Plagioclase 21
2.3.1.3. Deformation Types and Mechanisms 22
2.4. Cathodoluminescence (CL) 24
2.5. Plutonic Lithics 25
2.5.1. Definitions 25
2.5.2. Significance 26
2.5.3. Traditional Approaches 26
2.6. Geologic Setting 28
2.7. Key Studies 32

Chapter Three – Determining the fabric forming mechanism for crystal alignment in plutonic lithics 45
Chapter Four – Progressive magmatic compaction and melt extraction revealed by a multi-method approach to plutonic lithics 58
Chapter Five - Plutonic Lithics of the Akaroa Volcanic Complex 103
Chapter Six – Conclusions and Future Directions 157
Conclusions 157
Future Directions 159
Appendix 166
Chapter 3 Appendix 166
Chapter 4 Appendix 177
Chapter 5 Appendix 199

List of Figures

Figure 1.1 Student research and SEM facilities relevant to this thesis. 3
Figure 2.1 The ‘mush model’ (a) and dike and sill complex (b) from Cashman et al., 2017 and references therein. The rheological lock-up of a magma based on % crystallinity (c). 12
Figure 2.2 Flow chart of gabbroic cumulate formation from Morse et al. (2017). Processes separated in to ‘primary’ and ‘secondary’ that may influence cumulate microstructures. 16
Figure 2.3 Schematic representing the effects of reactive flow and interstitial melt migration on a partially crystalline magma from Leuthold et al. (2014). 18
Figure 2.4 Three types of plagioclase CPOs identified by Satsukawa et al., 2013. Magmatic and tectonically deformed plagioclase CPO patterns. 23
Figure 2.5 Map of ages of volcanism in New Zealand from Hoernle et al. (2006). 29
Figure 2.6 Schematic cross section of Canterbury (left) and Banks Peninsula (right) stratigraphy from Field and Browne (1985). 30
Figure 2.7 Expected lineation and foliation pole figures for tabular and elongate prisms and rods in plagioclase from Holness et al. (2017). 33
Figure 2.8 Schematic reactive flow model from Jackson et al. (2018). 37
Figure 2.9 Schematic thesis layout. 39
Figure 3.1 (A) Map of Banks Peninsula in New Zealand (inset). Akaroa Volcanic Complex (AVC) designated by grey shading. Black square shows Goat Rock (43°43’13.48”S 173°3’58.48”E). (B) Field photo of rockfall slab with 3+ lithics present. Red lines indicate radial jointing at the contact between lithic and host. 48
Figure 3.2 (A) Equal area, lower hemisphere stereonets of the poles to principal plagioclase planes sample GR8b (representative of the cumulate lithics of this study). Contours are in multiples of uniform density. Contours and maximum densities reflect differences in strength of CPO. (B) Individual crystal orientations and rotation axes calculated from random pairs of points within individual twin domains, sample GR8b. All plots are equal area, lower hemisphere projections. Misorientation axes are limited to 3-10° rotation. Plagioclase orientations labelled by color. (C) Stereonet showing the positions of the maxima in rotation axis plots for all twin domains in eight individual grains (all data in Appendix). Individual grains and twins have distinctive rotation axes controlled both by the stress kinematics and the slip system of that specific twin. See Appendix for the same plot within the crystal reference frame. 49
Figure 3.3 Schematic diagram depicting the ideal CPO and rotation axis orientations under magmatic flow and compaction. Left side of the diagram refers to the primary organization of crystals, best evident in CPOs while the right side refers to deformation in the solid state reflecting internal crystal deformation. (A) Scenario in which accumulating crystals are mechanically arranged by flattening, followed by continued uniaxial compression in the solid state. (B) Cumulate formation initially controlled by flow. The initial organization of crystals in this state determines the way in which crystals deform in the solid state and will display a distinct pattern of rotation axes under either (secondary) flow or compaction. 51
Figure 3.4 (A) Equal area, lower hemisphere stereonets of the poles to principal plagioclase planes sample GR14, a lithic with a more silicic mineralogy than GR8b. Note that the CPO pattern is similar for both GR8b and GR14 but that GR8b (Figure 3.2A) has a much stronger CPO (J and MI). (B-C) Cross-polarized photomicrographs of (B) GR14 lithic with interstitial

melt (7%) outlined in red (cf. Holness et al. 2007) and (C) GR8b lithic with plagioclase-plagioclase grain boundaries and absence of melt (i.e. the cumulate). 53
Figure 4.1 A) Geologic map of Banks Peninsula adapted from Hampton et al. (2009). Goat Rock Dome is located on the eastern flank of the main AVC edifice. B) Image of rockfall block containing plutonic lithics. Note the radial jointing propagating into the grey, host material from the light-colored lithics. 64
Figure 4.2 Sample descriptions for the three categories of Goat Rock lithics and their representative thin section. Left, petrographic images with 10 mm scale bar and right, color-CL images show plagioclase (pink), pyroxene and olivine (black), apatite (bright white, especially in GR20). Note the white, grain boundary filling lines particularly in GR8b and GR14 as well as the broader, splotchy areas of luminescent material in GR8b. 67
Figure 4.3 Cross polarized photomicrographs of A) GR8b, B) GR20, and C) GR14; D) grey plagioclase crystals in center forming glomerocryst-like texture found in GR14. Note the large plagioclase in (A) (top, left) with pinching twins and the grain just below with two extinction angles. GR8b (A) has the salt-and-pepper texture associated with mafic phases. Note the absence of this material in GR14 (C and D). Plagioclase in GR14 have more uniform extinction and twinning as well as straighter grain boundaries than plagioclase in GR8b. 70
Figure 4.4 A-B) Plagioclase deformation textures in GR8b. A) Bent grain in center of frame with visible subgrains highlighted by undulose extinction and pinching twins. B) Irregular, serrated grain boundary between two plagioclase. 71
Figure 4.5 Crystallographic preferred orientations of plagioclase in principal pole to plane, equal area, lower hemisphere projections. CPO strength represented by the maximum density of clusters (i.e. Max) using 10° halfwidth contours. CPOs rotated to common reference frame. 73
Figure 4.6 A) Individual plagioclase grain from GR8b, rainbow scale (B) shows 7º misorientation (blue-red) relative to the Euler angle at the starting circle in red. Grain outline and misorientation transects in (C). D) Angle of misorientation (y-axis) vs distance (x-axis) along the long axis of the crystal starting at the red dot. E) Angular misorientation along the short axis of the crystal starting at orange square. Corrected for 180° albite twins. 75
Figure 4.7 A) Plane-polarized image of a mafic enriched domain surrounding an Fe-Ti oxide in GR8b with corresponding image outlining the material in black (below). B) Color-CL frame of GR14 showing bright, luminescent material associated with grain boundaries above and the same bright CL areas highlighted by black outline below. 77
Figure 4.8 TAS diagram of whole rock (large circles) and bright CL areas (line shapes) for each lithic of this study. Black triangles and squares are the only other plutonic material exposed in the AVC (Onawe gabbro and syenite, respectively). All AVC eruptives (from Hartung 2011, Msc) are in grey. Two points labelled GR04/10 exist for the GR8b whole rock composition because not enough lithic remained to get an adequate composition. GR04 and 10 are the most similar to GR8b in terms of mineralogy and texture. Note the two populations of GR20 (green triangles). 78
Figure 4.9 . A) Plagioclase EMPA chemistries plotted as silica vs alkalis and B) average ternary anorthite number with standard deviation error bars. 80
Figure 4.10 Variation diagrams of silica vs major oxides for A) GR8b, B) GR20, and C) GR14. Plagioclase chemistries (EMPA) for each sample in grey overlain by whole rock (circle with black outline) and bright CL lenses (EDS, open shape). Red crosses in GR8b are mafic enriched domain compositions (EDS, see text for discussion). Note the broad range of silica in the high K_2O, low CaO arm of GR20. 82

Figure 4.11 A) EBSD phase diagram image of an area in GR14, B) the same area in color-CL, and C) an IPF map of the same area. Black box designates the zoomed in area of the three images below: D) color-CL image showing the bright CL regions and E) IPF orientation map. The different colors in E represent different lattice orientations. F) our interpretation of the boundaries of the plagioclase crystals compared to the areas of bright CL. Note that, in some areas, the bright CL seems to be a continuation of one crystal (A and A') that terminates at the grain boundary of crystal C. 84
Figure 4.12 Top row, individual color-CL frame A) GR8b, B) GR20, C) GR14, scale bar same for each image. Bottom, processed image of the area of bright CL from the above image. Red boxes denote diffuse melt in GR8b (A). Note the variability in bright CL distribution at grain boundaries in GR20. 86
Figure 4.13 Summary table of Goat Rock plutonic lithic populations. Left, schematic volcanic system adapted from Cashman et al. (2017). Potential lithic resident locations in mush indicated by red (GR8b), green (GR20), and blue (GR14) circles. Colored circles correspond to schematic of lithic type samples: plagioclase (grey rectangles), mafic phases (black ovals), mafic enriched domains (red regions), and bright CL areas (purple regions). Right, corresponding data and interpretations for each component of plutonic lithic. 91
Figure 5.1 Outline of New Zealand (a) and geologic map of Banks Peninsula. Black boxes designate location of lithics associated with this study. Only AVC lithics are investigated here. Map after Ring and Hampton (2009). 106
Figure 5.2 Left, a section from the 1992 Sewell et al. geologic map of Banks Peninsula showing the two major eruptive phases identified by the authors (af; main phase and ae; late stage). Right, the same area overlain with mapping data from the Frontiers Abroad mapping initiative. Legend on the right. Transects in 1 and 2 show a more detailed and more diverse sequence of lava flow compositions than seen on the Sewell et al. (1992) map. 107
Figure 5.3 Geochemical transects of lava flows based on stratigraphy. Modified from Beckham (2016). Red dots denote Pa Bay and Goat Rock Dome with the Ducksfoot lava flows between them. For a detailed plot of the Ducksfoot transect with Goat Rock dome, see Appendix. 109
Figure 5.4 Cross polarized thin section images showing variations in mineralogy, crystal size, and apparent crystal alignment for (a) Goat Rock, (b) Eastern Pigeon Bay, (c) Paua Bay, (d) Haylocks Bay, and (e) LeBons Bay Peak. Scale bar 10 mm. 114
Figure 5.5 Histogram of corrected mineralogy proportion based on EBSD phase maps. Modal mineralogy determined as a percentage of points indexed as each mineral from EBSD maps. Non-indexed points and accessory phases are removed and corrected to 100%. Note the significant proportion of plagioclase in Goat Rock and the comparatively high amounts of pyroxene in LeBons and Haylocks Bay. 118
Figure 5.6 Pa Bay, Ducksfoot, and Goat Rock relationship. Volcanic sectors. Inset modified from Hampton (2010)..... 120
Figure 5.7 a) Major element silica wt. % vs alkalis for whole rock compositions, b) plagioclase chemistries, and c) bright CL chemistries. Colors designate different lithic-bearing location. Closed circles are lithic whole rock, open circles are host whole rock, open triangle is lithic plagioclase chemistry, open square is host plagioclase chemistry, grey tick represents plagioclase phenocryst chemistry of the underlying lavas (i.e. Ducksfoot), crosses are lithic bright CL chemistry, and pluses are host bright CL chemistry. 123
Figure 5.8 Major element silica wt.% variation diagrams of bulk rock compositions for each lithic location and its host. Colors designate different lithic-bearing location. Closed circles are lithic whole rock, open circles are host whole rock. 125

Figure 5.9 Silica vs Zr (a) and Rb (b) from lithic and host whole rock compositions. (c) MgO (wt. %) vs Sr (ppm) and (d) MgO wt. % vs CaO wt. % including bright CL chemistries..... 126
Figure 5.10 Major element variation diagrams of lithic and host plagioclase phenocryst chemistries..... 127
Figure 5.11 Equal area, lower hemisphere pole to plane figures for representative lithic samples. 15 halfwidth contours. Density of points highest (red) to lowest (blue). 129
Figure 5.12 Stitched full thin section color cathodoluminescence images for Eastern Pigeon Bay (a-b), Paua Bay (c-d), Haylocks Bay (e-f), LeBons Bay Peak (g), and Goat Rock (h). All images have been black-balanced so that direct comparison of color and luminescence can be made across samples. Not the bright, white areas found in many of the samples (i.e. 'bright CL areas'). 131
Figure 5.13 Major element silica wt.% variation diagrams of bright CL chemistries for each lithic location and its host. Colors designate different lithic-bearing location. Crosses are lithic bright CL chemistry, and pluses are host bright CL chemistry. Note the absence of Haylocks BCL in Na_2O and K_2O as these elements are not present in Haylocks BCL. 133
Figure 5.14 Major element variation diagrams for all Goat Rock data. 134
Figure 5.15 Major element variation diagrams for all Haylocks Bay data. 136
Figure 5.16 Major element variation diagrams for all Paua Bay data. 138
Figure 5.17 Major element variation diagrams for all Eastern Pigeon Bay data. 139
Figure 5.18 Silica vs alkalis plot of lithics discussed in this study (colored areas) overlain on whole rock compositions from AVC erupted deposits (grey points, Hartung et al., in review). Dotted outline designate bright CL compositions for their respective lithic. 143
Figure 5.19 Schematic of progressive cone-building and magmatic structure of the AVC. Multi-staged cone building represented by greyscale cones, underlying sedimentary units that source some of the Pa Bay non crystalline lithics highlighted by shallowing dipping lines. Basement and magmatic system represented by grey ticks. Idealized mush-bodies in varying stages of crystallization, settling, compaction, etc. and their pathways represented by dotted lines. Number 1-5 designate the possible host-lithic relationships identified in this study and their relationship to the volcanic stratigraphy. 147
Figure 6.1 Proposed lithic terminology classification. The schematic reads from broad lithic classification to more refined. Plutonic and non-plutonic lithics are separated and then described in terms of their relationship to the deposit they reside in. Then, textural features are used to characterize the processes that produce any visible crystal fabrics. Note that this textural extension of the diagram can also be used for xenoliths as well as non-plutonic lithics. 163
Figure 6.2 Lithics found at Sleepy Bay including pyroxene (with little to some plagioclase) crystal clusters. 165

List of Tables

Table 1 Modal mineralogy (%) normalized from EBSD map phase percentages for each lithic. Modal mineralogy determined as a percentage of points indexed as each mineral. Non-indexed points and accessory phases are removed and corrected to 100%. 72

Table 2 Average major element compositions for each lithic of this study and the host whole rock. Average plagioclase and bright CL compositions also included for the three lithics. 79
Table 3 Bright CL as a percentage of total area for four representative frames for each lithic 87
Table 4 Lithic-bearing location with host and lithic features. From field observations. 112

Chapter One – Introduction

1.1. Context of Study

Volcanoes pose a number of risks to human life and infrastructure throughout the world. Processes within the crustal magmatic system are vital to understanding volcanic hazards (Cashman et al., 2017). This link between a buried and constantly changing magmatic structure and comparatively short-lived and sporadic eruptions has posed a number of challenges to the petrologic community. These challenges exist because active magmatic systems are not observable at the surface and only plutons cooled, deformed, and exhumed over time can be examined directly. The compromise is that eruption-initiating conditions are obscured and modified by subsequent processes (Marsh, 1981; Paterson et al., 1998; Holness et al., 2017). Therefore, researchers have relied on clues found in volcanic deposits (ex Hildreth, 2004). However, it has become clear that these volcanic deposits do not represent the whole magmatic system geochemically and certainly do not preserve the physical processes superseding eruption. Indeed, not all magmas have an erupted counterpart (Freundt-Malecha et al., 2001). Indirect methods of observation have been developed, especially monitoring of active volcanoes and geophysically imaging of proposed magmatic regions below volcanic complexes (Till et al., 2015). These methods add to the larger puzzle of timescales of volcanic and magmatic processes but still leave significant gaps related to the mechanisms of magmatism and eruption.

Along with the physical challenges of observing the link between a subsurface and surficial process is that of different scales of space and time (Marsh, 1981). The magmatic system feeding a single volcano is large, long-lived, and constantly changing. In comparison, a volcanic eruption represents an ephemeral condition and portion of the larger magmatic system. Reconciling the two continues to be a challenge but significant developments are constantly adding to our understanding of magmatic and volcanic systems.

Recently, observations from geochemistry, experiments, numerical modelling, and microstructural studies have led to more refined models of the architecture of magmatic systems. For large silicic and arc systems, this is the ‘mush model’ and the concept of cold

storage and rapid remobilization (Marsh, 1981; Bachman and Bergantz, 2004; Cooper and Kent, 2014). The mush model can be applied to large, long-lived magma chambers (eg. Hildreth, 2004) as a way to characterize the proportion of crystals to melt and, therefore, the eruptibility of a magma. For smaller, basaltic systems this model is a dike and sill plexus model and the effect of reactive flow in moving eruptible melt and incrementally building smaller mush bodies (Cashman et al., 2017 Jackson et al., 2018). These models provide an approximation of the magmatic system and help explain geochemical relationships found in the volcanic record.

One approach to directly link the plutonic and volcanic systems are studies of erupted plutonic lithics. Plutonic lithics that have originated in the active magmatic system may preserve the chemical and physical conditions acting within a mush, preserved in a snapshot in time due to entrainment in the erupting magma rather than being overprinted by the long cooling of a pluton. In addition, plutonic lithics have passed from the crustal magmatic system in to the surficial volcanic system. The plutonic lithic and its host provide textural and geochemical avenues that can close the gap between the magmatic and volcanic realms (Upton et al., 2000; Wolff et al., 2000; Freundt-Malecha et al., 2001; Chadwick et al., 2013).

This thesis aims to describe and discuss the physical and chemical signatures from the magmatic system preserved in plutonic lithics first by collating the relevant literature on magmatic models, plutonic lithics, and microstructural analysis of igneous plagioclase. This microstructural analysis is applied to Akaroa Volcanic Complex (AVC) plutonic lithics to determine cumulate-fabric formation and the coupling of compaction and melt extraction. Finally, this study ends with a focus on the relationship between a lithic and its volcanic host at all lithic-bearing sites found at the AVC, and how these clues can be combined to refine our models of magmatic systems and volcanic eruptions.

1.2. Research Framework

Several Frontiers Abroad students have conducted semester-long undergraduate research projects on AVC plutonic lithics under my co-supervision (Lawlor and Teeter) during the duration of this thesis:

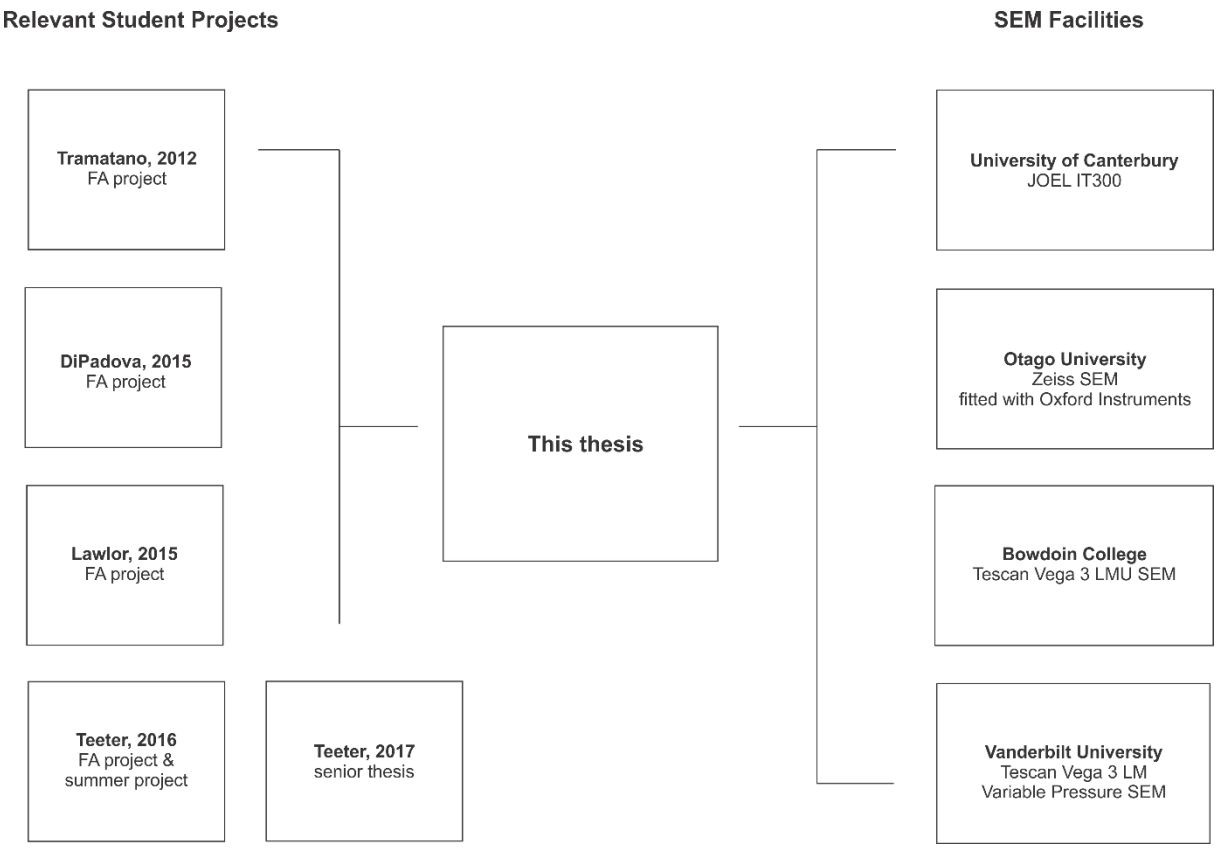

Figure 1.1 Student research and SEM facilities relevant to this thesis.

In 2012, a Frontiers Abroad mapping group discovered plutonic lithics in rock fall blocks (due to the Canterbury Earthquake Sequence) at Goat Rock Dome, a small, basaltic volcanic dome within the Akaroa volcanic phase of Banks Peninsula, New Zealand. A preliminary geochemical study was undertaken on the lithics by Sam Tramatano. Starting in 2014, I took up the project as a Frontiers Abroad student, then as a research assistant, and finally as a doctoral student. The research undertaken in each of these positions makes up the work that follows with

the bulk of field work, data collection and analysis, and all of the writing taking place as part of the PhD.

I found the Flea Bay and Paua Bay lithic locations on Frontiers Abroad mapping modules with Caroline Lawlor and Elizabeth Teeter, respectively. I also identified the other lithic locations including Mt. Sinclair (not sampled) and Eastern Pigeon Bay on subsequent Frontiers Abroad mapping modules. Eastern Pigeon Bay and the LeBons Bay Peak lithics of this study were sampled with a core drill in 2018. Sampling at Goat Rock Dome was completed with an unwieldy concrete saw (2015) to retrieve samples indicated by E. Dipadova's variability study. Pa Bay lithics (both plutonic and country rock) were sampled as part of Frontiers Abroad student Abra Atwood's project in 2014 for which I was the field assistant.

All chapters in this thesis focus around applying Scanning Electron Microscope (SEM) techniques to plutonic lithics. Four main SEMs and their respective experts were involved in this research and data was collected at each of these facilities. The reason for the number of SEMs used is due to the expertise of the researchers at each university;

Dr. Prior of Otago University: EBSD expertise, microstructural analysis of plagioclase, deformation mechanisms

Dr. Beane of Bowdoin College: Combined EBSD-EDS-CL expertise, color-CL mapping expertise

Dr. Gualda of Vanderbilt University: Crystal microstructure and SEM methods expertise and application of MELTs modelling

To complete the main objective of this research, namely to understand the structure of the AVC magmatic system and how it is connected to the cone-building features preserved on the surface, we combined a number of textural and geochemical techniques. First, to understand crystal fabrics and their genesis, we focused on crystal microstructures beginning with Electron Backscatter Diffraction (EBSD). Color cathodoluminescence (CL) and Energy Dispersive Spectroscopy (EDS) compliment the EBSD findings by identifying and characterising

compaction, melt extraction, and reactive flow features. The rest of the techniques used are predominately geochemical (whole rock major and trace XRF, mineral chemistry EMPA data, and Energy Dispersive Spectroscopy (EDS)) to give additional context to fabric-forming magmatic processes.

Because the methods used in this thesis are diverse and apply to each chapter specifically, no stand-alone methods section is included here so as to avoid repetition. Each chapter includes a background on the methods used and the details of their application to the specific study. The literature review (chapter 2) includes an overview of the main microstructural methods to give necessary context to the reader and emphasize the significance of these techniques as they are applied in chapters 3-5.

Aims and Objectives

The AVC is a system with a complex magmatic system that is not exposed at the surface, with only the record left behind in plutonic lithics to analyse the magmatic system. The overarching aim of this thesis is to utilize plutonic lithics to bridge the gap between pluton and volcanic deposit at the AVC.

To complete this larger aim, a number of specific objectives relating to the mechanisms of mush evolution, crystal deformation, and melt segregation need to be examined. These objectives are as follows:

To collate the relevant published literature on how plutonic lithics have been used to understand basaltic, crustal magmatic systems using a multi-method approach.
To determine the fabric forming mechanism for crystal alignment in plutonic lithics using microstructural analysis.
To apply multiple SEM-based methods to explain the factors responsible for variations in plutonic lithic fabrics and chemistries.
To document, relate, and interpret all known occurrences of plutonic lithics in the Akaroa Volcanic Complex with the methods utilized in the previous two objectives.

Thesis Layout

The objectives defined above in section 1.2 pertain to each of the next three chapters.

Chapter 2 aims to collate the relevant published literature on how plutonic lithics have been used to understand basaltic, crustal magmatic systems using a multi-method approach.

Chapter 2 contextualizes the relevant literature and the knowledge gaps that apply to the main three chapters (3-5) by achieving the following subobjectives:
2A) To establish the questions that remain within the plutonic-volcanic connection, the importance of cumulates, melt extraction, and intracrystalline deformation to magmatic processes.
2B) To summarise the methods other authors have used to provide a more holistic understanding of these processes, and how the application of these methods to plutonic lithics can illuminate the link between magmatic processes and volcanic eruptions.

Chapter 3 aims to determine the fabric forming mechanism for crystal alignment in plutonic lithics using microstructural analysis.

Chapter 3 is an article published in *Geology*. The paper addresses the SEM methods used at the intersection of multiple fields. As such, a handful of gaps exist which this chapter bridges by providing a holistic, methodological approach and achieving the following subobjectives:
3A) To add to the limited but growing literature on igneous plagioclase fabrics quantified using EBSD and provide the first application of EBSD to igneous plagioclase in plutonic lithics.
3B) To use microstructural analysis to decipher the magmatic process responsible for a plagioclase crystallographic preferred orientation (CPO) in an igneous system.

This study provides a roadmap for attributing uniaxial compaction to cumulate formation which bridges a gap in the magmatic evolution literature.

Chapter 4 aims to understand what factors are responsible for variations in plutonic lithic fabrics and chemistries by applying multiple SEM-based methods.

Chapter 4 examines the relationship between a compaction CPO and evidence for melt extraction across a variety of plutonic lithics from the same location. This chapter uses new applications of colour-CL and EDS in conjunction with EBSD to characterize and link minimum melt and its extraction with the relative magnitude of compaction to achieve the following subobjectives:

4A) To describe the luminescent material associated with plagioclase boundaries and interpret this material as the last, quenched melt population in the mush.

4B) To explore the chemical composition of the luminescent material using high resolution EDS mapping.

In summary, this chapter makes a call for a multi-method approach to fully investigating the microstructural evidence of cumulate formation and melt extraction.

Chapter 5 aims to document, relate, and interpret all known occurrences of plutonic lithics in the Akaroa Volcanic Complex with the methods utilized in the previous two objectives.

Chapter 5 ties together the findings of the preceding two chapters in the context of the AVC magmatic system. Chapter 5 also collates and describes all previously known and newly discovered plutonic lithics in the AVC and achieves the following subobjectives:

5A) To introduce new lithic-bearing locations at the AVC and describes the volcanic deposit they reside in.

5B) To analyse the geochemical relationship between lithic and host, the plagioclase CPO in the lithics, and the relationship between the chemistry of features within the lithics to trends in the AVC volcanic record.

In summary, Chapter 5 will create a more refined model of the magmatic structure and the connection to the volcanic deposits of the AVC.

The overarching aim of this thesis is to utilize plutonic lithics to bridge the gap between pluton and volcanic deposit at the AVC using a textural and geochemical multi-method approach.		
Topic	**Objectives**	**Chapter**
Plutonic Lithic Framework and Literature Review	*To collate the relevant published literature on how plutonic lithics have been used to understand basaltic, crustal magmatic systems using a multi-method approach.*	Chapter 2
EBSD Method and Cumulate Formation	*To determine the fabric forming mechanism for crystal alignment in plutonic lithics using microstructural analysis.*	Chapter 3
EBSD, CL, and Geochemistry for Deciphering Magmatic Processes	*To apply multiple SEM-based methods to explain the factors responsible for variations in plutonic lithic fabrics and chemistries by.*	Chapter 4
Application to Banks Peninsula and a Model for AVC Magmatism	*To document, relate and interpret all known occurrences of plutonic lithics in the Akaroa Volcanic Complex with the methods utilized in the previous two objectives.*	Chapter 5

Chapter Two – Background and Context

Chapter 2 collates the relevant published literature on how plutonic lithics have been used to understand basaltic, crustal magmatic systems using a multi-method approach.

2.1. The Plutonic-Volcanic Connection

One of the foremost questions in petrology is how plutons reflect their active volcanic counterparts; which plutons are associated with eruptive events (Hildreth, 2004), how does melt accumulate and store before eruption (Till et al., 2015; Rubin et al., 2017), and what are the timescales over which this takes place (Cooper and Kent, 2014; Glazner et al., 2016)? Especially in large, silicic eruptions, the question of storage conditions and the thermal triggers of eruptions are seriously investigated as they directly impact on the eruptibility of a magma (Szymanowski et al., 2017). Many of the questions apply to intraplate volcanoes as well, indeed, many of the advances in our understanding of the plutonic-volcanic connection comes from observations of basaltic systems.

To better describe this connection, the 'mush model' was proposed whereby the magmatic system is divided in to the rigid sponge, crystal mush, and melt based on crystallinity (Hildreth, 2004; Bachmann and Bergantz, 2004; Cashman and Giordano, 2014). The mush model has proved to be a useful way to structure the discussion on how igneous bodies source volcanic eruptions. However, this model does not resolve some outstanding questions which will be explored below.

Part of the reason the plutonic-volcanic connection is so elusive is because we cannot directly observe both the magmatic conditions/processes and the triggers of eruption at the same time. Investigating volcanic deposits or cooled and exhumed plutons provide valuable clues but the

link between the two is still difficult to reconcile. As a result, plutonic lithics that are entrained in volcanic deposits are used to better constrain the connection between the two systems.

2.1.1. Crustal Magmatic Architecture

2.1.1.1. Mush Model

The 'mush model' came to the forefront of igneous petrology based largely on work done by Marsh (1981) who used crystallinity to determine the eruptibility of a magma. This concept has been utilized by others looking to quantify the timescales and volumes of eruptible melt that is stored in the crust (e.g. Miller, 2016). It has also been used to explain geochemical trends of erupted deposits and use them to reconstruct the parent magmatic system (Hildreth, 2004). Bachmann and Bergantz (2004, 2008) expanded on the mush model with quantitative numerical models of the eruptibility of magma. Bergantz et al.'s (2017) work on force chains begins to bridge the gap between traditional geochemical approaches to exploring the plutonic-volcanic connection and investigating specific mechanical processes that have remained challenges to the kinetics of the mush model.

Despite the advances in understanding of crustal magmatic systems propelled by the mush model, there are observations that are not easily explained by this model. For example, why is it difficult to see melt layers beneath active volcanoes (Till et al., 2015; Cashman et al., 2017)? How do we reconcile geochemical trends to physical mechanisms (Ganne et al., 2018)? One of the issues with the mush model is that paired microstructural and geochemical evidence does not always support the processes fundamental to the mush model (such as hindered settling and fractional crystallization). Much of this evidence is found within the layered igneous intrusion literature (e.g. Holness et al., 2017).

Furthermore, Jackson et al. (2018) argue that reactive melt flow is critical to the application of the mush model to natural systems, especially basaltic to intermediate, in answering the above questions. Indeed, the authors suggest that reactive melt flow better explains major and trace element trends in crustal magmatic systems than simple fractional crystallization and magma mixing (Jackson et al., 2018). Their quantitative modelling also describes the growth of mush

bodies and the removal of melt in which very thin (and potentially invisible to imaging techniques) layers of ephemeral melt form, ascend, and either cool or erupt on short timescales (Jackson et al., 2018). The small amounts of magma that ascend and the short timescales for which they are melt-rich matches recent observations of long periods of 'cold-storage' of magma in which crystals record extended periods of sub-solidus conditions punctuated by short phases of elevated temperature (Cooper and Kent, 2014; Szymanowski et al., 2017).

2.1.1.2. Dike and Sill Complexes

Important to the plutonic-volcanic connection is the relationship between time (elucidated by temporarily constrained erupted deposits) and space (the depth and spatial distribution of plutons; Marsh, 2004). Over time, mushes create 'interconnected stacks of sheets and chambers' that interact and evolve in complex ways (Marsh, 2004).

Annen et al. (2015) review the different crustal magmatic system geometries and the mechanisms of emplacement. For basaltic, intraplate systems such as discussed in this thesis, an incremental amalgamation of sills, either stacked or forming a funnel, is the most plausible geometry.

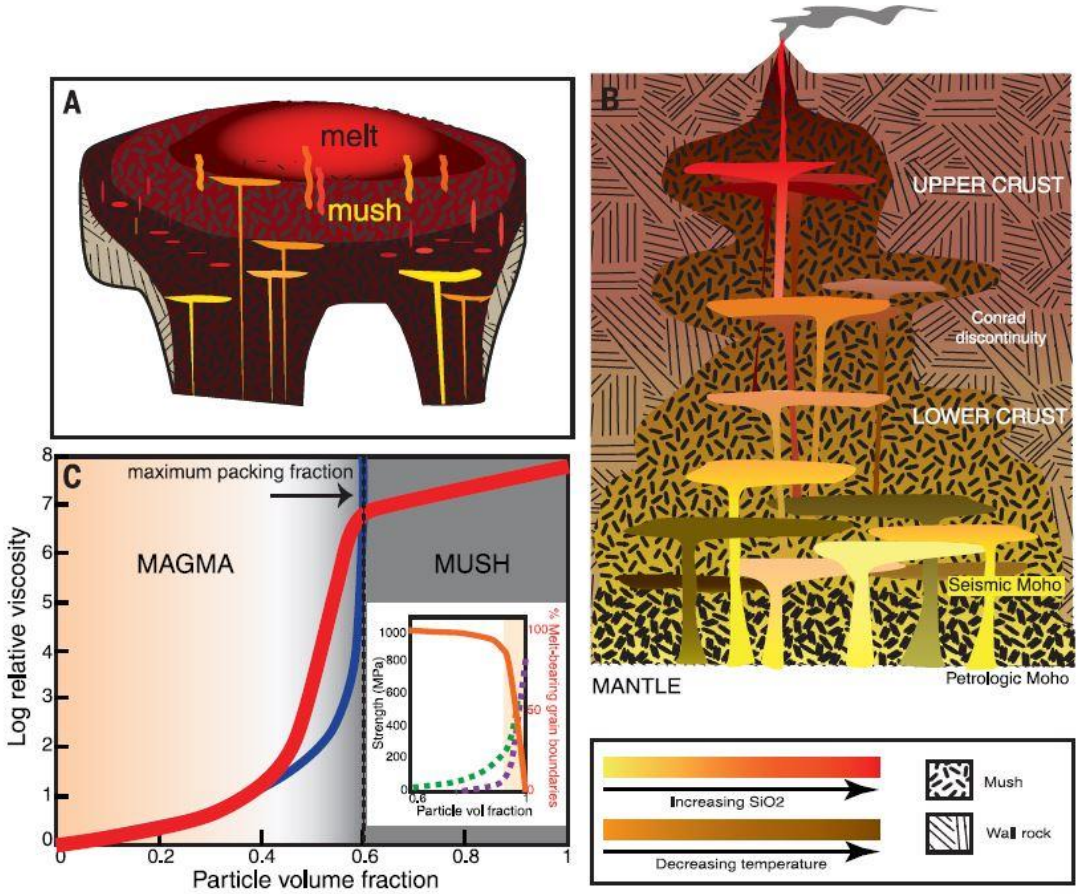

Figure 2.1 The 'mush model' (a) and dike and sill complex (b) from Cashman et al., 2017 and references therein. The rheological lock-up of a magma based on % crystallinity (c).

In their review of large magmatic reservoirs, Cashman and Giordano (2014) address the poor compatibility of a traditional mush model to basaltic systems. Instead, they use the concept of a plexus of sills and dikes (Figure 2.1) that interact spatially and temporally to produce eruptive sequences (Vinet and Higgins, 2010; Cashman and Giordano, 2014). Many have noted that the buoyant migration of melt in the middle and lower crust can incrementally accumulate in the shallow crust in this way (Solano et al., 2014; Jackson et al., 2018 and references therein).

Summary of Section 2.1

The mush model was developed for, and best applies to, large silicic systems which Banks Peninsula is not. However, the relatively limited research on crustal magmatism on Banks

Peninsula relies on many of the implications of this model. Data provided in this thesis and, in particular, Chapter 5 refine the AVC crustal magmatism model and suggest that a stacked dike and sill complex provides a better fit.

Like most volcanic systems in the world, the Akaroa Volcanic Complex does not have a well understood plutonic and volcanic relationship. This is exacerbated by the lack of exposed, *in situ* plutonic material in the AVC. The use of plutonic lithics, therefore, is critical to making observations on the AVC plutonic-volcanic connection and the observation of cumulate textures in lithics provides some of the best clues on crystal accumulation, melt segregation, and the creation of eruptible magma in the AVC.

2.2. Cumulates

2.2.1. Definitions

Many have noted that cumulates are a necessary product of a differentiating crystal mush (Marsh, 2004; Miller, 2016; Szymanowski et al., 2017) and numerous studies have attempted to reconcile cumulate chemistries and mineralogies to volcanic bulk-rock compositions.

'Cumulate' is, colloquially, a broadly defined and oft used term to describe the residual material left behind in cooling intrusions. There are different types of cumulates, however, and a plethora of mechanisms that contribute to their formation. The viability of these mechanisms is an ongoing debate within the petrologic community and one of the key themes of this thesis.

Hunter (1996) provides a detailed overview of cumulate terminology. The main distinction is between orthocumulate and adcumulate endmember textures. Orthocumulates are comprised of one or more cumulus mineral and an intercumulus liquid that crystallizes unmodified by chemical or mechanical processes (Hunter, 1996). Orthocumulates are defined by high interstitial pore material and zoned cumulus crystals which reflect closed-system growth. Post-cumulus phases are often poikilitic and diverse. The lack of modification of intercumulus liquid is considered rare and are thus associated with high accumulation rates of cumulus crystals.

The other end member is adcumulates which are the result of continual modification of the interstitial liquid by interaction with the overlying magma and continued growth of the cumulus phases (Hunter, 1996). Necessarily, adcumulates are defined by low proportions of pore material and lack the uniform growth zoning of orthocumulates. Adcumulates are formed from 'perfect' crystal fractionation whereas orthocumulates and mesocumulates have some amount of trapped liquid that evolves and crystallizes to form minerals of more evolved compositions (Morse et al., 2017). This, of course, assumes that crystal fractionation, and perhaps diffusion from mixing magmas, is the dominant process acting on the mush. The localized complexity created by the migration and reactive flow of this melt has been less rigorously applied to cumulate formation but is potentially significant in describing geochemical variations and resolving the physical complexities.

More recently, Fiedrich et al. (2017) define a cumulate as having low melt, a strong, non-random CPO, and evidence of intracrystalline deformation. The authors suggest that a melt portion between 20-30% is expected for a cumulate. However, they define 'melt' as the mineral population that crystallizes after rheological lockup. Picard et al. (2013) define the rheological transition based on crystal fraction, size, shape, and strain rate. They also note that a solid framework forms at 30% crystal fraction for plagioclase rather than 50% for isometric minerals (Picard et al., 2013). The Fiedrich et al. (2017) definition of melt is very limiting to microstructural studies of solid-state deformation and melt extraction where liquid fraction less than 20% are considered important to magmatic evolution and accumulation of widely dispersed melt in to an eruptible body (Solano et al., 2014; Bergantz et al., 2017).

The chemical interaction between the mush and bulk magma and the physical mechanisms of crystal accumulation and melt extraction constitute the main debate on cumulate formation and are discussed below.

2.2.2. Crystal Accumulation and Cumulate Formation

Settling of crystals or 'hindered settling' is frequently used to explain the bulk composition of volcanics and the presence or absence of crystal accumulation textures or melt segregation

mineralogies. While likely an important process in high melt fraction magmas with dense, early crystallizing phases, hindered settling has been found to be ineffective as an accumulation mechanism within crystal mushes (Holness, 2018). Although focused on large silicic systems, Holness (2018) systematically reviews some of the most common interpretations of crystal accumulation, finding that micro-settling (a form of gravitational compaction) is unlikely based on detachment kinetics and timescales. Many melt segregation processes are mechanically difficult in high silica system (Holness, 2018). In early stages of magmatic differentiation, crystal settling may contribute to the first phases of magmatic evolution (Figure 2.2) but is unlikely to be a main driver on its own for cumulate formation.

Many have linked cumulate formation, particularly adcumulates, to compaction and melt extraction. To consider the mechanical side of Bowen's reaction series, some have argued that, in a closed system, single magma body, fractional crystallization produces a layered or compositionally zoned pluton (Lee et al., 2015). Melt must be removed from a crystallizing mush and, perhaps, the most obvious mechanism is compaction (Duchesne and Charlier, 2005; Lee et al., 2015). McKenzie (1984) used this basic idea to create a quantitative model for compaction within a melt-rich body. McKenzie (1984), in his seminal paper, describes compaction as a 'coupled process of melt migration and matrix deformation'. Compaction, or any other cumulate-forming process, requires removal of liquid from a solid framework (Solano et al., 2014).

However, the exact mechanism of crystal accumulation, cumulate formation (requiring viscous deformation), and melt extraction are poorly understood and processes such as hindered settling, compaction, and simple crystal fractionation are often suggested without being examined in detail (Holness, 2018). In addition, the necessary microstructural evidence of viscous deformation for compaction is rarely observed.

Those working on large igneous layered intrusions have identified other cumulate-forming processes including boundary layer convective flow (Figure 2.2; Holness et al., 2017; Vukmanovic et al., 2018). Holness et al. (2017) were the first to investigate quantitative microstructural evidence for compaction in cumulates and instead postulated that, in the Skaergaard Layered Intrusion, mass transport in a thin layer due to boundary layer flow

produced cumulate textures. The authors did not find evidence of intracrystalline deformation which, in a compacting mush, is linked to melt extraction (Fiedrich et al., 2017). Instead of cumulates forming at the base of a pile of settling crystals, Holness et al. (2017) propose that adcumulates form at the top of the mush and that dihedral angles in cumulates are associated with the first appearance of the liquidus phase in the last stages of crystallization (Holness et al., 2005; Holness et al., 2017).

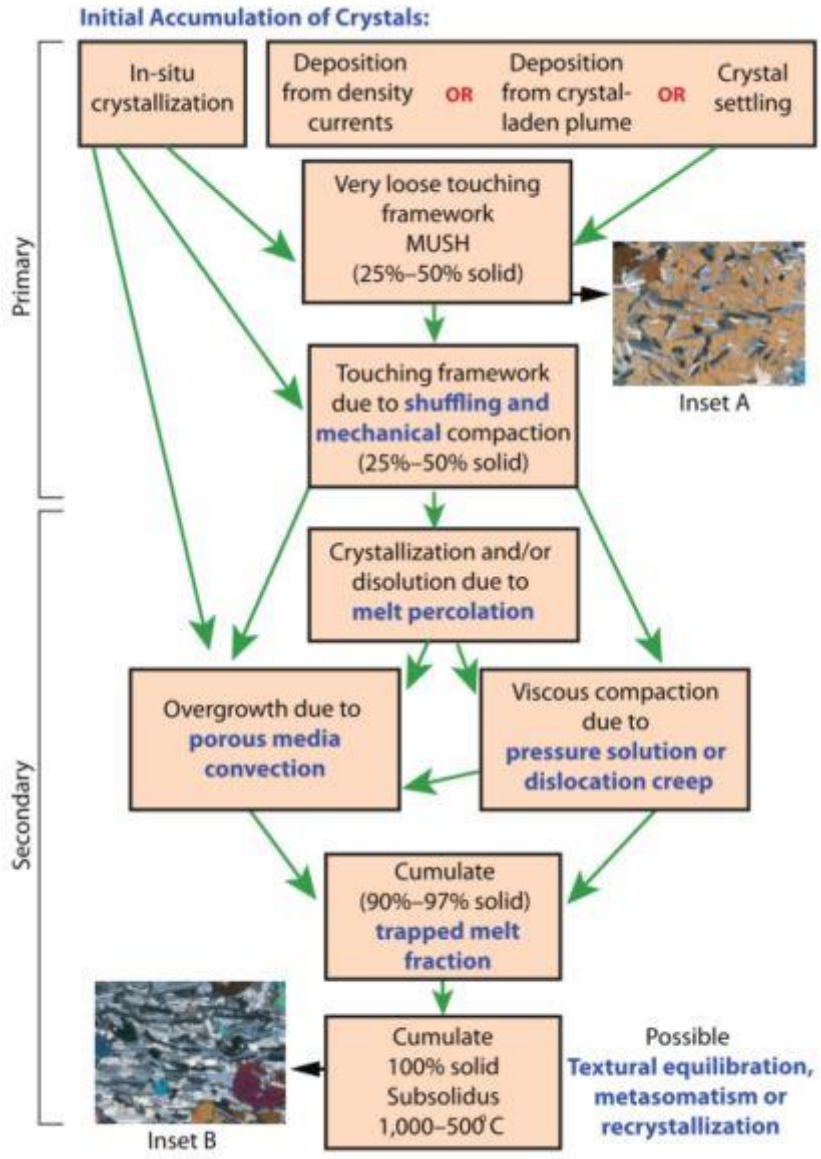

Figure 2.2 Flow chart of gabbroic cumulate formation from Morse et al. (2017). Processes separated in to 'primary' and 'secondary' that may influence cumulate microstructures.

2.2.3. Melt Segregation and Compaction

The separation of crystals and melt in crystallizing plutons is seen as a natural process for differentiating magmas to undergo (Duchense and Charlier, 2005; Dufek and Bachmann, 2010). The crystal fraction at which melt segregation is ideal is postulated to be 50-70% crystals (Dufek and Bachmann, 2010). At crystallinities above 65%, compaction becomes too slow to be a main driver for melt extraction (Bachmann and Bergantz, 2008). A crystallinity window between 45 and 65% in silicic systems is optimal for compaction induced melt segregation (Bachmann and Bergantz, 2008). If melt is removed along grain boundaries, it quenches (Marsh, 1981). However, Solano et al. (2014), using a quantitative model of component transfer, note that compaction is important at melt fractions less than 10% in the effective removal of buoyant melt along grain boundaries. The fundamental difference in these models is that crystal fractionation requires high melt fractions to produce the geochemical trends observed in magmatic systems while reactive flow can act effectively at low melt fractions and still produce the compositional and physical variability found in natural systems. This finding is fundamental to cumulate formation and the removal of melt that may contribute to volcanic eruptions.

Many researchers use the composition or abundance of minerals that crystallize from melt trapped in the crystal framework to investigate melt segregation and mush evolution (Fiedrich et al., 2017; Morse et al., 2017). At liquid fractions above 2%, melt is connected along grain boundaries and a permeable matrix is created (Solano et al., 2014 and references therein). The relative buoyancy of melt initiates a pressure gradient that allows the melt to flow relative to the matrix which causes the matrix to undergo viscous compaction (McKenzie, 1984). The matrix is deformed via melt-enriched creep (Solano et al., 2014), similar to the ‘wet’ deformation of Rybacki and Dresen (2000, 2004). The migration of melt along grain boundaries is an efficient transfer of heat and mass such that there is thermal and compositional equilibrium which allows melt to evolve as it migrates (Solano et al., 2014) and compaction of the crystal mush to occur (McKenzie, 1984).

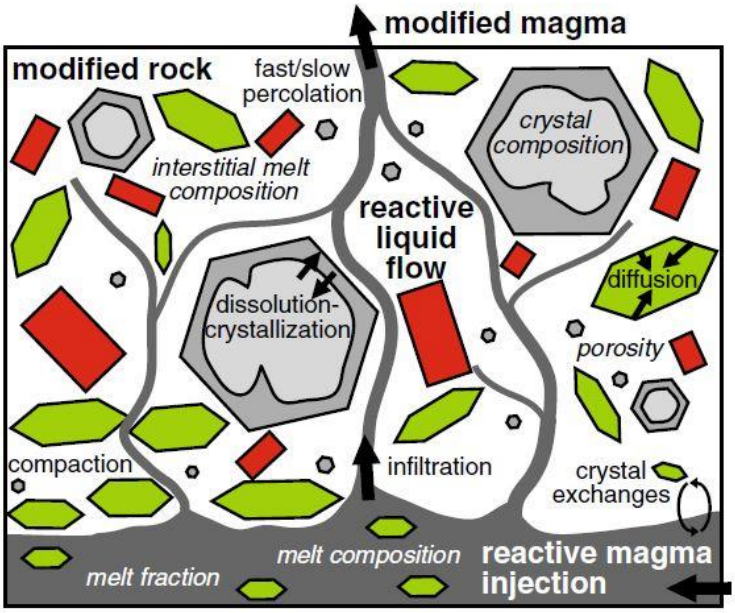

Figure 2.3 Schematic representing the effects of reactive flow and interstitial melt migration on a partially crystalline magma from Leuthold et al. (2014).

2.2.3.1. Reactive Flow and Immiscible Melts

Solano et al. (2014) apply their component transfer model to various systems to model melt migration and the formation of stratified igneous bodies and high porosity melt layers that they liken to the Rum Layered Intrusion in Scotland and the cooling of the Holyoke Flood Basalt (Connecticut, USA). The migration of melt along grain boundaries results in the exchange of heat and mass between solid and liquid fractions such that adjacent melt and crystals remain in thermal and chemical equilibrium (Figure 2.3; Leuthold et al., 2014; Solano et al., 2014). This local equilibrium may create significant chemical variation throughout the crystal mush that bulk rock compositions cannot account for. Reactive flow of melt is also critical to the formation of stacked sill igneous bodies. Importantly, Jackson et al. (2018) find that high melt fraction layers can form in response to changes in bulk magma composition as well as heat inputs.

In numerical models, melt differentiates in a crystal mush and segregates in to incompatible enriched melt at the top and depleted minerals at the base of a mush in response to each intrusion of heat and magma (Jackson et al., 2018). The interplay of heat transfer, bulk magma and melt

disequilibrium, buoyant melt migration, and reactive alteration of local composition causes incrementally growing and segregating bodies of mush and thin melt layers to form. The dichotomy of evolved melt-rich layers and mushes with compositions similar to the composition of an intruding primitive magma constitutes the Daly Gap (i.e. a compositional gap in erupted material that may be represented in the plutonic record) found in many oceanic volcanic systems (Jackson et al., 2018).

Freundt-Malecha et al. (2001) found evidence for intermediate magma generation in presence of intermediate plutonic clasts in erupted rhyolites in an oceanic system, suggesting that a Daly Gap may be a reflection of the inability of intermediate magmas to erupt rather than an inability to create them. Additionally, they found evidence for percolation of interstitial fluids in variations in trace elements in the volcanic suite (Freudnt-Malecha et al., 2001). Meade et al. (2014) suggested instead that bimodality may be the result of progressively inhibited crustal assimilation as the magmatic system forms and grows. These, and a reactive flow model may all contribute to the presence of a Daly Gap at the AVC.

Liquid immiscibility (a more specific type of melt percolation characterised by the presence of high silica and low silica melt end members) has been used to describe the formation of layering in igneous layered intrusion such as the Skaergaard (Jakobsen et al., 2005; Charlier et al., 2011; Namur et al., 20152005; Charlier et al., 2011; Namur et al., 2015). In the Skaergaard Layered Intrusion, Holness et al. (2017) identify symplectites characterized by fine-grained intergrowths of anorthite and pyroxene or olivine which grow outward from Fe-Ti oxides and replace cumulus plagioclase. They also describe ‘illmenite-rich polymineralic pockets’. Further up in the layered intrusion, granophyre (intergrown quartz and alkali feldspar) is found. The authors use the presence of such reactive textures to indicate that open system conditions prevailed in the Skaergaard and attribute the granophyre texture to a late-stage, highly evolved silicic melt (Holness et al., 2017). The zoning patterns seen in the cumulus minerals are also attributed to the trapped interstitial melt (Holness et al., 2017). Namur et al. (2015) suggest that the presence of Fe-Ti oxides in all layers of the Skaergaard and the observation of reactive textures like symplectites and plagioclase zoning may reflect the presence of immiscible liquids.

Summary of Section 2.2

A concerted effort has recently been made to reacquaint the igneous petrology community with the more rigorous definitions of cumulates and to prove or disprove the mechanisms of cumulate formation in natural samples (Holness et al., 2017; Vukmanovic et al., 2017; Holness, 2018). This is especially important in relation to hindered settling and viscous compaction where these processes are frequently assigned to igneous textures (or, more concerningly, just igneous compositions) without a microstructural investigation in to the crystal orientations. Chapters 3 and 4 of this thesis specifically explore the physical processes responsible for cumulate formation and melt extraction in plutonic lithics with cumulate-like mineralogies, chemistries, and textures.

The influence of the reactive flow of immiscible melts is also of importance, both to the formation of cumulates in the AVC and to the presence of the Daly Gap in Akaroa volcanics. Chapter 5 explores the magmatic processes preserved within plutonic lithic crystal textures in conjunction with new observation of the morphology of the Akaroa Complex itself. The combination of these broad and micro scale observations coincides in support of a stacked dike and sill magmatic model where reactive flow, in conjunction with uniaxial compaction, are among the processes responsible for magmatic differentiation and cumulate formation.

2.3. Deformation and Strain Indicators

There are many types of deformation and ways that strain presents in different minerals. This research is concerned with plagioclase and the deformation that can happen within magmatic systems. Therefore, I have focussed on the deformation mechanisms most often attributed to plagioclase deformation in crustal magmatic systems: primarily, grain boundary migration in either the dislocation creep or diffusion creep regime.

2.3.1. Electron Backscatter Diffraction

2.3.1.1. Application to Igneous Petrology

Electron Backscatter Diffraction patterns are images of bands refracted from a characteristic crystalline lattice. The band angles are specific to a particular mineral phase. These patterns are matched to a database of lattice patterns and a mineral phase is identified (Prior et al., 1999). Defects and deviations from this lattice and its 3D orientation can be determined.

Plagioclase is a triclinic mineral and the low symmetry of its lattice makes it particularly challenging to index correctly. The abundance of feldspar in igneous systems initially made the application of EBSD to igneous petrology fraught with errors (Prior et al., 1999). However, the use of EBSD in describing magmatic textures and processes lends itself to simpler mineral lattices such as quartz, biotite, and zircon. Subsequent refinements in indexing accuracy allowed feldspars to be analyzed. The use of EBSD is particularly prevalent in the layered intrusion literature where it is used to conduct microstructural analysis of crystals in differentiated layers to decipher the process of segregation and evolution (Cheadle and Gee, 2017; Holness et al., 2017; Vukmanovic et al., 2018).

There is a substantial body of literature dedicated to deformation regimes using EBSD for minerals such as quartz (Hirth and Tullis, 1992), biotite (Paterson et al., 2007; Zak et al., 2007; 2008), calcite (Bestmann and Prior, 2003), and zircon (Kovaleva et al., 2016). The literature on feldspar deformation is largely focussed on metamorphic or tectonically deformed lower crustal samples (Rosenberg and Stunitz, 2003; Beane and Field, 2007; Svahnberg and Piazolo, 2010; Zhou et al., 2012; Negrini et al., 2014; Okudaira et al., 2015; Miranda et al., 2016; among others). The remaining studies for feldspar deformed under magmatic conditions can be split in to experimental and natural studies.

2.3.1.2. Plagioclase

The majority of plagioclase EBSD literature comes from experimental and natural metamorphic studies. The pressure-temperature conditions of such systems are often well constrained or can

be determined from key minerals (ex. garnet, zircon). As plagioclase is triclinic, it poses additional challenges to EBSD indexing, therefore, the initial exploration of plagioclase deformation benefitted from the constraints which simpler minerals such as quartz and biotite provide in metamorphic shear zones.

2.3.1.3. Deformation Types and Mechanisms

The crystallographic challenges of plagioclase make the experimental, synthetic feldspar literature particularly key to applying strain mapping techniques to magmatically deformed plagioclase (Rybacki and Dresen, 2000; Picard et al., 2011). Experiments of feldspar deformed at conditions found in magmatic systems focus proportionally more on compression rather than shearing or twisting (Picard et al., 2011) and the effect of compression on melt fraction. Movement of magma occurs as a result of strain localization (Picard et al., 2013). Rybacki and Dresen (2000, 2004) produced experiments on wet and dry natural and synthetic plagioclase at a variety of temperature, stress, compositional, and grain size parameters to study the transition from diffusion creep to dislocation creep in grain boundary migration and dynamic recrystallization. Bergantz et al. (2017) take the relationship between deformation and melt extraction even further with numerical modelling of particle force chains and 'lock-up' conditions. Rheological lockup is a critical state in crystal mushes and varies depending on the minerals present and thermal and mass equilibration considerations. The experiments and modelling undertaken to determine rheologic lockup and its effect on melt movement are important to the larger crustal magmatism models and the generation of eruptible magma.

Outside of the experimental strain rate and deformation mechanism literature is a limited amount of research focused on plagioclase textures in magmatic systems. These studies have focused on plagioclase indicators of strain such as misorientation (Wheeler et al., 2001), CSD quantification of SPO (Romeo et al., 2007), and CPOs from EBSD analysis (Satsukawa et al., 2013; Ji et al., 2014; Miranda et al., 2016; Fiedrich et al., 2017; Holness et al., 2017; Vukmanovic et al., 2018).

EBSD produces crystallographic preferred orientations (CPOs) which are stereographic plots of the orientation of a point within a crystal lattice in reference to the sample or the crystal

orientation (ex. Figure 2.4). Analysis of CPOs is used to determine tectonic and igneous crystal fabrics. Igneous plagioclase may be tabular, prismatic, or oblate and the CPO will be influenced, to some degree, by crystal shape. Generally, a plagioclase foliation is defined by point maxima pole clusters about the [010] and great circle girdles in [100] and [001] (Figure 2.4; Satsukawa et al., 2013). Lineation is defined by a preferred alignment of [100] and is characteristic of a crystal-plastic overprint of a magmatic foliation utilizing the (010)[100] slip system common to plagioclase (Figure 2.4; Satsukawa et al., 2013; Holness et al., 2017). A shape preferred orientation (SPO) in conjunction with a CPO is convincing evidence of deformation, however, a SPO can be easily overprinted during viscous deformation (Holness et al., 2017).

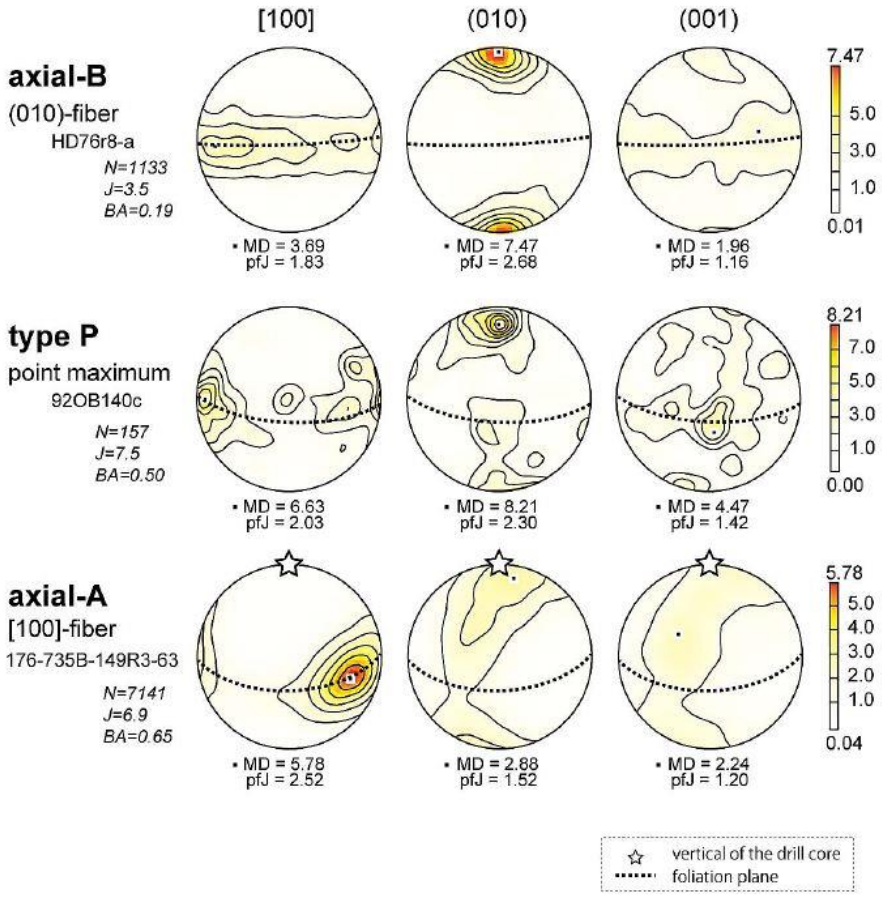

Figure 2.4 Three types of plagioclase CPOs identified by Satsukawa et al., 2013. Magmatic and tectonically deformed plagioclase CPO patterns.

Lattice misorientations are reflected in undulose extinction patterns and subgrains as well as a non-random CPO (Holness et al., 2017). Dislocation creep (which is one of the mechanisms

required for viscous lattice deformation) is always accompanied by dynamic recrystallization (i.e. the formation of new grains and recovery, or subgrains; Holness et al., 2017) which can be identified by crystal size distribution (CSD), SPO, or CPO analysis. Full recrystallization requires high temperature and strain to produce dislocation-free grains (Holness et al., 2017).

Summary of Section 2.3

There is a scarcity of microstructural studies conducted on igneous plagioclase. One of the main contributions of this thesis is to add to the scanty igneous plagioclase EBSD literature and to provide natural examples of crystals deformed via uniaxial compaction within a magmatic system (Chapter 3 and 4). Chapters 3, 4, and 5 each focus on CPOs of plagioclase in plutonic lithics. CPOs are combined with additional lattice deformation measures (Chapter 3) and petrographic features that have been linked to grain boundary migration processes (Chapters 3 and 4).

2.4. Cathodoluminescence (CL)

Cathodoluminescence (CL) has been used in igneous petrology, predominately, to image individual crystals for age and trace element analysis and to illustrate magmatic processes such as dissolution of growth conditions through zoning patterns. CL has found particular use in determining Ti contents in quartz to decipher temperature signatures.

There is a lack of clear consensus on precisely what causes luminescence and, especially, different colors in color-CL. Generally, there are activator (cause luminescence) and depressor (darken features) elements (Gotze and Kempe, 2009). Activators can be compositional or structural (e.x. lattice defects). Mora and Ramseyer (1992) found that CL activators in metamorphic anorthosite are sensitive to recrystallization and fluid interaction. Of particular interest, they also found that the red peak is sensitive to An content (Mora and Ramseyer, 1992). In a study of igneous enclaves Slaby et al. (2008) note that Ba acts as an activator through structural Al defects. They then used CL and trace element data to identify magma mixing in the enclaves (Slaby et al., 2008).

Beane and Wiebe (2012) utilize EDS and CL to study quartz clusters in the Vinalhaven granite and porphyry. They specifically investigate the orientations of quartz crystals in contact to quantify how frequent random, parallel, and Esterel twin orientations are. They conclude that synneusis, both of random and oriented clusters, occurs during crystal accumulation.

Summary of Section 2.4

This thesis uses color-CL mapping. Whole thin sections are able to be imaged and crystals directly compared because of black balancing of the image. Color-CL will be used in chapters 4 and 5 to describe features of interest to compaction and melt extraction mechanisms.

2.5. Plutonic Lithics

2.5.1. Definitions

'Plutonic lithic' is a broad term used throughout the literature to describe any igneous, magmatic (i.e. crystalline) rock found in an extrusive volcanic deposit. Graeter et al. (2015) define plutonic lithics as a holocrystalline rock that reached solidus conditions prior to or during volcanic eruption.

There are a plethora of names for similar material; enclaves, xenoliths, plutonic blocks, autoliths, mafic magmatic enclaves, microgranitoid enclaves, and plutonic lithics. Some have certain connotations or reflect specific processes: *mafic magmatic enclaves* and *microgranitoid enclaves* usually reflect magma mixing of hot mafic magma with cooler silicic magmas (Vernon and Paterson 1993; Barbarin 2005); *xenoliths* are foreign material (not necessarily magmatic) included in plutonic or volcanic rock (Bacon et al., 2007); while *autoliths* (or *cognate xenoliths)* and *plutonic blocks* are plutonic material found in pyroclastic deposits (Bacon et al., 2007). The remaining terms are more general, which is perhaps why they have been used in such diverse applications. *Enclave* is a much-used term that refers to a melt-rich magma that interacts with a resident magma and is used for both cogenetic and non-cogenetic interactions. *Plutonic lithic* has been variously used to describe solidified magmas from previous eruptive or intrusive

events, mixed magmas, roof or wall crystallization, and remnant crystal residue (see Burt et al., 1998 and Graeter et al., 2015 for examples).

Plutonic lithics that are entrained and erupted with volcanic deposits may be used to interpret magmatic processes in systems with complicated or missing exposed plutons. All terms are used to describe rocks that are texturally and chemically distinct from the rock they reside in, however, no differentiation between entrainment within other plutonic material or erupted volcanic rock is necessitated by any of the available terms. 'Plutonic lithic' does not carry any assumptions about genesis and is general enough to encompass a wide variety of plutonic material entrained in other, usually volcanic, rock, thus we have chosen this term for this thesis. We use plutonic lithic to describe plutonic igneous rocks found, specifically, in erupted volcanic rocks such as lava flows, domes, dikes, pyroclastic flows, etc.

2.5.2. Significance

In areas with little exposed plutonic material such as the AVC, plutonic lithics provide a window in to conditions and processes within the magmatic system of an active volcano (Graeter et al., 2015). While notable for their ability to reveal mixing and mingling processes (especially in granitoid plutons with mafic inclusions, Vernon, 1984; Martin et al., 2006), microstructural and geochemical analysis of plutonic lithics can reveal mush processes such as compaction, cumulate formation, and melt extraction in rocks that represent a snapshot in time. This is an advantage in systems where large, long-lived plutons may overprint primary physical processes. These processes are a direct window in to eruption-forming processes and hence, the connection between the magmatic system and the erupted deposits.

2.5.3. Traditional Approaches

The vast majority of studies on plutonic lithics (and similar, but differently named rocks) have predominately relied on geochemical relationships. The most common method being a bulk rock comparison of plutonic lithics to either its host rock (Vernon, 1984; Burt et al., 1998; Cole et al., 2001), other plutonic material (Barbarin, 2005), or other volcanic products of suspected eruptions (Bacon et al., 2007). Trace element modelling (Brown et al., 1998), isotope

geochemistry (Burt et al., 1998; Cole et al., 2001), and mineral chemistry (Burt et al., 1998; Kuscu and Floyd, 2001) or glass analyses are frequently used. There is a substantial amount of work done on magmatic textures from field-scale observations, most notably the work of Paterson et al. (1998) and others (Johnson et al., 2004; Zak and Klominsky, 2007). While many of these studies note the field relationships and petrographic information, very few studies apply quantitative textural analysis to questions about plutonic lithic origin, host relationships, and magmatic conditions prior to entrainment relying, instead, on bulk chemistry to infer magmatic conditions and processes.

A few notable exceptions exist where plutonic lithics have been studied from a quantitative textural perspective. Graeter et al. (2015) use EBSD to characterize quartz glomerocrysts, suggesting that Okataina lithics erupted in the high-silica rhyolite Kaharoa eruption from the Tarawera Volcanic Complex in the Taupo Volcanic Zone (NZ) formed from synneusis and settling of phenocrysts. Some of the studies above note the presence of glass in plutonic lithics as indicators of the level of solidification of the mush prior to entrainment but Holness et al. (2007) quantify glass abundance in plutonic lithics in detail. Microstructural analysis is an important piece of evidence to support or refute chemical signatures found in lithics but is often overlooked.

Summary of Section 2.5

Plutonic lithics have been long recognized for their value in relating eruptions to plutons or to revealing uneruptible portions of magmatic systems. However, interpretations have traditionally relied on geochemical trends alone without examining the textural evidence for the processes suggested. Chapters 3, 4, and 5 all use plutonic lithics to investigate the AVC magmatic system with a focus on microstructural analysis. The work in each of these chapters results in a better understanding of the relationship of the plutonic lithics to their host deposit, the larger AVC, as well as the conditions and processes acting on the mush. Because of this, ‘plutonic lithic’ may be too broad of a definition for these rocks. In Chapter 6, a new naming classification is suggested.

2.6. Geologic Setting

This research deals with plutonic lithics associated with the Akaroa Volcanic Complex (AVC), Banks Peninsula, New Zealand. Banks Peninsula is the site of significant intraplate volcanism in the Miocene (Figure 2.5; Timm et al., 2009). Intraplate volcanism was widespread on the South Island of New Zealand during the Miocene, most notably including the Otago Peninsula and the associated Dunedin Volcanic Field (Figure 2.5). At this time, New Zealand had rifted from Gondwana and oblique subduction accommodated by the Alpine Fault was beginning (Hoernle et al., 2006). They speculate that warping of the Pacific plate as this tectonic environment initiated caused the lithosphere to thin and centers of volcanism to develop in the Canterbury Basin and Otago Region. Timm et al. (2009) propose this model of lithospheric delamination and asthenospheric upwelling as the source of Banks Peninsula Volcanism. Ring and Hampton (2012) further speculate that reinitiated faults associated with the Chatman Rise acted as conduits for upwelling magma that focused volcanism in the modern Banks Peninsula region.

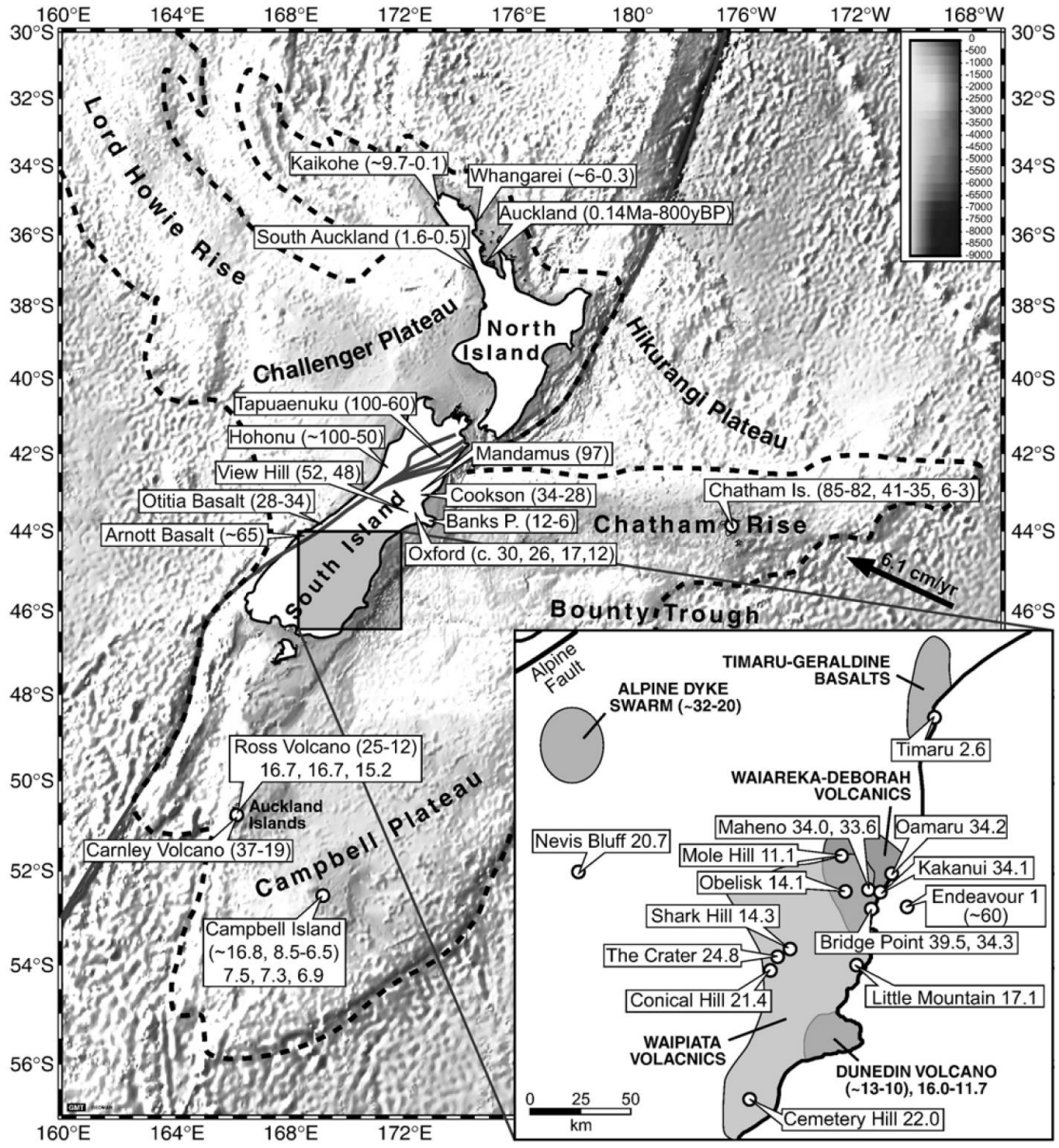

Figure 2.5 Map of ages of volcanism in New Zealand from Hoernle et al. (2006).

Magmatism at Banks Peninsula occurred in the Cenozoic during a period of substantial but dispersed volcanism in Zealandia (Timm et al., 2009). The dominant type of volcanism in the South Island was intraplate, characterized by alkaline eruptives (Weaver et al 1989; Hampton, 2010). The Mt. Herbert (9.7-8.0 Ma) eruptive sequence occurred after Lyttelton and contemporaneous with Akaroa phases (Figure 2.5). The youngest Diamond Harbour (7.0-5.8 Ma) phase was small and localized and erupted in to the already eroded Lyttelton Harbour (Hampton and Cole, 2009).

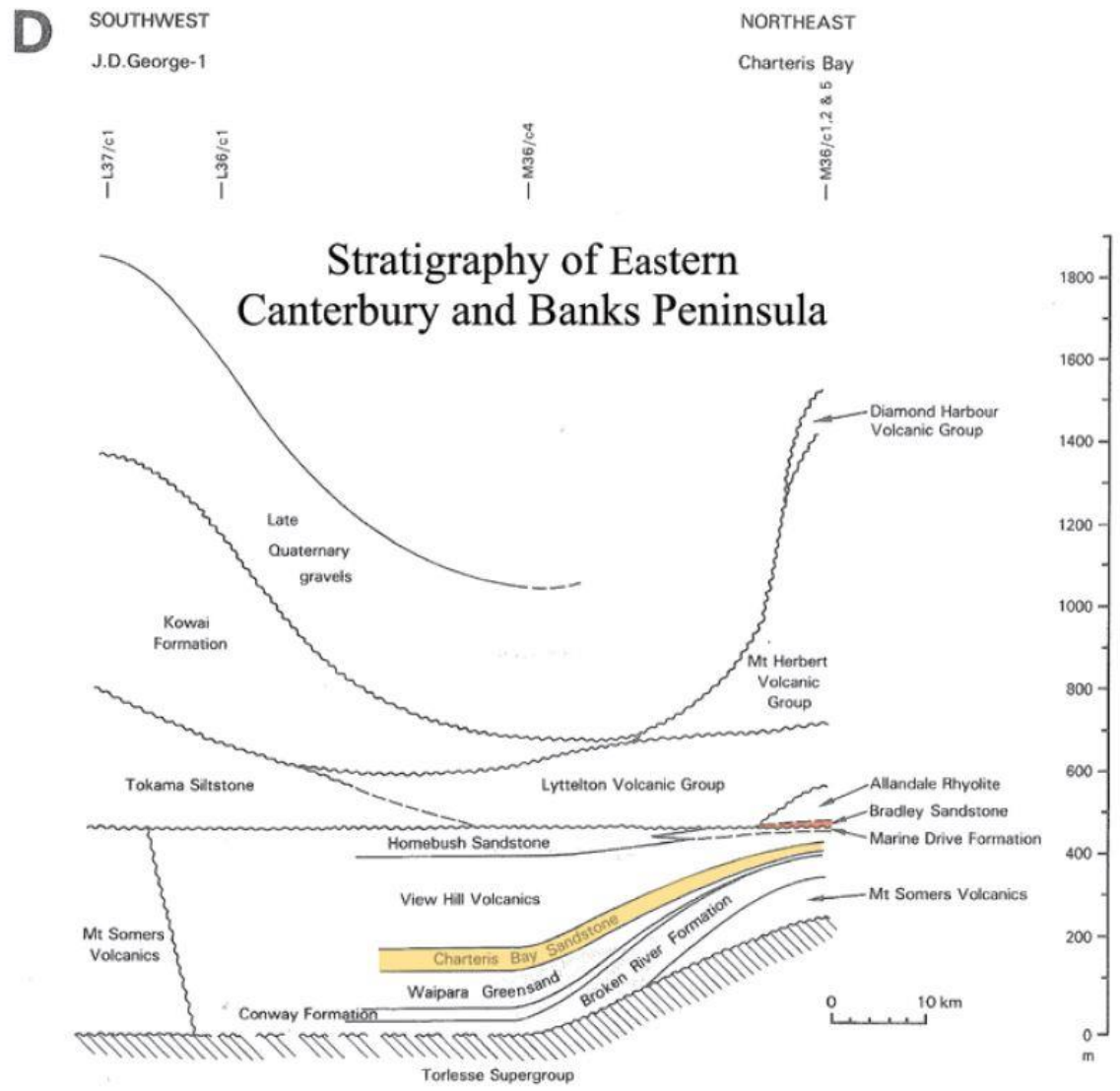

Figure 2.6 Schematic cross section of Canterbury (left) and Banks Peninsula (right) stratigraphy from Field and Browne (1985).

The Akaroa Volcanic Complex is poorly understood compared to the Lyttelton Phase although little has been anaylzed other than the tectonic setting and initial source of magmatism on the Peninsula (Weaver, 1989; Timm et al., 2009), preliminary ages (Timm et al., 2009), and a more constrained model of vent regions and the erosion history of Lyttelon Volcano (Hampton, 2010). However, the Akarao Volcanic Complex is home to a number of plutonic lithics that have been used to deduce the depth and source of AVC magmatism (Sewell et al., 1993; Hartung, 2011).

The most in-depth analysis of the AVC magmatic system was undertaken by Hartung as part of an unpublished Msc thesis (2011). Hartung used whole rock and mineral chemistry of an extensive suite of volcanic samples from, what she defined as, the early and main eruptive phases of the AVC. Geochemistry, coupled with MELTs modelling were used to create a model where primitive, mantle derived (25-30 km) magma ascends to the mid crust (15-20 km) where it stalls and differentiates. Lavas progressively erupt from this differentiating magma. The late-stage trachytes found in dikes and domes around the AVC are postulated to be a product of further magmatic ascent to the shallow crust (10-15 km) where further fractional crystallization occurs (Hartung, 2011).

Plutonic lithics (solidified portions of a magmatic system erupted with extrusive volcanic deposits) within the AVC were first documented by Dorsey in an unpublished doctoral thesis (1988). The first and only published documentation was done by Sewell et al. (1993) who notes the unusual nature of ultramafic xenoliths in LeBons Bay Peak, a large, basanite plug. Sewell attributes the xenoliths to a deeper, mantle source, primarily on geochemical evidence. Since then, Barbara Hobden analysed lithics from LeBons Bay Peak in an honours thesis (1990). Hartung (2011) expanded upon Dorsey's collection of plutonic lithics from Haylocks Bay and uses trace element modelling and mineral chemistries to deduce that the lithics and associated formation of early sequence lava flows are co-magmatic.

Hartung (2011) identifies a compositional gap between 50 and 60 SiO_2 wt % that she proposes as a Daly Gap. Mafic enclaves from Haylocks Bay are suggested to be the magmatic residue of deep-seated differentiated magmas and represent the unreputable portion of the AVC reflected in the Daly Gap. Increasingly, researchers are finding a link between melt segregation (specifically the development of immiscible melts) and compositional gaps (i.e. Daly Gap) commonly observed in volcanic systems like the Akaroa Volcanic Complex (Dufek and Bachmann, 2010; Charlier et al., 2011; Jackson et al., 2018).

Plutonic lithics investigated in this thesis all come from the AVC. Chapter 5 specifically deals with plutonic lithics in relation to their host deposit and the implications on AVC crustal magmatism.

2.7. Key Studies

A few studies are particularly relevant to this thesis and are discussed in depth here. Four studies are selected for being multi-method, microstructurally focused analyses of magmatic processes related to cumulate formation and melt segregation (Fiedrich et al., 2017; Holness et al., 2017; Holness, 2018; Vukmanovic et al., 2018). Two other studies are especially pertinent to a magmatic model that fits crustal, basaltic systems while incorporating the role of physical processes with localized melt movement in the building, structuring, and eruption-forming processes of volcanic complexes (Solano et al., 2014; Jackson et al., 2018).

Holness et al. (2017) begin by questioning the common assumption that igneous foliations and crystal fractionation are the result of compaction of the overlying mush. This process is often attributed to adcumulate formation without the microstructural evidence of viscous deformation to back it up. Additionally, this requires that the interstitial liquid in the cumulate framework has been removed, the mechanisms of which the authors investigate in this study. Holness et al. focus on gabbroic samples from layered intrusions which they propose represents general igneous systems. They are also careful to distinguish between primary processes and those that may obscure a magmatic fabric (i.e. subsolidus). In addition to a thorough review of previous cumulate-forming mechanism studies, the types of deformation at work in such systems, and the clarification of ambiguously used terms, the authors conduct a rigorous analysis of the CPO, zoning patterns, and microstructural indicators of deformation on Skaergaard layered adcumulates.

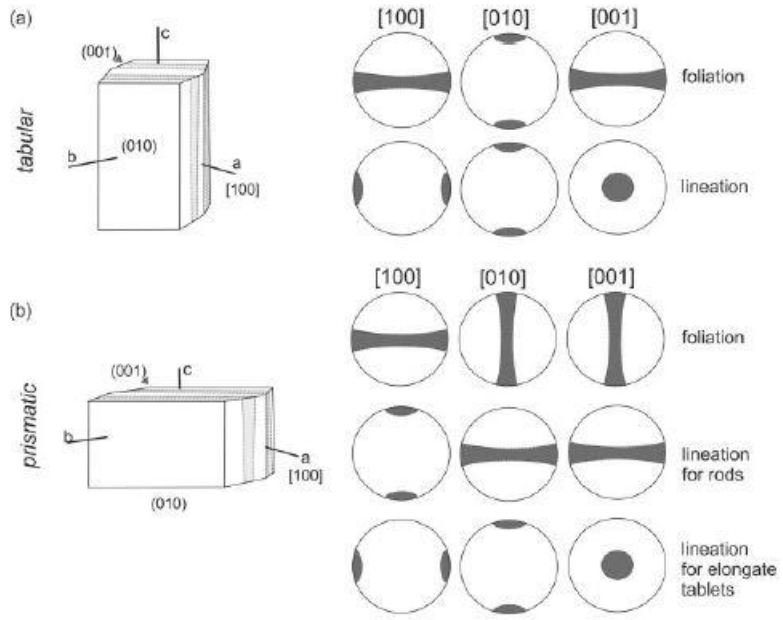

Figure 2.7 Expected lineation and foliation pole figures for tabular and elongate prisms and rods in plagioclase from Holness et al. (2017).

Plagioclase CPOs mostly correspond to fabrics characteristic of primary and secondary magmatic flow and, upwards in the layered stratigraphy, a CPO usually representative of subsolidus recrystallization in the dislocation creep regime. However, the authors find no evidence of plastic deformation in the crystals and attribute the CPO, instead, to changes in plagioclase crystal shape (Figure 2.6). Holness et al. also do not find a correlation between deformation and the amount of interstitial liquid. Instead of compaction of the already formed cumulate pile, the authors interpret the Skaergaard adcumulates as the result of primary or secondary processes acting either during crystal accumulation or at the boundary between the mush and bulk magma. In the Skaergaard, it appears that processes related to boundary layer dynamics account for cumulate formation, however, the relative thinness of the layers effectively prevent compaction of a mush pile which may be more effective in larger, slower cooling systems.

This study is seminal as a rigorous microstructural approach to cumulate formation processes to either confirm or challenge assumptions about magmatic processes made based on bulk magma geochemistry. In particular to this these, this study provides a good comparison of plagioclase CPOs, compositional patterns, and deformation indicators in gabbroic cumulates

which is particularly relevant to chapters 3 and 4. Like chapter 3, this study makes a strong call for detailed microstructural work in deciphering magmatic processes.

Holness et al. (2017) also question some of the assumptions of adcumulate formation upwards within the Skaergaard. They note that in situ fractionation of the interstitial liquid, especially an immiscible Fe-rich conjugate and subsequent loss of an Si-rich conjugate could create the appearance of adcumulates higher in the stratigraphy that are, instead, a result of buoyant migration of melt. This is an important consideration being increasingly applied to igneous systems: many of our models of magmatic evolution may be complicated by the influence of immiscible, migrating melts rather than bulk magma dynamics. This influence becomes important in the discussion in chapter 5 where we attempt to explain magmatic processes within the larger AVC system.

Vukmanovic et al. (2018) also investigate crystal accumulation in the Skaergaard Layered Intrusion. The focus of this study are trough features and a combined EBSD and chemical mapping (QEMSCAN) approach is taken to determine the magmatic processes responsible for these features. Like Holness et al. (2017), the authors of this study do not find evidence of viscous deformation, thereby ruling out compaction. In this contribution, the authors rely on field-scale observations of the morphology of the troughs to support their conclusion that the troughs are the result of primary sedimentation processes associated with magmatic flow.

Vukmanovic et al. (2018) find features characteristic of immiscible interstitial liquid migration (i.e. reactive symplectites). The amount and style of reactive features changes throughout the Skaergaard stratigraphy, reflecting the migration of the buoyant Si-rich melt, stalling of the Fe-rich melt, and retention of the Si-rich melt in the upper layers of the intrusion (as opposed to being lost completely from the system). The authors also note the association of Si-rich liquid and plagioclase and the Fe-rich liquid with mafic phases and oxides, a relationship that is significant to the discussion in chapter 4 of this thesis. The authors argue that wetting properties, as well as density, control immiscible liquid movement.

This study is another key contribution that utilizes multiple methods, with an emphasis on textural analyses, to describe magmatic processes related to crystal accumulation, cumulate

formation, and melt migration. This thesis also addresses these questions but in a system with a known volcanic counterpart in an attempt to explain the significance of cumulate formation and melt migration to the evolution of a volcanic complex.

Fiedrich et al. (2017) examine crystal accumulation textures by using textural and geochemical data from igneous plagioclase. This study is of particular relevance as it utilizes as combination of EBSD, geochemistry, and cathodoluminescence to explore compaction and melt extraction in the context of a plutonic-volcanic connection. Again, the authors argue that a textural component, in this instance a quantification of interstitial melt, is a necessary complement to geochemical analyses. An important distinction is that the authors of this study define interstitial liquid as any phases that crystallize after rheological lock-up (50%) which is different from the definition used by Holness et al. (2017) and this thesis. Note that for feldspars, which this study focuses on, rheological lockup can occur at <30% particle volume (Philpotts et al., 1999).

Regardless of the way interstitial melt is defined and calculated, the authors find a correlation between foliation strength (based on CPO) and the 'maximum trapped liquid' calculated. That is, the strongest foliation fabrics have the least preserved trapped liquid, suggesting that compaction and subsequent melt extraction occurred. This is supported by intracrystalline lattice deformation of up to 15°. They distinguish between extraction within the 'extraction window' (50-70% crystals) and 'late-stage' (due to compaction). The authors suggest that most melt extraction happened in the extraction window.

The final key study dealing with the microstructural evidence of cumulate formation and melt extraction processes is a review of these processes in silicic systems conducted by Holness (2018). Like the authors' main point in Holness et al. (2017), crystal accumulation processes such as hindered settling and viscous compaction are often assumed without specifically exploring the microstructural record. Holness (2018) argues that this is an even more common problem in silicic systems, complicated by the fact that crystal accumulation and melt extraction is much more subtle and complicated in large, silicic systems. However, these processes are especially important in understanding the mechanisms by which large rhyolitic eruptions are formed. Holness reviews three main mechanisms; hindered settling, microsettling, and viscous compaction representing the fastest to slowest processes, respectively (Bachmann and

Bergantz, 2004) as well as other, less common potential melt extraction mechanisms. This study provides important background and context to the main issues dealt with in this thesis and reviews their current state in the literature. It also provides the reader of this thesis with an understanding of some of the mechanisms referred throughout the following chapters. An examination of these processes essentially shows that all three are unlikely to be effective in silicic system. In their subsequent discussion, Holness reviews the applicability of magma recharge, gas filter-pressing, and external stresses to silicic melt extraction. These proposed processes tie well in to the next key studies that deal with reactive melt flow and its role in the construction of crustal magmatic systems.

The next two studies are of particular relevance to how the processes discussed above move eruptible melt through crustal magmatic systems. The first is a study conducted by Solano et al. (2014) that uses a quantitative model to explain component transfer and the movement of heat and mass through a crustal igneous system. The significant finding of this study is that the chemical reactions caused by local melt migration and equilibration produces major and trace element variations that are not explained by more simple, bulk geochemistry models nor heat and mass transfer models.

Five scenarios are explored, all of which allow a mush of either homogenous or heterogenous composition to compact with or without the influence of heating or cooling. The third scenario, in which a chemically homogenous mush is heated to above the solidus and allowed to compact without further heating or cooling is the most applicable to the model proposed in chapter 4 of this thesis. The result of this scenario is the formation of a melt layer that migrates through the column and causes local changes to bulk and trace element composition because of this migration of the liquid fraction.

Solano et al. (2014) use the scenarios explored by this model to discuss how mushes and replenishing magmas from depth interact to create eruptible, or at least mobile, accumulations of melt. This incrementally building plutonic system that periodically erupts evolving magmas is more in line with dike plexus models such as reviewed by Cashman et al. (2017) and seems more applicable to the AVC than traditional magma chamber models. This discussion is relevant to the magmatic model of the AVC discussed in chapter 5 of this thesis. Furthermore,

the local reactions caused by melt migration along grain boundaries may help explain the symplectites-style textures described in chapters 4 and 5.

Finally, work by Jackson et al. (2018) that builds on a crustal igneous model of reactive flow is used to provide further context to the proposed AVC model of this thesis. The authors suggest that reactive flow (i.e. the migration and local equilibration of melt and adjacent crystals) accounts for many of the discrepancies in crystal fractionation and basaltic rejuvenation models. Reactive flow is used to explain the formation and accumulation of relatively felsic magmas, the presence of older crystals caught in this migrating melt, the rapid remobilization of magma, and major and trace element variations often seen in natural systems (Figure 2.7).

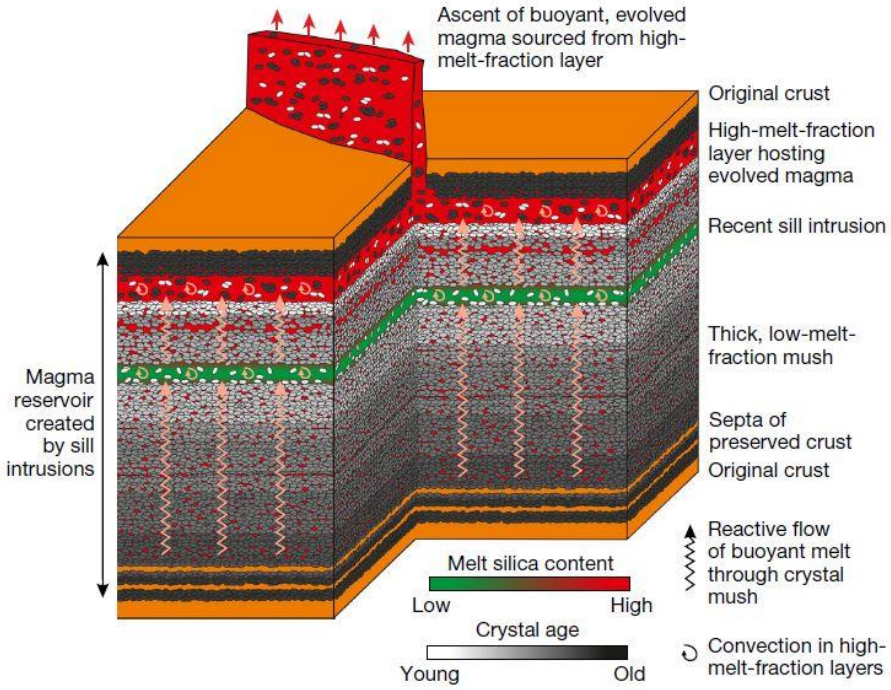

Figure 2.8 Schematic reactive flow model from Jackson et al. (2018).

The numerical model details the evolution of a mush following intrusion of hotter magma. At first, melt fraction is low and local disequilibrium creates compositional heterogeneity throughout the body. The melt fraction increases until permanent melt creates a mush state. This buoyant melt then migrates through the mush, evolving as it comes in to contact with crystals at different temperatures. The melt becomes trapped and accumulates instead of leaving the mush because of the presence of the solidus isotherm. Once the melt layer reaches at least 70%

liquid fraction, it is able to move to shallower portions of the magmatic system or erupt. This sequence is repeated, and the magmatic system grows (Figure 2.7). It is this model and additional observations from studies such as Cashman et al. (2017) and Holness et al. (2017) that provides important context for our study of compaction, cumulate formation, and melt migration and their roles in the evolution of the AVC magmatic system.

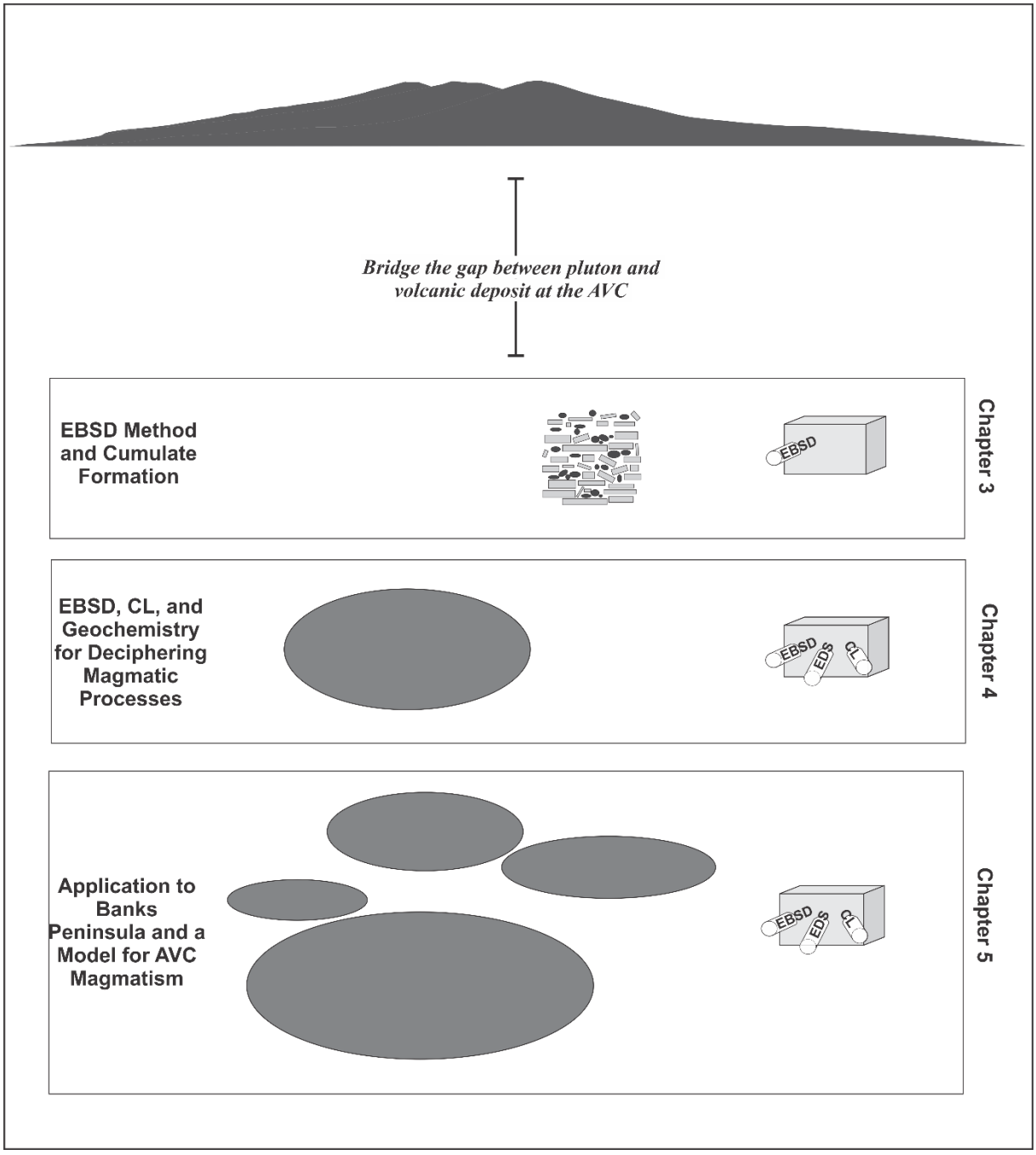

Figure 2.9 Schematic thesis layout.

REFERENCES

Annen, C., Blundy, J. D., Leuthold, J., & Sparks, R. S. J. (2015). Lithos Construction and evolution of igneous bodies : Towards an integrated perspective of crustal magmatism. *Lithos*, 230, 206–221. https://doi.org/10.1016/j.lithos.2015.05.008

Bachmann, O., & Bergantz, G. (2008). The Magma Reservoirs That Feed Supereruptions. *Elements*, 4(1), 17-21. https://doi.org/10.2113/GSELEMENTS.4.1.17

Bachmann, O., & Bergantz, G. W. (2004). On the Origin of Crystal-poor Rhyolites : Extracted from Batholithic Crystal Mushes, *Journal of Petrology*, 45(8), 1565–1582. https://doi.org/10.1093/petrology/egh019

Bacon, C. R., Sisson, T. W., & Mazdab, F. K. (2007). Young cumulate complex beneath Veniaminof caldera, Aleutian arc, dated by zircon in erupted plutonic blocks. *Geology*, 35(6), 491. https://doi.org/10.1130/G23446A.1

Barbarin, B. (2005). Mafic magmatic enclaves and mafic rocks associated with some granitoids of the central Sierra Nevada batholith, California: nature, origin, and relations with the hosts. *Lithos*, 80(1–4), 155–177. https://doi.org/10.1016/j.lithos.2004.05.010

Beane, R. J., & Field, C. K. (2007). Kyanite deformation in whiteschist of the ultrahigh-pressure metamorphic Kokchetav Massif, Kazakhstan. *Journal of Metamorphic Geology*, 25(2), 117–128. https://doi.org/10.1111/j.1525-1314.2007.00692.x

Beane, R., & Wiebe, R. A. (2012). Origin of quartz clusters in Vinalhaven granite and porphyry, coastal Maine. *Contributions to Mineralogy and Petrology*, 163(6), 1069–1082. https://doi.org/10.1007/s00410-011-0717- 1

Bergantz, G. W., Schleicher, J. M., & Burgisser, A. (2017). On the kinematics and dynamics of crystal-rich systems. *Journal of Geophysical Research: Solid Earth*, 122(8), 6131–6159. https://doi.org/10.1002/2017JB014218

Bestmann, M., & Prior, D. J. (2003). Intragranular dynamic recrystallization in naturally deformed calcite marble: diffusion accommodated grain boundary sliding as a result of subgrain rotation recrystallization. *Journal of Structural Geology*, 25(10), 1597–1613. https://doi.org/10.1016/S0191-8141(03)00006-3

Burt, R. M., Brown, S. J. A., Cole, J. W., Shelley, D., & Waight, T. E. (1998). Glass-bearing plutonic fragments from ignimbrites of the Okataina caldera complex, Taupo Volcanic Zone, New Zealand: remnants of a partially molten intrusion associated with preceding eruptions. *Journal of Volcanology and Geothermal Research*, 84(3–4), 209–237. https://doi.org/10.1016/S0377-0273(98)00039-0

Cashman, K. V., & Giordano, G. (2014). Calderas and magma reservoirs. *Journal of Volcanology and Geothermal* Research, 288, 28–45. https://doi.org/10.1016/j.jvolgeores.2014.09.007

Cashman, K. V., Sparks, R. S. J., & Blundy, J. D. (2017). Vertically extensive and unstable magmatic systems: A unified view of igneous processes. *Science*, 3055(March). https://doi.org/10.1126/science.aag3055

Chadwick, J. P., Troll, V. R., Waight, T. E., van der Zwan, F. M., & Schwarzkopf, L. M. (2013). Petrology and geochemistry of igneous inclusions in recent Merapi deposits: a window into the sub-volcanic plumbing system. Contributions to Mineralogy and Petrology, 165(2), 259–282. https://doi.org/10.1007/s00410-012-0808-7

Charlier, B., Namur, O., Toplis, M. J., Schiano, P., Cluzel, N., Higgins, M. D., Auwera, J. Vander. (2011). Large-scale silicate liquid immiscibility during differentiation of tholeiitic basalt to granite and the origin of the Daly gap. *Geology*, 10, 907-910. https://doi.org/10.1130/G32091.1

Cheadle, M. J., & Gee, J. S. (2017). Quantitative Textural Insights into the Formation of Gabbro in Mafic Intrusions. *Elements*, 13(6), 409–414. https://doi.org/10.2138/gselements.13.6.409

Cole, J., Gamble, J., Burt, R., Carroll, L.., & Shelley, D. (2001). Mixing and mingling in the evolution of andesite– dacite magmas; evidence from co-magmatic plutonic enclaves, Taupo Volcanic Zone, New Zealand. *Lithos*, 59(1–2), 25–46. https://doi.org/10.1016/S0024-4937(01)00056-1

Cooper, K. M., & Kent, A. J. R. (2014). Rapid remobilization of magmatic crystals kept in cold storage. *Nature*, 506(7489), 480–483. https://doi.org/10.1038/nature12991

Dorsey, C. J. (1988). The Geology and Geochemistry of Akaroa Volcano, Banks Peninsula, New Zealand. *University of Canterbury Doctoral Thesis*. http://ir.canterbury.ac.nz/handle/10092/7524

Duchesne, J. C. T., & Charlier, B. (2005). Geochemistry of cumulates from the Bjerkreim – Sokndal layered intrusion (S . Norway). Part I : Constraints from major elements on the mechanism of cumulate formation and on the jotunite liquid line of descent, *Lithos*, 83, 229–254. https://doi.org/10.1016/j.lithos.2005.03.004

Dufek, J., & Bachmann, O. (2010). Quantum magmatism : Magmatic compositional gaps generated by melt-crystal dynamics. *Geology*, 38 (8): 687-690. https://doi.org/10.1130/G30831.1

Fiedrich, A. M., Bachmann, O., Ulmer, P., Deering, C. D., Kunze, K., & Leuthold, J. (2017). Mineralogical, geochemical , and textural indicators of crystal accumulation in the Adamello Batholith (Northern Italy). *American Mineralogist*, 102, 2467–2483.

Field, B. D. (1989). *Cretaceous and Cenozoic sedimentary basins and geological evolution of* 227 *the Canterbury Region, South Island, New Zealand*. Lower Hutt, N.Z.: New Zealand 228 Geological Survey.

Freundt-Malecha, B. (2001). Plutonic rocks of intermediate composition on Gran Canaria: the missing link of the bimodal volcanic rock suite. Contributions to Mineralogy and Petrology, 141(4), 430–445. https://doi.org/10.1007/s004100100250

Ganne, J., Bachmann, O., & Feng, X. (2018). Deep into magma plumbing systems : Interrogating the crystal cargo of volcanic deposits, Geology, 46(5), 415-418. https://doi.org/10.1130/G39857.1.

Gençalioğlu Kuşcu, G., & Floyd, P. A. (2001). Mineral compositional and textural evidence for magma mingling in the Saraykent volcanics. *Lithos*, 56(2–3), 207–230. https://doi.org/10.1016/S0024-4937(00)00051-7

Glazner, A. F., Bartley, J. M., & Coleman, D. S. (2016). We need a new definition for magma. Eos, Transactions American Geophysical Union, 97(September), 1–9. https://doi.org/doi:10.1029/2016EO059741

Graeter, K. A., Beane, R. J., Deering, C. D., Gravley, D., & Bachmann, O. (2015). Formation of rhyolite at the Okataina Volcanic Complex, New Zealand: New insights from analysis of quartz clusters in plutonic lithics. *American Mineralogist*, 100(8–9), 1778–1789. https://doi.org/10.2138/am-2015-5135

Götze J., Kempe U. (2009) Physical Principles of Cathodoluminescence (CL) and its Applications in Geosciences. In: Gucsik A. (eds) Cathodoluminescence and its Application in the Planetary Sciences. Springer, Berlin, Heidelberg

Hampton, S. J. (2010). Growth, Structure and Evolution of the Lyttelton Volcanic Complex, Banks Peninsula, New Zealand, *University of Canterbury Doctoral Thesis*. https://doi.org/10.1130/2010.0018(02).

Hampton, S. J., & Cole, J. W. (2009). Geomorphology Lyttelton Volcano , Banks Peninsula , New Zealand : Primary volcanic landforms and eruptive centre identification. *Geomorphology*, 104(3–4), 284–298. https://doi.org/10.1016/j.geomorph.2008.09.005

Hartung, E. (2011). Early magmatism and the formation of a 'Daly Gap' at Akaroa Shield Volcano, New Zealand. *Master of Science Thesis*, University of Canterbury, 1–79. http://ir.canterbury.ac.nz/handle/10092/5584

Hildreth, W. (2004). Volcanological perspectives on Long Valley, Mammoth Mountain, and Mono Craters: Several contiguous but discrete systems. *Journal of Volcanology and Geothermal Research*, 136(3–4), 169–198. https://doi.org/10.1016/j.jvolgeores.2004.05.019

Hirth, G., & Tullis, J. (1992). Dislocation creep regimes in quartz aggregates, *Journal of Structural Geology*, 14(2), 145-159.

Hobden, B.J. (1990). The Volcanic Geology and Geochemistry of the LeBons Bay Area, Akaroa, Banks Peninsula. *Bachelor of Science Honours Thesis*, University of Canterbury.

Hoernle, K., White, J. D. L., Bogaard, P. Van Den, Hauff, F., Coombs, D. S., Werner, R., Timm, C., Garbe-Schonberg, D., Reay, A., Cooper, A. F. (2006). Cenozoic intraplate volcanism on New Zealand : Upwelling induced by lithospheric removal, *Earth and Planetary Science Letters*. 248, 335–352. https://doi.org/10.1016/j.epsl.2006.06.001

Holness, M. B. (2018). Melt segregation from silicic crystal mushes: a critical appraisal of possible mechanisms and their microstructural record. *Contributions to Mineralogy and Petrology*, 173(6), 48. https://doi.org/10.1007/s00410-018-1465-2

Holness, M. B., Cheadle, M. J., & McKenzie, D. (2005). On the use of changes in dihedral angle to decode late-stage textural evolution in cumulates. *Journal of Petrology*, 46(8), 1565–1583. https://doi.org/10.1093/petrology/egi026

Holness, M. B., Vukmanovic, Z., & Mariani, E. (2017). Assessing the Role of Compaction in the Formation of Adcumulates : a Microstructural Perspective. *Journal of Petrology*, 58(4), 643–674. https://doi.org/10.1093/petrology/egx037

Holness, M.B., Anderson, A.T., Martin, V.M., Maclennan, J., Passmore, E. & Schwindinger, K. (2007) Textures in partially solidified crystalline nodules: a window into the pore structure of slowly cooled mafic intrusions. *Journal of Petrology*, 48: 1243-1264, doi.org/10.1093/petrology/egm016

Hunter, R. H. (1996). Texture Development in Cumulate Rocks. Developments in Petrology, 15(C), 77–101. https://doi.org/10.1016/S0167-2894(96)80005-4

Jackson, M. D., Blundy, J., & Sparks, R. S. J. (2018). Chemical differentiation, cold storage and remobilization of magma in the Earth's crust. *Nature*. https://doi.org/10.1038/s41586-018-0746-2

Jakobsen, J.K., Veksler, I.V., Tegner, C., Brooks C.K. (2005). Immiscible iron- and silica-rich melts in basalt petrogenesis documented in the Skaergaard intrusion. *Geology*; 33 (11): 885–888. doi: /10.1130/G21724.1

Ji, S., Shao, T., Salisbury, M. H., Sun, S., Michibayashi, K., Zhao, W., Long, C., Liang, F., Satsukawa, T. (2014). Plagioclase preferred orientation and induced seismic anisotropy in mafic igneous rocks. *Journal of Geophysical Research: Solid Earth*, 119(11), 8064–8088. https://doi.org/10.1002/2014JB011352

Johnson, S. E., Vernon, R. H., & Upton, P. (2004). Foliation development and progressive strain-rate partitioning in the crystallizing carapace of a tonalite pluton: Microstructural evidence and numerical modeling. *Journal of Structural Geology*, 26(10), 1845–1865. https://doi.org/10.1016/j.jsg.2004.02.006

Kovaleva, E., Klötzli, U., & Habler, G. (2016). On the geometric relationship between deformation microstructures in zircon and the kinematic framework of the shear zone. *Lithos*, 262, 192–212. https://doi.org/10.1016/j.lithos.2016.07.001

Lee, C.T.A., Morton, D.M., Farner, M.J., Moitra, P., (2015). Field and model constraints on silicic melt segregation by compaction/hindered setline: The role of water and its effect on latent heat release. *American Mineralogist*, 100, 1762-1777. http://dx.doi.org/10.2138/am-2015-5121

Leuthold, J., Mu, O., Baumgartner, L. P., & Putlitz, B. (2014). Petrological Constraints on the Recycling of Mafic Crystal Mushes and Intrusion of Braided Sills in the T orres del Paine Mafic Complex (Patagonia). *Journal of Petrology*, 55(5), 917–949. https://doi.org/10.1093/petrology/egu011

Marsh, B. (2004). A magmatic mush column rosetta stone: The McMurdo Dry Valleys of Antarctica. Eos, *Transactions American Geophysical Union*, 85(47), 497. https://doi.org/10.1029/2004EO470001

Marsh, B. D. (1981). On the Crystallinity, Probability of Occurrence, and Rheology of Lava and Magma, *Contributions to Mineralogy and Petrology*, 85–98.

Martin, V. M., Pyle, D. M., & Holness, M. B. (2006). The role of crystal frameworks in the preservation of enclaves during magma mixing. *Earth and Planetary Science Letters*, 248(3–4), 787–799. https://doi.org/10.1016/j.epsl.2006.06.030

McKenzie, D. (1984). The Generation and Compaction of Partially Molten Rock. *Journal of Petrology*, Volume 25, Issue 3, Pages 713–765, https://doi.org/10.1093/petrology/25.3.713

Meade, F. C., Troll, V. R., Ellam, R. M., Freda, C., Font, L., Donaldson, C. H., & Klonowska, I. (2014). Bimodal magmatism produced by progressively inhibited crustal assimilation. Nature Communications, 5(1), 4199. https://doi.org/10.1038/ncomms5199

Miller, C. F. (2016). Eruptible magma. *Proceedings of the National Academy of Sciences*, 113(49), 13941–13943. https://doi.org/10.1073/pnas.1617105113

Miranda, E. A., Hirth, G., & John, B. E. (2016). Microstructural evidence for the transition from dislocation creep to dislocation-accommodated grain boundary sliding in naturally deformed plagioclase. *Journal of Structural Geology*, 92, 30–45. https://doi.org/10.1016/j.jsg.2016.09.002

Mora, C., Ramseyer, K., Cathodoluminescence of coexisting plagioclases, Boehls Butte anorthosite: CL activators and fluid flow paths. *American Mineralogist* ; 77 (11-12): 1258–1265.

Morse, S. A., Davidson, J. P., & Tepley, F. J. (2017). Plagioclase Zonation: An Archive of Trapped Liquid and Crustal Contamination. *Elements*, 13(6), 403–408. https://doi.org/10.2138/gselements.13.6.403

Namur O. et al. (2015) Igneous Layering in Basaltic Magma Chambers. In: Charlier B., Namur O., Latypov R., Tegner C. (eds) Layered Intrusions. *Springer Geology*. Springer, Dordrecht

Negrini, M., H. Stünitz, P. Nasipuri, L. Menegon, and L. F. G. Morales (2014). Semibrittle deformation and partial melting of perthitic K-feldspar: An experimental study, *Journal of Geophysical Research: Solid Earth*, 119, 3478–3502, doi:10.1002/2013JB010573.

Okudaira, T., Jerabek, P., Stunitz, H., & Fusseis, F. (2015). High-temperature fracturing and subsequent grain-size- sensitive creep in lower crustal gabbros: Evidence for coseismic loading followed by creep during decaying stress in the lower crust? *Journal of Geophysical Research*: Solid Earth, 120, doi:10.1002/2014JB011708.

Paterson, S. R., Fowler, T. K., Schmidt, K. L., Yoshinobu, A. S., Yuan, E. S., & Miller, R. B. (1998). Interpreting magmatic fabric patterns in plutons. *Lithos*, 44(1–2), 53–82. https://doi.org/10.1016/S0024-4937(98)00022- X

Philpotts, A. R., Brustman, C. M., Shi, J., Carlson, W. D., & Denison, C. (1999). Plagioclase- chain networks in slowly cooled basaltic magma. *American Mineralogist*, 84(11–12), 1819–1829.

Picard, D., Arbaret, L., Pichavant, M., Champallier, R., & Launeau, P. (2013). The rheological transition in plagioclase-bearing magmas. *Journal of Geophysical Research: Solid Earth*, 118(4), 1363–1377. https://doi.org/10.1002/jgrb.50091

Picard, D., Arbaret, L., Pichavant, M., Champallier, R., & Launeau, P. (2013). The rheological transition in plagioclase-bearing magmas. *Journal of Geophysical Research: Solid Earth*, 118(4), 1363–1377. https://doi.org/10.1002/jgrb.50091

Picard, D., Arbaret, L., Pichavant, M., Champallier, R., & Launeau, P. (2011). Rheology and microstructure of experimentally deformed plagioclase suspensions. *Geology*, 39(8), 747–750. https://doi.org/10.1130/G2217.1

Prior, D. J., Boyle, A. P., Brenker, F., Cheadle, M. C., Austin, D., Lopez, G., Peruzzo, L., Pott, G., Reddy, S., Spiess, R., Timms, N., Trimby, P., Wheeler, J., Zetterström, L. (1999). The application of electron backscatter diffraction and orientation contrast imaging in the SEM to textural problems in rocks. *American Mineralogist*, 84(11–12), 1741–1759.

Riley, G. N., Kohlstedt, D. L., & Richter, P. M. (1990). Melt migration in a silicate liquid-olivine system: An experimental test of compaction theory. *Geophysical Research Letters*, 17(12), 2101–2104. https://doi.org/10.1029/GL017i012p02101

Ring, U., & Hampton, S. (2012). Faulting in Banks Peninsula : tectonic setting and structural controls for late Miocene intraplate volcanism , New Zealand. *Journal of the Geological Society, London*, 169(Barnes 1994), 773–785. https://doi.org/10.1144/jgs2011-167.Faulting

Romeo, I., Capote, R., Lunar, R., & Cayzer, N. (2007). Polymineralic orientation analysis of magmatic rocks using Electron Back-Scatter Diffraction: Implications for igneous fabric origin and evolution. *Tectonophysics*, 444(1–4), 45–62. https://doi.org/10.1016/j.tecto.2007.08.006

Rosenberg, C. L., & Stünitz, H. (2003). Deformation and recrystallization of plagioclase along a temperature gradient: an example from the Bergell tonalite. *Journal of Structural Geology*, 25(3), 389–408. https://doi.org/10.1016/S0191-8141(02)00036-6

Rubin, A. E., Cooper, K. M., Till, C. B., Kent, A. J. R., Costa, F., Bose, M., Gravley, D., Deering, C., Cole, J. (2017). Rapid cooling and cold stroage in a silicic magma reservoir recorded in individual crystals, *Science*. 1156(June), 1154–1156.

Rybacki, E., & Dresen, G. (2000). Dislocation and diffusion creep of synthetic anorthite aggregates. *Journal of Geophysical Research*: Solid Earth, 105(B11), 26017–26036. https://doi.org/10.1029/2000JB900223

Rybacki, E., & Dresen, G. (2004). Deformation mechanism maps for feldspar rocks. *Tectonophysics*, 382(3–4), 173–187. https://doi.org/10.1016/j.tecto.2004.01.006

Satsukawa, T., Ildefonse, B., Mainprice, D., Morales, L. F. G., Michibayashi, K., & Barou, F. (2013). A database of plagioclase crystal preferred orientations (CPO) and microstructures- implications for CPO origin, strength, symmetry and seismic anisotropy in gabbroic rocks. *Solid Earth*, 4(2), 511–542. https://doi.org/10.5194/se-4-511-2013

Sewell, R. J., Hobden, B. J., & Weaver, S. D. (1993). Mafic and ultramafic mantle and deep crustal xenoliths from Banks Peninsula, South Island, New Zealand. *New Zealand Journal of Geology and Geophysics*, 36(2), 223–231. https://doi.org/10.1080/00288306.1993.9514570

Słaby, E., Götze, J., Wörner, G., Simon, K., Wrzalik, R., & Śmigielski, M. (2008). K-feldspar phenocrysts in microgranular magmatic enclaves: A cathodoluminescence and geochemical study of crystal growth as a marker of magma mingling dynamics. *Lithos*, 105(1–2), 85–97. https://doi.org/10.1016/j.lithos.2008.02.006

Solano, J. M. S., Jackson, M. D., Sparks, R. S. J., Blundy, J. (2014). Evolution of major and trace element composition during melt migration through crystalline mush: Implications for chemical differentiation in the crust. *American Journal of Science*, 314, 895–939. doi: 10.2475/05.2014.01

Svahnberg, H., & Piazolo, S. (2010). The initiation of strain localisation in plagioclase-rich rocks : Insights from detailed microstructural analyses. Journal of Structural *Geology*, 32(10), 1404–1416. https://doi.org/10.1016/j.jsg.2010.06.011

Szymanowski, D., Wotzlaw, J., Ellis, B. S., Bachmann, O., & Guillong, M. (2017). Protracted near-solidus storage and pre-eruptive rejuvenation of large magma reservoirs, *Nature Geoscience*, (September). https://doi.org/10.1038/ngeo3020

Till, C. B., Vazquez, J. A., & Boyce, J. W. (2015). Months between rejuvenation and volcanic eruption at Yellowstone caldera , Wyoming. *Geology*, 43(8), 695-698. https://doi.org/10.1130/G36862.1

Timm, C., Hoernle, K., van den Bogaard, P., Bindeman, I., & Weaver, S. (2009). Geochemical evolution of intraplate volcanism at Banks Peninsula, New Zealand: Interaction between asthenospheric and lithospheric melts. *Journal of Petrology*, 50(6), 989–1023. https://doi.org/10.1093/petrology/egp029

Upton, B. G. ., Semet, M. ., & Joron, J.-L. (2000). Cumulate clasts in the Bellecombe Ash Member, Piton de la Fournaise, Réunion Island, and their bearing on cumulative processes in the petrogenesis of the Réunion lavas. Journal of Volcanology and Geothermal Research, 104(1–4), 297–318. https://doi.org/10.1016/S0377-0273(00)00212-2

Vernon, R. H. (1984). Microgranitoid enclaves in granites—globules of hybrid magma quenched in a plutonic environment. *Nature*, 309(5967), 438–439. https://doi.org/10.1038/309438a0

Vernon, R.H. & Paterson, S.R., (1993). The Ardara pluton, Ireland: deflating and expanded intrusion. *Lithos*, 31, 17-32.

Vinet, N., & Higgins, M. D. (2010). Magma Solidification Processes beneath KilaueaVolcano, Hawaii : a Quantitative extural and Geochemical Study of the 1969 - 1974 Mauna Ulu Lavas, *Journal of Petrology*, 51(6), 1297–1332. https://doi.org/10.1093/petrology/egq020

Vukmanovic, Z., Holness, M. B., Monks, K., & Andersen, J. C. Ø. (2018). The Skaergaard trough layering: sedimentation in a convecting magma chamber. *Contributions to Mineralogy and Petrology*, 173(5), 43. https://doi.org/10.1007/s00410-018-1466-1

Weaver, S.D., and Smith, I.E.M. (eds.), 1989. New Zealand Intraplate Volcanism. Intraplate Volcanism in Eastern Australia and New Zealand. 157-188.

Wheeler, J., Prior, D., Jiang, Z., Spiess, R., & Trimby, P. (2001). The petrological significance of misorientations between grains. *Contributions to Mineralogy and Petrology*, 141(1), 109–124. https://doi.org/10.1007/s004100000225

Wolff, J. ., Grandy, J. ., & Larson, P. . (2000). Interaction of mantle-derived magma with island crust? Trace element and oxygen isotope data from the Diego Hernandez Formation, Las Cañadas, Tenerife. Journal of Volcanology and Geothermal Research, 103(1–4), 343–366. https://doi.org/10.1016/S0377-0273(00)00230-4

Žák, J., & Klomínský, J. (2007). Magmatic structures in the Krkonoše–Jizera Plutonic Complex, Bohemian Massif: evidence for localized multiphase flow and small-scale thermal–mechanical instabilities in a granitic magma chamber. *Journal of Volcanology and Geothermal Research*, 164(4), 254–267. https://doi.org/10.1016/j.jvolgeores.2007.05.006

Žák, J., & Klomínský, J. (2007). Magmatic structures in the Krkonoše–Jizera Plutonic Complex, Bohemian Massif: evidence for localized multiphase flow and small-scale thermal–mechanical instabilities in a granitic magma chamber. *Journal of Volcanology and Geothermal Research*, 164(4), 254–267. https://doi.org/10.1016/j.jvolgeores.2007.05.006

Žák, J., Verner, K., & Týcová, P. (2008). Grain-scale processes in actively deforming magma mushes: New insights from electron backscatter diffraction (EBSD) analysis of biotite schlieren in the Jizera granite, Bohemian Massif. *Lithos*, 106(3–4), 309–322. https://doi.org/10.1016/j.lithos.2008.08.006

Zhou, Y., Rybacki, E., Wirth, R., He, C., & Dresen, G. (2012). Creep of partially molten fine-grained gabbro under dry conditions. *Journal of Geophysical Research: Solid Earth*, 117(B5), n/a-n/a. https://doi.org/10.1029/2011JB008646

Chapter Three – Determining the fabric forming mechanism for crystal alignment in plutonic lithics

This chapter constitutes the first of three main sections of this thesis and answers objective 2: *determining the fabric forming mechanism for crystal alignment in plutonic lithics using microstructural analysis.*

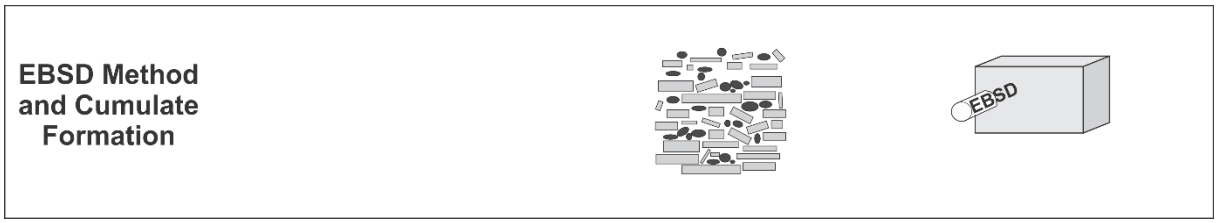

From Figure 2.9 showing the relevant section to this chapter.

The findings of this study provide important textural evidence for uniaxial compaction and melt extraction as a cumulate forming mechanism – a process commonly invoked but not previously backed by direct physical evidence. In this study, we identify textural indications of dislocation creep in conjunction with a foliation-style plagioclase CPO and rotation axis pattern. This is important in definitively attributing compaction to cumulate formation. Others rarely undertake a microstructural analysis to back up geochemical evidence of compaction and melt extraction and, in those that do, a foliation-type CPO does not always contain solid state dislocation creep deformation features, thereby ruling out uniaxial compaction which requires deformation of the crystal lattice. The addition of rotation axis analysis takes this one step further in confirming lattice deformation within the foliation plane. In addition, preliminary evidence of melt removal is correlated to CPO strength, suggesting melt extraction accompanied compaction: a key process required for compaction-induced cumulate formation.

The following is a modified format of the article published in *Geology* in March 2019.

Compacted Cumulates Revealed by Electron Backscatter Diffraction Analysis of Plutonic Lithics

E.M. Bertolett[1], D.J. Prior[2], D.M. Gravley[1], S.J. Hampton[1], B.M. Kennedy[1]

[1]Department of Geological Sciences, University of Canterbury. West Building, Private Bag 4800, Christchurch 8140, New Zealand

[2]Department of Geology, University of Otago. PO Box 56, Dunedin 9054, New Zealand

ABSTRACT

Cumulates, exposed as plutonic lithics in a volcanic host, provide insight in to the storage conditions, evolution, and eruptibility of an otherwise invisible magmatic system. Here, we present electron backscatter diffraction (EBSD) analysis of plagioclase-rich cumulates erupted from the Akaroa Volcanic Complex in New Zealand. Plagioclase {010} is clustered normal to foliation with girdle distributions of {100} and {001}. This crystallographic preferred orientation (CPO) does not definitively distinguish magmatic compaction from flow. However, the rotation axes of distortion for plagioclase observed in this study lie in the foliation plane, indicating compaction drove both crystal organization and further deformation in the solid-state. As such, we propose that these lithics represent cumulates formed first from uniaxial compression involving alignment of shaped grains by rigid rotation in magma, followed by grain distortion by dislocation creep and accompanying grain boundary migration associated with melt expulsion. Petrographic evidence of decreasing glass abundance with increasing fabric strength further confirms melt extraction. Our quantitative microstructural analysis on the preferred orientation and deformation of plagioclase grains in erupted gabbroic lithics is an important complement to more traditional geochemical approaches and improves our

understanding of how crystal mush evolution is physically linked to melt extraction and, possibly, volcanic eruption.

INTRODUCTION

Plutonic lithics are sampled from magma bodies by volcanoes and, hence, form the important and elusive connection between magmatic and volcanic systems. Geochemical studies have dominated research in this field beginning with Bowen (1928). Instead, we use microstructural analysis as a powerful, quantitative tool that directly relates physical crystal relationships within volcanic deposits to magmatic processes. This study is the first to link microstructural deformation within the magmatic system to erupted deposits via plutonic lithics which provides a more complete picture of the evolution of magma from the plutonic to volcanic realm.

Plutonic lithics (xenoliths, cumulates, enclaves) may represent the bulk liquid or the crystal residue of magmatic bodies that reached solid or near solid-state conditions. Crystal phases in plutonic lithics accumulate by crystallization, crystal settling, magmatic flow, and/or compaction (Sewell et al., 1993; Burt et al., 1998; Bacon et al., 2007; Graeter et al., 2015). In concert with these processes of crystal accumulation, interstitial melt can be extracted and stored separately (*cf*. mush model; Bachmann and Bergantz, 2008), and ultimately erupt.

In this study, gabbroic plutonic lithics were sampled from Goat Rock Dome, a trachy-andesitic lava dome on the flank of the extinct Akaroa Volcanic Complex (AVC) (Figure 3.1A). Lithics were discovered following a rockfall event during the Canterbury Earthquake Sequence (September 2010). The lithics exhibit a strong foliation defined by framework-forming plagioclase (40%, Figure 3.1B) and, to a lesser extent, pyroxene (13%), and olivine (14%). We use a combination of crystallographic preferred orientations (CPOs) and microstructures to determine the magmatic processes responsible for plagioclase accumulation and alignment.

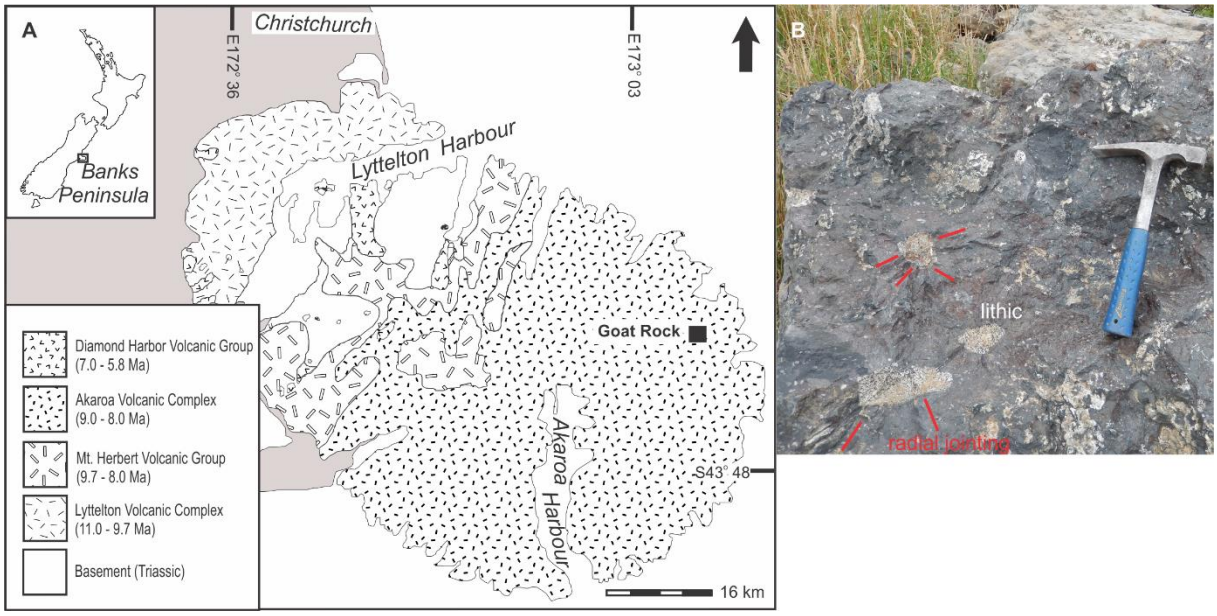

Figure 3.1 (A) Map of Banks Peninsula in New Zealand (inset). Akaroa Volcanic Complex (AVC) designated by grey shading. Black square shows Goat Rock (43°43'13.48"S 173°3'58.48"E). (B) Field photo of rockfall slab with 3+ lithics present. Red lines indicate radial jointing at the contact between lithic and host.

ELECTRON BACK-SCATTER DIFFRACTION ANALYSIS

The microstructures of lithics with the most conspicuous plagioclase alignment (*e.g.* Figure 3.1B) were quantified using Electron Backscatter Diffraction (EBSD). EBSD enables mapping of crystallographic orientations (Prior et al., 1999), which in the last decade has been applied more frequently to igneous rocks and illuminated processes that include magmatic flow, cumulate and glomerocryst formation (*i.e.* synneusis vs crystal growth), and melt extraction (Žák et al., 2008; Beane & Wiebe, 2012; Satsukawa et al., 2013; Ji et al., 2014; Graeter et al., 2015; Fiedrich et al., 2017; Cheadle and Gee, 2017; Holness et al., 2017). The application of EBSD to plagioclase in plutonic lithics is limited but critical in determining how magmas separate and erupt- a problem that geochemistry alone is unable to answer without this textural context.

Goat Rock plutonic lithics contain elongate plagioclase crystals up to 10 mm that define a planar foliation (all data that follows refers to plag). EBSD maps were collected from entire polished

thin sections of five samples (see Appendix) using a step size of 50µm with one sample (GR8b) remapped at a higher resolution (5µm step). All CPOs are characterized by point maxima of the {010} perpendicular to foliation and great circle girdle distributions of the {100} (Figure 3.2A). Generally, poles to {001} are also distributed about a great circle. The following data in this paper refers to the representative sample, GR8b.

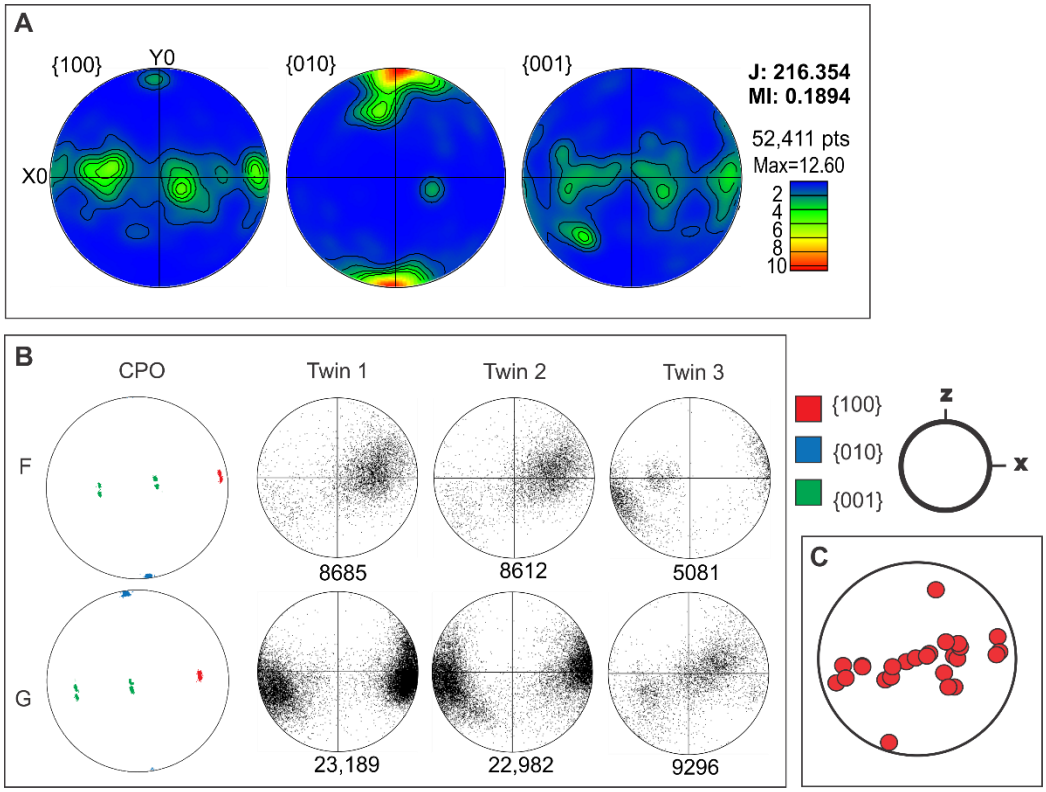

Figure 3.2 (A) Equal area, lower hemisphere stereonets of the poles to principal plagioclase planes sample GR8b (representative of the cumulate lithics of this study). Contours are in multiples of uniform density. Contours and maximum densities reflect differences in strength of CPO. (B) Individual crystal orientations and rotation axes calculated from random pairs of points within individual twin domains, sample GR8b. All plots are equal area, lower hemisphere projections. Misorientation axes are limited to 3-10° rotation. Plagioclase orientations labelled by color. (C) Stereonet showing the positions of the maxima in rotation axis plots for all twin domains in eight individual grains (all data in Appendix). Individual grains and twins have distinctive rotation axes controlled both by the stress kinematics and the slip system of that specific twin. See Appendix for the same plot within the crystal reference frame.

Misorientations are differences in the crystal orientation of different points in a crystal lattice (Figure 3.2 Appendix). Intragrain misorientation transects reveal individual plagioclase grains

are continuously distorted up to 10˚ corresponding to bent twin boundaries and undulatory or patchy extinction (Figure 3.1C). Boundaries between plagioclase grains are irregular and sometimes lobate (Figure 3.1C). Plagioclase crystals impinged on by other grains are common and are visibly bent (Figure 3.1C).

The conventional approach of plotting misorientations of neighboring pixels gives large errors on rotation axis orientations, as misorientation angles between neighboring pixels are very small (Prior, 1999). Therefore, we plotted the orientation of rotation (misorientation) axes calculated from randomized pairs of points within individual twins in the sample reference frame (Figure 3.2B, Michels el al., 2015). Rotation axes from individual twins generally form tight point clusters (Figure 3.2B) although some have double clusters or more smeared distributions (see Appendix). Importantly, when all twin sets from all grains are taken together, rotation axes align along a shared great circle perpendicular to the maximum in the {010} (Figure 3.2C).

ALIGNMENT AND DEFORMATION DURING UNIAXIAL COMPRESSION

Crystal Organization in Magmatic Fabrics

EBSD studies on magmatic fabrics have focused on minerals such as quartz, olivine, and biotite (Romeo et al., 2007; Žák et al., 2008; Beane & Wiebe, 2012; Graeter et al., 2015), whereas studies on magmatic plagioclase CPOs are rare (Satsukawa et al., 2013, Ji et al., 2014, Holness et al., 2017; Fiedrich et al., 2017).

Observations of orthogonal cuts of Goat Rock lithics in hand sample are consistent with elongate plagioclase shapes in 3D (*i.e.* a>b>c). Plagioclases are mostly elongate normal to {010} (see Appendix) and have average axial ratios, measured in the thin section plane, of 2.7. This is likely an underestimate of the ratio of the long and intermediate axes in the plane perpendicular to {010}. Lithics have very distinct plagioclase CPOs (Figure 3.2A) that are

characteristic of elongate crystals that have been mechanically rearranged to form a foliation via uniaxial shortening (Figure 3.3A, Axial-B of Satsukawa et al. (2013) and Type A of Ji et al. (2014)). Weak lineation fabrics may also have this CPO, however, elongate crystals in a flowing medium are generally characterized by clusters in all three directions ({100}, {010}, and {001}) orthogonal to each other (Figure 3.3B). Goat Rock CPOs are best explained by elongate crystals that were free to arrange themselves within a foliation plane with no constraint on a preferred direction (Figure 3.3A). Rotation axis orientations provide a means of definitively distinguishing CPOs that may be attributed to compaction or weak magmatic flow.

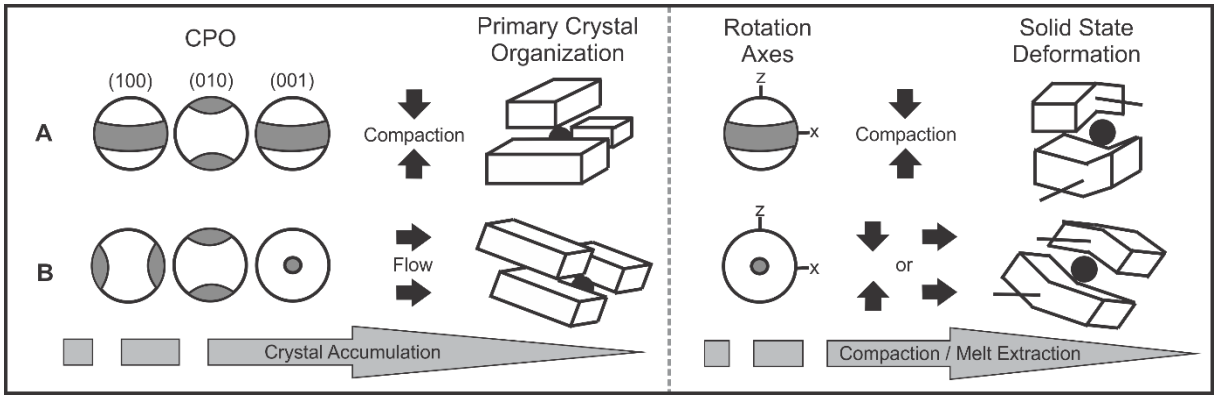

Figure 3.3 Schematic diagram depicting the ideal CPO and rotation axis orientations under magmatic flow and compaction. Left side of the diagram refers to the primary organization of crystals, best evident in CPOs while the right side refers to deformation in the solid state reflecting internal crystal deformation. (A) Scenario in which accumulating crystals are mechanically arranged by flattening, followed by continued uniaxial compression in the solid state. (B) Cumulate formation initially controlled by flow. The initial organization of crystals in this state determines the way in which crystals deform in the solid state and will display a distinct pattern of rotation axes under either (secondary) flow or compaction.

Magmatic Compaction vs Flow in the Solid State

An important distinction can be made between the organization of crystals under liquid-rich conditions and the intra-crystalline deformation that occurs with continuing stress after rheological lock-up (Arzi, 1978; Paterson et al., 1989; Philpotts et al., 1999). The former is within the presence of melt and any further crystal growth will reflect this stress (*i.e.* chemical

zoning will by asymmetric, Holness et al., 2017) while the latter refers to the kinematics of crystallographic deformation in the solid or near solid state.

The CPOs have a cylindrical symmetry consistent with uniaxial compaction. Furthermore, microstructural indicators such as bent crystals and lobate grain boundaries indicate compaction accommodated by grain boundary migration in the dislocation creep regime (Figure 3.1C, (Rybacki & Dresen, 2000)). As soon as a rigid framework of crystals is formed (< ~33% crystals, (Philpotts, et al., 1996)), grains interact (*i.e.* bend and rotate) during continued uniaxial compaction and remaining melt expulsion (Figure 3.3). The spread of rotation axes related to plagioclase distortion in the foliation plane (Figure 3.2C) is consistent with uniaxial stress and continued compaction in the solid state (Figure 3A).

Under compaction, crystals are free to deform internally without the constraint of a secondary direction (other than the direction of uniaxial compression). Rotation axes of all twins will be related by a shared great circle (Figure 3.2C), reflecting the plane in which compacting crystals can bend and rotate as they are compressed (Figure 3.3A). In a system initially organized by magmatic flow, rotation axes will be aligned within the foliation plane *i.e.* all points from each twin in a sample will plot in the same place (Figure 3.3B). GR8B rotation axes of all twins and crystals analyzed do not share the same orientation, instead they are dispersed across orientations connected by a great circle (*i.e.* a plane, Figure 3.2C). This indicates that a uniaxial compressional stress controlled both the organization and deformation of plagioclase crystals, with no indication of magmatic flow or simple shear.

Compaction as an Adcumulate Forming Process

Extensive solid-state deformation (petrographic features, Figure 3.1C) in a compacting regime suggests that Goat Rock plutonic lithic fabrics reflect adcumulate formation. Strong CPOs and the persistence of rotation axes indicative of uniaxial compression make it clear that Goat Rock

plutonic lithics were subject to a compacting stress throughout both their organization and sub-solidus deformation (*i.e.* cumulate formation during melt extraction (Hunter, 1996; Schmidt et al., 2012)). While cumulate textures, due to their strength, may completely overprint initial crystal organization (Holness et al., 2017), we observe evidence of cumulate forming processes creating both the initial CPO and further reduction in porosity necessary for cumulate formation (Figure 3.3A). Petrographic observations of the cumulate lithic (GR8b) reveals no preserved inter-grain glass (*i.e.* interstitial melt, Figure 3.4C). In contrast, a plutonic lithic with a similar but weaker CPO (GR14, Figure 3.4A) and more silicic composition, hypothesized to have resided further 'upwards' in the magmatic system, has 7% glass (Figure 3.4B). We propose that compressional stresses acted on the system as crystals came together from settling through to deformation of the crystal pile during cumulate formation and a decreasing melt component (Table 3 Appendix, Bachmann et al., 2007 and references therein; Fiedrich et al., 2017).

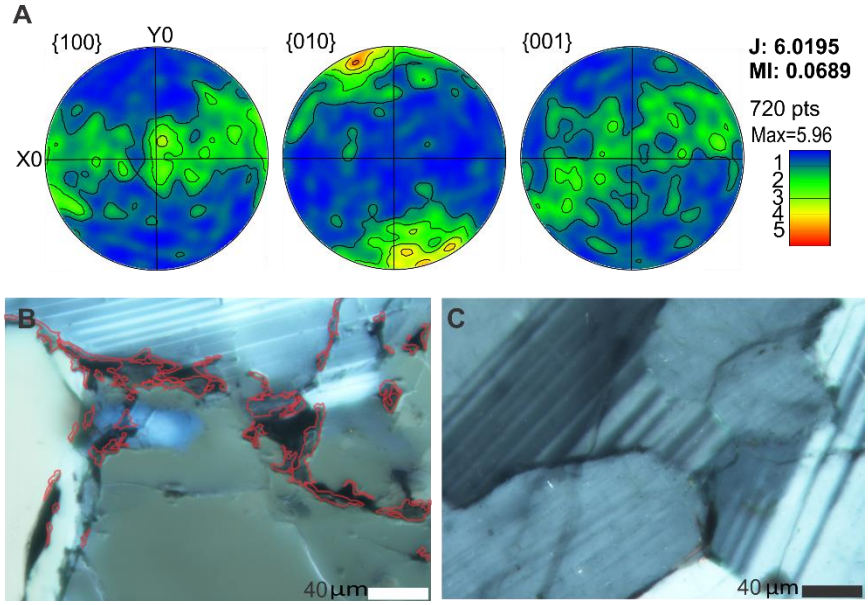

Figure 3.4 (A) Equal area, lower hemisphere stereonets of the poles to principal plagioclase planes sample GR14, a lithic with a more silicic mineralogy than GR8b. Note that the CPO pattern is similar for both GR8b and GR14 but that GR8b (Figure 3.2A) has a much stronger CPO (J and MI). (B-C) Cross-polarized photomicrographs of (B) GR14 lithic with interstitial melt (7%) outlined in red (cf. Holness et al. 2007) and (C) GR8b lithic with plagioclase-plagioclase grain boundaries and absence of melt (i.e. the cumulate).

The extraction and potential pooling of melt during porosity reduction (Bachmann et al., 2007; Bachmann & Bergantz, 2008, Cashman & Giordano, 2014; Cooper & Kent, 2014) are important stages in the development of magma that can ultimately erupt. The identification of features indicative of magmatic compaction and cumulate formation associated with decreasing residual melt provide compelling physical evidence for the segregation of the solid and liquid components of the magmatic system. In contrast to studies focusing on the plutonic realm of igneous complexes (Ji et al., 2014; Cheadle and Gee, 2017; Holness et al., 2017; Fiedrich et al., 2017, Vukmanovic et al., 2018), this study presents microstructural data on erupted plutonic lithics, providing insight in to how magmas differentiate and segregate melt (in cumulate–forming processes) in a system that had a known and active volcanic counterpart.

CONCLUSIONS

Plagioclase CPOs and rotation axis distortion occurs in the horizontal plane and defines a foliation. These patterns are characteristic of uniaxial compaction of elongate plagioclase, both in the arrangement and near solid-state deformation of grains. Rotation axis analysis reveals that uniaxial compression continued with decreasing porosity, and associated melt expulsion as seen in decreasing glass abundance in grain boundaries, as grains came in to contact and deformed. Microstructural analysis of the crystal residue left behind during melt extraction, as preserved in plutonic lithics, can elucidate physical processes occurring in the overlapping space between plutonic and volcanic systems.

ACKNOWLEDGMENTS

We would like to acknowledge useful reviews from Marian Holness, Mark Pearce, and Zoja Vukmanovic that improved this manuscript. Funding for this research comes from the Brian Mason Scientific and Technical Trust (grant 2015/03) and Frontiers Abroad Aotearoa Ltd. Thank you to Abra Atwood for assistance in sampling.

REFERENCES CITED

Arzi, A. A. (1978). Critical phenomena melted rocks in the rheology of partially. Tectonophysics, 44(1–4), 173–184.

Bachmann, O., and Bergantz, G., 2008, The Magma Reservoirs That Feed Supereruptions: Elements, v. 4, p. 17–21, doi:10.2113/GSELEMENTS.4.1.17/.

Bachmann, O., Miller, C. F., and de Silva, S. L., 2007, The volcanic–plutonic connection as a stage for understanding crustal magmatism: Journal of Volcanology and Geothermal Research, v. 167, p. 1–23, doi:10.1016/j.jvolgeores.2007.08.002.

Bacon, C. R., Sisson, T. W., and Mazdab, F. K., 2007, Young cumulate complex beneath Veniaminof caldera, Aleutian arc, dated by zircon in erupted plutonic blocks: Geology, v. 35, p. 491, doi:10.1130/G23446A.1.

Beane, R., & Wiebe, R. A., 2012, Origin of quartz clusters in Vinalhaven granite and porphyry, coastal Maine: Contributions to Mineralogy and Petrology, v. 163, p. 1069–1082, doi:10.1007/s00410-011-0717-1.

Bowen, N.L., 1928, The evolution of igneous rocks, Dover publications, 332 p.

Burt, R. M., Brown, S. J. A., Cole, J. W., Shelley, D., amd Waight, T. E., 1998, Glass-bearing plutonic fragments from ignimbrites of the Okataina caldera complex, Taupo Volcanic Zone, New Zealand: Remnants of a partially molten intrusion associated with preceding eruptions: Journal of Volcanology and Geothermal Research, v. 84, p. 209–237, doi:10.1016/S0377-0273(98)00039-0.

Cashman, K. V., and Giordano, G., 2014, Calderas and magma reservoirs: Journal of Volcanology and Geothermal Research, v. 288, p. 28–45, doi:10.1016/j.jvolgeores.2014.09.007.

Cheadle, M. J., and Gee, J. S., 2017, Quantitative Textural Insights into the Formation of Gabbro in Mafic Intrusions: Elements, v. 13, p. 409–414, doi:10.2138/gselements.13.6.409.

Cooper, K. M., and Kent, A. J. R., 2014, Rapid remobilization of magmatic crystals kept in cold storage: Nature, v. 506, p. 480–483, doi:10.1038/nature12991.

Fiedrich, A. M., Bachmann, O., Ulmer, P., Deering, C.D., Kunze, K., and Leuthold, J., 2017, Mineralogical, geochemical, and textural indicators of crystal accumulation in the Adamello Batholith (Northern Italy): American Mineralogist, v. 102, p. 2467-2483, doi:10.2138/am-2017-6026.

Graeter, K. A., Beane, R. J., Deering, C. D., Gravley, D., and Bachmann, O., 2015, Formation of rhyolite at the Okataina Volcanic Complex, New Zealand: New insights from analysis of quartz clusters in plutonic lithics: American Mineralogist, v. 100, p. 1778–1789, doi:10.2138/am-2015-5135.

Holness, M.B., Anderson, A.T., Martin, V.M., Maclennan, J., Passmore, E. & Schwindinger, K. (2007) Textures in partially solidified crystalline nodules: a window into the pore structure of slowly cooled mafic intrusions. Journal of Petrology, 48: 1243-1264, doi.org/10.1093/petrology/egm016

Holness, M. B., Vukmanovic, Z., and Mariani, E., 2017, Assessing the Role of Compaction in the Formation of Adcumulates : a Microstructural Perspective: Journal of Petrology, v. 58, p. 643–674, doi:10.1093/petrology/egx037.

Hunter, R. H., 1996, Texture Development in Cumulate Rocks, Developments in Petrology, v. 15, p. 77–101, doi:10.1016/S0167-2894(96)80005-4.

Ji, S., Shao, T., Salisbury, M. H., Sun, S., Michibayashi, K., Zhao, W., Long, C., Liang, F.,

and Satsukawa, T., 2014, Plagioclase preferred orientation and induced seismic anisotropy in mafic igneous rocks: Journal of Geophysical Research: Solid Earth, v. 119, p. 8064–8088, doi:10.1002/2014JB011352.

Michels, Z. D., Tikoff, B., Kruckenberg, S. C., and Davis, J. R., 2015, Determining vorticity axes from grain-scale dispersion of crystallographic orientations: Geology, v. 43, p. 803– 806, doi:10.1130/G36868.1.

Paterson, S. R., Vernon, R. H., & Tobisch, O. T. (1989). A review of criteria for the identification of magmatic and tectonic foliation in granitoids. Journal of Structural Geology, 11(3), 349–363.

Philpotts, A. R., Carroll, M., & Hill, J. M. (1996). Crystal-Mush Compaction and the Origin of Pegmatitic Segregation Sheets in a Thick Flood-Basalt Flow in the Mesozoic Hartford Basin, Connecticut. Journal of Petrology, 37(4), 811–836.

Philpotts, A. R., Brustman, C. M., Shi, J., Carlson, W. D., & Denison, C. (1999). Plagioclase-chain networks in slowly cooled basaltic magma. American Mineralogist, 84(11–12), 1819–1829.

Prior, D. J., Boyle, A. P., Brenker, F., Cheadle, M. C., Austin, D., Lopez, G., Peruzzo, L., Potts, G., Reddy, S., Spiess, R., Timms, N., Trimby, P., Wheeler, J., and Zetterström, L., 1999, The application of electron backscatter diffraction and orientation contrast imaging in the SEM to textural problems in rocks: American Mineralogist, v. 84, p. 1741–1759.

Romeo, I., Capote, R., Lunar, R., and Cayzer, N., 2007, Polymineralic orientation analysis of magmatic rocks using Electron Back-Scatter Diffraction: Implications for igneous fabric origin and evolution: Tectonophysics, v. 444, p. 45–62, doi:10.1016/j.tecto.2007.08.006.

Rybacki, E., & Dresen, G. (2000). Dislocation and diffusion creep of synthetic anorthite aggregates. Journal of Geophysical Research: Solid Earth, 105(B11), 26017–26036.

Satsukawa, T., Ildefonse, B., Mainprice, D., Morales, L. F. G., Michibayashi, K., and Barou, F., 2013, A database of plagioclase crystal preferred orientations (CPO) and microstructures- implications for CPO origin, strength, symmetry and seismic anisotropy in gabbroic rocks: Solid Earth, v. 4, p. 511–542, doi:10.5194/se-4-511-2013.

Schmidt, M. W., Forien, M., Solferino, G., and Bagdassarov, N., 2012, Settling and compaction of olivine in basaltic magmas: an experimental study on the time scales of cumulate formation: Contributions to Mineralogy and Petrology, v. 164, p. 959–976, doi:10.1007/s00410-012-0782-0.

Sewell, R. J., Hobden, B. J., and Weaver, S. D., 1993, Mafic and ultramafic mantle and deep crustal xenoliths from Banks Peninsula, South Island, New Zealand Banks Peninsula, South Island, New Zealand: New Zealand Journal of Geology and Geophysics, v. 36, p. 223-231, doi:10.1080/00288306.1993.9514570.

Vukmanovic, Z., Holness, M. B., Monks, K., & Andersen, J. C. Ø. (2018). The Skaergaard trough layering: sedimentation in a convecting magma chamber. Contributions to Mineralogy and Petrology, 173(5), 43.

Žák, J., Verner, K., and Týcová, P., 2008, Grain-scale processes in actively deforming magma mushes: New insights from electron backscatter diffraction (EBSD) analysis of biotite schlieren in the Jizera granite, Bohemian Massif: Lithos, v. 106, p. 309–322, doi:10.1016/j.lithos.2008.08.006.

Chapter Four – Progressive magmatic compaction and melt extraction revealed by a multi-method approach to plutonic lithics

Chapter 4 of this thesis deals with objective 3: *understanding what factors are responsible for variations in plutonic lithic fabrics and chemistries by applying multiple SEM-based methods.*

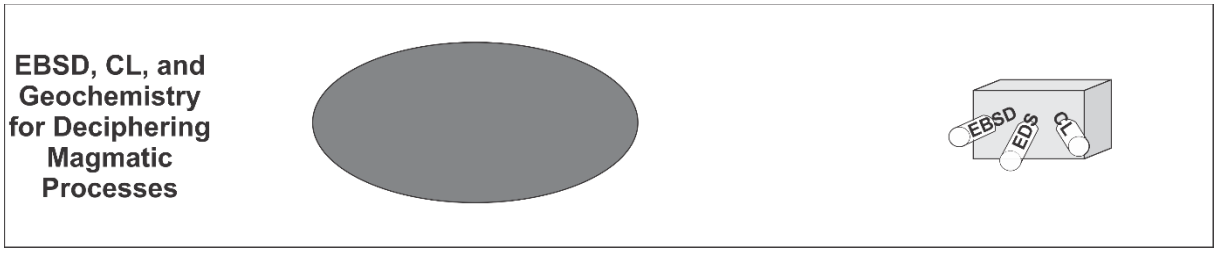

From Figure 2.9 showing the relevant section to this chapter.

This chapter uses EBSD, color-CL, and a variety of geochemical analyses to investigate compaction and melt extraction in a suite of plutonic lithics. Major element evolution in conjunction with CPO strength and bright plagioclase grain boundaries (representing residual melt) suggests that the lithics represent a theoretical column through a mush that was progressively compacting and extruding its residual melt fraction. This work builds on the interpretations of Chapter 3 which found preliminary petrographic evidence for melt extraction in conjunction with a foliation plagioclase CPO and lattice deformation in Goat Rock cumulates. This chapter identifies microstructural evidence for viscous compaction with the additional evidence of melt removal reflected in the decreasing proportion of bright CL plagioclase grain boundaries (residual melt) with increasing CPO strength. Bulk rock geochemistry, plagioclase chemistries, and bright CL compositions progressively evolve as crystal CPOs and textures progress towards equilibrium textures. This study is the first to find microstructural evidence of viscous compaction coupled with physical and chemical evidence of melt extraction in natural samples from a magmatic system with a volcanic counterpart.

The following is a modified version of a manuscript submitted to *Contributions to Mineralogy and Petrology* in November 2019.

Progressive magmatic compaction and melt extraction revealed by a multi-method approach to plutonic lithics

Bertolett E.M.[1], Gravley D.M.[1], Beane R.[2], Teeter E.[3], Gualda G.[3], Prior D.J.[4], Hampton S.J.[1], Kennedy B.M.[1]

[1]*Department of Geological Sciences, University of Canterbury. West Building, Private Bag 4800, Christchurch 8140, New Zealand*
[2]*Department of Earth and Oceanographic Science, 6800 College Station, Bowdoin College, Brunswick, Maine, USA 04011*
[3]*Earth and Environmental Sciences, Vanderbilt University, 2301 Vanderbilt Place, PMB 351805, Nashville, TN 37235-1805, USA*
[4]*Department of Geology, University of Otago. PO Box 56, Dunedin 9054, New Zealand*

Abstract

Plutonic lithics from volcanic outcrops in the Akaroa Volcanic Complex (8 Ma to 9.4 Ma), New Zealand reveal details of the magmatic origins of the volcano. These plutonic lithics are particularly well exposed at Goat Rock, a volcanic dome, and record evidence of melt extraction. Color-cathodoluminescence (CL) imaging reveals luminescent plagioclase overgrowths along plagioclase grain boundaries. The amount of these thin, luminescent regions inversely correlates to the strength of the plagioclase crystallographic preferred orientations (CPO) that record a magmatic foliation defined by poles in {010} and great circle girdles in {100} and {001}. In addition, the plagioclase, bright CL areas, and lithics all show increasing alkalic and silicic trends corresponding to increasing strength of the CPO. The inverse relationship between the amount of bright CL areas and strength of CPO for the plutonic lithics, combined with mineral and whole-rock geochemical trends, suggest that compaction influenced the extraction of liquid from the crystal framework of the mush that produced the Goat Rock volcanic dome.

Introduction

Magmatic fractionation, which separates liquid from a solid component, produces zones defined by crystal content and composition (Bowen 1928; Marsh 1981; Hildreth 2004). In mafic

systems, these may be vertically stacked, ephemeral pockets of crystals and melt in various stages of solidification (Cashman et al. 2017). These regions have been used to interpret the eruptibility of magmatic systems when combined with geochemical techniques (e.g. Barbarin, 2005) or numerical modelling (e.g. Bergantz et al., 2017). Pooling of magma, regardless of the timescales over which eruptible melt is stored, requires the physical extraction of liquid from a crystal framework. In the strictest sense, compaction-induced melt extraction from a crystal mush is controlled by deformation of the crystalline framework (Pistone et al., 2015; Cashman et al., 2017; Holness, 2018). Compaction leaves geochemical signatures and textural clues (Holness et al., 2017c). Thus, combining geochemical data with microstructural analyses (c.f. Hunter 1996) may illuminate how melts are extracted, and potentially erupt. Physical processes that segregate melt such as hindered settling, convective boundary layer flow, and viscous compaction are often invoked but rarely critically examined (see Holness, 2018 for a review of these processes).

Most natural microstructural evidence for the processes responsible for melt extraction comes from data on adcumulate formation. Cumulates are the residual crystal-rich portion of a differentiating magma and necessarily record a reduction in melt proportion, either by continued crystallization within the pore space (essentially closed-system, i.e. orthocumulate) or in the accumulation of cumulus minerals with a characteristic lack of interstitial phases (adcumulate) (Hunter, 1996). The challenge is to analyze growth, dissolution, and deformation microstructures to interpret how melt was removed.

The subvolcanic architecture of composite basaltic systems is thought to be composed of a branching network of dikes and sills, particularly in the upper reaches of the magmatic system (Vinet and Higgins, 2010), fed by incrementally intruding and evolving basaltic magmas (Marsh, 2004; Cashman et al., 2017) rather than a single, large body of magma. While mushy

reservoirs may have high volumes of melt for only short periods of time (Cashman et al., 2017 and references therein), large, crustal plutonic complexes themselves are long-lived. Evidence for melt extraction in plutons tends to be obscured by internal processes such as repeated intrusions and re-equilibration and by external processes such as hydrothermal alteration and tectonic events. Furthermore, it is relatively rare that volcanic rocks and a plutonic root are both exposed at one location.

Plutonic lithics that are entrained and erupted with volcanic deposits may be used to interpret magmatic processes in systems with complicated or missing exposed plutons. The term *plutonic lithic* has been variously used to describe solidified magmas from previous eruptive or intrusive events, mixed magmas, roof or wall crystallization, and remnant crystal residue (see Burt et al., 1998 and Graeter et al., 2015 for examples).

A multi-method approach

Important quantitative textural data on crystal organization, fabric-forming mechanisms, and melt extraction have recently been documented (Boorman, et al., 2004; Nasipuri and Bhattacharya 2007; Žák and Klomínský 2007; Miranda, et al., 2016; Fiedrich, et al., 2017; Holness, et al., 2017a; Holness, et al., 2017c; Bertolett et al., 2019). More specifically, the use of EBSD to decipher how plagioclase crystals are organized in magmas has been used to document mechanisms of segregation and cumulate formation (Satsukawa, et al., 2013; Fiedrich et al., 2017; Holness et al., 2017c; Vukmanovic et al., 2018, Bertolett et al., 2019), tectonic overprinting of plutonic systems (Miranda et al., 2016), and eruptive processes (Brugger and Hammer, 2015). The interpretation of the textural data may be enhanced when combined with cathodoluminescence (CL) imaging and geochemical analyses (Wark et al., 2007). In particular, the advent of color-CL and black balancing, which allow optimization for

all minerals in a specimen and a meaningful comparison of luminescence (de Wet et al., 2016), has broadened its application in igneous petrology.

In this contribution, we utilize a selection of techniques including EBSD, color-CL, and geochemistry (XRF, EDS, EMPA) to record the chemical and textural variations present in plutonic lithics from the Goat Rock volcanic dome within the Akaroa Volcanic Complex. This combined approach allows us to (1) quantify the type and strength of mineral fabrics and the magmatic processes that created them, (2) comment on the rheology of the solidifying magma via quantification of relative proportions of residual interstitial liquid to crystals, and (3) discuss the snapshots of the magmatic system provided by lithics no longer residing in the magmatic system (and, thus, not overprinted by the long, slow cooling of the plutonic complex). Together, these observations are used to construct a model that seeks to explain the evolution from crystallization to eruption of Goat Rock plutonic lithics.

Geological setting

Banks Peninsula is an amalgamation of several volcanic complexes that cover a total of 1200 km^2 exposed at the surface. Seismic reflection interpretation and information from boreholes suggest the termination of Banks Peninsula lava flows extend as far as 30 km from the present visible boundaries of the volcano (Bischoff et al., in press). One of multiple centers of Miocene volcanism in Zealandia, Banks Peninsula carries an alkaline signature characteristic of intraplate volcanism (Timm et al., 2009). No hotspot source has been identified, however, and the current interpretation is that asthenospheric delamination was responsible for intraplate volcanism in this region (Timm et al., 2009).

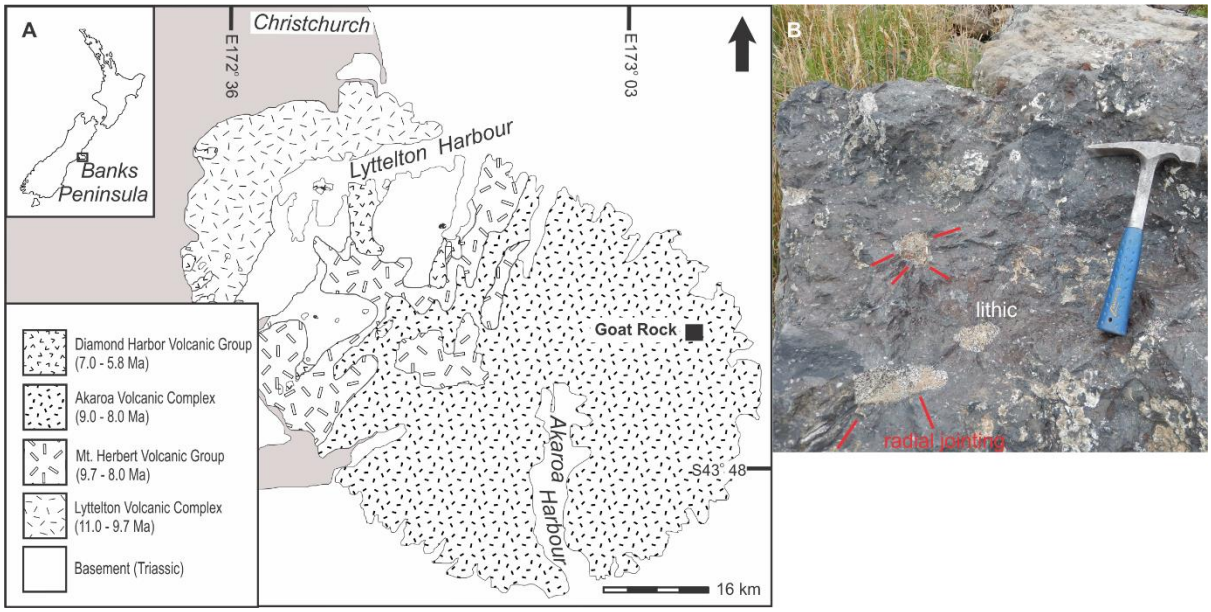

Figure 4.1 A) Geologic map of Banks Peninsula adapted from Hampton et al. (2009). Goat Rock Dome is located on the eastern flank of the main AVC edifice. B) Image of rockfall block containing plutonic lithics. Note the radial jointing propagating into the grey, host material from the light-colored lithics.

The Akaroa Volcanic Complex (AVC) is the younger (8.0-9.4 Ma, Ring and Hampton, 2012) and larger of two main volcanic edifices that make up Banks Peninsula (Akaroa and Lyttelton, Figure 4.1a). AVC lavas, domes, dikes, and pyroclastic material range from basaltic to trachytic compositions (~40-70 SiO_2 wt. %; Hartung, 2011). Stratigraphic variations in lava flow chemistry are hypothesized to be the result of cycles of differentiation in the middle to shallow crustal, rather than evolution and prolonged storage of one magma. Sequences of lava flows are frequently punctuated by trachytic (and occasionally basaltic) dikes and domes. Geochemical and geobarometry work has identified a Daly Gap, or lack of lavas of intermediate compositions, in the AVC (Hartung, 2011). Many oceanic volcanic complexes lack lavas of intermediate compositions (Daly, 1925), considered to be the result of progressive sill intrusion and reactive flow melt removal (Charlier et al., 2011; Jackson et al., 2018).

Analysis of radial dikes in the Lyttelton Volcanic Complex led to the identification of multiple volcanic centers (Hampton and Cole, 2009). Evidence for multiple eruptive centers supports

geomorphic observations of a complex volcanic edifice rather than a single stratavolcano. A volcanic complex morphology suggests a multi-level sill and dike magmatic system instead of a single reservoir model. This is supported by stratigraphic variations in lava chemistry and geobarometry analysis. Hartung (2011) suggests a multi-level crustal reservoir for the AVC.

Apart from Onawe Peninsula (a small, highly altered, and shallow intrusive outcropping of syenite and gabbro), AVC plutonic material can only be found in locally occurring plutonic lithics (Figure 4.1b; Sewell et al., 1993). Goat Rock Dome is a trachybasalt to basaltic trachyandesite volcanic dome on the eastern flank of the Akaroa complex (390 meters above sea level, Figure 4.1a). The Goat Rock lava dome intruded into the eroded vent area of a scoria cone within main vent lava flows on the outer flank of the AVC. Multiple domes and dikes dot the flanks of the AVC and are either basaltic or trachytic. Often, domes are fed by a dike: most notably Panama Rock dome and its feeder dike in LeBons Bay. Goat Rock dome (10^5 m^3) has abundant plutonic lithics located in slabs and boulders (Figure 4.1b) that were dislodged and exposed during the Canterbury Earthquake Sequence (2010 to present). In this contribution, analyses of Goat Rock plutonic lithics are used to reconstruct the magmatic system feeding Goat Rock dome and, further resolve the broader Akaroa magmatic system.

Methods

The diameters of nearly 300 lithics were measured and detailed observations of grain size and alignment, modal mineralogy and contact relation with the host rock were recorded. Eleven lithics (>5 cm) were sampled (most with a concrete saw) of which six were selected for detailed analyses based on variations in shape preferred orientations (SPOs) of crystals observed in hand sample. These field and hand sample observations were used to categorize the lithics (Figure 13 Appendix). Three categories are the focus of this study and are referred to by the names of the most representative sample (GR8b, GR20, and GR14, Figure 4.2).

Major element whole rock analysis was conducted on a Philips PW 2400 Sequential Wavelength Dispersive X-ray Fluorescence 63 Spectrometer at the University of Canterbury. The CAMECA SX50 Electron Microprobe at the University of Wisconsin-Madison was used to obtain major-element mineral compositions. Standards used are listed in the Appendix. The probe was calibrated to measure Si, Al, Na, Ca, K, Fe, and Sr for plagioclase, and Na, Mg, Cr, Mn, Ca, Ti, Si, Al, Fe, and Ni for olivine and pyroxene. The beam spot size was defocused at 10 μm, with an accelerating voltage of 15 kHz. Energy Dispersive Spectroscopy (EDS) maps were collected on a Tescan Vega 3 LM Variable Pressure Scanning Electron Microscope at Vanderbilt University and a JOEL IT300 at the University of Canterbury with standards (listed in the Appendix). Maps were collected for small areas at high resolution (see Appendix for SEM settings).

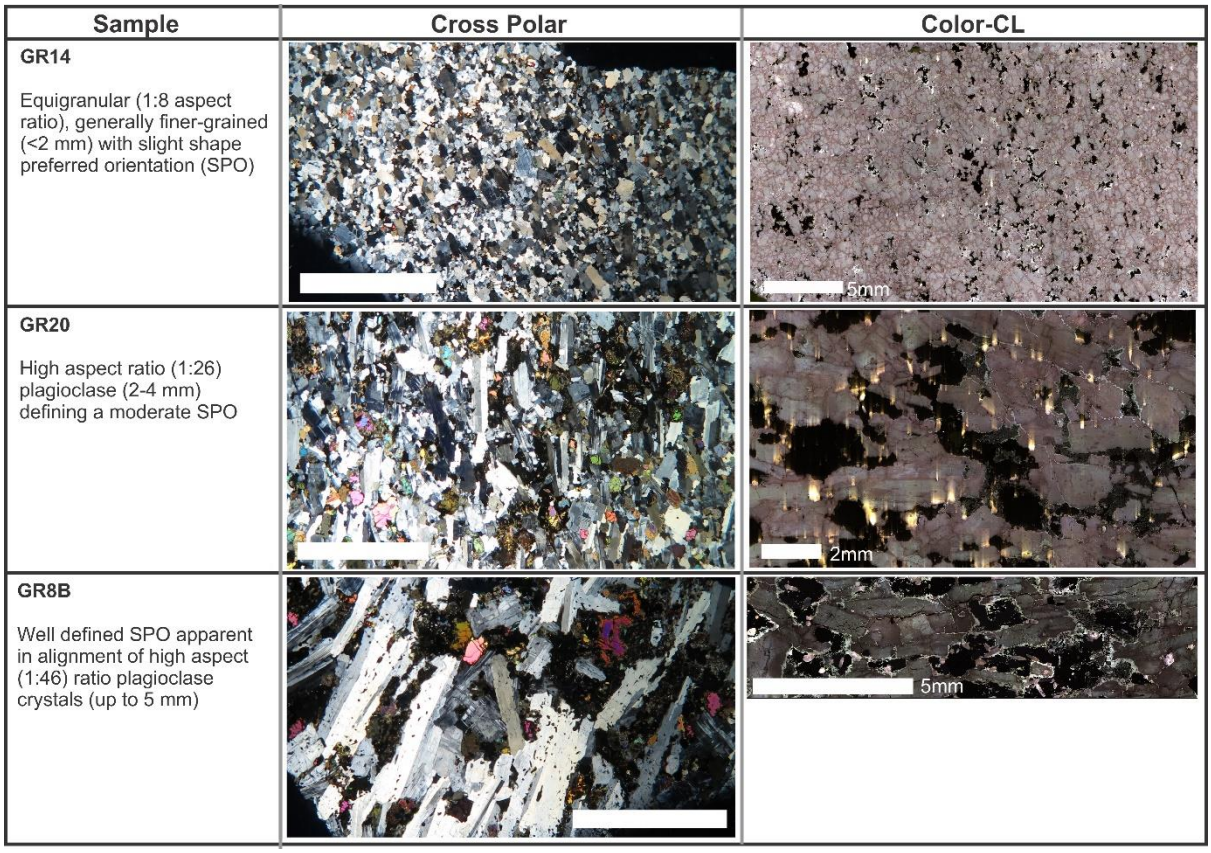

Figure 4.2 Sample descriptions for the three categories of Goat Rock lithics and their representative thin section. Left, petrographic images with 10 mm scale bar and right, color-CL images show plagioclase (pink), pyroxene and olivine (black), apatite (bright white, especially in GR20). Note the white, grain boundary filling lines particularly in GR8b and GR14 as well as the broader, splotchy areas of luminescent material in GR8b.

Probe-quality polished thin sections were prepared at the University of Canterbury. To facilitate electron backscatter diffraction analysis (EBSD), thin sections were further polished for ~ 3 hours in a non-crystallizing colloidal silica suspension on a Buehler Vibromet2 vibratory polisher (SYTON method of Fynn and Powell, 1979) at Bowdoin College. A light (~ 10 nm) thick carbon sputter coat was applied to dissipate charging during electron beam analysis.

Large area maps of electron backscatter diffraction (EBSD) data were collected on a Zeiss Sigma VP FEG scanning electron microscope (SEM) with an Oxford Instruments HKL INCA Premium Synergy system at the University of Otago and a Tescan Vega 3 LMU SEM with an Oxford Instruments Aztec system at Bowdoin College. The EBSD patterns were obtained using

an accelerating voltage of 20 kV (30 kV at Otago), 70 degree stage tilt and 20-100 micron step-size dependent on specimen grain size (with a finer 5.15 µm step size on the two textural end-member specimens- GR8b and GR14). To index the diffraction patterns, the measured EBSD patterns were compared to patterns modeled from known lattice parameters using a kinematic electron diffraction model (Prior et al., 1999). Plagioclase was indexed using the lattice parameters for anorthite from Angel et al. (1990). The relative precision of the indexed data is approximately 1° based on the number of bands (7-8) detected combined with the experimental work of Krieger-Lassen (1995). Indexed EBSD data was analyzed using Channel 5 software and MTEX (Mainprice et al., 2015).

Cathodoluminescence (CL) images across full thin sections were obtained using the TESCAN Vega 3 LMU SEM at Bowdoin College with a TESCAN Rainbow CL detector that splits the CL signal into red, green and blue wavelength components and combines them for a false-color CL image. The SEM parameters were 18 kV, 16-17 BI, 8 scan speed, and 16 mm working distance. Full thin section images took 12-14 hours each to collect. Luminescence varied across specimens; 'black balancing' was used to collect consistent and reproducible image data across specimens using the methods of DeWet et al. (2016). Black balancing allows full thin sections to be uniformly mapped so that comparisons between minerals and samples can be made. For 'black balancing,' a live CL image of a portion of a non-luminescing ('black') mineral (e.g. diopside) is obtained and the signal brightness for the red, green and blue components are adjusted to allow the three peaks to stack on top of each other on the histogram (see Appendix). Then contrast, gamma, and the minimum histogram value are adjusted until the non-luminescing mineral is truly black. These adjustments allow for comparisons between thin sections rather than optimizing for individual crystals and, thus, removing the ability to compare luminescence patterns of different crystal populations.

Results

Petrography

Plagioclase is abundant in GR8b (Table 1), forming large (often up to 5 mm), elongate, sub- to anhedral crystals that exhibit numerous features such as holes, cracks, irregular grain boundaries, patchy extinction, and rims with opaque dots (Figure 4.3a). Plagioclase crystals are visibly aligned along the apparent long axis (Figure 4.2). Plagioclase twins often appear to pinch together so that the spacing between twins visually becomes smaller (Figure 4.3a) and occasionally two sets of perpendicular twin directions are present. One or more twin sets occur in an average of 90% of plagioclase crystals (Table 1, Appendix). Long plagioclase crystals often appear bent and nearly all crystals have irregular extinction patterns (Figure 4.4a). Plagioclase-plagioclase grain boundaries are irregular and serrated (Figure 4.4b) though do not have as many disequilibrium textures as grain boundaries between plagioclase and mafic phases. Mafic phases (olivine, augite, and oxides) in GR8b are fractured and olivine (1-5 mm) has alteration halos. Often, multiple mafic crystals are clustered together and surrounded by pockets of fine-grained material comprised of small, opaque minerals, sometimes with small (<1 mm) plagioclase and augite crystals (Figure 4.3a). Occasionally, this fine-grained material has a ‘zebra’ texture in which fine dots of opaques are aligned with the spaces between individual crystals infilled by extremely fine silica-rich phases. These fine-grained minerals are sometimes aligned with the long axis of larger phenocrysts. This ‘zebra texture’ material is always associated with the mafic phases and is referred to as ‘mafic enriched domains’ from here. Mafic clusters and the associated mafic enriched domains make up between 20 and 30% of GR8b.

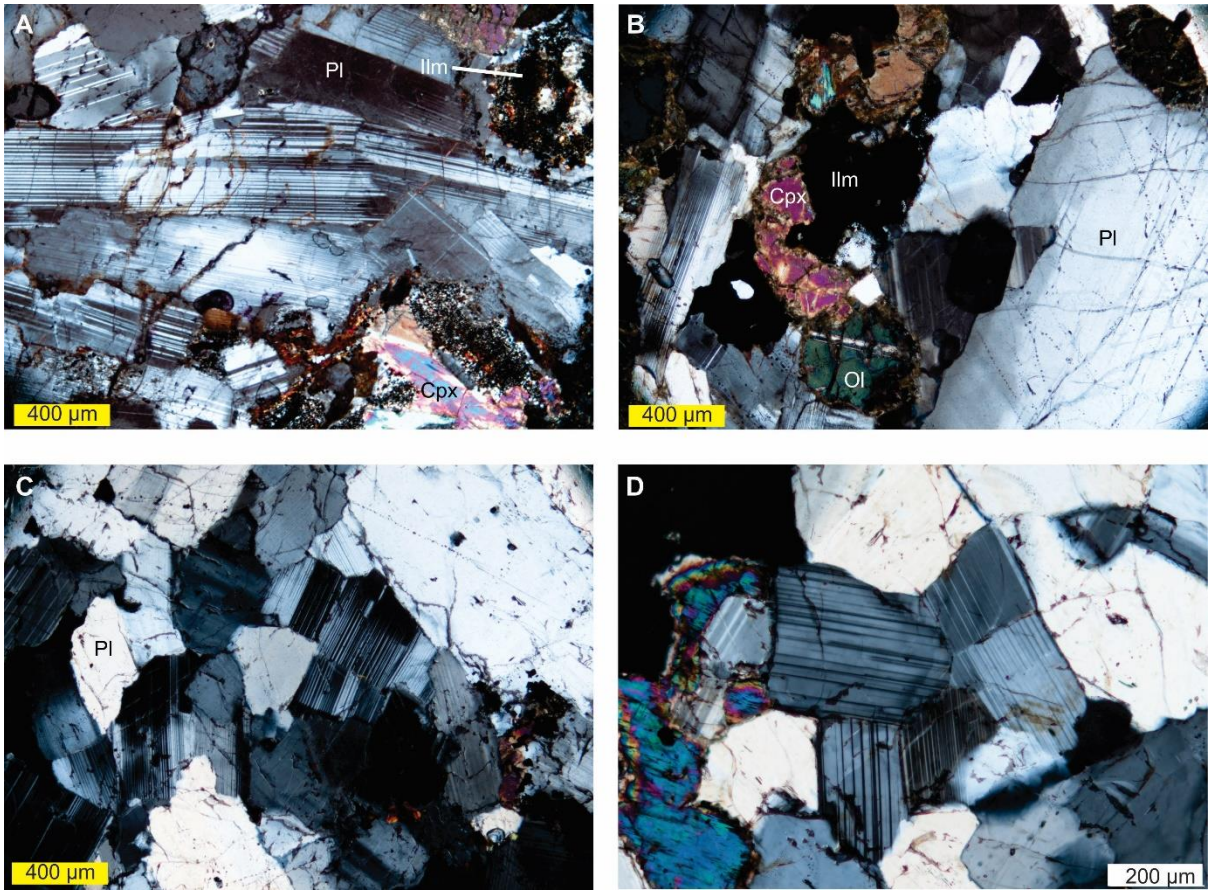

Figure 4.3 Cross polarized photomicrographs of A) GR8b, B) GR20, and C) GR14; D) grey plagioclase crystals in center forming glomerocryst-like texture found in GR14. Note the large plagioclase in (A) (top, left) with pinching twins and the grain just below with two extinction angles. GR8b (A) has the salt-and-pepper texture associated with mafic phases. Note the absence of this material in GR14 (C and D). Plagioclase in GR14 have more uniform extinction and twinning as well as straighter grain boundaries than plagioclase in GR8b.

GR20 has subhedral, long, large (2-4mm) plagioclase crystals and a second, scarcer population of more equigranular and smaller (<1mm) plagioclase. This second, smaller population is generally anhedral and some plagioclase (of both sizes) have lobate grain boundaries (Figure 4.3b). Plagioclase alignment is also visible in GR20 though less so than in GR8b (Figure 4.2). The majority of plagioclase crystals have patchy extinction and plagioclase-plagioclase grain boundaries are irregular. Twin incidence (percentage of plagioclase crystals that have one or more twin sets) is 54% for GR20. Pyroxene and olivine (up to 5 mm) are cracked but do not have the extensive pock-marks and rusty rims observed in GR8b. Mafic phases, particularly olivine and augite, are scarcer in this sample (Table 1) and more dispersed than GR8b. Mafic

enriched domains are also rarer (15-20%) and are concentrated in areas surrounding individual mafic crystals.

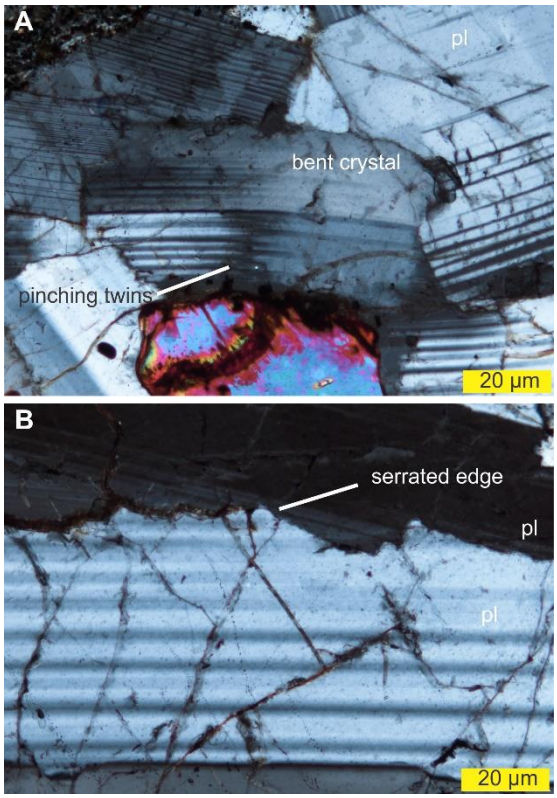

Figure 4.4 A-B) Plagioclase deformation textures in GR8b. A) Bent grain in center of frame with visible subgrains highlighted by undulose extinction and pinching twins. B) Irregular, serrated grain boundary between two plagioclase.

GR14 is characterized by equigranular subhedral to anhedral plagioclase crystals (<2 mm, most <1 mm) in significant proportions (Table 1). A slight shape preferred orientation is seen in thin section though it is not as strong as in GR8b (Figure 2). 52% of plagioclase in GR14 have twins and some plagioclase crystals are grouped in clusters (Figure 4.3c and 4.3d). Plagioclase extinction is not as irregular and patchy as in GR20 and GR8b and crystals exhibit fewer cracks and holes. The elongate grains that are present appear to have subgrains. Olivine and pyroxene are small (<2 mm) and fill in between a plagioclase framework. Very few (<5%) mafic enriched domains are associated with the mafic phases.

Table 1 Modal mineralogy (%) normalized from EBSD map phase percentages for each lithic. Modal mineralogy determined as a percentage of points indexed as each mineral. Non-indexed points and accessory phases are removed and corrected to 100%.

	Plagioclase	Olivine	Augite	Apatite
GR8b	75	15	10	trace
GR20	80	10	10	trace
GR14	93	3	4	trace

Electron Backscatter Diffraction

EBSD maps of full thin sections were collected to distinguish the textural variation of the three lithic categories. Plagioclase in each lithic is the most abundant and largest phase and forms the apparent shape preferred orientation that directed lithic classification. Analysis of crystallographic preferred orientations (CPOs), CPO strength, and misorientation was completed only for plagioclase. Plagioclase CPOs (i.e. fabric) are determined here from pole to plane pole figures (Figure 4.5). The three Goat Rock lithics share a similar plagioclase CPO. {010} poles are clustered and both {100} and {001} lie in a great circle normal to {010} (Figure 4.5).

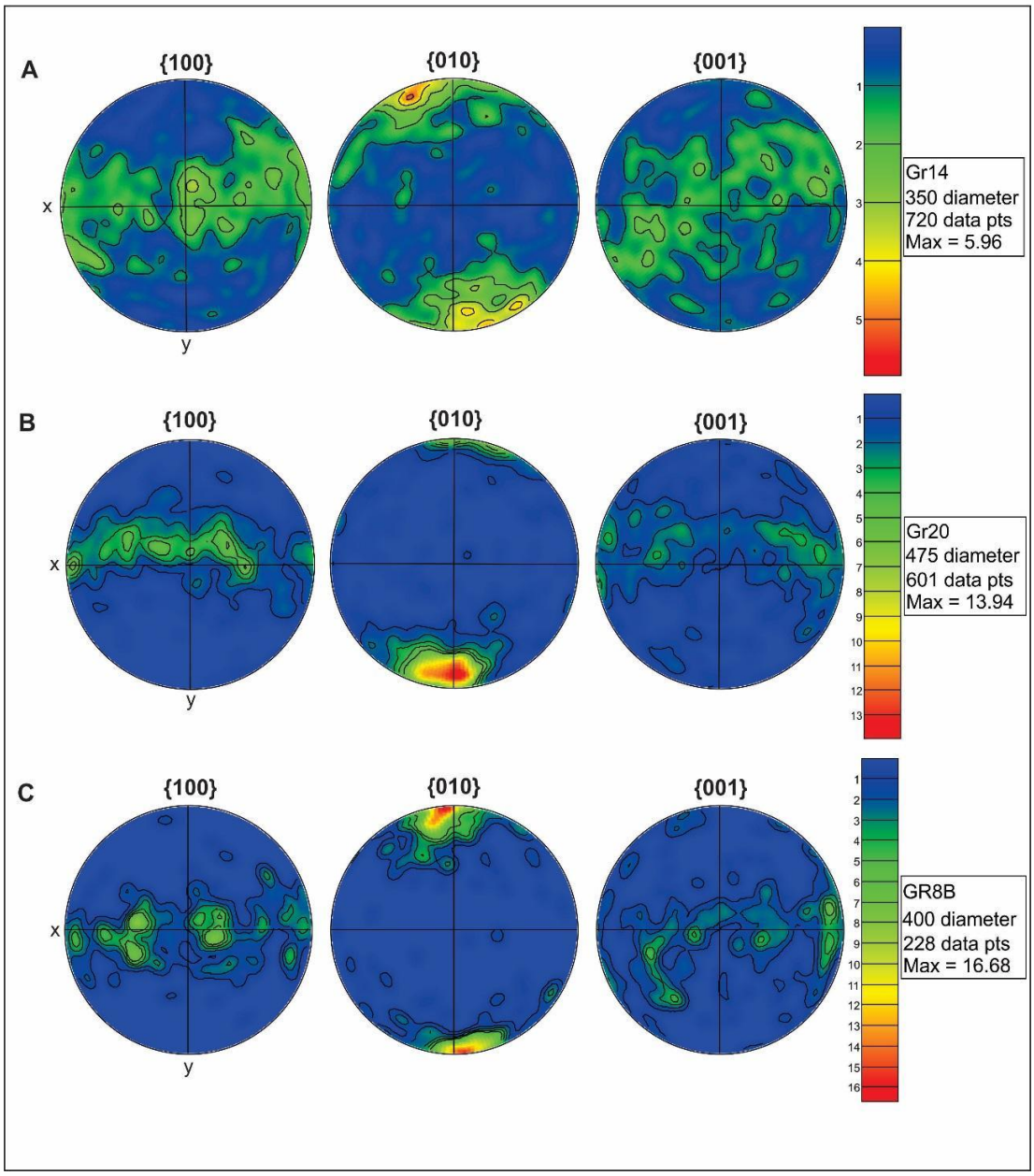

Figure 4.5 Crystallographic preferred orientations of plagioclase in principal pole to plane, equal area, lower hemisphere projections. CPO strength represented by the maximum density of clusters (i.e. Max) using 10° halfwidth contours. CPOs rotated to common reference frame.

Quantification of the density of clustering of poles helps determine the strength of the CPO and the conditions that created it. Maximum densities of poles in clusters range from 5.96 (GR14) to 16.68 (GR8b) (higher number indicates stronger CPO, Figure 4.5) though caution must be

taken in relying on maximum densities to define fabric strength, as this is dependent on the number of grains. Plagioclase crystals are extensively cracked or complicated by areas of no indexing, therefore, analysis of the CPO and its strength at various grain sizes (diameters) is used to explore the impact of large grains on CPO strength. Analysis of the largest grains in each sample does not alter the CPO pattern in any meaningful way, though it does strengthen each CPO, especially in GR20. There is a greater disparity in the number of points between lithics with large grain sizes and, potentially, a more inaccurate representation of the relative strength of the CPO. Analysis of only the smallest grain diameters also does not alter the CPO. The maximum densities presented above are calculated from pole figures of plagioclase grains larger than 350-475 μm (depending on the sample) which encompasses all but the smallest crystals or portions of grains. The number of data points for each lithic in this grouping is more similar than using all points (which is primarily a function of crystal fracturing), mitigating the influence of larger crystals without compromising any orientations of smaller crystal populations.

The CPO shape (clusters in {010} and girdles in {100} and {001}) is shared by all three lithics. Only the strength (maximum density) of the CPO varies: GR8b has the strongest CPO, followed by GR20, and GR14 has the same, but weakest CPO.

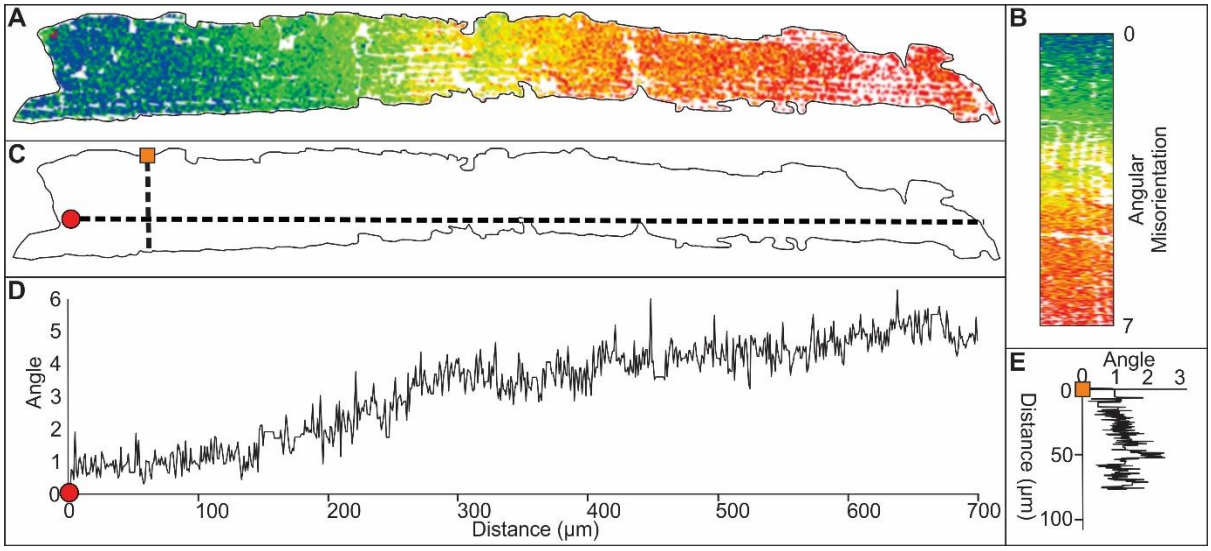

Figure 4.6 A) Individual plagioclase grain from GR8b, rainbow scale (B) shows 7º misorientation (blue-red) relative to the Euler angle at the starting circle in red. Grain outline and misorientation transects in (C). D) Angle of misorientation (y-axis) vs distance (x-axis) along the long axis of the crystal starting at the red dot. E) Angular misorientation along the short axis of the crystal starting at orange square. Corrected for 180° albite twins.

Misorientation, or the angular difference between the crystal lattice at two points in a crystal, is a way to quantify crystal deformation. A particular focus on the textural and compositional end members (GR8b and GR14) reveals intragrain deformation and subgrain formation (Figure 4a and 6). Misorientation from a starting point across the (apparent) long axis and short axis of a selection of grains was calculated. Misorientation across neighboring pixels between 2 and 10° delineates a subgrain and greater than 10° misorientation is a grain boundary. Subgrains are found in all samples with some indication of internal deformation (distortion in both the long and short axis) in GR14 (Figure 4.6).

Cathodoluminescence

Full thin section, color-CL maps reveal differences between the lithics not seen in optical or backscatter images. This study documents exceptionally bright plagioclase along grain boundaries (Figure 4.2b). The brightly luminescent boundary plagioclase is not as luminescent as apatite. For clarity, the thin zones of material found along plagioclase grain boundaries will be referred to as bright CL (Figure 4.7b) while mafic enriched domains (Figure 4.7a) described

in the petrography section refer to the larger patches of fine-grained material associated with mafic phases.

GR8b contains dull pink plagioclase crystals (less luminescent) that exhibit sparse but irregular zoning (Figure 4.2b). Plagioclase with bright CL occurs along grain boundaries. The bright CL along boundaries is typically thin (a few microns) but locally up to tens of microns (Figure 4.2b). This material is distinctly different from the small variations in plagioclase luminescence and not observable optically. The mafic enriched domains textures around the mafic phases appear in CL as splotchy, luminescent areas in uneven distribution and greater thickness than the thin, very luminescent material along plagioclase grain boundaries. Although both features are brightly luminescent and stand out from the other minerals, the thickness, distribution, and association with mafic phases differentiates mafic enriched domains from the bright CL (Figure 4.7). Mafic enriched domains are abundant and bright CL, while present, is comparatively sparse in this sample.

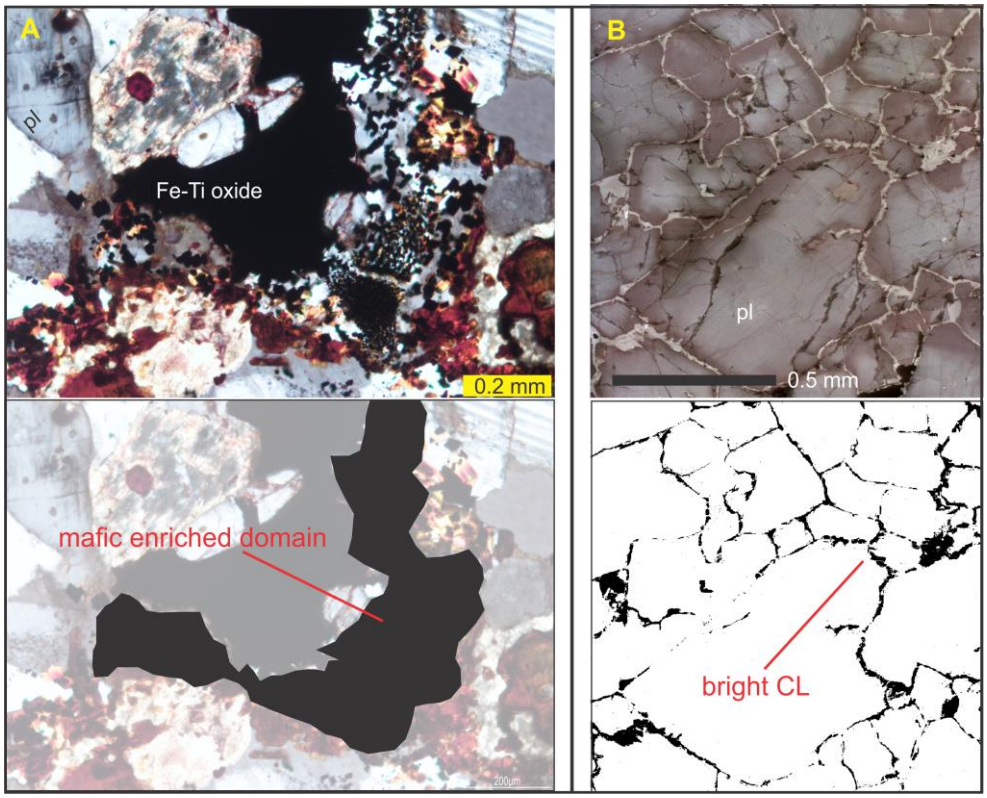

Figure 4.7 A) Plane-polarized image of a mafic enriched domain surrounding an Fe-Ti oxide in GR8b with corresponding image outlining the material in black (below). B) Color-CL frame of GR14 showing bright, luminescent material associated with grain boundaries above and the same bright CL areas highlighted by black outline below.

Plagioclase crystals in GR20 luminesce brighter than GR8b and have significantly less imperfections (Figure 4.2b). GR20 has much less of the mafic enriched domain texture found in GR8b (partially because there are less mafic minerals). The mafic enriched domains are observed more clearly in BSE images than in color-CL images. The distribution of bright CL areas in GR20 is variable. It can be found at all grain boundaries in a few select areas, but elsewhere only occurs as short, thin and disconnected lenses.

In color-CL images for GR14, plagioclase appears bright, light pink with variation in brightness within a single crystal (due to zoning, Figure 4.2b). Generally, plagioclase rims appear darker than cores but not all crystals have this pattern, and many crystals do not have uniform zoning. Luminescence patterns also highlight clustering of plagioclase into single phase clusters. Bright

CL areas in this sample are more evenly distributed than GR20; most grain boundaries have at least a thin layer of the material (Figure 4.7b). It is thickest around the few, small mafic crystals that are present or around clusters of plagioclase but mafic enriched domains are non-existent. Fractures occur in all samples, especially in GR8b. Fractures occur within crystals as well as larger cracks that cut through multiple crystals. In rare cases, bright CL areas correspond to these internal fractures but are not observed in the cross-cutting fractures.

Geochemistry

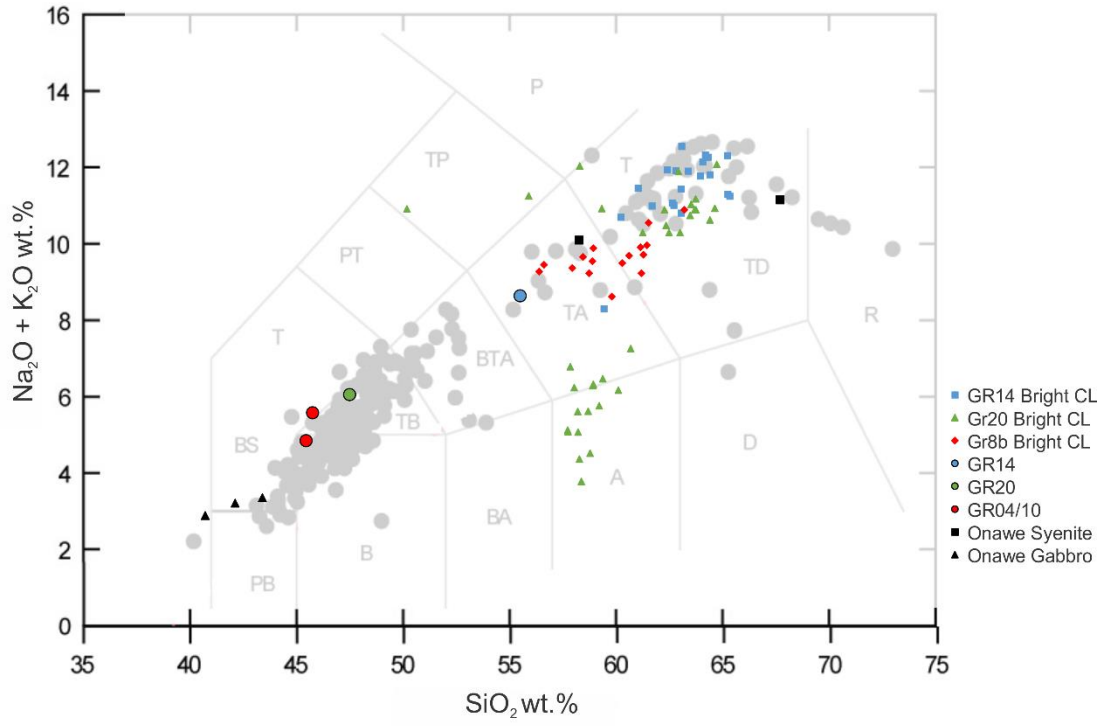

Figure 4.8 TAS diagram of whole rock (large circles) and bright CL areas (line shapes) for each lithic of this study. Black triangles and squares are the only other plutonic material exposed in the AVC (Onawe gabbro and syenite, respectively). All AVC eruptives (from Hartung 2011, Msc) are in grey. Two points labelled GR04/10 exist for the GR8b whole rock composition because not enough lithic remained to get an adequate composition. GR04 and 10 are the most similar to GR8b in terms of mineralogy and texture. Note the two populations of GR20 (green triangles).

Whole rock major element XRF analyses for all Goat Rock lithics analyzed to date (n=17, see Appendix for full data set) range from 45 to 55 SiO_2 wt. %. The Goat Rock lithics in this study represent this range and are presented in Figure 4.8. See Table 2 for the compositions of the

three Goat Rock lithics analyzed as part of this study and the host. Host and lithics have similar compositions though there is some variation: GR8b is the most mafic of the lithics, followed by GR20, then GR14 (Figure 4.8). The whole rock composition of GR8b is characterized by lower SiO_2 (46.2 wt. %), Al_2O_3 (17.0 wt. %), Na_2O (4.15 wt.%), and K_2O (0.66-0.85 wt. %) but higher MgO (3.35-4.40 wt. %) and CaO (8.0-8.45 wt. %) than GR20 (47.3 SiO_2 wt. %) and, especially GR14 (55.0 SiO_2 wt. %, Table 2). GR14 is notably higher in Na_2O (7.10 wt. %) and K_2O (1.40 wt. %) but low in MgO (0.87 wt. %) and CaO (5.13 wt. %). GR20 falls in the middle of these two end members but close to GR8b except for MgO concentration. The host generally falls in between the lithic end-member compositions for all major elements (49.6 SiO_2 wt. %, Table 2).

Table 2 Average major element compositions for each lithic of this study and the host whole rock. Average plagioclase and bright CL compositions also included for the three lithics.

	Whole Rock				Plagioclase			Interstitial Material		
Sample	GR8b*	GR20	GR14	Host	GR8b	GR20	GR14	GR8b	GR20	GR14
SiO_2	46.2	47.3	55.0	49.6	58.1	59.7	60.4	59.1	59.1	63.0
TiO_2	3.17	2.80	1.87	2.31				0.80	1.49	0.37
Al_2O_3	17.1	17.4	21.0	17.0	26.12	25.5	23.9	22.8	23.5	22.0
Total Fe	14.3	14.7	7.50	12.7	0.19	0.20	0.25	2.60	4.38	1.33
MnO	0.23	0.23	0.13	0.22						
MgO	3.96	2.99	0.87	3.08				0.77	0.99	0.18
CaO	8.20	7.25	5.13	6.75	7.27	6.47	4.92	4.71	4.74	3.27
Na_2O	4.44	4.99	7.08	5.22	6.94	7.30	7.85	7.32	5.66	8.05
K2O	0.75	0.98	1.37	1.90	0.94	1.21	1.49	2.10	2.50	3.11
P_2O_5	1.67	1.38	0.08	1.25						
Total	100.00	100.00	100.00	100.00	99.56	100.40	98.85	100.00	99.89	100.00

As it is the fabric forming mineral, a focus was placed on plagioclase. Plagioclase compositions (EMPA) of all lithics follow a similar trend from low silica, low alkalis and high An to high silica, high alkalis and low An that matches the whole rock trends (Figure 4.9a). While distinct, plagioclase compositions in the three lithic types have considerable overlap (Figure 4.9a). However, average An shows a decrease from An37 in GR8b to An24 in GR14 (Figure 4.9b). Note that GR8b has a range of plagioclase compositions (esp. silica) while GR14 is more

constrained (Figure 4.9a, 4.10). A small number of points from all samples plot further from the trend of increasing silica, decreasing CaO and Al_2O_3, and increasing K_2O (Figure 4.10). These points are high in silica with elevated K_2O (>2.30 wt. %) and total FeO (>0.50 wt. %) and lower Al_2O_3, CaO, and Na_2O (see Figure 15 Appendix).

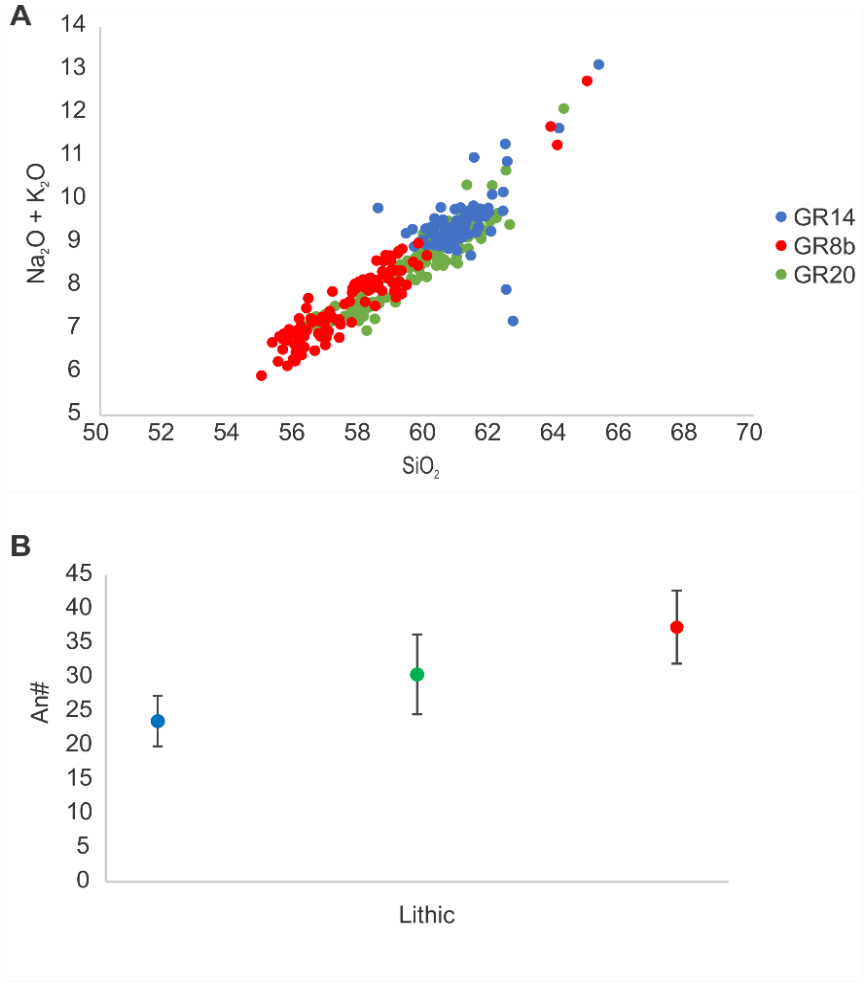

Figure 4.9 . A) Plagioclase EMPA chemistries plotted as silica vs alkalis and B) average ternary anorthite number with standard deviation error bars.

GR8b, GR20, and GR14 follow a progressive trend from lower SiO_2 whole rock values and high An plagioclase to relatively high SiO_2 whole rock and low An plagioclase. GR8b has a strong CPO and many disequilibrium textures while GR20, and especially GR14, have the same, but weaker type of CPO. This relationship also corresponds to the amount of mafic enriched domains and bright CL. Furthermore, the greater amount of mafic enriched domains

and thinner, sparser amount of bright CL corresponds to the stronger CPO of GR8b. The opposite is true for GR14: this sample has almost no mafic enriched domains but extensive and comparatively thick bright CL regions associated with weaker crystal alignment.

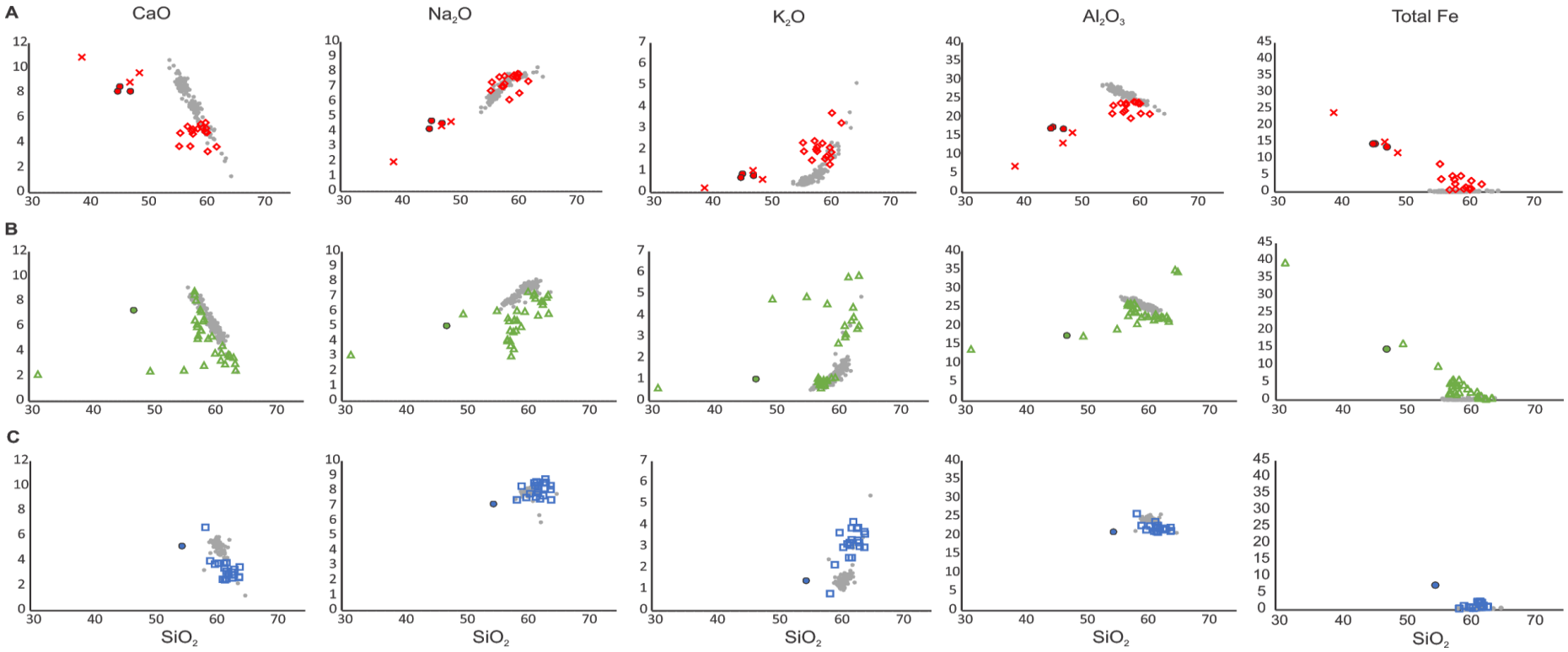

Figure 4.10 Variation diagrams of silica vs major oxides for A) GR8b, B) GR20, and C) GR14. Plagioclase chemistries (EMPA) for each sample in grey overlain by whole rock (circle with black outline) and bright CL lenses (EDS, open shape). Red crosses in GR8b are mafic enriched domain compositions (EDS, see text for discussion). Note the broad range of silica in the high K_2O, low CaO arm of GR20.

Bright CL Areas

Observation of highly luminescent material in color-CL maps was unexpected. While mafic enriched domains can be observed in optical microscope images, the thin, grain boundary defining bright CL seen in color-CL maps can not be identified in petrographic analysis. High resolution EBSD maps were collected for select areas of all lithics to further investigate the bright CL regions and their relationship to the plagioclase crystals. The material is seen in color-CL as a very thin (as little as a few microns thick) and continuous film where crystals meet (Figure 4.12). In EBSD maps, this material is not visible: instead the plagioclase lattices are continuous up the adjacent crystal (Figure 4.11). When the color-CL image and orientation maps are correlated, the distribution of the bright CL areas can be compared to the termination of the plagioclase grain boundary (Figure 4.11). A 150 nm step line scan across a bright CL area in GR14 indexes a plagioclase lattice up to the grain boundary. Importantly, the plagioclase crystals are continuous up to the adjacent plagioclase crystal. The bright CL identified in color CL is thicker than the resolution of this line scan. In other words, the bright CL has the same lattice parameters as the plagioclase crystals and is not a different material such as glass. The high luminescence of the bright CL regions may instead come from lattice defects or incorporation of elements incompatible with the plagioclase framework.

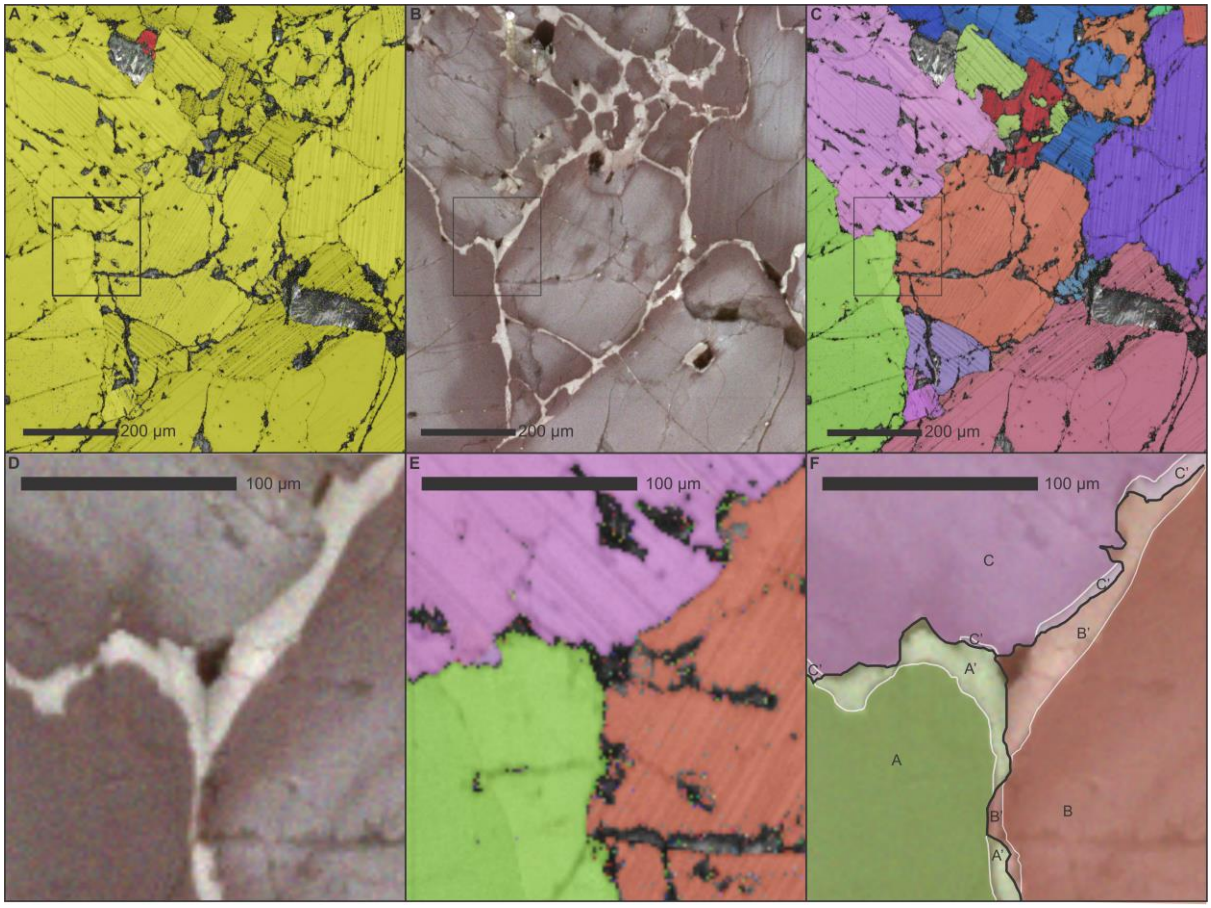

Figure 4.11 A) EBSD phase diagram image of an area in GR14, B) the same area in color-CL, and C) an IPF map of the same area. Black box designates the zoomed in area of the three images below: D) color-CL image showing the bright CL regions and E) IPF orientation map. The different colors in E represent different lattice orientations. F) our interpretation of the boundaries of the plagioclase crystals compared to the areas of bright CL. Note that, in some areas, the bright CL seems to be a continuation of one crystal (A and A') that terminates at the grain boundary of crystal C.

We collected small, high resolution EDS maps of plagioclase-plagioclase grain boundaries to determine if compositional information could be obtained (see Appendix for acquisition conditions). Due to the small and irregular area under analysis, it is possible that some of the chemical variation is an artifact of the data, however, we have tried to mitigate this as much as possible by collecting data from areas of the material rather than points. EDS was chosen because of the small spatial distribution of the material and the ability to collect maps. This is critical as the bright CL is invisible under optical imaging and requires mapping either in CL or EDS to see its distribution.

EDS maps highlight the bright CL material because of its elevated levels of Na_2O, K_2O, and FeO. Generally, bright CL compositions are similar to, but slightly more evolved (higher SiO_2, Na_2O, K_2O) than the plagioclase population of its lithic and significantly more so than the whole rock compositions (Figure 4.10). Bright CL for GR8b is on average 59 SiO_2 wt. % and 62 SiO_2 wt. % for GR14 (Table 2). In contrast, GR20 bright CL areas have an average silica composition of 48 wt. %. GR20, and to some extent GR8b, has a comparatively large range in silica (Figure 4.8) while GR14 bright CL is much more tightly clustered across all oxides (Figure 4.10).

The bright CL in all lithics has a similar range of silica as plagioclase (~55-64 SiO_2 wt. %) but generally higher potassium (1-7 wt. % vs <3 wt. % K_2O) and, sometimes, Na_2O (Figure 4.8). The exception is GR20 which has lower Na_2O than its plagioclase population and rare points with less than its whole rock composition. The same is true for K_2O where GR20 has two populations; high K_2O (~3-6 wt. %) and low K_2O (~.5-1.5 wt. %) (Figure 4.8). GR20 plagioclase share the low K_2O trend up to ~2 wt. %. These two GR20 bright CL populations are also seen, to a lesser degree, in Na_2O and CaO (Figure 4.10). In addition, GR20 has at least four points that extend across a broad range of silica (31-65 SiO_2 wt. %, Figure 4.8). These same data make up a high total Fe population and cut across the high and low Na_2O populations described above. The multiple GR20 bright CL populations are indistinguishable in CL but are distinct in EDS mapping. Note that, while there are multiple bright CL populations in GR20, there is only one population of plagioclase for the lithic (Figure 4.10).

Bright CL from all three lithics have FeO and MgO greater than zero (Figure 4.10) while normally luminescent plagioclase interiors have near zero FeO and MgO. Bright CL total FeO is as high as 39 wt. % (GR20) though the majority of analyzed bright CL is between 0.4 and 8 total wt. % FeO (Table 2). While the bright CL compositions can have substantial overlap with plagioclase compositions, the presence of FeO and MgO suggests that bright CL is a not

compositionally pure plagioclase and may reflect late-stage incorporation of other elements during the final stages of crystallization.

EDS data for mafic enriched domains were also collected from GR8b. This material plots away from the bright CL compositions of all lithics but nearer the whole rock composition of GR8b (Figure 4.10). It is more primitive than the bulk lithic and the normal and bright CL plagioclase compositions. This is consistent with the high proportion of Fe-Ti oxides visible in the mafic enriched domains.

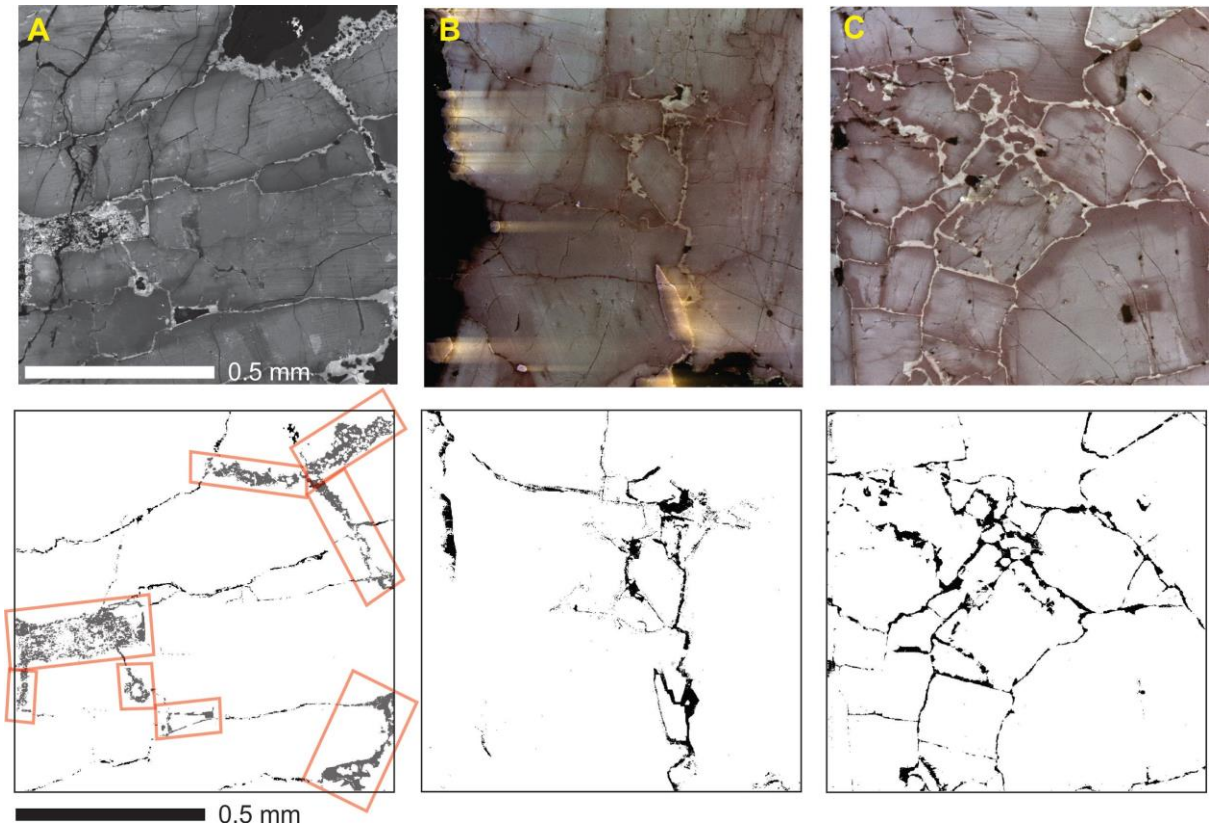

Figure 4.12 Top row, individual color-CL frame A) GR8b, B) GR20, C) GR14, scale bar same for each image. Bottom, processed image of the area of bright CL from the above image. Red boxes denote diffuse melt in GR8b (A). Note the variability in bright CL distribution at grain boundaries in GR20.

We observe a correlation between CPO strength, SPO, and bright CL distribution. To investigate this correlation, we calculated the area of bright CL for individual color-CL frames using ImageJ image analysis (Figure 4.12, see Appendix for methods). Analyzed GR8b frames contain both bright CL and mafic enriched domains because it was prohibitively challenging to

analyze a frame without mafic enriched domains (Figure 4.12a). The other two lithics were analyzed only for bright CL.

The percentage of bright CL corresponds to the relative strength of fabric; GR14 has an average bright CL portion of 6%, GR20 has 3%, and GR8b has 2.5% (with mafic enriched domains removed, Table 3). This average gives a good indication of sample-wide trends though results from the individual frames also provide insight: GR8b and GR14 are notable for their consistency in bright CL area across the sample (Table 3). In contrast, GR20 has a heterogeneous distribution of bright CL fractions that range from <1% to 6%.

Table 3 Bright CL as a percentage of total area for four representative frames for each lithic

Area of Bright CL	**GR14**	**GR20**	***GR8B with mafic enriched domains**	**GR8B no mafic enriched domains**	**Incidence of Bright CL**	**GR14**	**GR20**	**GR8b**
Frame 1	5.4	1.8	6.8	1.8	Line 1	95.1	47.8	85.7
Frame 2	6.3	0.7	9.0	3.9	Line 2	98.5	50	100
Frame 3	7.0	3.1	5.8	2.0	Line 3	97.8	84.6	100
Frame 4	5.6	6.0	6.0	2.2				
Average Area (%)	**6.1%**	**2.9%**	**6.9%***	**2.5%**	**Average Incidence (%)**	**97.2%**	**60.8 %**	**95.2%**

Interpretation

Goat Rock plutonic lithic CPOs for the three samples highlighted in Figure 4.5 are defined by clusters of {010} poles and a great circle distribution of {100} and, to a lesser extent, {001} normal to {010} which defines a foliation. No evidence of lithic-wide lineations are present. A similar magmatic foliation signature defined by Satsukawa et al. (2013, Axial-B) is characteristic of a magmatic foliation organized and deformed under uniaxial compaction. Bertolett et al. (2019) highlighted the importance of using rotation axis analysis in addition to

CPOs to definitively determine sub-solidus fabric formation and confirmed that Goat Rock cumulate plutonic lithic CPOs formed due to uniaxial compaction.

Although not an exhaustive investigation, there are microstructural features observed in Goat Rock plutonic lithics that can be linked to processes of crystal accumulation and melt removal. First, the presence of pinching twins (indicative of mechanical deformation) and irregular plagioclase extinction in Figure 4a can be associated with crystalline deformation during crystal accumulation and melt extraction (cf. Holness, et al. 2017b; Holness et al., 2017c; Vukmanovic et al., 2018). Irregular and lobate plagioclase-plagioclase grain boundaries (Figures 4.3a and 4.4b) have been linked to dislocation creep induced grain boundary migration (Rybacki and Dresen, 2000). These features, coupled with up to 8° of lattice bending in Goat Rock plagioclase (Figure 4.6) supports CPO and SPO evidence of a plagioclase fabric and, therefore, reduction of the initial liquid fraction (Fiedrich et al., 2017).

Because of its composition, distribution, and orientation, we interpret the highly luminescent, grain boundary-defining, bright CL documented in this contribution as residual melt trapped and crystallized as plagioclase overgrowth on the existing plagioclase framework as porosity decreased during crystallization and magmatic compaction.

Some bright CL occurs within cracks that run through plagioclase but it is never found in cracks that cross multiple crystals. Where bright CL is found in fractures, it is always where the crack is connected to a grain boundary with bright CL. Because of this, we suggest that the bright CL was concurrent with super-solidus magmatism rather than a post solidification injection or alteration.

Mafic enriched domains (Figure 4.7a) are comprised of fine (μm) plagioclase and Fe-Ti oxide crystals and glass (Figure 18, Appendix). Its strong association with mafic phases and broader, more irregular morphology and distinct textures suggest that mafic enriched domains formed

from a different process than the thin bright CL. For this reason, we discuss its distribution separately. GR8b is unique in that most of the inter-grain material is observed as mafic enriched domains, or broader fine-grained patches of material associated with mafic minerals (Figure 4.12a). GR04, an analogous sample to GR8b (based on CPO strength and mineralogy, see Figure 13 Appendix) has no mafic enriched domains and a comparatively low amount of bright CL, supporting this assumption.

There is also a difference in thickness between bright CL and mafic enriched domains as well as between bright CL across samples. This is best seen in the difference between bright CL percent vs incidence (Table 3). While most grain boundaries in GR8b and GR14 have bright CL, the relative proportion takes up a larger area of GR14 than GR8b (Table 3). However, there are larger and fewer grains in GR8b than GR14.

The composition of the bright CL and the correlation between dislocation creep indicators and bright CL requires comparatively high crystal contents. We propose that the bright CL described in this study is a late-stage (near solidus conditions) combination of plagioclase and residual melt which crystallized within the adjacent plagioclase framework, incorporating a higher proportion of elements incompatible in a pure plagioclase framework as temperature dropped.

Textural and Geochemical Evolution of the Goat Rock Magmatic Source

The constrained nature of lithic whole rock as well as plagioclase chemistries suggests that all Goat Rock plutonic lithics grew in a similar, if not the same, magmatic reservoir with very little disruptive or preserved influx of magma (with the exception of the Goat Rock lava that eventually entrained and erupted the lithics). Goat Rock is an approximately 750,000 cubic meter lava dome with exposure of plutonic lithics in moderately high density in the northeast face of the dome. Plutonic lithics are only found on the northeast side of the dome: rare crystal

clusters and large, individual plagioclase crystals are sporadically found in the rest of the dome. The spatial concentration of lithics in the small Goat Rock dome, as well as the remarkably homogenous size, shape, and modal mineralogy of the lithics, implies that erupting lava disaggregated and entrained solidified magmatic material from a single portion of the subvolcanic system rather than from multiple vertical regions and stages of entrainment. From this, combined with the textural evidence for compaction and melt extraction, we suggest the source area to be something like a shallow, mushy sill(s) (Figure 4.13).

Schematic Magmatic System	*Lithic Type Samples*	*Analytical Properties*	*Interpreted Relationships / Processes*
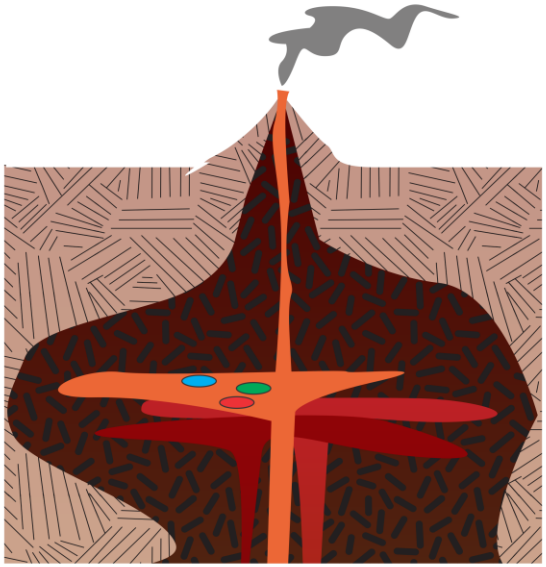	GR 14 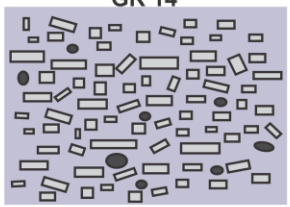	**Whole Rock SiO_2 wt.%:** 55 **Plag. %:** 93 % **CPO:** Weak **An#:** 24 **Bright CL %:** 6 % **Bright CL SiO_2 wt.%:** 63 **Mafic Enriched Domain %:** N/A **Mafic Enriched Domain SiO_2 wt.%:** N/A	**Mush:** *Crystal accumulation of more evolved phases in a comparatively felsic magma* **Compaction:** *Weak compaction aligning crystals* **Bright CL:** *Continuous and homogenous distribution of felsic residual melt, preserved as interstitial material crystalizing around phenocrysts* **Mafic Enriched Domains:** *None present*
	GR 20 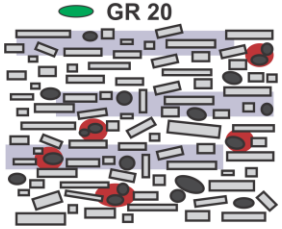	**Whole Rock SiO_2 wt.%:** 47 **Plag. %:** 80 % **CPO:** Moderate **An#:** 30 **Bright CL %:** 3 % **Bright CL SiO_2 wt.%:** 59 **Mafic Enriched Domain %:** Trace **Mafic Enriched Domain SiO_2 wt.%:** N/A	**Mush:** *Crystal accumulation and settling/sorting in a semi-evolved magma* **Compaction:** *Moderate compaction sorted and aligned crystals* **Bright CL:** *Two populations of IM - a high silica and K_2O and a low silica, high FeO group* **Mafic Enriched Domains:** *Trace present*
	GR 8b 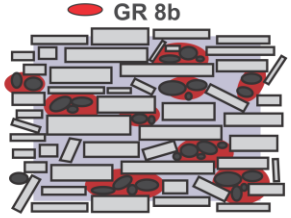	**Whole Rock SiO_2 wt.%:** 46 **Plag. %:** 75 % **CPO:** Strong **An#:** 37 **Bright CL %:** 2.5 % **Bright CL SiO_2 wt.%:** 59 **Mafic Enriched Domain %:** 4.5 **Mafic Enriched Domain SiO_2 wt.%:** 45	**Mush:** *Crystal accumulation and settling in a comparatively less evolved magma.* **Compaction:** *Cumulate fabric formed from moderate-strong uniaxial compression* **Bright CL:** *Very little felsic intergrain material* **Mafic Enriched Domains:** *High amounts of trapped silica-poor melt form MED*

Figure 4.13 Summary table of Goat Rock plutonic lithic populations. Left, schematic volcanic system adapted from Cashman et al. (2017). Potential lithic resident locations in mush indicated by red (GR8b), green (GR20), and blue (GR14) circles. Colored circles correspond to schematic of lithic type samples: plagioclase (grey rectangles), mafic phases (black ovals), mafic enriched domains (red regions), and bright CL areas (purple regions). Right, corresponding data and interpretations for each component of plutonic lithic.

Whole rock compositions vary systematically for the three lithics: GR8b is less evolved than GR14 and GR20 falls between the two (Table 2). This relationship is echoed by major elements (i.e. Al_2O_3 Na_2O K_2O MgO CaO, Table 2) and corresponds to the variation in CPO strength (Figure 13).

As with whole rock data, the trend of feldspar compositions between lithics is smooth and best explained by a progressively evolving crystal population as cooling and crystallization progresses. The spread of plagioclase compositions progressively narrows in higher silica samples (i.e. GR8b has the greatest spread, then GR20, GR14 is comparatively clustered, Figure 4.10). In a mush that has an evolving and migrating melt component, we may expect to see this tightening of the crystal population as minerals segregate out and the remaining, more evolved melt crystallizes towards a more albite rich end-member (Morse et al., 2017).

While broad lithic compositions seem to reflect progressive differentiation and evolution within the crust, mineral compositions of each lithic suggest that the system was complex and locally variable. Lithics have related but distinguishable plagioclase populations (see Figure 16 Appendix), suggesting that they resided in slightly different areas of a mush but were affected by similar cooling and crystallization conditions. The absence of sample-wide consistent rim compositions or trends of evolution or rejuvenation from cores to rims could imply that the mush was crystallizing, continually removing melt, and cutting off replenishing melt permeability such that local magma composition affected crystal compositions more than mush-scale rejuvenation and convection (Jackson et al., 2018).

Plagioclase compositions generally follow this trend in increasing fractionation and decreasing strength of compaction from GR8b to GR14. As expected, An# decreases as whole rock SiO_2

increases and CaO and MgO decrease. GR8b has an average plagioclase An# of 37 while GR14 plagioclase have an average of An24; GR20 falls in the middle (An#30, Figure 4.9b). Plagioclase compositions overlap across lithic samples, though crystal populations of an individual lithic remain distinct and reflect the evolving trend in whole rock compositions from GR8b to GR14 (Figure 4.10). This suggests plagioclase generally grew as primocrysts and is best seen in change in average An# for each lithic.

When chemical and textural data are combined a pattern emerges, wherein GR8b is the least evolved lithic and has the strongest compaction fabric, followed by GR20, then GR14 with the most felsic composition and weakest compaction CPO (Figure 4.13).

Textural evidence, both qualitative petrographic observations and quantitative EBSD data, supports the interpretation of an evolving body of magma and adds additional context to plutonic lithics that are removed from their in situ location. The proportion of plagioclase varies from 75% in GR8b to 80% in GR20 to 93% in GR14 (Table 1). Plagioclase crystals become more equigranular and have fewer disequilibrium textures (such as holes, cracks, lobate grain boundaries, complex zoning, etc.) with increasing SiO_2 content suggesting the more felsic lithics are closer to textural equilibrium (Holness et al., 2007). Mafic minerals also progressively decrease from 25% in GR8b to 7% in GR14 along with a change from multi-crystal clusters to small, intergranular crystals.

Local, non-hydrostatic stresses must have occurred in the near solid state (i.e. low melt fractions) due to the prevalence of dislocation creep indicators and grain boundary migration (Rybacki and Dresen, 2000). Indeed, compaction is acknowledged as being an important force in melt fractions less than 2% where buoyant melt migrates along permeable grain boundary networks and ascends as the solid fraction compresses (Solano et al., 2014).

The concurrent expulsion of melt is a key mechanism required for magmatic compaction to produce an adcumulate fabric without other convective or tectonic forces (Holness et al., 2017c). Bright CL in Goat Rock plutonic lithics decreases with fabric strength: The lithic with the lowest silica, strongest fabric, most mafic phases, and greater deformation indicators has the least bright CL areas (GR8b: 2.5%, Figure 4.13). The other lithics follow this pattern: GR20 has, on average, more bright CL areas (2.9%) and GR14 has the most bright CL areas (6.1%). The correlation between fabric strength and amount of grain boundary associated bright CL is compelling evidence of compaction-induced melt extraction through an evolving mush (Figure 4.13).

In all variation diagrams, bright CL compositions of the three lithics follow the same relative progression with GR8b defining one end member characterized by lower SiO_2 and GR14 making up the other end member (Figure 4.10). GR8b has lower Na_2O and K_2O and GR14 the highest with GR20 generally falling in the middle (Figure 4.8). GR8b has the highest CaO followed by GR20, then GR14. Al_2O_3 does not strictly follow this trend, however, GR8b is more spread than GR14. This is also true for total Fe and Na_2O. In Na_2O and Al_2O_3, GR14 plagioclase and bright CL compositions are very similar but they diverge in CaO and K_2O; bright CL is lower in CaO and higher in K_2O than its plagioclase population (Figure 4.10).

Importantly, the composition of bright CL in GR14 is higher in SiO_2, Na_2O, and K_2O and lower in CaO than the bright CL in GR8b (Figure 4.8). That is, melt in the more texturally and compositionally mature lithic is more fractionated than the melt in a more immature lithic (Figure 4.13). The bright CL of GR14 is also far more constrained than that of GR20 and GR8b. In addition, the two bright CL groups in GR20 compositions converge at higher silica (Figure 4.10). This could reflect melt migrating through the mush and fractionating as it diffuses and crystallizes (Solano et al., 2014; Jackson et al., 2018).

Framework-forming plagioclase settled and grew under compressive forces and porosity was reduced via compaction in conjunction with melt extraction (Figure 4.13; Bertolett et al., 2019). Here, the strongest fabric is attributed to the least chemically evolved lithic (GR8b), the weakest fabric to the most evolved lithic (GR14, Figure 4.13). Plagioclase compositions in GR14 have lower An numbers, reflecting crystallization of an evolved magma that had already begun to crystallize and segregate out less evolved crystal phases (i.e. the more An rich plagioclase and greater proportion of mafic phases in GR8b). Despite the absence of in situ orientation information available for these samples (due to the lithics being randomly emplaced in a volcanic dome), this data is used to envision a differentiating and evolving mushy sill.

Mafic enriched domains

Mafic enriched domains are more abundant in the least mature lithics: GR8b has extensive regions of the material, GR20 has some and GR14 has none (Figure 4.3). The plutonic lithics with mafic enriched domains have abundant clinopyroxene, olivine, and Fe-Ti oxide clusters similar to the association of mafic phases and fine-grained microstructures of Vukmanovic et al. (2018). Bright CL compositions (for GR20 in particular) can fall in to two groups generally defined by high FeO or K_2O, suggestive of Fe and Si conjugate immiscible melts (McBirney 1975; Philpotts 1978; Fiedrich et al., 2017; Holness et al., 2017b). The compositions of the mafic enriched domains are also low in SiO_2 but enriched in total FeO (Figure 17 Appendix).

The strong association of mafic enriched domains with mafic phases, specifically olivine, clinopyroxene, and Fe-Ti oxides, and its inverse correlation with silica rich bright CL suggests these regions have an association with late stage melt processes and the percolation of reactive melt. Further analysis is needed to confirm whether the bright CL populations represent end members of an immiscible melt. Mafic enriched domain EDS data for GR8b and GR20 (none was

found in GR14) are plotted with Si and Fe immiscible liquid end member compositions from the Skaergaard Intrusion (Humphreys, 2011; Figure 17 Appendix). Mafic enriched domains, especially in GR8b, correlate well with Fe-rich immiscible liquids from the Skaergaard studies. Bright CL of this study generally corresponds to the Si-rich immiscible liquids, particularly in the range of SiO_2. Goat Rock bright CL is higher in Al_2O_3 and Na_2O and lower in FeO than the Skaergaard data, however. This could be due to the more calc-alkalilne signature of AVC volcanism. Silica rich immiscible melt inclusions from alkali xenoliths prove a very good match with Goat Rock bright CL (Hurai et al., 1998; Figure 17 Appendix).

Immiscible melts may have formed due to density differences such that Si- and K-rich melt migrated away from a compacting mush while Fe-rich melt could not ascend and became trapped as porosity closed off. Conversely, compositional differences between an intruding interstitial melt and the crystal mush may produce the chemical variations and textures described. This melt would be in disequilibrium with the surrounding crystals and begin to react. Local disequilibrium could cause alteration of mafic phases as melt evolved in small, locally diverse pores connected by thin melt channels (Solano et al., 2014). This explanation addresses the larger area of mafic enriched domains found in GR8b which may be a Fe-rich conjugate that was trapped with the early forming crystals with which it was in disequilibrium as porosity reduced with extensive compaction. The buoyant Si-rich conjugate could utilize grain boundaries to migrate away from this part of the mush and could be related to the silica rich bright CL found more abundantly in GR14. Tie lines between Goat Rock mafic enriched domains and bright CL are similar to those of immiscible liquid end-members in Jakobsen et al. (2005). The kinematics of melt immiscibility and buoyant melt migration could be a driver for continued compaction (Solano et al., 2014).

We favor an explanation that includes reactive melt flow because of the association of bright CL volume and CPO strength, the presence of compaction CPOs, and the compositional and textural evolution of the lithics that suggest mush stratification (Solano et al., 2014; Jackson et al., 2018). Such an explanation fits with the small plagioclase and bright CL compositional variations we find within the larger trend of evolution and compaction that might reflect local variability rather than bulk magma evolution.

AVC magmatism

The Akaroa magmatic system is hypothesized as multiple crustal reservoirs where ascending magma stalled and differentiated (Hartung, 2011). Such crustal reservoirs could be described by incremental and overlapping mushy sills that intruded over the lifetime of the complex and were cut by a system of dikes that fed main vent and flank eruptions. Plutonic lithics are abundant in the northern portion of the lava dome and have radial cooling joints propagating out into the dome material (Figure 4.1b). Lithics are intact and undeformed but do not exhibit chilled margins, suggesting that the plutonic material was solidified but not cooled when Goat Rock magma intruded and entrained them. The abundance of plutonic material of similar crystalline textures and dominantly intermediate compositions, as well as ubiquitous large (1-3 cm) individual crystals, in the dome is suggestive of a shallow mush source rather than a deeper, mafic (e.g. Kennedy and Stix, 2006; Kennedy et al., 2015) or complex multi-staged source.

The plutonic lithic whole rock compositions are mafic-intermediate (Figure 4.8) rather than ultramafic AVC lithics such as the LeBons Bay Peak lower crustal xenoliths (Sewell et al., 1993). Some of the Goat Rock plutonic lithics are similar to the composition of the Goat Rock dome lava (Figure 15 Appendix). Goat Rock Lava Dome compositions sit in the middle of the trend for the lithics in all major elements (Figure 15 Appendix). In a closed system where the host represents

the lava dome and the lithics the solid fraction, we would expect a host lava composition that is more evolved than the lithics. Because this is not the case, the host magma must have intruded a mush from a distinct magma batch and entrained the nearly solidified lithics. This may be a common occurrence in shallow sill and dike complexes (Cashman et al., 2017) such as the AVC.

A model of progressive compaction and melt extraction coupled with reactive flow fits the magmatic structure of a sequence of mushy sills progressively intruded by dikes that is more appropriate for the Akaroa Volcanic Complex than single reservoir models. This interpretation cannot be reached without a combined geochemical and textural approach. This multi-method study more precisely unravels an origin for Goat Rock plutonic lithics and, therefore, a more specific term than *plutonic lithic* may be appropriate in the future.

Conclusions

The multi-method approach of this study allows for better identification of the origin and evolution of AVC plutonic lithics. Textural categories, supplemented by CPO and intragrain deformation analysis, reveal progressions in textural and chemical maturity lost within geochemical analysis alone. The three lithics progress from mafic to intermediate and high An to low An in conjunction with decreasing strength of compaction fabrics (Figure 4.12). GR8b crystallized and was deformed in a comparatively immature portion of the mush than GR14. Bright CL, interpreted as residual melt, is mapped from color-CL images and is interpreted to correspond to decreasing pore space and interstitial liquid in a compacting mush: GR8b has the least bright CL while GR14 has the most. Bright CL compositions are more evolved than their respective whole rock and plagioclase compositions, suggesting that percolating melt migrated and evolved progressively within the mush. We suggest that the representative lithics described are evidence of strictly-defined compaction with accompanying melt extraction in a system with an observable volcanic

counterpart. This analysis presents a model of a cooling magma progressively crystallizing and undergoing compaction and immiscible melt extraction. These interpretations may help explain the magmatic processes at work beneath the AVC as well as aid our understanding of how crystal frameworks deform and extract melt.

Acknowledgements

We would like to thank Frontiers Abroad students Emily DePadova and Caroline Lawlor for their contributions to the lithic classifications. Thank you to Frontiers Abroad student Emily Beckham for collecting the EMPA data and Kari Cooper for feedback on an early draft of this manuscript. Funding for this project comes from Frontiers Abroad, a University of Canterbury Doctoral Scholarship, Brain Mason Science and Technology grant (2015/03), a Bowdoin College Kibbe Science Fellowship, and University of Canterbury Visiting Erskine Fellowship and National Science Foundation grant 1530963. Any opinions, findings, conclusions or recommendations expressed in this work are those of the authors and do not necessarily reflect the views of the National Science Foundation.

References

Angel RJ, Carpenter MA, Finger LW (1990). Structural variation associated with compositional variation and order-disorder behavior in anorthite-rich feldspars. *American Mineralogist,* 75:150-162

Barbarin, B. (2005). Mafic magmatic enclaves and mafic rocks associated with some granitoids of the central Sierra Nevada batholith, California: nature, origin, and relations with the hosts. *Lithos, 80(1-4),* 155-177. doi:10.1016/j.lithos.2004.05.010

Bergantz, G. W., J. M. Schleicher, A. Burgisser (2017). On the kinematics and dynamics of crystal-rich systems, *Journal of Geophysical. Research, Solid Earth*, 122, doi:10.1002/2017JB014218.

Bertolett, E. M., Prior, D. J., Gravley, D. M., Hampton, S. J., Kennedy, B. M. (2019). Compacted cumulates revealed by electron backscatter diffraction analysis of plutonic lithics, *Geology*, 47(5), 1–4. https://doi.org/10.11

Bischoff, A., Nicol, A., Barrier, A., and Wang, H. (in press). Paleogeographic and Morphologic Reconstruction of a Buried Monogenetic Volcanic Field. *Bulletin of Volcanology*.

Bowen, N.L., (1928), The evolution of igneous rocks, Dover publications, 332 p.

Brugger CR & Hammer JE (2015). Prevalence of growth twins among anhedral plagioclase microlites. *American Mineralogist,* 100(2-3):385-395 doi:10.2138/am-2015-4809

Burt, R. M., Brown, S. J. A., Cole, J. W., Shelley, D., Waight, T.E. (1998). Glass-bearing plutonic fragments from ignimbrites of the Okataina caldera complex, Taupo Volcanic Zone, New Zealand: remnants of a partially molten intrusion associated with preceding eruptions. *Journal of Volcanology and Geothermal Research, 84(3-4),* 209-237. doi:10.1016/S0377-0273(98)00039-0

Cashman, K. V., Sparks, R. S. J., Blundy, J. D. (2017). Vertically extensive and unstable magmatic systems: A unified view of igneous processes. *Science*, *3055*(March). https://doi.org/10.1126/science.aag3055cca

Charlier, B., Namur, O., Toplis, M. J., Schiano, P., Cluzel, N., Higgins, M. D., Auwera, J. Vander. (2011). Large-scale silicate liquid immiscibility during differentiation of tholeiitic basalt to granite and the origin of the Daly gap. *Geology*, https://doi.org/10.1130/G32091.1

de Wet, C., Teeter, E., Peterman, E., Beane, R., (2016). Optimizing Cathodoluminescence imaging on the SEM. *Geological Society of America Abstracts with Programs*, v. 48, no. 7.

Fiedrich AM, Bachmann O, Ulmer P, Deering CD, Kunze K, Leuthold J (2017). Mineralogical, geochemical, and textural indicators of crystal accumulation in the Adamello Batholith (Northern Italy). *American Mineralogist,* 102(12):2467-2483 doi:10.2138/am-2017-6026

Fynn GW & Powell WJA (1979). The cutting and polishing of electrooptic materials. Adam Hilger, London

Graeter KA, Beane RJ, Deering CD, Gravley D, Bachmann O (2015). Formation of rhyolite at the Okataina Volcanic Complex, New Zealand: New insights from analysis of quartz clusters in plutonic lithics. *American Mineralogist,* 100(8-9):1778-1789 doi:10.2138/am-2015-5135

Hampton, S. J., & Cole, J. W. (2009). Geomorphology Lyttelton Volcano, Banks Peninsula, New Zealand: Primary volcanic landforms and eruptive centre identification. *Geomorphology*, 104(3–4), 284–298. https://doi.org/10.1016/j.geomorph.2008.09.005

Hartung, E., (2011). Compositional diversity and the formation of a 'Daly Gap' in the basaltic to trachytic magmatic system of the Akaroa Volcanic Group, New Zealand. *Master's Thesis, University of Canterbury.*

Hildreth W (2004). Volcanological perspectives on Long Valley, Mammoth Mountain, and Mono Craters: several contiguous but discrete systems. *Journal of Volcanology and Geothermal Research,* 136(3-4):169-198 doi:10.1016/j.jvolgeores.2004.05.019

Holness, M.B., Anderson, A.T., Martin, V.M., Maclennan, J., Passmore, E. & Schwindinger, K. (2007) Textures in partially solidified crystalline nodules: a window into the pore structure of slowly cooled mafic intrusions. Journal of Petrology, 48: 1243-1264, doi.org/10.1093/petrology/egm016

Holness MB, Cawthorn RG, Roberts J (2017a). The thickness of the crystal mush on the floor of the Bushveld magma chamber. *Contributions to Mineralogy and Petrology,* 172(11-12) doi:10.1007/s00410-017-1423-4

Holness MB, Nielsen TFD, Tegner C (2017b). The Skaergaard Intrusion of East Greenland: Paradigms, Problems and New Perspectives. *Elements,* 13(6):391-396 doi:10.2138/gselements.13.6.391

Holness MB, Vukmanovic Z, Mariani E (2017c). Assessing the Role of Compaction in the Formation of Adcumulates: a Microstructural Perspective. *Journal of Petrology,* 58(4):643-673 doi:10.1093/petrology/egx037

Holness, M. B. (2018). Melt segregation from silicic crystal mushes: a critical appraisal of possible mechanisms and their microstructural record. *Contributions to Mineralogy and Petrology, 173(6)*, 48. doi:10.1007/s00410-018-1465-2

Humphreys, M.C.S. (2011). Silicate Liquid Immiscibility within the Crystal Mush: Evidence from Ti in Plagioclase from the Skaergaard Intrusion, *Journal of Petrology*, 52(1):147–174 doi:10.1093/petrology/egq076

Hunter, R. H. (1996). Texture Development in Cumulate Rocks. *Developments in Petrology, 15(C)*, 77-101. doi:10.1016/S0167-2894(96)80005-4

Hurai, V., Simon, K., Wiechert, U. et al. *Contributions to Mineralogy and Petrology,* (1998) 133: 12. https://doi.org/10.1007/s004100050433

Jackson, M. D., Blundy, J., Sparks, R. S. J. (2018). Chemical differentiation, cold storage and remobilization of magma in the Earth's crust. *Nature*, https://doi.org/10.1038/s41586-018-0746-2

Jakobsen, J.K., Veksler, I.V., Tegner, C., Brooks C.K. (2005). Immiscible iron- and silica-rich melts in basalt petrogenesis documented in the Skaergaard intrusion. *Geology*; 33 (11): 885–888. doi: /10.1130/G21724.1

Krieger-Lassen NC (1995). The relative precision of crystal orientations measured from electron backscattering patterns. *Journal Microscopy,* 181:72–81

Marsh, B. D. (1981). On crystallinity, Probability of Occurrence, and Rheology of Lava and Magma, *Contributions to Mineralogy and Petrology*, 85-98.

Marsh, B. (2004). A magmatic mush column rosetta stone: The McMurdo Dry Valleys of Antarctica. Eos, *Transactions American Geophysical Union*, 85(47), 497. https://doi.org/10.1029/2004EO470001

Mainprice D, Bachmann F, Hielscher R, Schaeben H (2015). Descriptive tools for the analysis of texture projects with large datasets using MTEX: strength, symmetry and components. *Geological Society, London, Special Publications*, 409(1):251-271 doi:10.1144/sp409.8

McBirney AR (1975). Differentiation of the Skaergaard Intrusion. *Nature* 253

Miranda EA, Hirth G, John BE (2016). Microstructural evidence for the transition from dislocation creep to dislocation-accommodated grain boundary sliding in naturally deformed plagioclase. *Journal of Structural Geology,* 92:30-45 doi:10.1016/j.jsg.2016.09.002

Morse SA, Davidson JP, Tepley FJ (2017). Plagioclase Zonation: An Archive of Trapped Liquid and Crustal Contamination. *Elements*, 13(6):403-408 doi:10.2138/gselements.13.6.403

Nasipuri P & Bhattacharya A (2007). Melt-assisted interior to margin switch from dislocation to diffusion creep in coarse grained plagioclase: Evidence from a deformed anorthosite pluton. *Journal of Structural Geology,* 29(8):1327-1338 doi:10.1016/j.jsg.2007.04.005

Pistone, M., Arzilli, F., Dobson, K. J., Cordonnier, B., Reusser, E., Ulmer, P., Marone, F., Whittington, A. G., Mancini, L., Fife, J. L., Blundy, J. D. (2015). 'Gas-driven filter pressing in magmas: insights into in-situ melt segregation from crystal mushes.', *Geology*., 43 (8). pp. 699-702

Philpotts A (1978). Textural evidence for liquid imiscibility in tholeiites. *Mineralogical Magazine,* 42(324)

Prior, D.J., et al., (1999). The application of electron backscatter diffraction and orientation contrast imaging in the SEM to textural problems in rocks: *The American Mineralogist*, v. 84, p. 1741–1759, https:// doi .org /10 .2138 /am -1999 -11 -1204.

Ring U & Hampton S (2012). Faulting in Banks Peninsula: tectonic setting and structural controls for late Miocene intraplate volcanism, New Zealand. *Journal of the Geological Society,* 169(6):773-785 doi:10.1144/jgs2011-167

Rybacki, E., & Dresen, G. (2000). Dislocation and diffusion creep of synthetic anorthite aggregates. *Journal of Geophysical Research: Solid Earth,* 105(B11), 26017-26036. doi:10.1029/2000JB900223

Satsukawa T, Ildefonse B, Mainprice D, Morales LFG, Michibayashi K, Barou F (2013). A database of plagioclase crystal preferred orientations (CPO) and microstructures – implications for CPO origin, strength, symmetry and seismic anisotropy in gabbroic rocks. *Solid Earth,* 4(2):511-542 doi:10.5194/se-4-511-2013

Sewell RJ, Hobden BJ, Weaver SD (1993). Mafic and ultramafic mantle and deep crustal xenoliths from Banks Peninsula, South Island, New Zealand. *New Zealand Journal of Geology and Geophysics,* 36(2):223-231 doi:10.1080/00288306.1993.9514570

Solano, J. M. S., Jackson, M. D., Sparks, R. S. J., Blundy, J. (2014). Evolution of major and trace element composition during melt migration through crystalline mush: Implications for chemical differentiation in the crust. *American Journal of Science*, 314, 895–939. doi: 10.2475/05.2014.01

Timm, C., Hoernle, K., van den Bogaard, P., Bindeman, I., & Weaver, S. (2009). Geochemical evolution of intraplate volcanism at Banks Peninsula, New Zealand: Interaction between asthenospheric and lithospheric melts. *Journal of Petrology*, *50*(6), 989–1023. doi.org/10.1093/petrology/egp029

Vinet, N., & Higgins, M. D. (2010). Magma Solidification Processes beneath Kilauea Volcano, Hawaii : a Quantitative textural and Geochemical Study of the 1969-1974 Mauna Ulu Lavas, *Journal of Petrology*, *51*(6), 1297–1332. https://doi.org/10.1093/petrology/egq020

Vukmanovic Z, Holness MB, Monks K, Andersen JCØ (2018). The Skaergaard trough layering: sedimentation in a convecting magma chamber. *Contributions to Mineralogy and Petrology,* 173(5) doi:10.1007/s00410-018-1466-1

Wark, D. A., Hildreth, W., Spear, F. S., Cherniak, D. J., & Watson, E. B. (2007). Pre-eruption recharge of the Bishop magma system. *Geology*, 35(3), 235–238. https://doi.org/10.1130/G23316A.1

Žák J & Klomínský J (2007). Magmatic structures in the Krkonoše–Jizera Plutonic Complex, Bohemian Massif: evidence for localized multiphase flow and small-scale thermal–mechanical instabilities in a granitic magma chamber. *Journal of Volcanology and Geothermal Research,* 164(4):254-267 doi:10.1016/j.jvolgeores.2007.05.006

Chapter Five - Plutonic Lithics of the Akaroa Volcanic Complex

Chapter 5 fulfils objective 4 of this thesis: *to document and relate all known occurrences of plutonic lithics in the Akaroa Volcanic Complex with the methods utilized in the previous two objectives.*

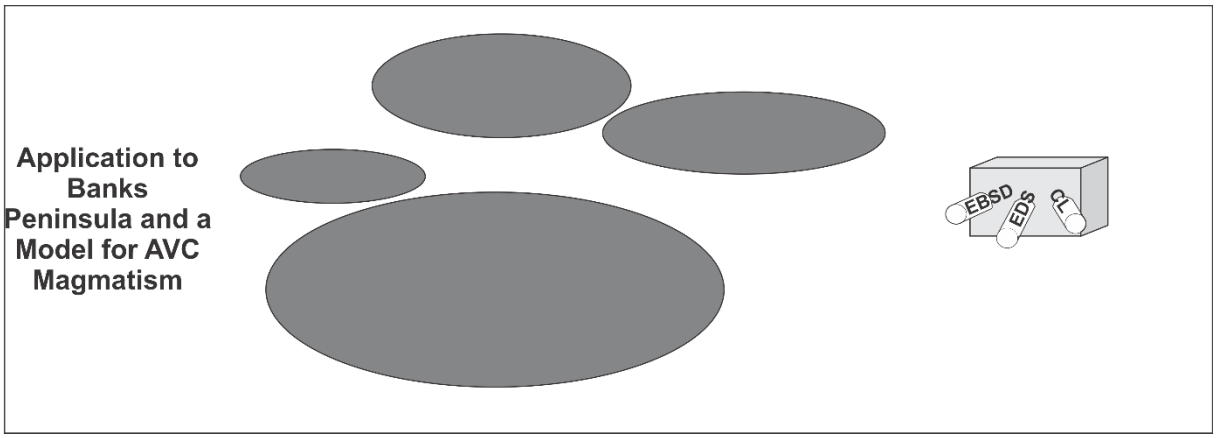

From Figure 2.9 showing the relevant section to this chapter.

Chapter 5 collates data from all plutonic lithic - bearing locations for the AVC and presents new chemical and textural data for three previously recognized locations and four new locations. This study couples microstructural and geochemical analysis of plutonic lithics with broad-scale geomorphic observations of the Akaroa Volcanic Complex to infer the architecture of the crustal magmatic system and how the system grew, evolved, and sourced volcanic eruptions.

The AVC magmatic-volcanic relationship informed by geochemical and microstructural analysis of plutonic lithics

Bertolett E.M.[1], Hampton S.J.[1], Gravley D.M.[1], Teeter E.[2], Beane R.[3], Gualda G.[2], Kennedy B.M.[1]

[1]Department of Geological Sciences, University of Canterbury. West Building, Private Bag 4800, Christchurch 8140, New Zealand
[2]Earth and Environmental Sciences, Vanderbilt University, 2301 Vanderbilt Place, PMB 351805, Nashville, TN 37235-1805, USA
[3]Department of Earth and Oceanographic Science, 6800 College Station, Bowdoin College, Brunswick, Maine, USA 04011

Abstract

Plutonic lithics can impart clues on the magmatic processes active during crustal magmatism in systems where plutonic material is absent. However, geochemical analysis alone is inadequate in providing important context for the crystallization and entrainment histories of plutonic lithics within volcanic deposits. This study uses electron backscatter diffraction (EBSD) and color-cathodoluminescence (CL) mapping in conjunction with bulk rock, mineral, and late-stage melt chemistries to understand crustal magmatism at the Akaroa Volcanic Complex (AVC). Field evidence of plutonic lithic-bearing deposits and hand sample observations of lithic diversity (mineralogy and apparent crystal alignment) add to quantitative analyses and reveal a complexity of magmatic evolution and processes not previously appreciated at the AVC. Non-random plagioclase crystallographic preferred orientations (CPOs) are indicative either of uniaxial compaction or flow/shearing. CPOs often correlate with the way bright CL regions (inferred to be residual melt) are distributed. The chemistries of these bright CL regions frequently correlate with lava flow compositions or with postulated low silica immiscible melts, suggesting that the melt extracted from crystal accumulation may result in volcanic eruptions. This contribution collates

all plutonic lithic data for the AVC and, by comparing lithic and host compositions, reveals a multi-mush system more in line with a stacked sill and dike plexus than a large magma chamber.

Introduction

The chemical and textural signatures preserved in plutonic lithics can be used to reconstruct the magmatic architecture and processes occurring in the, now-extinct, AVC crustal magmatic system. The Akaroa Volcanic Complex (AVC), located on Banks Peninsula on the east coast of the South Island (Figure 5.1), is part of the largest center of Cenozoic intraplate volcanism in New Zealand. Banks Peninsula has excellent cross-sectional exposure of two basaltic volcanic complexes but there is a lack of knowledge on the crustal magmatic architecture of the systems responsible for cone building.

Most published work on the AVC focuses on the larger tectonic setting and the mantle source of magmatism (Hoernle et al., 2006; Timm et al., 2009) or the morphology of the volcano (Hampton and Cole, 2009). AVC volcanism is postulated to be the result of lithospheric delamination that caused asthenospheric upwelling and decompression melting that produced magma with a alkaline intraplate signature. (Timm et al., 2009). The Akaroa Volcanic Group (9.0-8.0 Ma) is the younger and larger of two main cone-building phases that formed Banks Peninsula (Figure 5.1; Sewell et al 1985; 1992; Forsyth et al., 2008; Ring and Hampton, 2012). The older sequence, the Lyttelton Volcanic Group (11.0-9.7 Ma), is slightly more felsic than the Akaroa phase (Sewell et al., 1992). Two smaller phases, the Mt. Herbert and Diamond Harbour phases, occur concurrently and after Akaroa phase volcanism respectively. The Akaroa Volcanic Group refers to the erupted deposits associated with this center of volcanism, however, as we deal with the entire volcanic and magmatic system, we prefer the term ‘Akaroa Volcanic Complex’ following Hampton and Cole (2009).

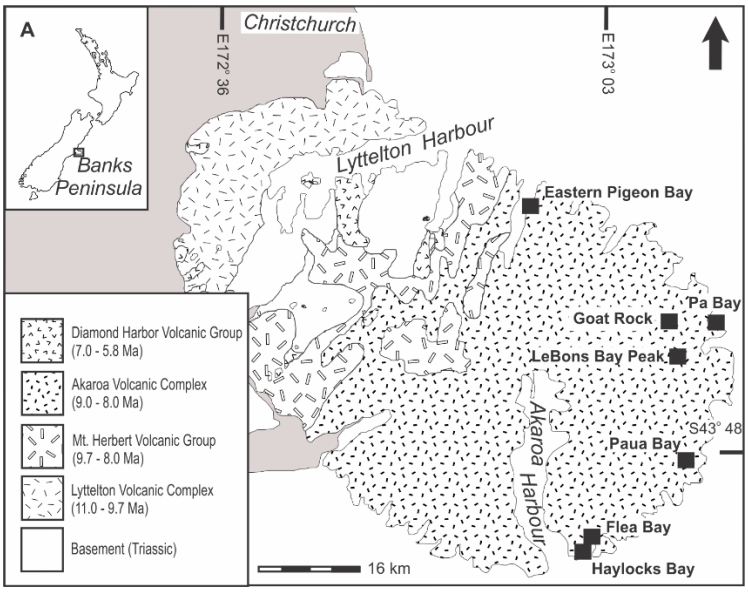

Figure 5.1 Outline of New Zealand (a) and geologic map of Banks Peninsula. Black boxes designate location of lithics associated with this study. Only AVC lithics are investigated here. Map after Ring and Hampton (2009).

Until recently, very little attention was paid to the mechanisms of crustal magmatism associated with the Akaroa Volcanic Complex (AVC). Indeed, much of our understanding of AVC crustal magmatism comes from unpublished theses (Sewell unpublished thesis, 1985; Dorsey unpublished thesis, 1988; Hartung unpublished thesis, 2011).

Our understanding of crustal magmatic system geometries has evolved since the Sewell model was proposed. The 'magma chamber' model in which a large body of melt is kept above the solidus for long periods of time is unable to account for many of the geochemical and geochronological signatures found in erupted deposits (eg. Cooper and Kent, 2014), the kinematics of crystallization, nor the thermodynamics of melt, crystals, and gases (Gualda and Ghiorso, 2013). In their review of large magmatic reservoirs, Cashman and Giordano (2014) address the poor compatibility of a traditional mush model to basaltic systems. Instead, they propose the concept of a plexus of sills and dikes that interact spatially and temporally to produce eruptive sequences (Vinet and Higgins,

2010; Cashman and Giordano, 2014) which better fits with the way buoyant melt is segregated and incrementally migrates through the crust (Solano et al., 2014).

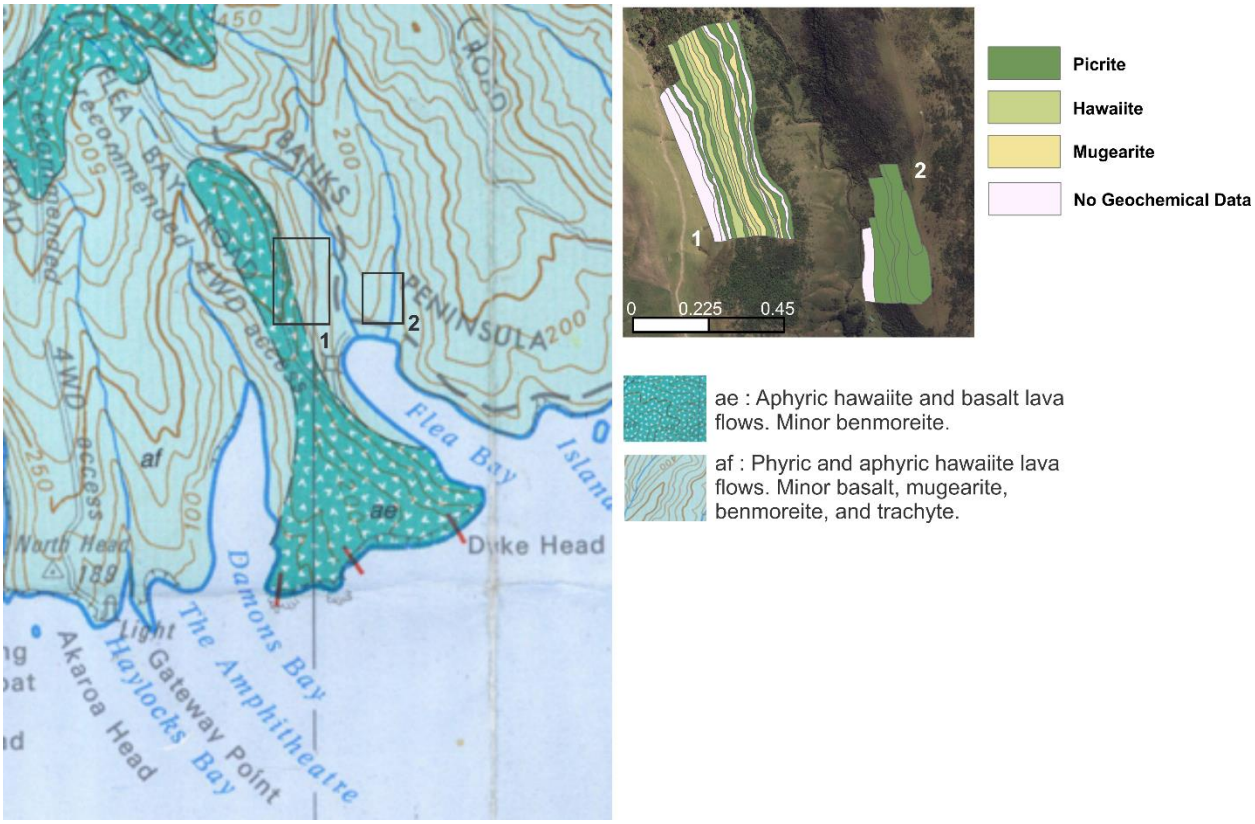

Figure 5.2 Left, a section from the 1992 Sewell et al. geologic map of Banks Peninsula showing the two major eruptive phases identified by the authors (af; main phase and ae; late stage). Right, the same area overlain with mapping data from the Frontiers Abroad mapping initiative. Legend on the right. Transects in 1 and 2 show a more detailed and more diverse sequence of lava flow compositions than seen on the Sewell et al. (1992) map.

The Sewell et al. (1985, 1992) AVC crustal magmatism model proposes a progressive evolution from picrite to trachyte over the whole lifetime of the AVC based on geochemical analysis of select lava flows. This cone-building model uses a stratovolcano morphology where a single center of activity sources lava flows (Sewell, 1985; Dorsey, 1988; Sewell et al., 1992; Figure 5.2). This whole-scale evolution from picrite to trachyte implies a relatively simple, single magmatic source in the style of the, increasingly debunked (Cashman et al., 2017), ‘magma chamber’ model.

Hartung (2011, unpublished thesis) expanded on this model with temperature and pressure modelling and the classification of an early cone-building phase and main-phase eruptives. Hartung (2011) identified a Daly Gap in the AVC where lava chemical compositions between 50 and 60 wt.% SiO_2 are missing. This gap, and whole rock and mineral chemistry trends, are explained using a multi-stage fractionation sequence in which deeply sourced magma stalls at the crust-mantle boundary and produces the predominant picrite-hawaiite trend found at the AVC (Hartung, 2011). This magma then ascends and stalls, first in the mid-crust where it fractionates, and then again ascends and stalls in the upper crust from which evolved trachytes are extracted (Hartung, 2011, see chapter 2.6 of this thesis). While the Hartung (2011) model adds the important complexity of multiple stages of magmatic differentiation at different depths, it primarily relies on a vertically contiguous source of magma that doesn't necessarily draw a distinction between the classic 'magma chamber' model and a more complex arrangement of dikes and sills (cf. Cashman et al., 2017). The physical processes required by this model are still indicative of large, single magma chamber dynamics that construct a substantial cone edifice.

Hartung (2011) and Sewell's (1992) model has prevailed until recent work as part of another unpublished thesis (Beckham, 2016). Beckham's (2016) model is based on careful stratigraphic field sampling linking each lava flow in the stratigraphy to a geochemical data point (note that Beckham's thesis is part of an ongoing study on the AVC conducted jointly by Frontiers Abroad Aotearoa and the University of Canterbury, see Figure 1.1 of this thesis). Instead of evolving from basalt to trachyte over the whole cone-building sequence of the AVC, Beckham's (2016) research demonstrates a repeated pattern whereby erupted magmas evolve, reset, and repeat (Figure 5.2). Figure 5.2 compares the different crustal magmatic models of early (basaltic) and late-stage (trachytic) eruptives (Sewell 1985; Dorsey, 1988; Hartung, 2011) to this new, more complex

model (Beckham, 2016) where primitive and evolved lavas are intermixed throughout stacked stratigraphic sequences (Figure 5.3) indicative of a stacked dike and sill plexus (Cashman and Giordano, 2014). Figure 5.2 highlights the evidence that evolved magmas erupted during many stages of the AVC's edifice growth.

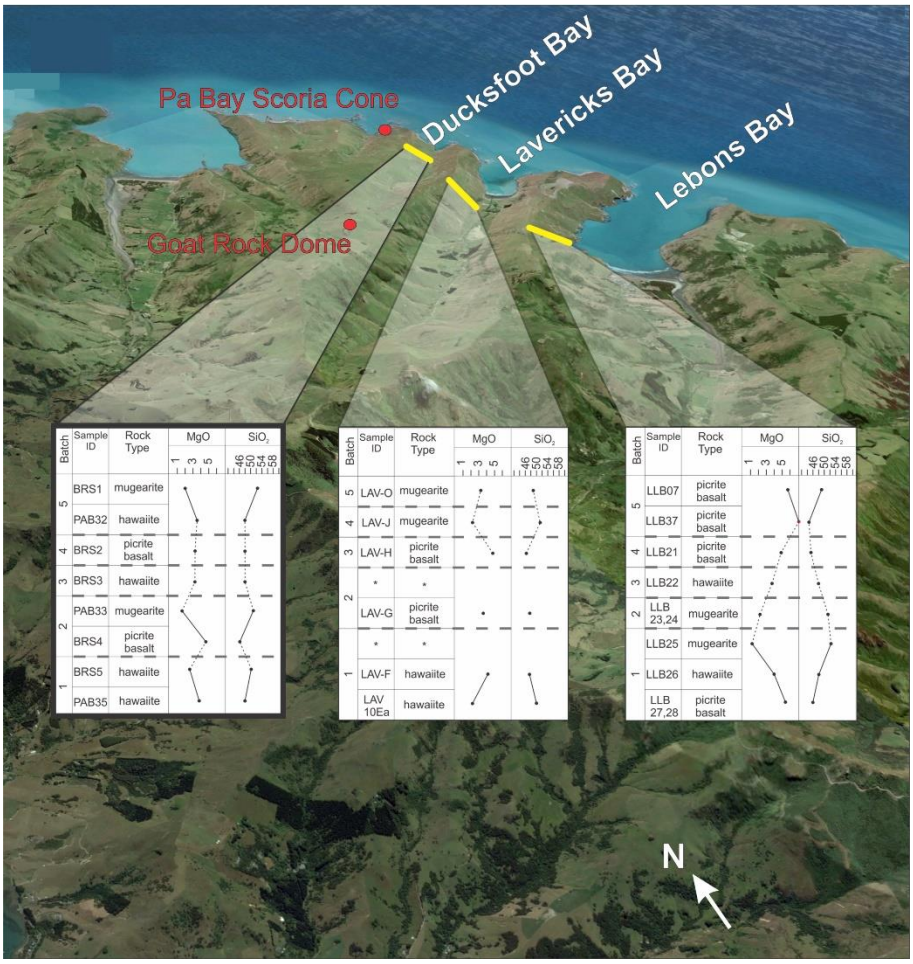

Figure 5.3 Geochemical transects of lava flows based on stratigraphy. Modified from Beckham (2016). Red dots denote Pa Bay and Goat Rock Dome with the Ducksfoot lava flows between them. For a detailed plot of the Ducksfoot transect with Goat Rock dome, see Appendix.

Similar trends at the Lyttelton Volcanic Complex are linked to edifice morphology. Recent work on the vent location of the Lyttelton complex suggests that, instead of a single vent source, up to six vent regions were active over the life of the LVC (Hampton, 2010 unpublished thesis).

Hampton (2010) uses a combination of eruptive packages highlighted by cone morphology, dike orientations, valley and ridge orientations, and the extension of the shore platform to define volcanic sectors (i.e. pie-slice shaped sections of stacked lava flows radiating outward from the crater rim region). This framework is also applied to the Akaroa Volcanic Complex (Hampton, 2010) and supported by radial dikes observed along the heavily eroded crater rim region (Goldman et al., in review). Each sector's lava flows connect back to a distinct region in the central vent region, further suggesting that the AVC was a complex, composite cone with multiple, but closely spaced, vents. Instead of referring to a single point source for cone-building lava flows, we refer to the source of the extensive AVC lava flows as the central region of the volcanic complex to encompass a multi-vent, composite volcano model that better fits these more detailed field and petrologic observations. This study brings together unpublished data with new geologic, textural, and geochemical findings on the AVC, with a particular focus on plutonic lithics and the volcanic facies that host them to refine the crustal magmatic model at the AVC.

The above observations suggest that multiple batches of magma or multiple cycles of magmatic evolution occurred within the AVC subvolcanic system. This contribution explores the signatures from the AVC magmatic system that may reflect this heterogeneity using SEM-based microstructural and geochemical techniques applied to plutonic lithics.

Previous AVC lithic studies

Plutonic lithics are useful in unravelling crustal magmatic processes in systems with little exposed plutonic material (Graeter et al., 2015) and provide a missing link between plutonic and volcanic systems (Bertolett et al., 2019). Crystal textures preserve magmatic conditions and can reflect processes such as deformation, melt extraction, convection, and tectonic overprinting (Holness et al., 2007; Miranda et al., 2016; Fiedrich et al., 2017; Holness et al., 2017; Vukmanovik et al., 2018;

Bertolett et al., 2019). These signatures can also be found in plutonic lithics which adds the additional insight of having passed from the magmatic in to the volcanic realm. Previous work on a small selection of plutonic lithics from Goat Rock Dome in the AVC provided evidence for compaction of a crystallizing mush (Bertolett et al., 2019). Here, we briefly review the plutonic material exposed at the AVC and introduce new locations where plutonic lithics have been found. Onawe Peninsula, located in the center of Akaroa Harbour, is the only *in situ* exposure of plutonic rock associated with the AVC. Onawe Peninsula's tip is made up of highly weathered syenite with rare outcroppings of gabbro (Dorsey, 1988). Other than the late-stage Onawe Peninsula, erupted lithics are the only exposed plutonic material within the AVC. Plutonic lithics within a lava flow at Haylocks Bay were the first recognized lithics within the AVC (Dorsey, 1988; Table 4; see Appendix). Sewell et al. (1993) identified ultramafic xenoliths in LeBons Bay Peak, a large basanite dome likely associated with the Diamond Harbour Phase (Timm et al., 2009), in the first published account of Banks Peninsula plutonic lithics (see Appendix). Recently, Hartung (2011) investigated the AVC magmatic architecture using geochemical and geobarometry modelling of AVC deposits, including enclaves from Haylocks Bay. Hartung (2011) conclude from this magmatic model that plutonic lithics in the AVC are cumulate residue from a fractionation sequence and represent the uneruptible portion of the magmatic system (i.e. the Daly Gap). Following the Canterbury Earthquake Sequence (beginning in 2010), hundreds of plutonic lithics were discovered at Goat Rock Dome within columnar jointed rockfall blocks (Bertolett et al., 2019).

Table 4 Lithic-bearing location with host and lithic features. From field observations.

Volcanic Feature	AVC Location	Feature Description	Lithic Populations and Descriptions	Feature Elevation
Lava flow	Paua Bay	Overthickened lava flow, radial fracturing	Variety of mineralogies, sizes, and fabrics	42m
	East Pigeon Bay	Lava flow with small lithics	Limited mineralogical variations	131m
	Flea Bay	Dense scoriacious / breccia, sparse lithics	Two plutonic lithics found, only one able to be sampled. Similar mineralogy to Goat Rock	75m
	Haylocks Bay	Shore platform lava flow	Two main types of mineralogies and crystal sizes	1.8m
Scoria Cone	Pa Bay	Layered scoria and tephra flank deposits, xenolith-rich	Wide variety of crystalline and non-crystalline lithics	7m
Dome	Goat Rock	Columnar jointing, radial fractures around lithics	Abundant crystalline lithics, all relatively similar size (10-20 cm) and mineralogy	395m
	LeBons Bay Peak	Large, jointed dome, very altered lithics	Large variety of plutonic lithic mineralogy and textures	419m

Subsequent field expeditions have revealed multiple, previously unrecognized locations within the AVC that contain plutonic lithics. While not ubiquitous, lithics are more prolific than previously recorded, and reside in diverse types of deposits including lava flows, volcanic domes, and scoria deposits (Table 4). In addition, the type of material entrained varies, reflecting the complex relationship of volcanic stratigraphy, basement lithologies, and the underlying magmatic system.

This study collates all lithic-bearing locations currently known and attempts to explain AVC crustal magmatism from a geochemical and microstructural investigation of plutonic lithics, their host, and the relationship between lithics at different AVC locations using the context provided by broad-scale geomorphic observations.

Methods

Field work

Field work was undertaken over a course of four years as part of a field teaching course in which the lava flows and features of the AVC were mapped in stratigraphic detail. Multiple sections of the Akaroa Volcanic Complex were traversed and the location of lithic-bearing features recorded for subsequent removal (Table 4). Sampling was undertaken primarily with the use of a concrete saw or portable core-drill as host lithologies were usually very indurated and lithics frequently shatter (if removed using hammer and/or chisel).

Care was taken to sample a representative selection of lithic types (mineralogy, crystal alignment, etc.) if applicable (Figure 5.4). Where a large number of lithics are present, a field classification was undertaken to assist this selection processes (Bertolett et al., in review, Figure 1.1 of this thesis). The host deposit in which lithics were found was also samples and field observations on deposit type, features, and distribution of lithics within it were recorded (Table 4).

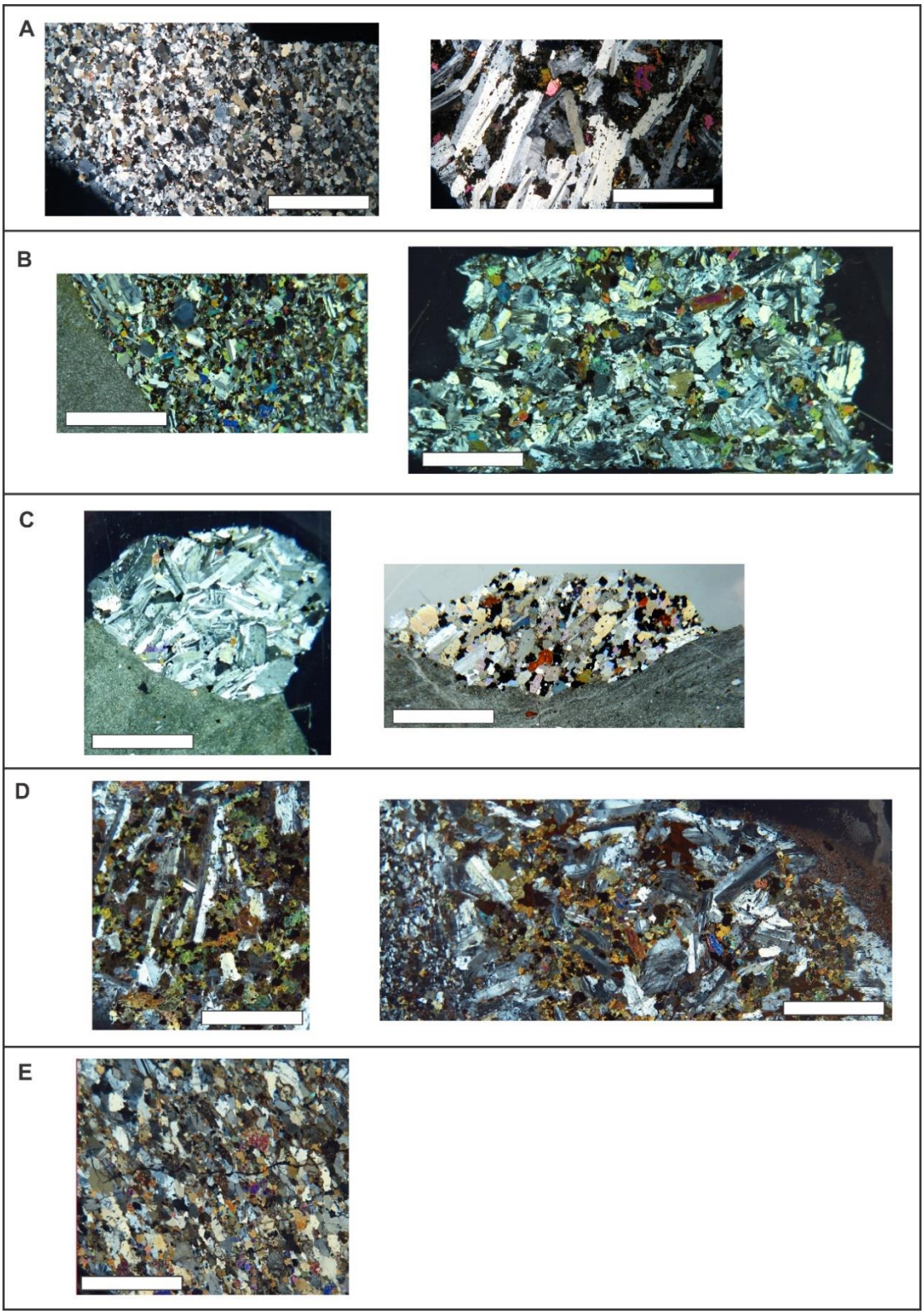

Figure 5.4 Cross polarized thin section images showing variations in mineralogy, crystal size, and apparent crystal alignment for (a) Goat Rock, (b) Eastern Pigeon Bay, (c) Paua Bay, (d) Haylocks Bay, and (e) LeBons Bay Peak. Scale bar 10 mm.

SEM techniques

Samples were selected for EBSD analysis based primarily on apparent shape preferred orientation (SPO). Some plutonic lithics have only subtle crystal alignment. See Table 1 for a summary of the location and type of data available for AVC plutonic lithics.

Major element whole rock analysis for Goat Rock host and lithics, Ducksfoot lava flows, and Pa Bay lithics was conducted on a Philips PW 2400 Sequential Wavelength Dispersive X-ray Fluorescence 63 Spectrometer at the University of Canterbury. Paua Bay, E. Pigeon Bay, LeBons Bay Peak, and Haylocks Bay lithics and host of this study were analyzed by CRL.

The CAMECA SX50 Electron Microprobe at the University of Wisconsin-Madison was used to obtain major-element mineral compositions for Goat Rock.

Probe-quality polished thin sections (Goat Rock and Paua Bay) were prepared at the University of Canterbury and Bowdoin College. Energy Dispersive Spectroscopy (EDS) maps were collected on a Tescan Vega 3 LM Variable Pressure Scanning Electron Microscope at Vanderbilt University, a Tescan Vega 3 LMU SEM with an Oxford Instruments Aztec system at Bowdoin College, and a JOEL IT300 at the University of Canterbury with standards. Maps were collected for small areas at high resolution (see Appendix).

An ~ 10 nm thick carbon sputter coat was applied to thin sections to dissipate charging during electron beam analysis. Large area maps of electron backscatter diffraction (EBSD) data were collected on a Zeiss Sigma VP FEG scanning electron microscope (SEM) with an Oxford Instruments HKL INCA Premium Synergy system at the University of Otago and a Tescan Vega 3 LMU SEM with an Oxford Instruments Aztec system at Bowdoin College. EBSD patterns were obtained using an accelerating voltage of 20 kV (Bowdoin College and 30 kV (University of

Otago), 70° stage tilt and 20-100 micron step-size dependent on specimen grain size (a finer 5.15 μm step size was used for features of interest). For details of the various data collection methods and parameters used, see Bertolett et al. (in review).

Cathodoluminescence (CL) images for full thin sections were obtained using the TESCAN Vega 3 LMU SEM with a TESCAN Rainbow CL detector at Bowdoin College. 'Black balancing' was used to collect consistent and reproducible image data across specimens following the methods of DeWet et al. (2016).

Results

Scoria cones, volcanic domes (both basaltic and trachytic), and dikes are identified throughout the AVC on the 1992 Banks Peninsula map (Sewell et al., 1992). Extensive, landscape-forming lava flows extend from the central region of the volcanic complex. Large volcanic domes are primarily trachytic in composition (Sewell et al., 1992) (i.e. Panama Rock, Hampton and Lewis 2015). However, basaltic domes are also common (ex. Goat Rock, and Lebons Bay Peak). Generally, volcanic domes at the AVC are found at elevations between 350 and 650 meters (Goldman et al., in review). Many domes are dike fed, and some such as Panama Rock, have clear feeder dike relationships. Dikes, like domes, are either basaltic or trachytic. Radial dikes intersecting the modern AVC topographic rim are predominately trachyte and postulated to have been emplaced in the later stages of AVC volcanism (Goldman et al., in review). Scoria cones are common in the AVC. Generally, there is a concentration of scoria cones forming the modern shore platform. However, scoria cones are occasionally associated with domes (such as at Goat Rock) and are also found along the topographic rim of the AVC. Volcanic domes seem to be mostly late-stage (based on field relationships) but scoria cones have relative age relationships suggesting both early

emplacement in the cone-building sequence and concurrent with active volcanism. Plutonic lithics are rare but are found in all the main types of AVC volcanic deposits.

Lithics presented and discussed in this study are from seven locations within the AVC (Table 4) that we separate into scoria cone, dome, and lava flow. We separate these due to the differing eruptive process in creating these features, and potential differences within the magmatic system.

Lava Flow Hosted Plutonic Lithics

Lava flows are the predominant cone-building feature of the AVC. Typical lava flows are 1-3 m thick, laterally extensive a'a flows and are sourced from the central AVC region. Small-scale, discrete lava flows are commonly associated with scoria cones but are not important to the wider morphology of the complex. The lava flow hosted lithics presented in this study are located on the outer flanks of the volcanic complex and in regions where connectivity to the central region of the AVC is linked by observations, mapping, and projected correlations.

Haylocks Bay, Eastern Pigeon Bay, Paua Bay, and Flea Bay are locations where a central region lava flow hosts a population of lithics. Haylocks Bay lithics are found in a lava flow that makes up the shore platform on the outer southeastern flank of the AVC (Figure 5.1). Haylocks Bay has two types of lithics: both have the same mineral assemblage (plagioclase, pyroxene>olivine>oxides, Figure 5.5) but one has large, 1-4 cm crystals with an apparent crystal fabric.

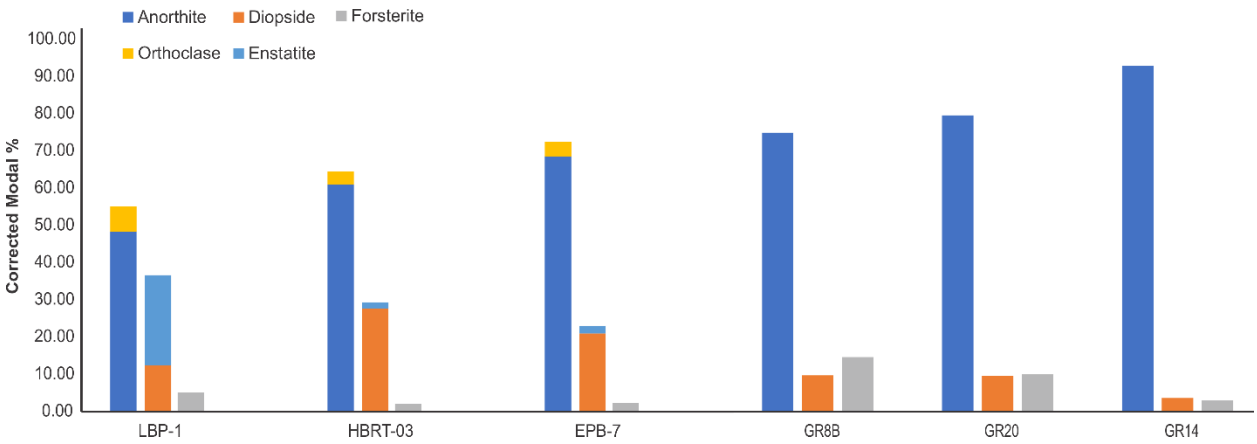

Figure 5.5 Histogram of corrected mineralogy proportion based on EBSD phase maps. Modal mineralogy determined as a percentage of points indexed as each mineral from EBSD maps. Non-indexed points and accessory phases are removed and corrected to 100%. Note the significant proportion of plagioclase in Goat Rock and the comparatively high amounts of pyroxene in LeBons and Haylocks Bay.

Paua Bay lithics are found on a small ridge just above sea level on the outer flanks of the complex (Figure 5.1). The lava flow that contains the lithics forms a low ridge within the valley. The presence of vertical columnar jointing on the shoreward side and thinner, horizontal jointing on the opposite side of the ridge, and inferred connectivity to larger lava flows in the valley suggest that the deposit is an over-thickened toe of a lava flow sourced from the central volcanic region. Paua Bay has a substantial diversity of plutonic lithics including lithics that are almost all feldspar, some that are predominately pyroxene, others that are pyroxene,olivine>>plagioclase and, more commonly, plagioclase>pyroxene>olivine plutonic lithics. Paua Bay lithics range from a few centimetres in diameter to one sample 20 cm in diameter.

Eastern Pigeon Bay lithics are found in a lava flow on the eastern outer flanks of the complex, but much higher above sea level than the two locations discussed above (Figure 5.1). Like most of the other main vent region lava flows in the AVC, the lithic-bearing lava flow at Eastern Pigeon Bay is 1-2 meters thick and laterally extensive. Eastern Pigeon Bay plutonic lithics are comparatively homogenous and have plagioclase>pyroxene>olivine>oxides (Figure 5.5) and no clear crystal

alignment. At all three locations, lithics are spatially constrained and the lava flows themselves, other than containing lithics, are not texturally or chemically different than other AVC lavas.

Two plutonic lithics were found in a deposit on the valley edge of Flea Bay (Figure 5.1). The lithics are similar to the majority of other AVC lithics (plg>pyx>>ol,oxides). The deposit they reside in is obscured by dense vegetation and steep topography. The host deposit is red and rubbly but field observations do not suggest a relationship with a scoria cone. It is possible that the host is the rubbly base of a lava flow that, due to flow along paleo topography or the cross section exposed by erosion, is thickened.

Scoria Cone Hosted Lithics

Scoria cones occur throughout the AVC (Sewell et al 1992). In this study, lithics found at Pa Bay, a coastal scoria cone, are described (Figure 5.1, Table 4). Additional scoria cone associated lithics have been recognised during field mapping but were not sampled as the analysis required to fully describe them and their vent is beyond the scope of this research.

Numerous sedimentary lithics are found in the flanks of a parasitic scoria cone at Pa Bay. Pa Bay is home to a complex sequence of parasitic scoria cones, a fissure vent, dikes, and overlapping main vent lava flows. The scoria cone containing lithics is preserved on one side of Pa Bay: a cross section through the flank deposit shows the internal stratigraphy of the scoria cone. The scoria cone was eroded and AVC central region lava flows were deposited around and on top of the truncated cone (Figure 5.6).

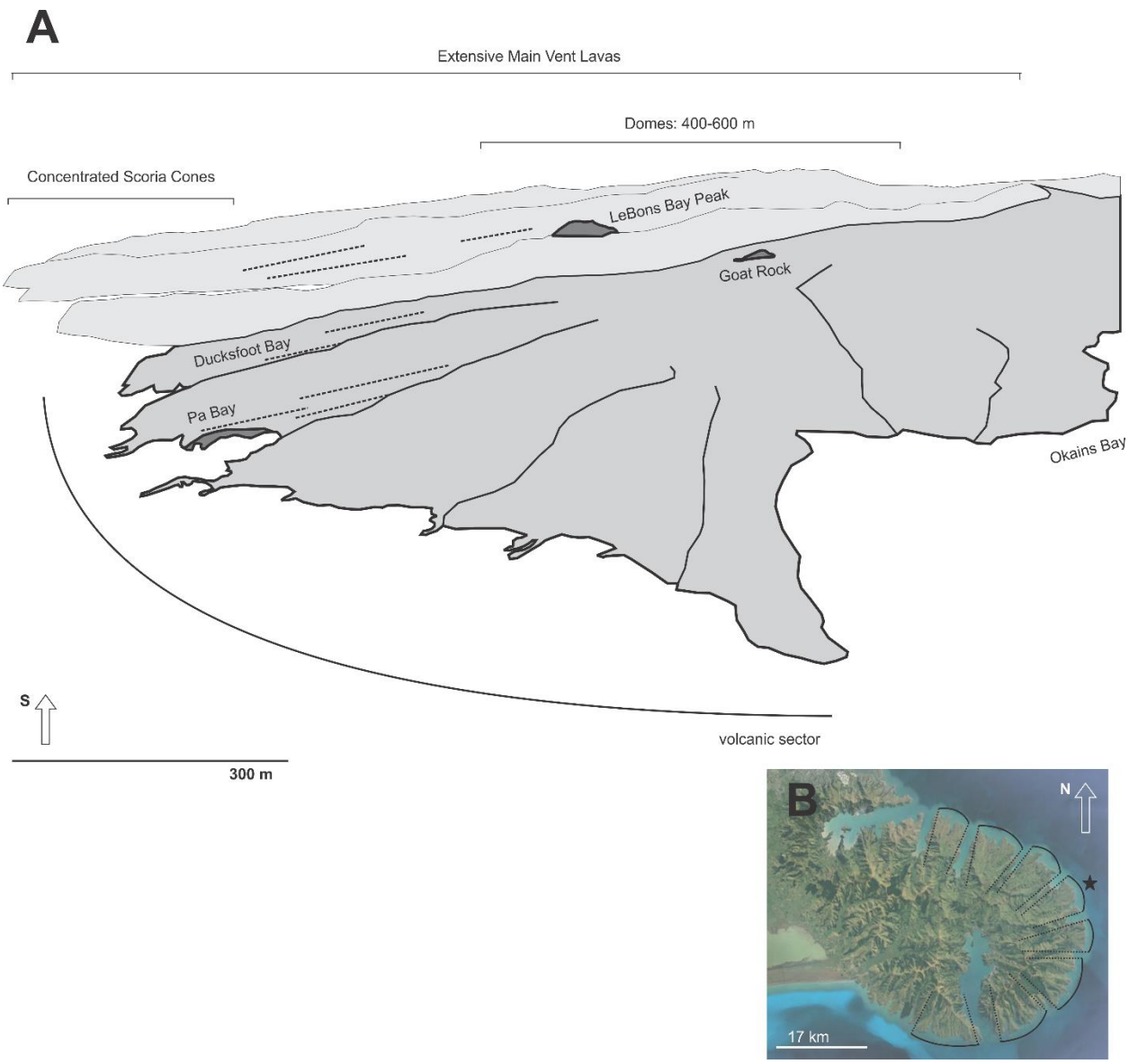

Figure 5.6 Pa Bay, Ducksfoot, and Goat Rock relationship. Volcanic sectors. Inset modified from Hampton (2010).

Pa Bay lithics reside in the layered eruptives on the flank of this small satellite scoria cone. The scoria cone has a number of non-crystalline inclusions including small (<10 cm) fine to very fine grained, quartz rich sandstone occasionally interbedded with volcanic ash, chert, and clasts of lava flows and large (1-3 cm) single crystals (Atwood et al., 2014). The non-crystalline lithics represent the young sedimentary units on top of the Torlesse Basement rock on which the AVC sits (see

Figure 2.6 in Chapter 2 of this thesis). The localized occurrence of these sedimentary lithics in a small scoria cone indicates that they are sourced from the shallow subsurface (Atwood et al., 2014). Crystalline plutonic lithics are also found in the Pa Bay scoria deposits though are not as common as sedimentary lithics nor large, pyroxene crystals. As this study deals with crustal magmatism associated with the volcanic evolution of the AVC, we focus on plutonic lithics. All further discussion of Pa Bay lithics is constrained to these crystalline lithics. Pa Bay plutonic lithics are small (<5 cm) and comprised of plagioclase > pyroxene > olivine > Fe-Ti oxides.

Volcanic Dome Hosted Plutonic Lithics

Goat Rock is a trachybasalt to basaltic tracyandesite volcanic dome on the Eastern flank of the AVC, outcropping at 395 meters (Figure 5.1, Table 4). The dome intruded a, now eroded, scoria cone and sits on top of a sequence of lava flows called the Ducksfoot Bay lavas (Figure 5.6). This lava flow sequence is younger than the Pa Bay scoria cone on the shore platform below (Figure 5.6). Whole rock geochemistry for this lava flow sequence is presented along with Goat Rock lithic compositions to understand how Goat Rock Dome and its lithics, the Pa Bay scoria cone, and the lava flows that sit between Pa Bay and Goat Rock Dome relate.

Plutonic lithics at Goat Rock dome all have the same mineralogy of plagioclase > pyroxene >> olivine (Figure 5.5) and are up to 20 cm in diameter. Lithics are found on the northern side of the dome in rockfall blocks (Bertolett et al., 2019). Goat Rock plutonic lithic mineralogy is relatively homogenous and differences between lithics are only seen in lithic size and crystal texture: some lithics have strongly aligned crystals, others have faint alignment, and many have no apparent crystal fabric (Figure 5.4).

LeBons Bay Peak is a prominent feature on the western side of LeBons Bay (Figure 5.1). LeBons Bay Peak is a basanite volcanic dome with a variety of lithics found throughout the dome. Sewell

et al. (1993) found lithics on the eastern side of the dome (see Sewell et al. 1993 for details of their lithic types) and plutonic lithics found in this study were extracted from the southern side of the dome. LeBons Bay Peak lithics observed in this study have diverse mineralogies: some are like Goat Rock lithics while others are predominately pyroxene or have pyroxene > olivine >> plagioclase (Figure 5.5).

Geochemistry

Plutonic lithics have been identified at nine locations in the AVC, six of which are reported for the first time in this contribution (see Appendix). The majority of AVC plutonic lithics have a similar mineralogy of plagioclase > pyroxene > olivine > Fe-Ti oxides (Figure 5.5). The exceptions are LeBons Bay Peak lithics and some Paua Bay plutonic lithics that have more pyroxene compared to the other locations (Figure 5.5). Other than mineralogy, variation between lithics is due largely to crystal size and apparent crystal alignment.

Lithics from Haylocks Bay (n=15) range from 38 to 49 SiO_2 wt.% (Table 3, Appendix). The lava flow that the lithics reside in have 46 wt.% SiO_2 and are slightly higher in Na_2O and K_2O than the lithics (Figure 5.7a). Eastern Pigeon Bay lithics (n=2) have an average of 46 wt.% SiO_2. The host is slightly more evolved with 48 wt.% SiO2 and 6.5 wt.% alkalis (compared to 3.2 wt.% alkalis in the lithics). Goat Rock plutonic lithics (n=13) have the largest SiO_2 range (45.6 – 55 wt. %). Goat Rock also has the most silica enriched lithic and the majority of samples are higher in alkalis than lithics from other locations, placing them more in line with the immediately underlying lava flows (i.e. Ducksfoot Bay; Figure 5.7a). Goat Rock Dome has the most evolved host composition of all the lithic locations. However, unlike many of the other lithic-host relationships, Goat Rock Dome has a silica-alkali composition that falls within that of its lithics (Figure 5.7a).

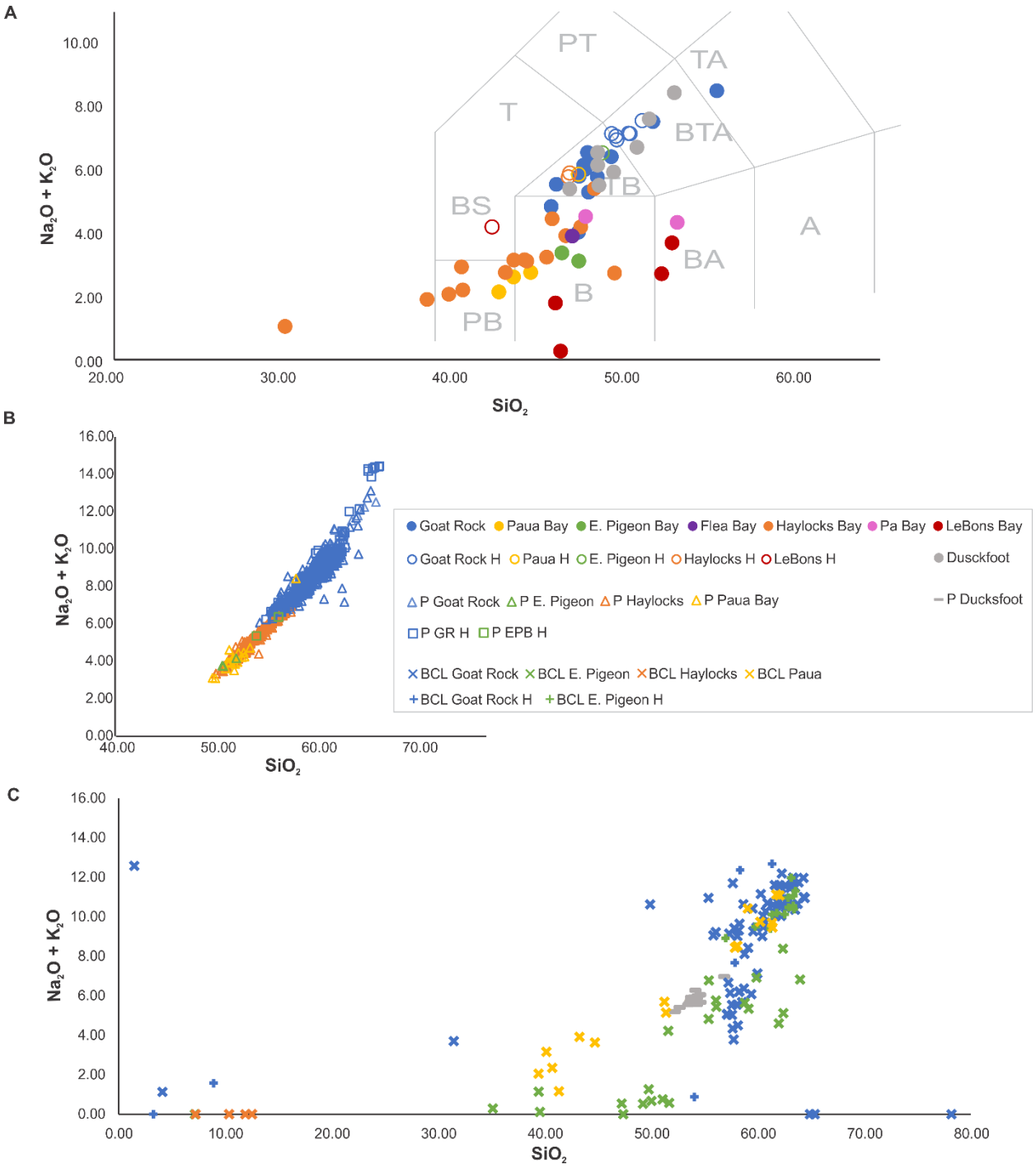

Figure 5.7 a) Major element silica wt. % vs alkalis for whole rock compositions, b) plagioclase chemistries, and c) bright CL chemistries. Colors designate different lithic-bearing location. Closed circles are lithic whole rock, open circles are host whole rock, open triangle is lithic plagioclase chemistry, open square is host plagioclase chemistry, grey tick represents plagioclase phenocryst chemistry of the underlying lavas (i.e. Ducksfoot), crosses are lithic bright CL chemistry, and pluses are host bright CL chemistry.

Only one lithic from Flea Bay was able to be extracted (only 2 were found). The lithic has a similar mineralogy and apparent crystal size distribution to Goat Rock and falls at the least evolved end of the Goat Rock lithic spread (Figure 5.7a). On silica vs. alkali plots, Flea Bay and Pa Bay overlap. Only whole rock compositions of plutonic lithics from Pa Bay are included here. While relatively constrained to the middle of the AVC lithic silica vs alkali trend, one Pa Bay lithic sits apart from the main trend and next to the comparatively high silica, low alkali LeBons Bay Peak lithics (Figure 5.7a). LeBons Bay Peak lithics (n=4, from Sewell et al., 1993 and this study) deviate the most from the similar trend of the other AVC lithics. LeBons Bay Peak lithics are notably low in alkalis and high in MgO and CaO (Figure 5.8).

In trace element variation diagrams, particularly Zr and Rb, the host samples for all locations form a group elevated in Zr and Rb (Figure 5.9a,b). The underlying lava flows also populate this group while the lithics are comparatively depleted (Figure 5.9a,b). In both plots, Goat Rock lithics are slightly higher in Zr and Rb than the other lithics. This pattern holds true in SiO_2 vs. Ba and La variation diagrams where the host samples and the Ducksfoot lava flows sit apart from the lithics (Table 3, Appendix). The only exception is the Haylocks Bay host which has less than 10 ppm La. Goat Rock is also enriched in Ba and La (Table 3, Appendix).

Plagioclase chemistries from Eastern Pigeon Bay are higher in SiO_2 than the lithics and host whole rock compositions (Figure 5.7). Plagioclase in the host lava flow are higher in SiO_2 and alkalis than the lithic plagioclase and especially more than the lithic itself. Paua Bay plagioclase sits on the same trend as the rest of the locations but are some of the least evolved chemistries (Figure 5.10).

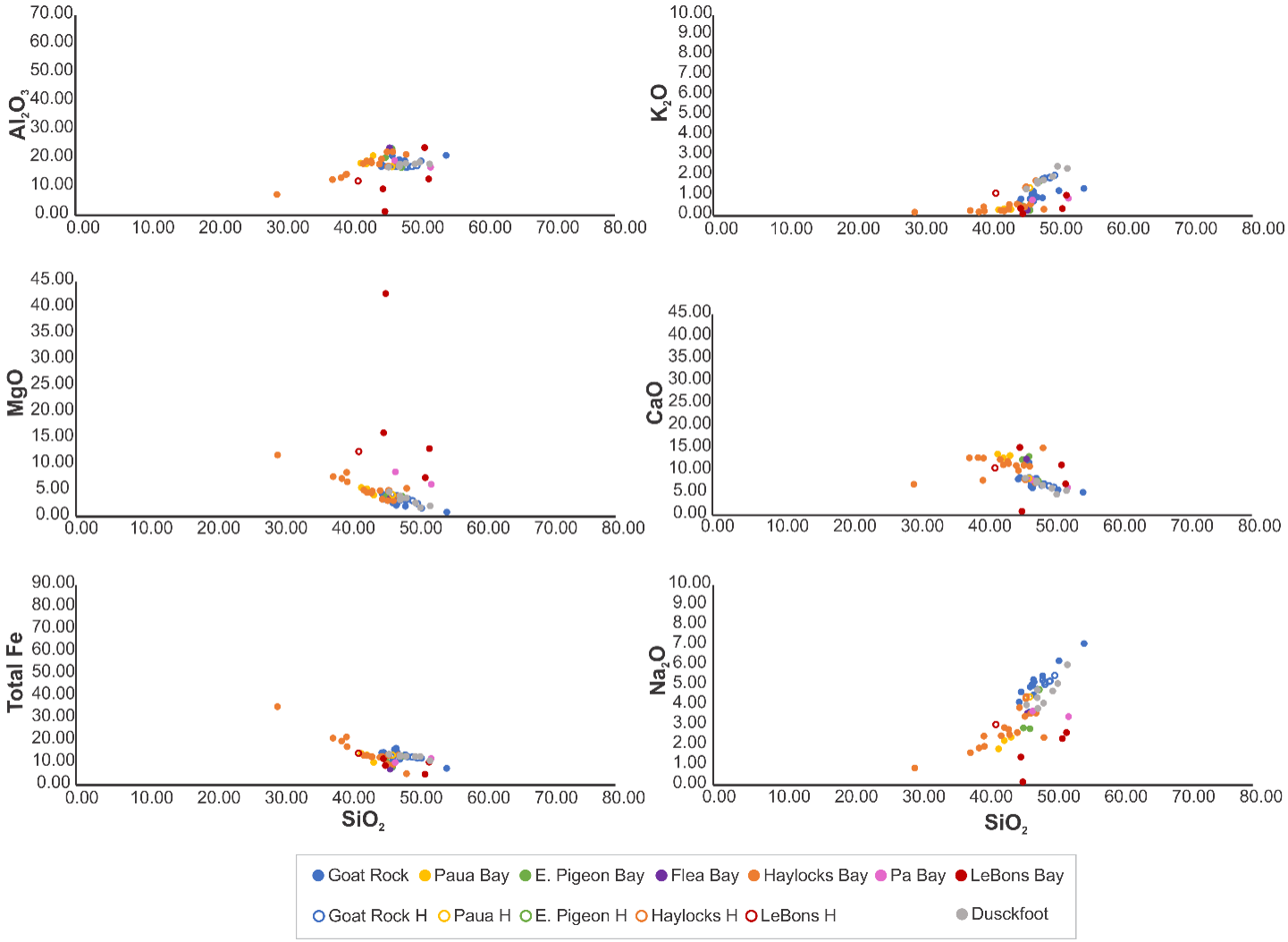

Figure 5.8 Major element silica wt.% variation diagrams of bulk rock compositions for each lithic location and its host. Colors designate different lithic-bearing location. Closed circles are lithic whole rock, open circles are host whole rock.

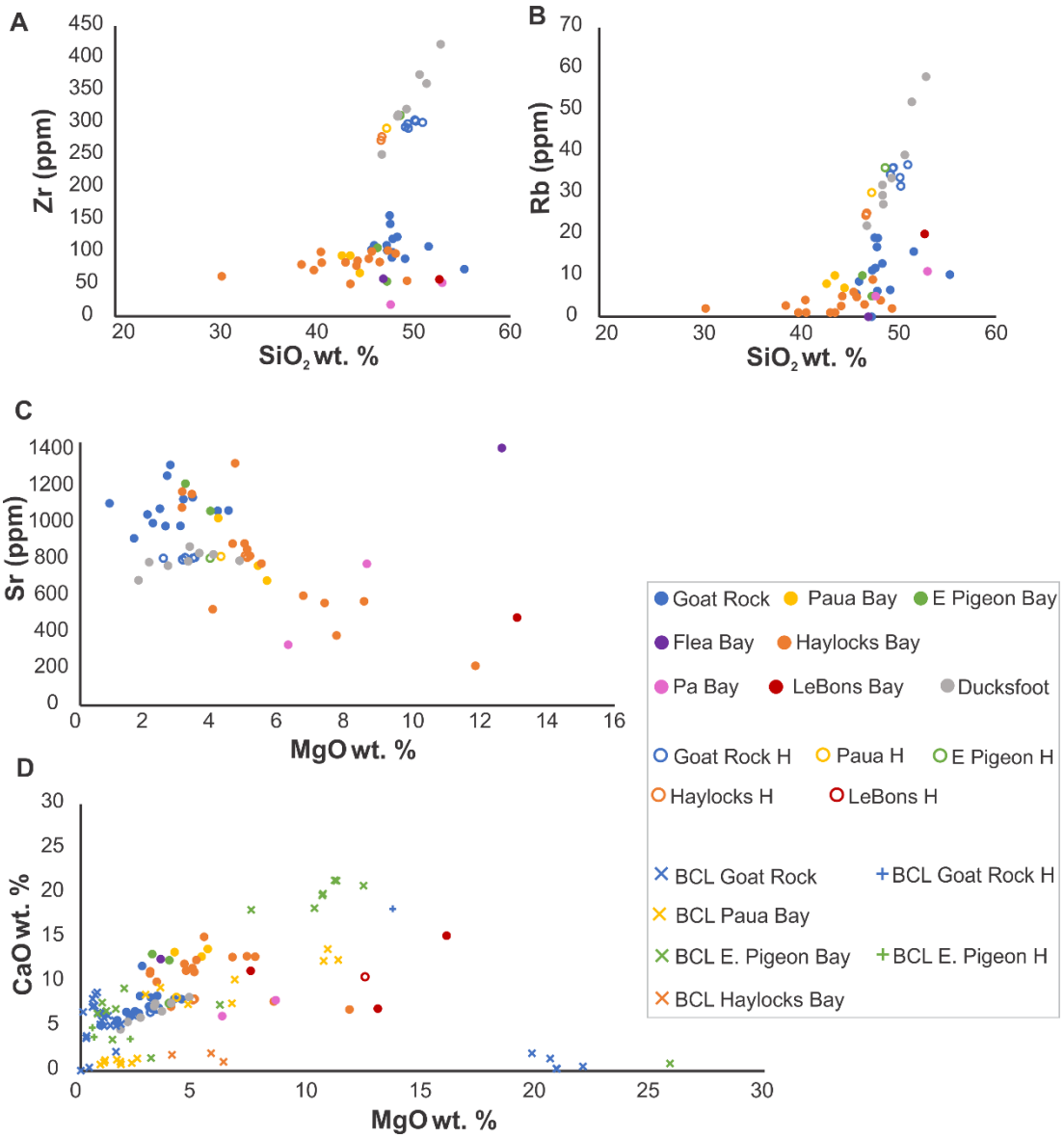

Figure 5.9 Silica vs Zr (a) and Rb (b) from lithic and host whole rock compositions. (c) MgO (wt. %) vs Sr (ppm) and (d) MgO wt. % vs CaO wt. % including bright CL chemistries.

Goat Rock plagioclase make up the more evolved end of the shared plagioclase trend but are slightly less constrained than the other locations. This is especially true in the high silica values and in Na_2O plots (Figure 5.10). The plagioclase in the Goat Rock host sits slightly apart from the other plagioclase chemistries: they are high in SiO_2 and K_2O but low in CaO (Figure 5.10). Host

plagioclase deviate from the trends in the AVC plagioclase data in Na_2O: they have higher SiO_2 but lower Na_2O. Goat Rock plagioclase have more SiO_2 but less CaO and Al_2O_3 than Haylocks Bay plagioclase (Figure 5.10). Goat Rock plagioclase are also enriched in Na_2O and K_2O compared to Haylocks Bay. Paua Bay plagioclase make up the least evolved end of this trend (Figure 5.10). Haylocks Bay and Eastern Pigeon Bay have some overlap with Paua Bay however Haylocks Bay plagioclase range from this less evolved end member to overlap slightly with Goat Rock plagioclase. Ducksfoot Bay plagioclase phenocrysts fill the gap between Paua Bay and Goat Rock plagioclase (Figure 5.10).

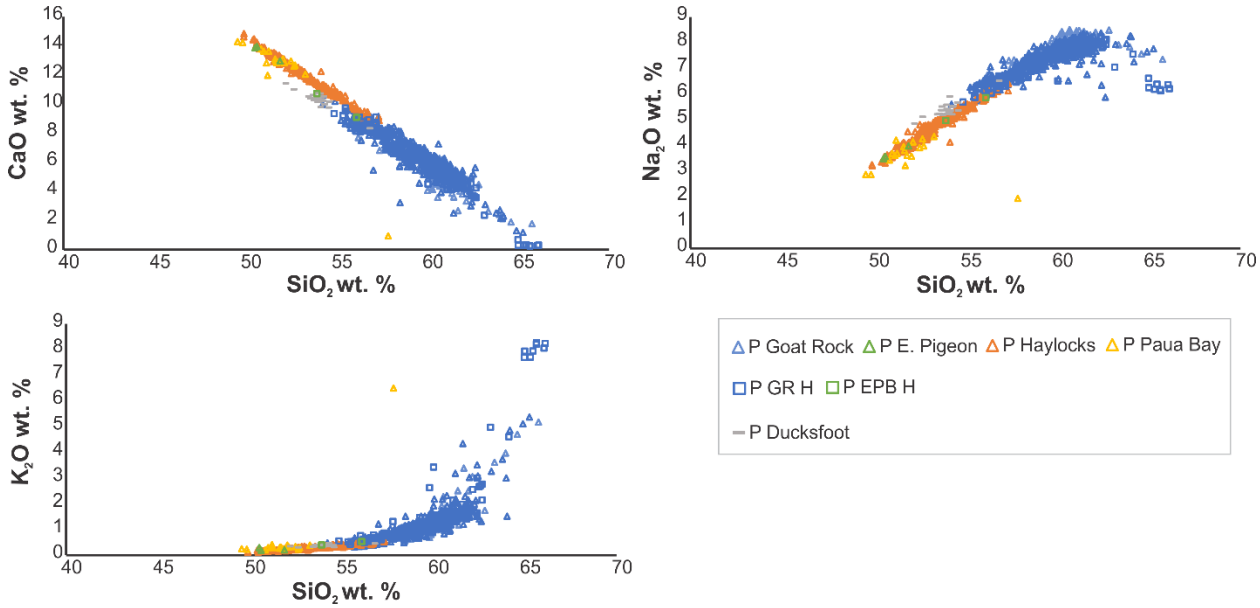

Figure 5.10 Major element variation diagrams of lithic and host plagioclase phenocryst chemistries.

Crystallographic Preferred Orientations

Plagioclase crystallographic preferred orientations (CPO) for the Eastern Pigeon Bay lithic do not have a defined pattern (Figure 5.11a). The Paua Bay lithics analyzed have significant amounts of pyroxene (Figure 5.4), making a distinguishable plagioclase CPO difficult to capture.

The lithic sample analyzed for Haylocks Bay has two holocrystalline regions separated by a relatively sharp contact (Figure 5.4d). One side has larger crystals (Figure 5.4d) while the other is dominated by smaller crystals. The region with large crystals does not have a clear CPO: there are strong point maxima with very little other orientations present (Figure 5.11b), likely due to very large plagioclase crystals dominating the CPO. Maxima are often in pairs. The other side of the contact has a CPO characterized by {100} and {001} great circle girdles and clustering about the poles in the {010} (Figure 5.11c).

Most Goat Rock lithic CPOs are characterized by {010} pole clusters and {100} and {001} great circle girdles (Figure 5.11d). One sample (9a) has faint girdles in both the {100} and {010} and random {001} pole distribution (Appendix). Two Goat Rock lithics have a random CPO; GR22 and GR26. GR26 has multiple zones defined by crystal size. The coarser of these regions has a very faint {001} and {010} great circle girdle though the rest of the sample as whole and individual regions has a random CPO.

Hand sample observations of the LeBons Bay Peak lithic highlight a strong plagioclase preferred orientation (Figure 5.4e). Plagioclase CPOs for this sample are defined by a {100} great circle girdle and random {001} CPO (Figure 5.11e). {010} poles form a cluster about the poles that faintly spreads in to a great circle girdle. Like Paua Bay, this sample has significant amounts of pyroxene, however, the CPO is strong enough to be distinguishable from the limited plagioclase lattice points.

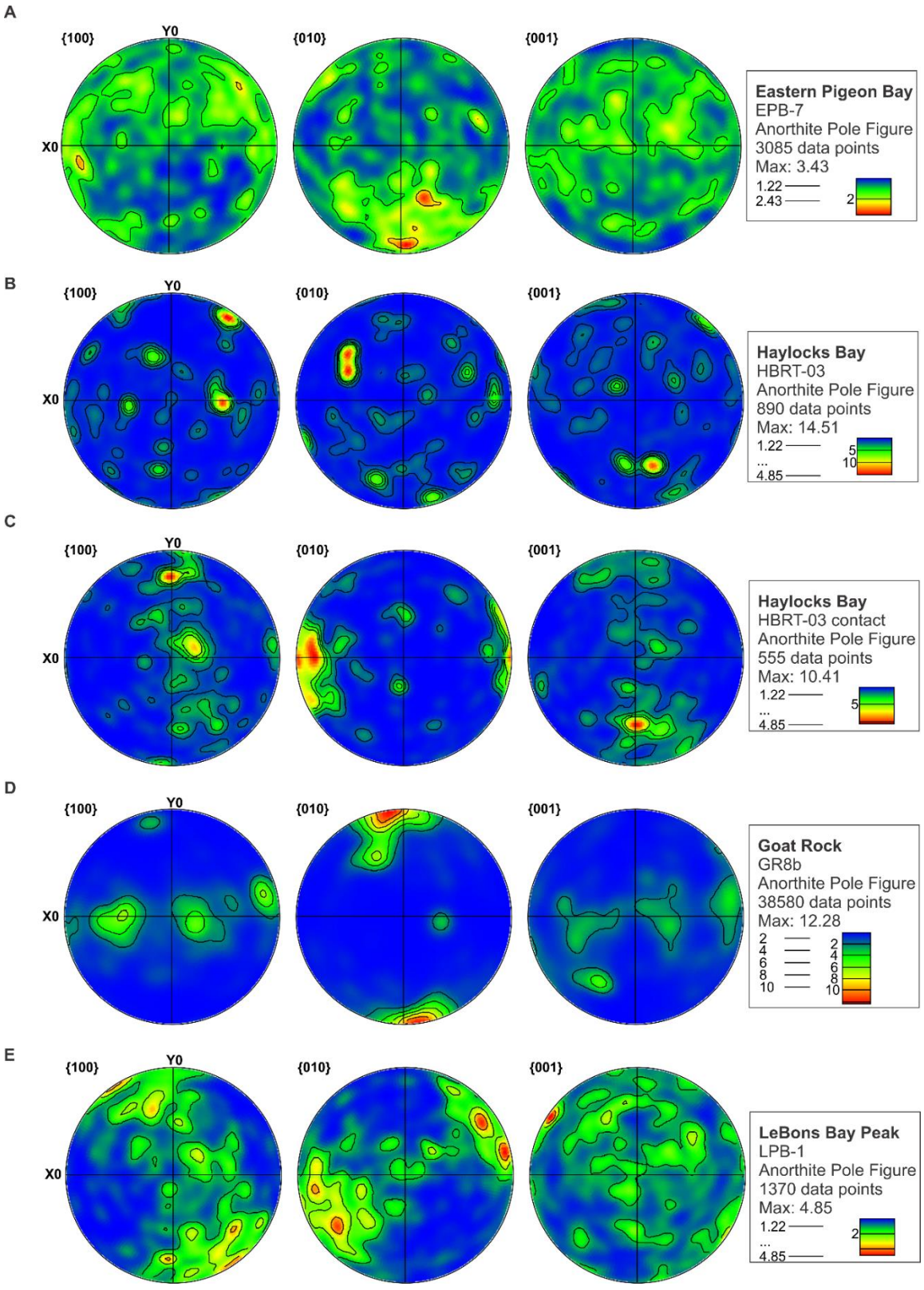

Figure 5.11 Equal area, lower hemisphere pole to plane figures for representative lithic samples. 15 halfwidth contours. Density of points highest (red) to lowest (blue).

Color-Cathodoluminescence

Color CL maps were collected for a selection of representative lithics from each location. Areas of exceptionally bright, luminescent material have previously been identified in Goat Rock plutonic lithics as, crystallographically, part of a contiguous plagioclase lattice, but compositionally akin to a late-stage evolved melt (Bertolett et al., in review). The boundary between the plagioclase crystal and the bright CL is sharp due to its different luminescence.

Areas of exceptionally bright (i.e. luminescent) material are found in nearly all AVC lithic samples analyzed. Sparse and inconsistent bright CL regions are found in the Eastern Pigeon Bay lithics, with small, disconnected lines at grain boundaries and cracks (Figure 5.12a-b). Paua Bay has constrained areas of splotchy or 'fine-grained' luminescent and depressing minerals (i.e. mafic minerals, Figure 5.12c-d). Haylocks Bay lithics have no bright CL at plagioclase grain boundaries, however, there are concentrated pockets of the material distributed throughout samples. Bright CL pockets are usually found in association with cracks and with mafic phases (Figure 5.12e-f). In contrast to the bright CL distribution in the other AVC plutonic lithics, the pockets in Haylocks Bay lithics are concentrated and localized, found in greater proportions in individual areas, and not present at grain boundaries or fractures. The LeBons Bay Peak sample analyzed has significant amounts of bright CL material at all plagioclase boundaries, in thicker outlines of mafic phases, and extensively in plagioclase crystal fractures (Figure 5.12g).

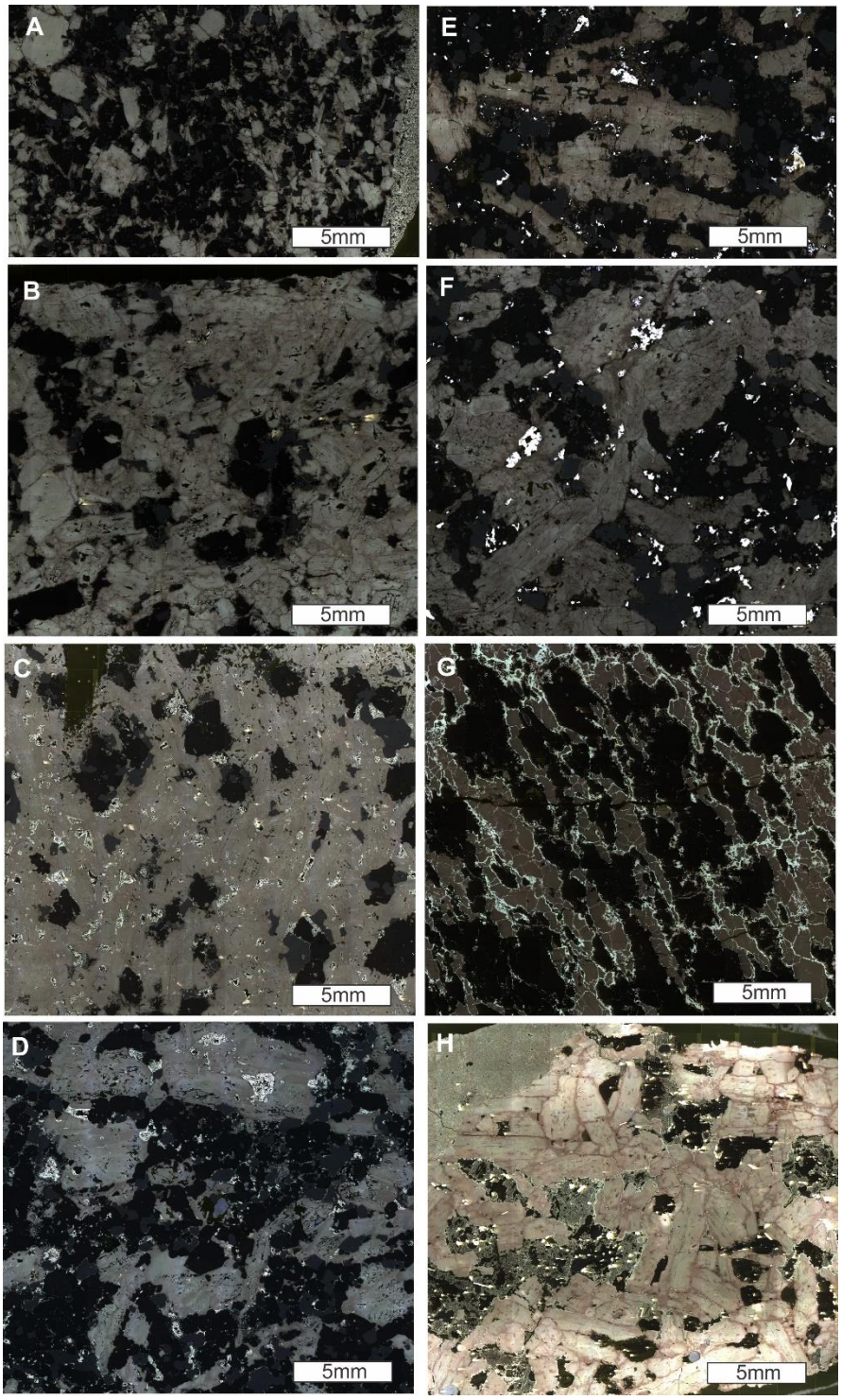

Figure 5.12 Stitched full thin section color cathodoluminescence images for Eastern Pigeon Bay (a-b), Paua Bay (c-d), Haylocks Bay (e-f), LeBons Bay Peak (g), and Goat Rock (h). All images have been black-balanced so that direct comparison of color and luminescence can be made across samples. Not the bright, white areas found in many of the samples (i.e. 'bright CL areas').

Figure 8h is an example of the different types of bright CL found in Goat Rock lithics. Most of the material is seen as very thin white lines at plagioclase grain boundaries. There are also significant concentrations of luminescent material intermixed with fine grain Fe-Ti oxide associated with the mafic phases. There are differing amounts of bright CL defining plagioclase-plagioclase grain boundaries but it is almost always present. Thick lines of bright CL highlight plagioclase-plagioclase grain boundaries as well as intra-crystalline fractures in the Goat Rock sample (Figure 5.12g).

Note that Goat Rock plagioclase crystals are much lighter and pinker than the other samples. LeBons Bay Peak has the darkest and most red plagioclase (Figure 5.12g).

Bright CL Chemistries

The thin, inconsistent distribution of the bright CL described above makes compositional analysis challenging. It is also nearly impossible to see the material except in color-CL. Therefore, EDS mapping of small areas was used to collect chemical information.

Bright CL compositions for three Goat Rock samples are all relatively constrained (Figure 5.13). A small population from one Goat Rock lithic has lower Na_2O than the other bright CL chemistries (Figure 5.14). Goat Rock plagioclase and bright CL often are similar in composition.

Goat Rock, Haylocks Bay, and Eastern Pigeon Bay all have a small population of bright CL chemistries that are low SiO_2 (<20 wt.%) and low Al_2O_3, CaO, and MgO but high total FeO (Figure 5.13).

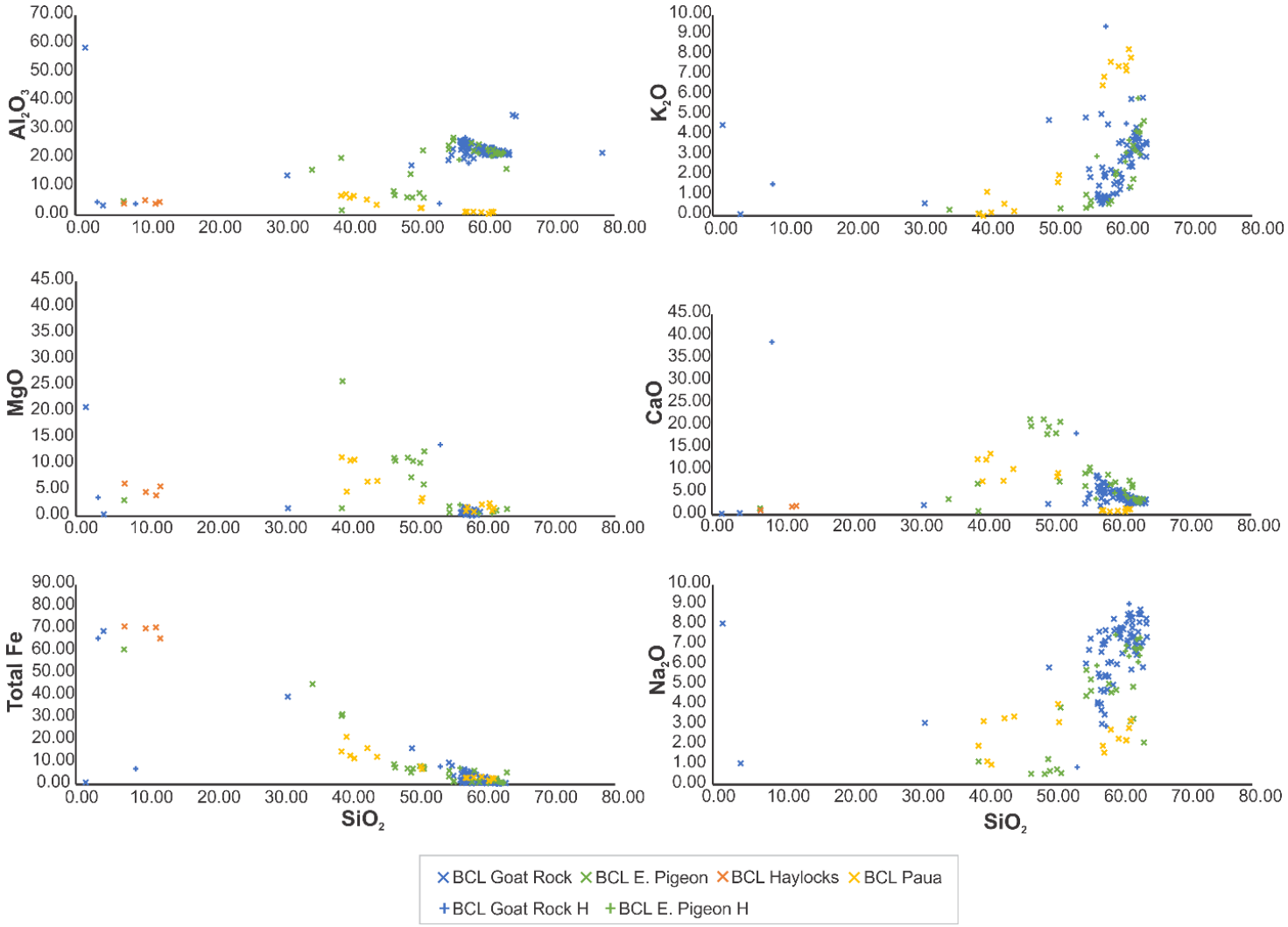

Figure 5.13 Major element silica wt.% variation diagrams of bright CL chemistries for each lithic location and its host. Colors designate different lithic-bearing location. Crosses are lithic bright CL chemistry, and pluses are host bright CL chemistry. Note the absence of Haylocks BCL in Na_2O and K_2O as these elements are not present in Haylocks BCL.

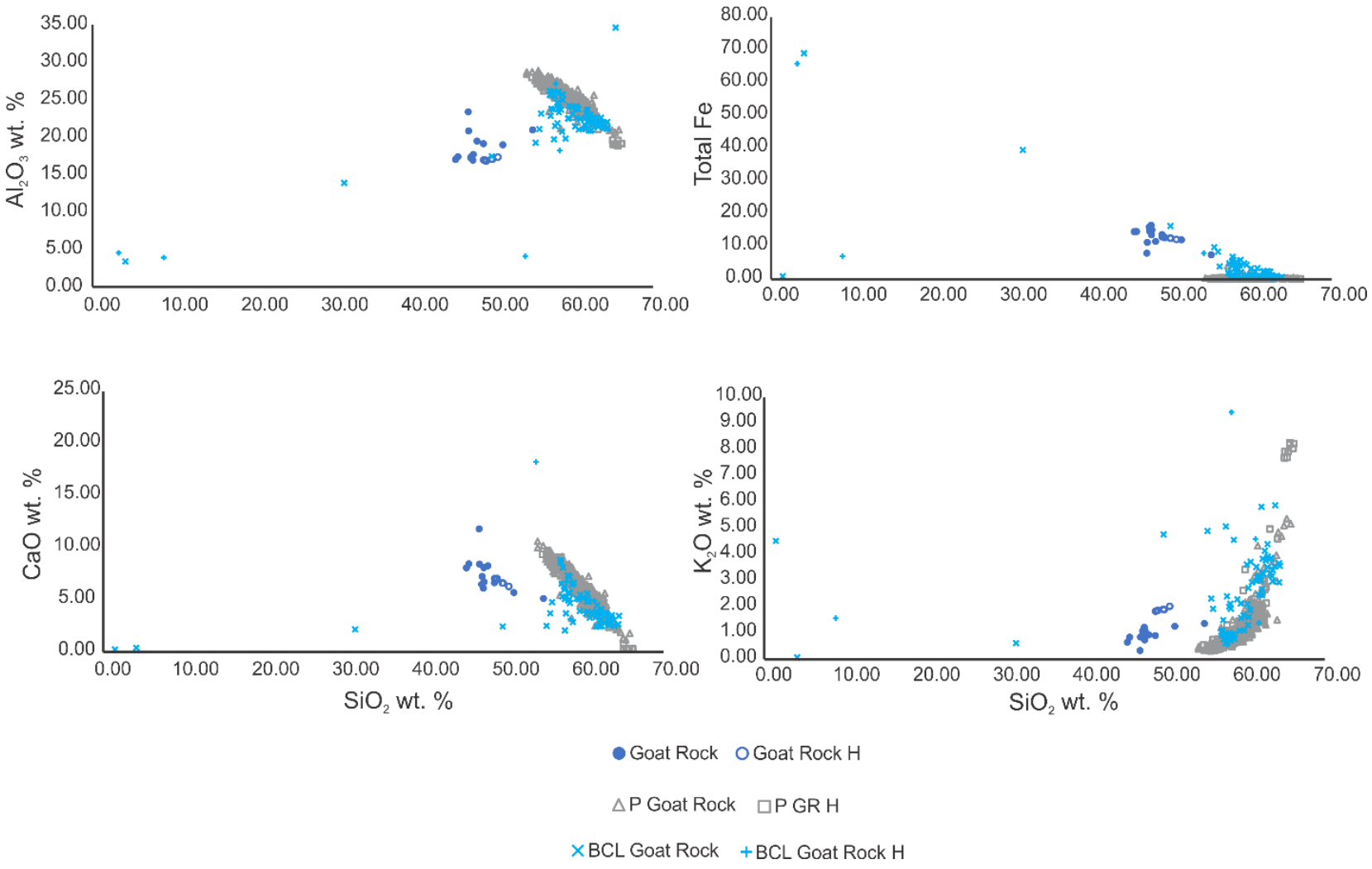

Figure 5.14 Major element variation diagrams for all Goat Rock data.

Haylocks Bay bright CL (from one sample) is also well constrained. Unlike bright CL in the other locations, Haylocks Bays bright CL is lacking in Na_2O and K_2O but high in total Fe, MgO and CaO (Figure 5.15). Compared to the other locations, bright CL in Haylocks Bay lithics sit distinctly away from the whole rock, host, and plagioclase chemistries from that location (Figure 5.15). The material has no K_2O and Na_2O but significant levels of total Fe.

Eastern Pigeon Bay and Paua Bay both have multiple bright CL populations. Paua Bay, in particular, has two different bright CL groups: one with higher SiO_2, Na_2O, and K_2O and another with lower SiO_2 but higher Al_2O_3, total Fe, MgO, and CaO (Figure 5.16). Bright CL within the lithics of Paua Bay also form two populations (Figure 5.16). One group has a wide range of SiO_2 and comparable amounts of CaO to plagioclase and whole rock (Figure 5.16). The second group is comparatively high in SiO_2 and low in CaO. The two Paua Bay bright CL groups are seen in all variation diagrams and are particularly notable in K_2O plots where there is a low K_2O population (<2.5 wt.%) and high K_2O population (6-9 wt.%).

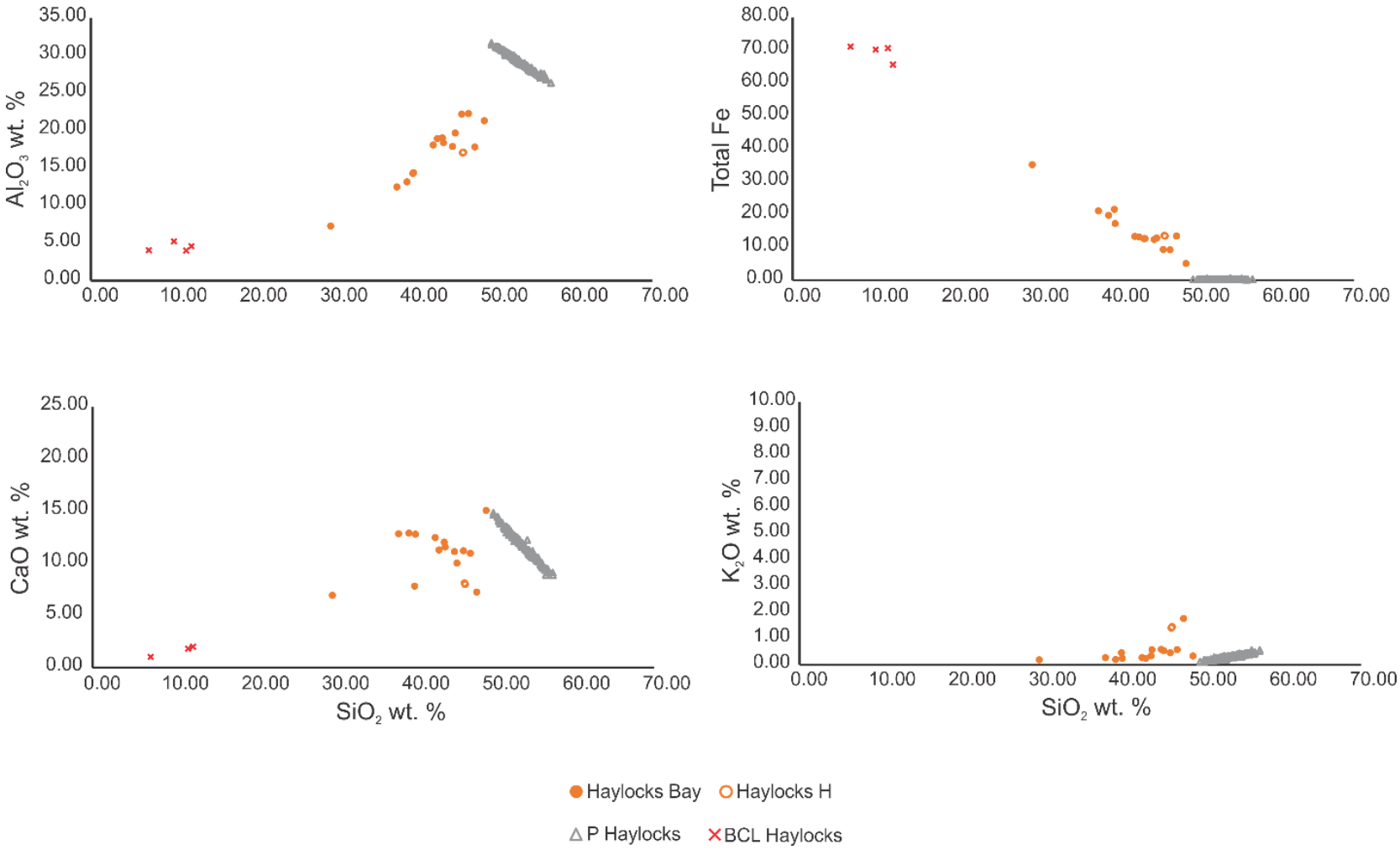

Figure 5.15 Major element variation diagrams for all Haylocks Bay data.

Eastern Pigeon Bay bright CL has the widest range of bright CL chemistries for the AVC lithics studies here. Bright CL from the host is the most silica enriched of all Eastern Pigeon Bay bright CL chemistries. This variability may be due to irregularities in the data as bright CL in these samples is sparse. Bright CL regions in one Eastern Pigeon Bay lithic has compositions that fall in to two groups; one that is moderately enriched in SiO_2 but has very little Na_2O or K_2O and another that has more SiO_2 and up to 8 wt. % alkalis (Figure 5.17). Bright CL within the Eastern Pigeon Bay lava flow (host), like the whole rock and plagioclase compositions, is higher in SiO_2 and alkalis than its lithic counterpart (Figure 5.17). Bright CL in the Eastern Pigeon Bay lava flow is constrained to relatively high SiO_2 and low CaO (Figure 5.17). Together, these data make up a rough trend of evolving compositions where the host is generally more evolved than the comparable feature in the lithic and the bright CL areas are more evolved than the plagioclase and the whole rock composition is the least evolved. Bright CL in one Eastern Pigeon Bay sample has two groups in CaO plots (low SiO_2, high CaO and low CaO, high SiO2, Figure 5.17). This high CaO population stands out from all the AVC lithic data (Figure 5.4b) while the Eastern Pigeon Bay lithic, host, plagioclase, and other bright CL chemistries generally conform to the main trends discussed above. This high CaO bright CL group is also notably lower in Al_2O3 and Na_2O and higher in MgO than the other AVC data (Figure 5.7). Eastern Pigeon Bay bright CL is occasionally enriched in total Fe and MgO compared to lithics and host (Figure 5.7).

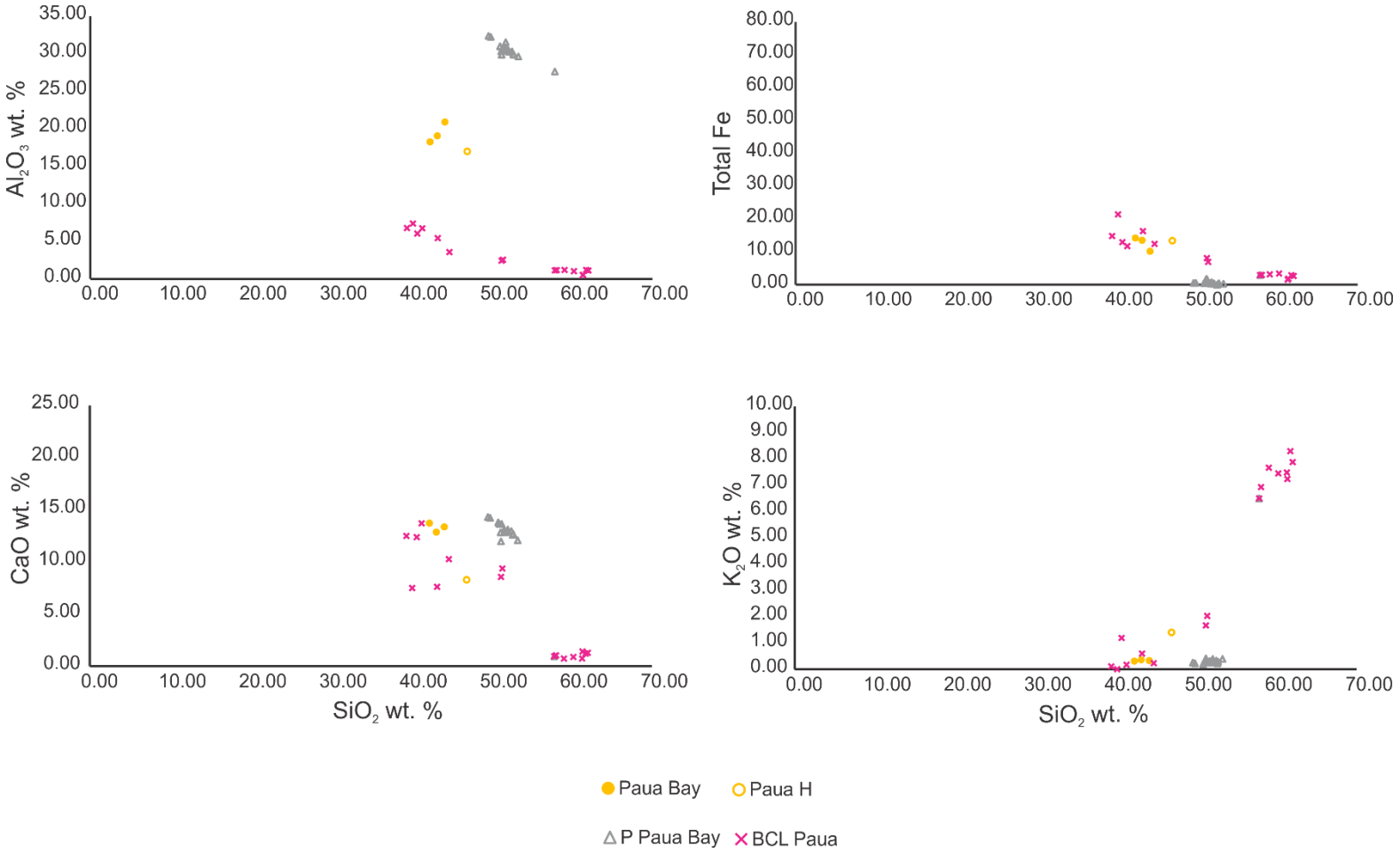

Figure 5.16 Major element variation diagrams for all Paua Bay data.

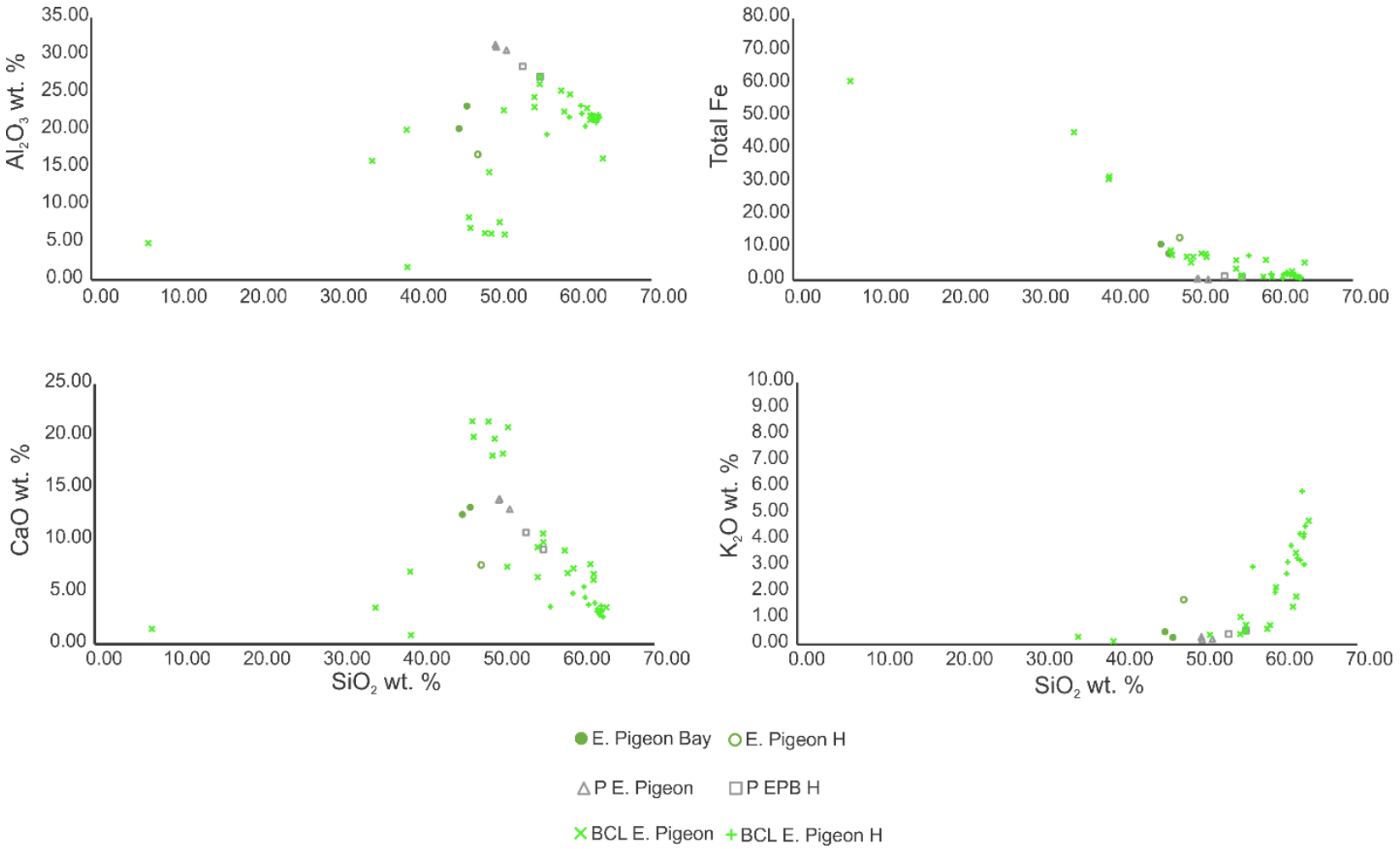

Figure 5.17 Major element variation diagrams for all Eastern Pigeon Bay data.

Interpretation

Lithic-Host Relationships

Lithic-host relationships are useful in uncovering how ascending magma interacted (or did not interact) with other parts of the AVC magmatic system. A basic, preliminary deduction can be made from observations about the host and lithic compositional relationship. If the host is more evolved than its lithics (in both silica and alkalis, ex. Eastern Pigeon and Paua Bay), it is possible that the host was part of the same mush body that the lithics crystallized in (i.e. stacked crystal mushes of Cashman et al., 2017). This co-genetic system may have been disturbed and erupted both its liquid and solid portion (see Chapter 2 of this thesis for a full discussion of mushes and open and closed magmatic systems). Of course, a more evolved magma from a different mush may have entrained and erupted the lithics, leaving behind very similar signatures. If host compositions fall within a spread of lithic compositions, it is more likely that the host and lithics are not cogenetic.

Geochemical data (specifically mineral chemistry and trace element concentrations) and the composition of bright CL regions can help to unravel these signatures. Bertolett et al. (in review) identify varying amounts of bright CL distributed at grain edges in proportion to the strength of compaction CPO in a suite of Goat Rock plutonic lithics. The distribution of bright CL varies considerably across the lithic-bearing locations. Bertolett et al. (in review) suggest that the bright CL material, crystallized as part of the adjacent plagioclase lattice, could represent the last crystallizing liquid in a mush that is the result of fast crystallization of late-stage magmatic liquid distributed along grain boundaries. The distribution of this material may lead to insights in to the state of the cooling mush.

Contemporaneous to AVC

Lithics can be classed as contemporaneous or non-contemporaneous to AVC volcanism based on large-scale mapped and dated host relationships.

Goat Rock lithic whole rock compositions have a relatively considerable range in SiO_2 and the lava dome host falls in the middle of this range (Figure 5.7a). This holds true in other major element variation diagrams except for SiO_2 vs K_2O where the host is separate from the low K_2O lithics (Figure 5.14). In SiO_2 vs V and Ba there is overlap between lithic and host. Goat Rock has the most homogenous lithic mineralogy, however, there is still a considerable silica vs alkali spread (Figure 5.7a). The host falls in the middle of this trend and in SiO_2 vs Zr and Rb, La, and Sr the host forms a distinct population from its lithics (Figure 5.9). Therefore, we hypothesise that a separate, ascending host magma intercepted an older, shallower mushy sill and entrained the Goat Rock lithics.

The Haylocks Bay lava flow that entrained plutonic lithics has higher alkalis than the large spread of lithic SiO_2 whole rock chemistries (Figure 5.7a) but falls in the middle of the lithic spread in other major element variation diagrams (Figure 5.8). At higher silica, the lithic chemistries become less constrained (i.e. there is a greater range in Al_2O_3, CaO, and K_2O at higher SiO_2 values). The host composition is often on the fringe of this greater spread but not so separate as other host locations (Figure 5.8). Haylocks Bay lithics are comparatively primitive but, unlike LeBons Bay Peak, still fall along the AVC alkaline trend (Figure 5.18). The Haylocks Bay lava flow that hosts the lithics is more evolved than the lithics and could be either cogenetic or represent an already differentiated magma that entrained lithics from another crystal mush. Indeed, in SiO_2 vs Sr and La plots, Haylocks Bay is the only host to sit alongside its lithics compositions. The agreement of

lithics and host trace element data suggests that, of all AVC host-lithic relationship, Haylocks Bay is the most likely to represent a cogenetic mush (lithic) and melt (lava flow host) interaction.

The Eastern Pigeon Bay and Paua Bay hosts have slightly more SiO_2 than their respective lithics. Both host compositions are more distinct from their lithics in CaO, K_2O, and Al_2O_3 than Goat Rock and Haylocks Bay (Figure 5.8). Paua Bay lithics, while similar to Haylocks Bay in relatively low silica values and host-relationship, have a large variability of lithic mineralogy not represented by the geochemical data (see field observations). This lithic diversity rules out a single, co-genetic mush body (i.e. Sewell model) and is more likely the result of the ascending, differentiating host intersecting multiple older mush bodies.

Eastern Pigeon Bay lithics are more evolved than the other lithics. This may mean that lithics come from a more evolved period of one evolving batch of magma (i.e. cogenetic). Although the Eastern Pigeon Bay host is more evolved than its lithic whole rock compositions, the bright CL in the lithics has three different populations, only one of which matches the host's bright CL composition (Figure 5.17). If the material is a residual melt, this disparity would be challenging to resolve in a shared mush.

Pa Bay lithics are the most diverse of any of the AVC lithic-bearing locations. It is also the only location with lithics entrained in explosively erupted deposits. Its eruption early in the Akaroa phase (evidenced by the erosion and subsequent emplacement of extensive lava flows above the scoria cone, Figure 5.6) and the explosive nature of entrainment and eruption may explain the inclusion of shallow sedimentary units that form the rise on which the AVC was built. Pa Bay plutonic lithics fall outside of the whole rock main trend of AVC eruptives (Figure 5.18) and many of the other plutonic lithic compositions. This divergence from the alkaline trend could be a reflection of the scoria cone's eruption early on in the Akaroa phase of magmatism. Conversely,

it could suggest that ascending magma utilized a different conduit system than that of the main vent region deposits similar to the flank eruption-feeding dikes of Mt. Etna (Acocella and Neri, 2003).

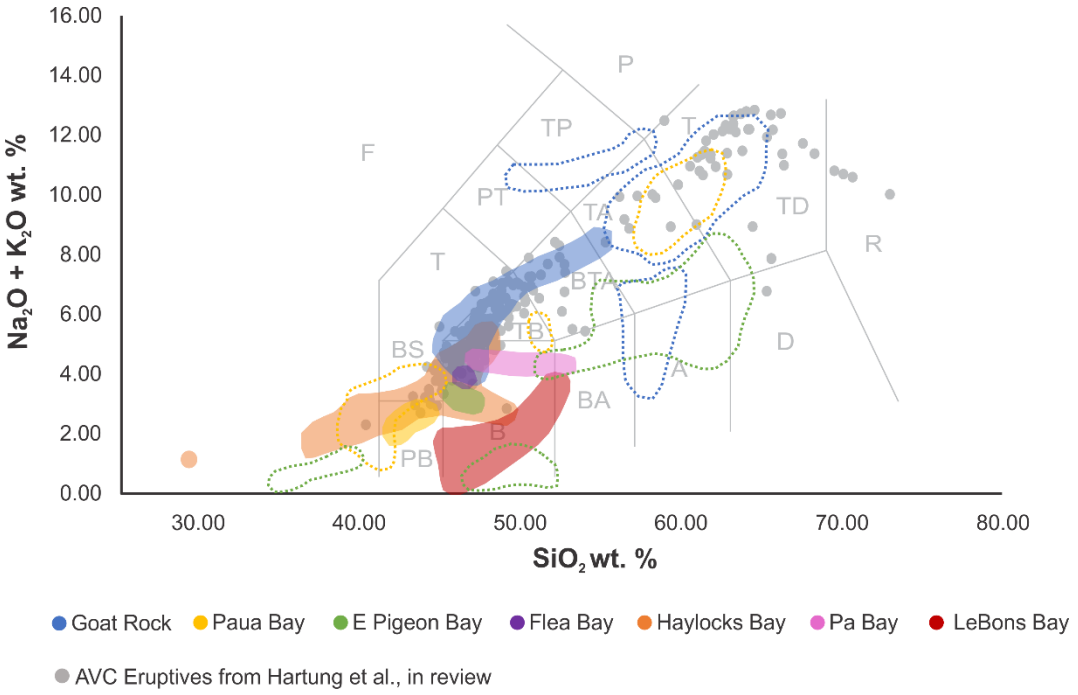

Figure 5.18 Silica vs alkalis plot of lithics discussed in this study (colored areas) overlain on whole rock compositions from AVC erupted deposits (grey points, Hartung et al., in review). Dotted outline designate bright CL compositions for their respective lithic.

Non-contemporaneous lithics

Sewell et al. (1993) identified three types of plutonic lithics at LeBons Bay Peak and attributed them to different magmatic sources and depths. The authors assigned the LeBons Bay Peak basanite dome to the younger Diamond Harbour volcanic phase based on dating and geochemical data (Sewell et al., 1993; Timm et al., 2009). LeBons Bay Peak is the only host that has lower SiO_2 than its lithics. LeBons Bay Peak lithics also deviate the most from the shared trend of the other AVC lithics (Figure 5.8). The younger dated age of LeBons Bay Peak and the lithic-host relationship is evidence of a post-AVC, Diamond Harbour Volcanic Group event. This is

supported by the diversity of lithic mineralogies (Figure 5.5) and chemistries (Figure 5.7) and suggests that lithics from multiple, already emplaced mushes were entrained by a younger magma (i.e. of the Diamond Harbour Volcanic Group). LeBons Bay Peak magma therefore interacted with multiple parts of the subvolcanic system (i.e. lithics of the AVC) and the diversity and anomalous compositions of entrained lithics may be representative of the wider crustal magmatic system (i.e. Maahunui Volcanic Field cf. Biscoff et al. in press) or deeper sources (i.e. Hikurangi Margin cf. Hobden 1990).

Preserved Magmatic Processes in Plutonic Lithics

Most lithics do not have any defined crystallographic preferred orientation (CPO), however, there are a number of patterns of interest (Figure 5.11). A random CPO is the most common and, perhaps, the most expected CPO for igneous samples. A random CPO would be expected from crystals growing undisturbed and unimpeded in a melt. The competition of different forces acting on a mush as well as the continual fluctuations in temperature and pressure often act to negate a coherent, preserved CPO if it does exist (Holness et al., 2017; Holness 2018; Vukmanovic et al., 2018). Others have argued that changes in the magmatic system over the long period of time that a pluton is above the solidus may overprint any relic of original, fabric-forming magmatic forces (Zak et al., 2008). This overprint signature can sometimes be deciphered from EBSD data (c.f. Jiang et al., 2000; Zak et al., 2008).

The most common, non-random CPO, in the AVC lithics is characterized by {010} clusters about the poles and {100} and {001} great circle girdles (Figure 5.11d). Goat Rock is particularly interesting as it has multiple of this CPO of varying strength, related to the amount of uniaxial compaction (Bertolett et al., in review). Despite the prevalence of compaction CPOs and the constrained nature of the geochemical data, Goat Rock lithics also have a number of random CPOs

(i.e. where no plagioclase orientation exists). The LeBons Bay Peak plutonic lithic analyzed has a very strong plagioclase shape preferred orientation (Figure 5.4e). The LeBons Bay Peak CPO is defined by a {100} broad great circle girdle and {010} pole clusters that spread in to a faint girdle (Figure 5.11e). This may indicate plastic deformation and shearing of plagioclase in excess of magmatic forces (Satsukawa et al., 2013) or boundary layer flow (Vukmanovic et al., 2018; see Bertolett et al., 2019 and Chapter 2 of this thesis for an overview of CPOs). Indeed, the primitive composition of the lithic and this strong foliation (and, potentially, lineation) CPO may reflect tectonic forces prevelant in the lower crust and upper mantle (Satsukawa et al., 2013; Ji et al., 2014; Cheadle and Gee, 2017). As multiple processes may create this type of CPO, additional microstructural analysis is required to definitively assign a process to this CPO.

Two lithics form Haylocks Bay were selected to represent the two main shape preferred orientations (SPOs) observed. One sample (Figure 5.4d, left) has very large (up to 3 cm) crystals and the CPO is dominated by these large crystals (i.e. point maxima; Figure 5.11b). Analysis of bins of different crystal sizes persist in this point maxima CPO. It is possible that this CPO reflects a glomerocryst texture where crystals come together along particular crystal faces as they settle (Beane and Weibe, 2012) although further directed analysis of adjacent crystal orientations is needed to confirm this hypothesis. The other Haylocks Bay sample has two regions visible in hand sample (Figure 5.4d, right). The main portion of the lithic has a random CPO, however, the finer grained portion has a compaction CPO (Figure 5.11c). Lithics with multiple textural regions within one lithic are not uncommon at the AVC however, this is the only lithic analyzed that has a non-random CPO in one of its portions. These contacts may be evidence of different magmas interacting. However, the similarity in mineralogy and chemistry of the two regions could also indicate that different forces were acting within one system.

Samples with no defined CPO have either very localized areas of bright CL or none at all. Natural crystal growth or slow settling within a mush creates pore space at crystal triple junctions (Holness, 2007). This pore space would be a site for any remaining liquid portion. For example, Paua Bay lithics have bright CL concentrated to triple junctions. In the samples where no bright CL is found (i.e. Eastern Pigeon Bay) the mush may have crystallized slow enough to allow crystallization of all remaining liquid or any residual melt (including incompatible elements) to be effectively removed prior to full solidification.

Goat Rock and LeBons Bay Peak are the two lithics with bright CL strongly associated with plagioclase grain boundaries and are the only samples to have a defined CPO, usually a compaction CPO (Satsukawa et al., 2013; Bertolett et al., 2019). The distribution of bright CL at grain boundaries could be the result of this compression of the crystal mush (Bertolett et al., in review) although more work on the compositional relationship between the bright CL and the adjacent minerals as well as a systematic investigation of the orientation of the crystal faces with bright CL is needed to properly explore this hypothesis.

Discussion

AVC Magmatic Structure

In this culminating study of lithics from the AVC, a schematic magmatic system of the AVC has been conceptualized (Figure 5.19). This shows the AVC magmatic system as a series of pathways from crystallization to eruption of the different lithic-bearing locations (1-5), in which magmas from different depths (eg. Hartung's model) or stages of evolution interact with the magmatic system. Lithic textures and lithic and host deposit chemistries inform the different types of relationship and pathways possible in the AVC crustal magmatic system.

Figure 5.19.1 represents a compositionally primitive host that ascends from depth and passes through an extensive and already mature network of solidified mushes. This pathway may be applicable to the ascent of the younger Diamond Harbour magma through the AVC magmatic system to form LeBons Bay Peak as well as to AVC-contemporaneous locations where a wide variety of plutonic lithic mineralogies and textures (such as Paua Bay) and less evolved plutonic lithic compositions (Haylocks Bay) are present.

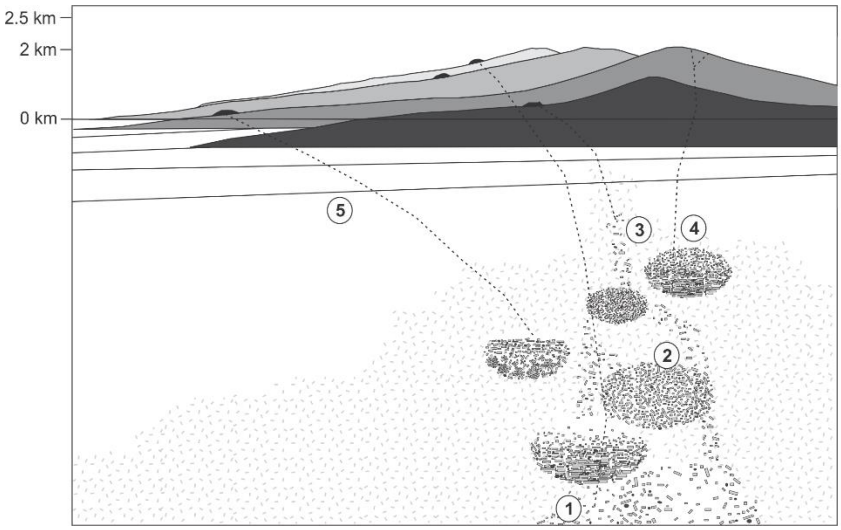

Figure 5.19 Schematic of progressive cone-building and magmatic structure of the AVC. Multi-staged cone building represented by greyscale cones, underlying sedimentary units that source some of the Pa Bay non crystalline lithics highlighted by shallowing dipping lines. Basement and magmatic system represented by grey ticks. Idealized mush-bodies in varying stages of crystallization, settling, compaction, etc. and their pathways represented by dotted lines. Number 1-5 designate the possible host-lithic relationships identified in this study and their relationship to the volcanic stratigraphy.

The type of host deposit may help inform where the erupting magma was sourced from. Lava flows such as Haylocks Bay, Paua Bay, and Eastern Pigeon Bay come from the central region of the volcanic complex and, therefore, the magmas would have passed through a more central conduit system. As AVC plutonic lithics are usually concentrated to specific flows and outcrops, it is likely that an ascending magma interacted with a lithic source on ascent, rather than the whole magmatic system mixing with and incorporating a substantial portion of an already-crystallized mush.

The diversity of lithic compositions at a single location is also informative. Goat Rock, Eastern Pigeon Bay, and Paua Bay plutonic lithics are all well constrained to an increasing silica and alkalis trend (Figure 5.7b). Lithics are very localized at each of these locations where they only occur within limited proximities (lava flows a <10 meter radius, domes <20m). The similarity in lithic whole rock composition, mineral chemistries, and bright CL chemistries at Eastern Pigeon Bay and Goat Rock is best explained by a single, crystallizing mush with separate host magma interactions for both of these locations (Figure 5.19.2).

Goat Rock plutonic lithics are more evolved than the other AVC lithics: indeed, one Goat Rock lithic is evolved enough to fall within the Daly Gap (Figure 5.18). No other plutonic material analyzed thus far in the AVC (other than one point from Onawe Peninsula) fits the hypothesis of the, compositionally, unerupted portion of the magmatic system representing the Daly Gap (Hartung, 2011). Indeed, as cumulates (particularly adcumulates) this hypothesis cannot be correct as the plutonic material has lost melt. Along with being the most evolved AVC lithics, Goat Rock also has notably homogenous lithic mineralogy and size. Goat Rock has the most lithics outcropping compared to the other locations. Part of this may be due to the exposure of lithics from rockfall. However, lithics at Goat Rock Dome are just as localized as in other locations: outside of an approximately 20 meter area lithic occurrence drops significantly and only very small lithic fragments or large crystals can be found. This, along with the evolved composition of the plutonic material, suggest that the ascending dome interacted with one, relatively shallow or evolved mush before erupting (Figure 5.19).

The homogeneity of Eastern Pigeon Bay lithics and its compositional relationship with the host lava flow suggest that the Eastern Pigeon Bay lithics were also sourced from a magma in a

comparatively advanced stage of evolution with little interaction with the rest of the magmatic system (Figure 5.19.2).

Haylocks Bay and Paua Bay lithics are less evolved than the other AVC-contemporaneous lithics. Haylocks Bay lithics are entrained within a lava flow outcropping at sea level while Paua Bay and, especially, Eastern Pigeon Bay lithics are found in younger flows further up the cone-building stratigraphy and sourced from the central region of the AVC. The chemical deviations seen in Haylocks Bay lithics and host may be the result of an earlier stage in a batch of magmatic evolution whereas Eastern Pigeon Bay may instead have lithics sourced from a more evolved period in this cyclicity. The subtler variations between the other lithic-bearing locations may reflect the repeating cycles of evolution seen in the lava flow stratigraphy and, therefore, the emplacement, evolution, and eruptions of small, stacked mushes in the crustal magmatic system. As AVC lava flows repeatedly cycle from picrite to trachyte, this lithic-host relationship may be a reflection on the lava flow's place in the stratigraphy and this evolving cycle of cone-building lavas.

Paua Bay, with its extensive diversity of lithic mineralogy may record entrainment of multiple mushes rather than the simpler entrainment history of Goat Rock and Eastern Pigeon Bay (Figure 5.19.3). Indeed, the presence of multiple lithic mineralogies rules out entrainment of lithics from only one crystallizing mush. Paua Bay lithics are also less evolved than many of the other AVC lithics (Figure 5.4). Like LeBons Bay Peak, ascending magma may have originated at greater depths and entrained material from different regions in the magmatic system (i.e. the stacked sill complex, cf. Cashman et al., 2017) on its way to the surface (Figure 5.19.3).

Haylocks Bay lithics and host show some evidence of a cogenetic relationship in which crystals and melt separate but are disturbed, producing an eruptible magma with entrained crystal residue (Figure 5.19.4). While also relatively primitive, the major and trace element evidence of,

potentially, shared lithic and lava flow sources suggests that single mush bodies in the AVC may have been capable of erupting without the disturbance of a foreign magma.

Lithic entrainment is further complicated in the environment of flank eruptives, where multiple eruptive phases have taken place within a localized area (i.e. Pa Bay). These multi-stage eruptive histories result in surficial deposits and shallow surface intrusives (remnant conduits), of which later stage eruptions, specifically shallow, small, explosive cone-building event, will intersect and rip up underlying lithologies and entrain these in the eruptive deposits (Figure 5.19.5). These eruptives can not only entrain materials from depth (plutonic lithics) but also shallower, i.e. basement sedimentary lithics.

As discussed earlier, LeBons Bay Peak is non-contemporaneous with the AVC and is attributed to the Diamond Harbour Volcanic Group based on crystal ages and compositions (Sewell et al., 1993). The lithics are extensively spread throughout the dome and, compared to the other lithic-bearing locations, LeBons Bay Peak has a wider variety and greater spatial distribution of plutonic material. This further supports geochemical evidence of a younger phase of magma ascending through the already crystallized AVC system and entraining material from multiple magma bodies including, potentially, lower crustal material (Figure 5.19.1).

AVC magmatic-volcanic connection

Whole rock compositions of lithics fit within the geochemical trends of the wider AVC eruptives compositions, particularly at SiO_2 values below 55 wt.% (Figure 5.18). Haylocks Bay and Eastern Pigeon Bay lithics are often near the least evolved end, extending further in to the picrite basalt compositions than the majority of AVC eruptives (Figure 5.18). Goat Rock lithics are the only lithic population that extend in to trachy-basalt and trachy-andesite (Figure 5.18). A number of lithics from Haylocks Bay, Pa Bay, and especially LeBons Bay Peak have equally high SiO_2 values

as the trachy-basalt Goat Rock lithics but have lower Na_2O and K_2O, placing them more in line with a tholeiitic trend compared to the dominantly alkaline trend of the AVC eruptives (Figure 5.18).

In major element variation diagrams, lithic-bearing host compositions for each location (other than LeBons Bay Peak) form a moderately well constrained population (especially in SiO_2 vs Al_2O_3, K_2O, MgO, CaO, and FeO; Figure 5.8). This group also includes the Ducksfoot lava flows. Mineral chemistries are tightly constrained in these plots but lithic bulk rock compositions and bright CL chemistries have greater variability (Figures 5.8 and 5.13). The grouping of the host compositions away from the lithic compositions may reflect the inherent eruptibility of certain ascending magmas and that AVC plutonic lithics generally represent magmatic residue, either from already segregated magmas or in mushes that are uneruptible.

Plutonic lithic bright CL chemistries are overlaid on AVC eruptive data from Hartung (2011) to compare a potential late-stage, differentiated melt to eruptive deposits in the AVC (Figure 5.18). Interestingly, a substantial portion of lithic bright CL chemistries plot near the more evolved trachy-andesite and trachyte AVC eruptives (Figure 5.18). These include data from Goat Rock, Paua Bay, and Eastern Pigeon Bay lithics. This does not necessarily mean that they are temporally late-stage however. Rather than the whole AVC evolving from picrite to trachyte over its lifetime, the AVC had multiple batches of magmatic evolution seen in repeating picrite through to trachy-andesite flows in the volcanic stratigraphy (Beckham, 2016).

Haylocks Bay bright CL could reflect a latter influx of melt as the material is exceptionally bright and sometimes associated with fractures. Compositionally, the bright CL in Haylocks Bay lithics are the most dissimilar to its lithic and host whole rock chemistries (Figure 5.15).

The rest of the bright CL compositions from Goat Rock and Eastern Pigeon Bay have similar SiO_2 values but less alkalis. The other Paua Bay bright CL data as well as another group from Eastern Pigeon Bay have silica values more in line with the lithic whole rock composition and Haylocks Bay bright CL areas have substantially lower alkalis (<4 wt. %, Figure 5.18). The high silica, low alkali bright CL compositions correspond loosely to the lithic plagioclase data which is consistent with the finding that bright CL at Goat Rock is, crystallographically, an extension of the adjacent plagioclase (Bertolett et al., in review). The bright CL chemistries align with some of these evolved (i.e. trachyte) lava and dome compositions and individually may represent the differentiation of one batch of magma. These grain boundary compositions that represent evolved and segregated melt, may therefore reflect batches of magmatic evolution. The coupling of crystal residue (lithics) with potentially eruptible melts (bright CL) may record a mush's full evolution from crystallization, melt segregation, and differentiation to eruption. While individual eruptives cannot be correlated to these lithics, it is significant that cumulate lithics contain the signatures of melt extraction related to AVC eruptions.

The cyclicity of magmatic evolution, the spatial distribution of localized outcroppings of lithics, and the diversity of lithic compositions all suggest the likelihood of multiple magma bodies and that these bodies coexisted spatially (and possibly temporally) during active AVC magmatism (Figure 5.19).

Conclusions

Bright CL regions in plutonic lithics, if truly representative of a late stage, differentiated melt, add significant insight in to the connection between uneruptible crystal mushes and volcanic deposits. Bright CL chemistries frequently agree with AVC lava flow compositions, suggesting that the trapped melt within plutonic lithics is related to the complex-building material erupted at the AVC.

Those compositions that do not fit the AVC eruptives data are typically very high in total FeO, CaO, and MgO. These compositions match many of the criteria for low silica immiscible melts that are being increasingly used to explain incremental accumulation and evolution of stacked sills in contributing to active volcanism.

Additionally, the magmatic processes revealed by plagioclase CPOs, petrographic observations, and bright CL distribution reveal a complexity of crystal accumulation mechanisms between lithic-bearing locations as well as within lithic populations at a single location. Lithic and host compositional relationships also suggest a variety of entrainment histories. The combined interpretation from these observations is that plutonic lithics reveal a complex crustal magmatic system with multiple stages of magmatic evolution and a variety of pathways that ascending magma takes through the crustal system on its way to the surface.

This plutonic lithic data supports new, detailed geomorphic observations of the lava flow stratigraphy and morphology of the AVC. There are independent crystallization histories evident in the entrained lithic populations and their hosts. The lithics represent different spatial and temporal crystallization sequences that is reflected in the cyclicity of lava flow compositions found in the stratigraphy. Corresponding observations from both the magmatic and volcanic realms reveal the complexity of the AVC crustal magmatic system.

References

Acocella, V., & Neri, M. (2003). What makes flank eruptions? The 2001 Etna eruption and its possible triggering mechanisms. Bulletin of Volcanology, 65(7), 517–529. https://doi.org/10.1007/s00445-003-0280-3

Atwood, A., (2014). Up From Below: Upper crustal xenoliths as indicators of underlying bedrock in scoria cone deposits. *Frontiers Abroad Research Project*.

Beckahm, E., (2016). Shallow magmatic recharge in an intraplate volcanic complex, Akaroa, Banks Peninsula, New Zealand. *Senior Thesis, Colorado College*.

Bertolett, E. M., Prior, D. J., Gravley, D. M., Hampton, S. J., Kennedy, B. M. (2019). Compacted cumulates revealed by electron backscatter diffraction analysis of plutonic lithics, *Geology*, 47(5), 1–4. https://doi.org/10.11

Bertolett, E. M., Gravley, D. M., Beane, R., Teeter, E., Gualda, G., Prior, D. J., Hampton, S. J., Kennedy, B. M. (in review). Progressive magmatic compaction and melt extraction revealed by a multi-method approach to plutonic lithics, *in review*.

Bischoff, A., Nicol, A., Barrier, A., and Wang, H. (in press). Paleogeographic and Morphologic Reconstruction of a Buried Monogenetic Volcanic Field. *Bulletin of Volcanology*.

Cashman, K. V., & Giordano, G. (2014). Calderas and magma reservoirs. *Journal of Volcanology and Geothermal* Research, 288, 28–45. https://doi.org/10.1016/j.jvolgeores.2014.09.007

Cashman, K. V., Sparks, R. S. J., & Blundy, J. D. (2017). Vertically extensive and unstable magmatic systems: A unified view of igneous processes. *Science*, 3055(March). https://doi.org/10.1126/science.aag3055

Cheadle, M. J., & Gee, J. S. (2017). Quantitative Textural Insights into the Formation of Gabbro in Mafic Intrusions. *Elements*, 13(6), 409–414. https://doi.org/10.2138/gselements.13.6.409

Cooper, K. M., & Kent, A. J. R. (2014). Rapid remobilization of magmatic crystals kept in cold storage. *Nature*, 506(7489), 480–483. https://doi.org/10.1038/nature12991

Dorsey, C.J. (1988). The Geology and Geochemistry of Akaroa Volcano, Banks Peninsula, New Zealand. *Doctoral Thesis, University of Canterbury*.

Fiedrich, A. M., Bachmann, O., Ulmer, P., Deering, C. D., Kunze, K., & Leuthold, J. (2017). Mineralogical, geochemical , and textural indicators of crystal accumulation in the Adamello Batholith (Northern Italy). *American Mineralogist*, 102, 2467–2483.

Forsyth, P. J., & Jongens, R. (2008).*Geology of the Christchurch area*. Lower Hutt, N.Z.: GNS Science.

Gualda, G. A. R., & Ghiorso, M. S. (2013). The Bishop Tuff giant magma body: an alternative to the Standard Model. Contributions to Mineralogy and Petrology, 166(3), 755–775. https://doi.org/10.1007/s00410-013-0901-6

Goldman, R.T., Albright, J.A., Gravley, D.M., Grosfils, E.B., Greg, P.M., Hampton, S.J. Stress control of dike deflection and flank eruption at Akaroa volcano, New Zealand. *In review*.

Graeter, K. A., Beane, R. J., Deering, C. D., Gravley, D., & Bachmann, O. (2015). Formation of rhyolite at the Okataina Volcanic Complex, New Zealand: New insights from analysis of quartz clusters in plutonic lithics. *American Mineralogist*, 100(8–9), 1778–1789. https://doi.org/10.2138/am-2015-5135

Hampton, S. J., & Cole, J. W. (2009). Geomorphology Lyttelton Volcano , Banks Peninsula , New Zealand : Primary volcanic landforms and eruptive centre identification. *Geomorphology*, 104(3–4), 284–298. https://doi.org/10.1016/j.geomorph.2008.09.005

Hampton, S. J. (2010). Growth, Structure and Evolution of the Lyttelton Volcanic Complex, Banks Peninsula, New Zealand, *University of Canterbury Doctoral Thesis*. https://doi.org/10.1130/2010.0018(02).

Lewis, G. M., & Hampton, S. J. (2015). Visualizing volcanic processes in SketchUp: An integrated geo-education tool. *Computers & Geosciences*, *81*, 93–100. https://doi.org/10.1016/j.cageo.2015.05.003

Hartung, E. (2011). Early magmatism and the formation of a 'Daly Gap' at Akaroa Shield Volcano, New Zealand. *Master of Science Thesis*, University of Canterbury, 1–79. http://ir.canterbury.ac.nz/handle/10092/5584

Hoernle, K., White, J. D. L., Bogaard, P. Van Den, Hauff, F., Coombs, D. S., Werner, R., Timm, C., Garbe-Schonberg, D., Reay, A., Cooper, A. F. (2006). Cenozoic intraplate volcanism on New Zealand : Upwelling induced by lithospheric removal, *Earth and Planetary Science Letters*. 248, 335–352. https://doi.org/10.1016/j.epsl.2006.06.001

Holness, M. B. (2018). Melt segregation from silicic crystal mushes: a critical appraisal of possible mechanisms and their microstructural record. *Contributions to Mineralogy and Petrology*, 173(6), 48. https://doi.org/10.1007/s00410-018-1465-2

Holness, M. B., Vukmanovic, Z., & Mariani, E. (2017). Assessing the Role of Compaction in the Formation of Adcumulates : a Microstructural Perspective. *Journal of Petrology*, 58(4), 643–674. https://doi.org/10.1093/petrology/egx037

Holness, M.B., Anderson, A.T., Martin, V.M., Maclennan, J., Passmore, E. & Schwindinger, K. (2007) Textures in partially solidified crystalline nodules: a window into the pore structure of slowly cooled mafic intrusions. *Journal of Petrology*, 48: 1243-1264, doi.org/10.1093/petrology/egm016

Miranda, E. A., Hirth, G., & John, B. E. (2016). Microstructural evidence for the transition from dislocation creep to dislocation-accommodated grain boundary sliding in naturally deformed plagioclase. *Journal of Structural Geology*, 92, 30–45. https://doi.org/10.1016/j.jsg.2016.09.002

Ji, S., Shao, T., Salisbury, M. H., Sun, S., Michibayashi, K., Zhao, W., Long, C., Liang, F., and Satsukawa, T., 2014, Plagioclase preferred orientation and induced seismic anisotropy in mafic igneous rocks: Journal of Geophysical Research: Solid Earth, v. 119, p. 8064–8088, doi:10.1002/2014JB011352.

Jiang, Z., Prior, D. J., & Wheeler, J. (2000). Albite crystallographic preferred orientation and grain misorientation distribution in a low-grade mylonite: implications for granular flow. Journal of Structural Geology, 22(11–12), 1663–1674. https://doi.org/10.1016/S0191-8141(00)00079-1

Ring, U., & Hampton, S. (2012). Faulting in Banks Peninsula : tectonic setting and structural controls for late Miocene intraplate volcanism , New Zealand. *Journal of the Geological Society, London*, 169(Barnes 1994), 773–785. https://doi.org/10.1144/jgs2011-167.Faulting

Satsukawa, T., Ildefonse, B., Mainprice, D., Morales, L. F. G., Michibayashi, K., & Barou, F. (2013). A database of plagioclase crystal preferred orientations (CPO) and microstructures- implications for CPO origin, strength, symmetry and seismic anisotropy in gabbroic rocks. *Solid Earth*, 4(2), 511–542. https://doi.org/10.5194/se-4-511-2013

Sewell, R. J. (1985). the Volcanic Geology and Geochemistry of Central Banks Peninsula and Relationships To Lyttelton and Akaroa Volcanoes, University of Canterbury Doctoral Thesis, 349.

Sewell, R.J., Weaver, S. D., and Reay, M. B., 1992. Geology of Banks Peninsula. Scale 1:100,000. Institute of Geological and Nuclear Sciences Map 3. Institute of Geological and Nuclear Sciences Ltd, Lower Hutt.

Sewell, R. J., Hobden, B. J., & Weaver, S. D. (1993). Mafic and ultramafic mantle and deep crustal xenoliths from Banks Peninsula, South Island, New Zealand. *New Zealand*

Journal of Geology and Geophysics, 36(2), 223–231. https://doi.org/10.1080/00288306.1993.9514570

Solano, J. M. S., Jackson, M. D., Sparks, R. S. J., Blundy, J. (2014). Evolution of major and trace element composition during melt migration through crystalline mush: Implications for chemical differentiation in the crust. *American Journal of Science*, 314, 895–939. doi: 10.2475/05.2014.01

Timm, C., Hoernle, K., van den Bogaard, P., Bindeman, I., & Weaver, S. (2009). Geochemical evolution of intraplate volcanism at Banks Peninsula, New Zealand: Interaction between asthenospheric and lithospheric melts. *Journal of Petrology*, 50(6), 989–1023. https://doi.org/10.1093/petrology/egp029

Vinet, N., & Higgins, M. D. (2010). Magma Solidification Processes beneath KilaueaVolcano, Hawaii : a Quantitative extural and Geochemical Study of the 1969 - 1974 Mauna Ulu Lavas, *Journal of Petrology*, 51(6), 1297–1332. https://doi.org/10.1093/petrology/egq020

Vukmanovic, Z., Holness, M. B., Monks, K., & Andersen, J. C. Ø. (2018). The Skaergaard trough layering: sedimentation in a convecting magma chamber. *Contributions to Mineralogy and Petrology*, 173(5), 43. https://doi.org/10.1007/s00410-018-1466-1

Žák, J., Verner, K., & Týcová, P. (2008). Grain-scale processes in actively deforming magma mushes: New insights from electron backscatter diffraction (EBSD) analysis of biotite schlieren in the Jizera granite, Bohemian Massif. *Lithos*, 106(3–4), 309–322. https://doi.org/10.1016/j.lithos.2008.08.006

Chapter Six – Conclusions and Future Directions

Conclusions

Plutonic lithics can provide important information on the conditions and processes acting within a magmatic system. This information is even more critical where no, or very little, plutonic material is exposed. However, bulk rock and mineral chemistry alone cannot fully explain the origin, formation, and entrainment of plutonic lithics. Microstructural analysis of crystals, when tied to geochemical data, provides a holistic picture of crystallization, deformation, and magmatic evolution. For plutonic lithics postulated to be the uneruptible residue of a magmatic system or that have cumulate mineralogies and textures the context provided by quantitative textural analyses is especially important.

A review of the literature in Chapter 2 of this thesis set out the gaps in our knowledge of crustal magmatic systems and the plutonic-volcanic connection. In Chapter 3 cumulate-forming processes for a selection of plutonic lithics at Goat Rock Dome in the Akaroa Volcanic Complex are explored using detailed EBSD analysis. This was expanded on in Chapter 4 where a suite of Goat Rock Dome plutonic lithics are found to represent a progressively compacting theoretical column of mush with a segregating and evolving melt fraction. Chapter 5 culminates with a synthesis of all plutonic lithic data from the AVC. Textural and geochemical observations of plutonic lithics and their host deposit are used to develop a more refined model of crustal magmatism at the AVC. The findings of these chapters provide evidence from natural magmatic systems with a known volcanic counterpart for the coupled processes of compaction and melt extraction as well as a, potentially, more direct plutonic-volcanic link in the similarity between newly identified residual melt in cumulates and lava flow chemistries.

The specific findings of Chapters 3-5 are outlined below:

Chapter 3

Plagioclase CPOs defined by point maxima of the {010} perpendicular to foliation and great circle girdle distributions of the {100} and, often, {001} suggest that compaction or magmatic flow produced the apparent crystal alignment observed. Rotation axis analysis can differentiate between flow and compression. Here, the alignment of twin sets in all plagioclase grains in a shared great circle perpendicular to the maximum in the {010} support CPO evidence of uniaxial compaction acting both in the organization and near solidus deformation of the crystals. This is novel evidence of viscous compaction in natural, igneous plagioclase.

Petrographic evidence of trapped melt (i.e. glass) present in a sample with a weak compaction CPO and absent in one with a strong cumulate CPO from the same location suggest that melt extraction accompanied uniaxial compaction. This observation is important to definitively attributing compaction to crystal alignment as, physically, the liquid fraction needs to be removed to produce adcumulates.

Chapter 4

The multi-method approach of this study allows for better identification of the origin and evolution of AVC plutonic lithics. The selected Goat Rock lithics progress from mafic to intermediate and high An to low An in conjunction with decreasing strength of compaction fabrics and increasing 'melt fraction'.

Bright CL regions associated with grain boundaries are crystallographically the same as the adjacent plagioclase but chemically distinct. Indeed, bright CL compositions are more evolved than their respective whole rock and plagioclase compositions. These observations and the correlation between CPO strength and the amount of bright CL implies that the material represents a residual melt trapped within the crystal framework and which cooled quickly, explaining its crystallographic affinity to the neighboring plagioclase. The evolved composition of the bright CL suggests that percolating melt migrated and evolved progressively within the compacting mush.

Outlying bright CL compositions and morphologically distinct ‘mafic enriched domains’ are similar to symplectites, potentially reflecting the influence of immiscible melt formed from the segregation of melt from the crystallizing framework.

Chapter 5

This study collates all existing and new data for plutonic lithics in the AVC. Three known locations are discussed and new data is presented. Four new lithic-bearing locations are identified.

The magmatic processes revealed by plagioclase CPOs, petrographic observations, and bright CL distribution in AVC plutonic lithics reveal a complexity of crystal accumulation mechanisms found at each lithic-bearing location as well as within lithic populations at a single location.

Lithic and host compositional relationships reveal a variety of entrainment histories, implying that the AVC crustal magmatic system was spatially and temporally complex. The plutonic lithic data supports new, detailed geomorphic observations of a multi-vent volcanic complex, with episodic magma fractionation or erupted batches.

Bright CL chemistries frequently agree with lava flow compositions, suggesting that the trapped melt within plutonic lithics is related to the materials erupted at the AVC. Those compositions that do not fit the AVC eruptives data are typically very high in total FeO, CaO, and MgO. These compositions match many of the criteria for low silica immiscible melts that are being increasingly used to explain incremental accumulation and evolution of sills contributing to active volcanism.

Future Directions

In undertaking this research some unresolved questions on the methods used, the additional data needed to resolve uncertainties in the interpretations made here, and future research needed on the

Akaroa Volcanic Complex and Banks Peninsula remain. The following is a synthesis of these unresolved or future research questions.

Method – Related

The SEM-techniques of this research have revealed several features that have not been described or fully analyzed before: in particular, luminescent plagioclase grain boundaries and pockets. The identification of luminescent plagioclase grain boundaries in color-CL would benefit from further investigation. These features are hypothesized to be residual melt that was thinly distributed along grain boundaries or trapped within pockets or at triple junctions. This material, either by reaching a critical thermal and mass threshold or from changes to conditions in the mush, quickly crystallized in to the adjacent plagioclase lattice. Compositionally, however, the bright CL material is not feldspar. This may be accounted for by a high concentration of incompatible elements that were within this residual melt. Significantly, these bright CL regions often (compositionally) overlap with erupted material at the AVC or form populations that may reflect immiscible melt end members. These bright CL regions are important for understanding near solidus conditions, the kinematics and thermodynamic conditions involved in melt segregation and migration, and the generation and extraction of eruptible melt.

Investigating the reason for the luminescence using color-CL in conjunction with high resolution trace element or isotope geochemistry would help to better identify the bright CL material. High resolution trace element data would also help explain the difference in luminescence between crystal and grain boundary (i.e. is it chemical or the result of lattice defects such as the inclusion of incompatible elements).

Symplectite-like features identified in this study as (‘mafic-enriched regions’, Chapter 4). require further investigation. Importantly, are mafic-enriched domains reactive features between immiscible liquids and certain phases or are they reaction textures from post entrainment disequilibrium conditions? Trace element analysis coupled with the color-CL images could begin to resolve these questions.

Process – Related

In addition to being of use to understanding the bright plagioclase grain boundaries, trace element analysis is vital to confirming cumulate-forming processes identified from the microstructural and major element geochemical studies, as conducted within this research. Detailed, texturally linked trace element analysis is the next progression in determining the precise relationship between lithic cumulus phases, residual melt, and volcanic deposits.

This research utilized bulk rock trace element data and some trace element data from EDS analysis. Mineral trace element data for both lithics and hosts would complement major element data presented in this thesis and trace element or isotopic analysis of features of interest (as described above) would help us to understand the processes that created these features. Specific trace element analysis would further establish the relationship between cumulate-forming mush processes and volcanic eruptions, as previously discussed in Holness et al., 2017.

An interesting observation from this study is the correlation between CPO type and strength and the distribution of bright CL material. Goat Rock Dome and a LeBons Bay Peak lithic have the most distinct CPOs of all the AVC lithics analyzed. Lithics in both suggest that compaction (Goat Rock Dome) and, potentially, flow either within the magmatic system or due to tectonic stress (LeBons Bay Peak) contributed to plagioclase alignment. Goat Rock Dome and a LeBons Bay Peak lithics are the only lithics to have extensive bright CL at plagioclase grain boundaries. Bright CL within the other AVC lithics are concentrated to pockets, triple junctions, cracks, or mineral alteration zones. Goat Rock and LeBons Bay Peak plutonic lithics have strong CPOs and bright CL is distributed around plagioclase grain boundaries. Future research could measure the thickness of the luminescent material compared to crystal orientation, and look to answer the following; Do bright CL grain boundaries preferentially occur at certain crystal faces? Are bright CL grain boundaries a product of interface growth? What role does compression of the crystalline mush have in the development of these luminescent grain boundaries?

Terminology

This research has focussed on the lithics of the AVC however, as indicated within Chapter 2, there are broad and inconsistent classifications and terminologies relating to lithics within the literature. This research has also specifically identified the processes that created AVC plutonic lithics and their relationship to their host, AVC eruptive deposits, and the larger AVC crustal magmatic structure. These interpretations render the term *plutonic lithic* too generalized and do not adequately represent what these rocks are. This study highlights the ability to refine the origins and therefore the classification of lithics (Chapters 3 and 4) and their significance in understanding crustal magmatic systems (Chapter 5).

Based on the specific findings of this thesis we argue that, as a consequence of deciphering the range of pre-entrainment magmatic processes and textures in the AVC lithics, a suite of well-defined terms more refined than *plutonic lithic* is both appropriate and required. The diversity of lithic compositions, textures, and host-relationships in the AVC provides an opportunity to better define the plutonic lithic terminology and can be utilised as a platform to further develop specific terminologies. We have developed a preliminary classification scheme (Figure 6.1) for lithic terminologies based on textures, which are often neglected in identifying plutonic lithics, and host relationships. This classification scheme utilizes terminology already common in the literature as well as the addition of ‘contextus’, the Latin word for fabric, to describe the presence or absence of crystal alignment (either a SPO or CPO). Reading from right to left, this classification scheme allows more refinement of the terminology based on the level of analysis and interpretation of magmatic processes and relationship to either the host or other erupted deposits. The farthest left are potential processes responsible for a crystal fabric, and can be used to define a descriptive terminology, i.e. boundary layer flow contextus antelith.

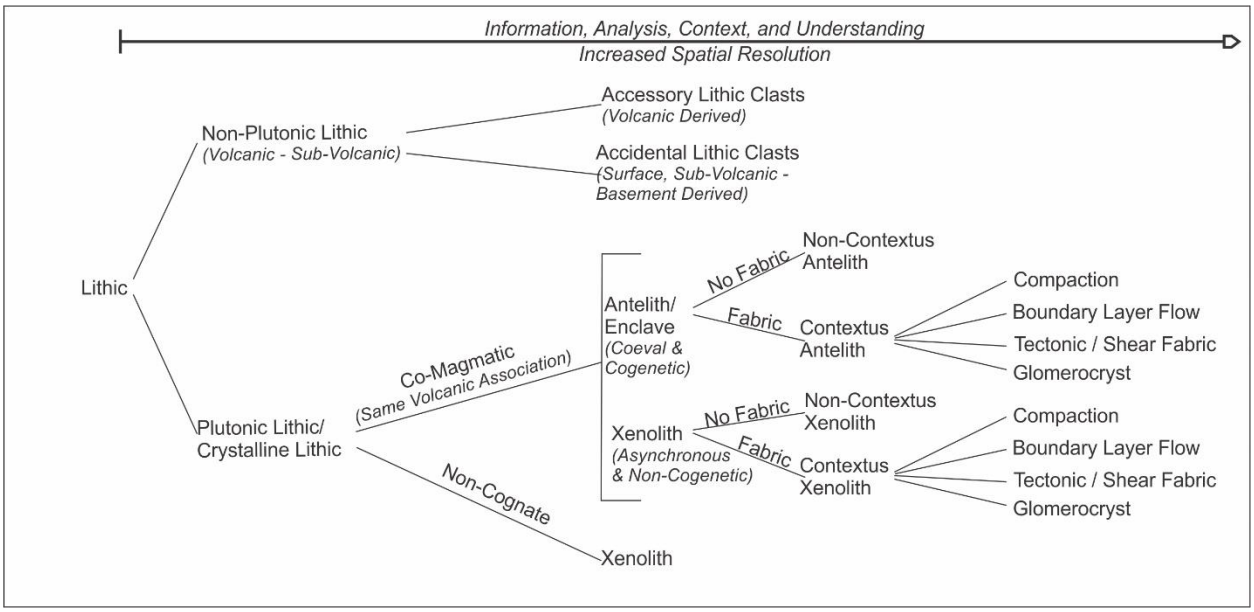

Figure 6.1 Proposed lithic terminology classification. The schematic reads from broad lithic classification to more refined. Plutonic and non-plutonic lithics are separated and then described in terms of their relationship to the deposit they reside in. Then, textural features are used to characterize the processes that produce any visible crystal fabrics. Note that this textural extension of the diagram can also be used for xenoliths as well as non-plutonic lithics.

Banks Peninsula Volcanism and AVC – Related

This research has highlighted the insights that lithics can provide to magmatic systems. In the continued geologic research on Banks Peninsula, and specifically Akaroa, more and more lithics have been identified. These were beyond the scope of this project, but the continued discovery of lithics provides further opportunities for studying the AVC magmatic system. At the AVC, additional lithic-bearing locations include a small dome at Mt. Sinclair, large ash deposits at Stony Bay, a scoria cone in Sleepy Bay, and scoria eruptives at Pa Bay (proximal spatter deposits to medial ash-rich units).

Perhaps the most obvious question that remains unresolved at the Akaroa Volcanic Complex relates to Onawe Peninsula. Long assumed to be the volcanic plug/neck of the complex, dating of the only in situ plutonic material on Banks Peninsula shows that it is some of the youngest material in the AVC (Timm et al., 2009). In addition, the intrusives at the harbour end of Onawe sit relatively high within the volcanic structure, suggesting that is was not part of the main, active magmatic system. However, more analysis (particularly trace element and isotope geochemistry) on the relationship between the plutonic material described in this study and the Onawe syenite and gabbro will help establish their relationships to the magmatic system and phase(s) of the AVC's episodic magmatism.

The crystal cargo of lava flows and domes and their relationship to their host and the plutonic material at the AVC is another important opportunity for insight in to the magmatic system and how it interacted with the eruptible portion of the system. The diversity of large crystals within scoria flank eruptives at Pa Bay (and other AVC scoria cones) would also provide this important insight.

The dating of plutonic lithics themselves can resolve the age relationships of diverse lithics, i.e. lithics that are contemporaneous with AVC volcanism, lithics from older crustal magmatism potentially related to the Hikurangi Rise (cf. Hobden, 1990), and the possibility of LeBons Bay Peak magma passing through and entraining lithics from an already mature AVC magmatic system.

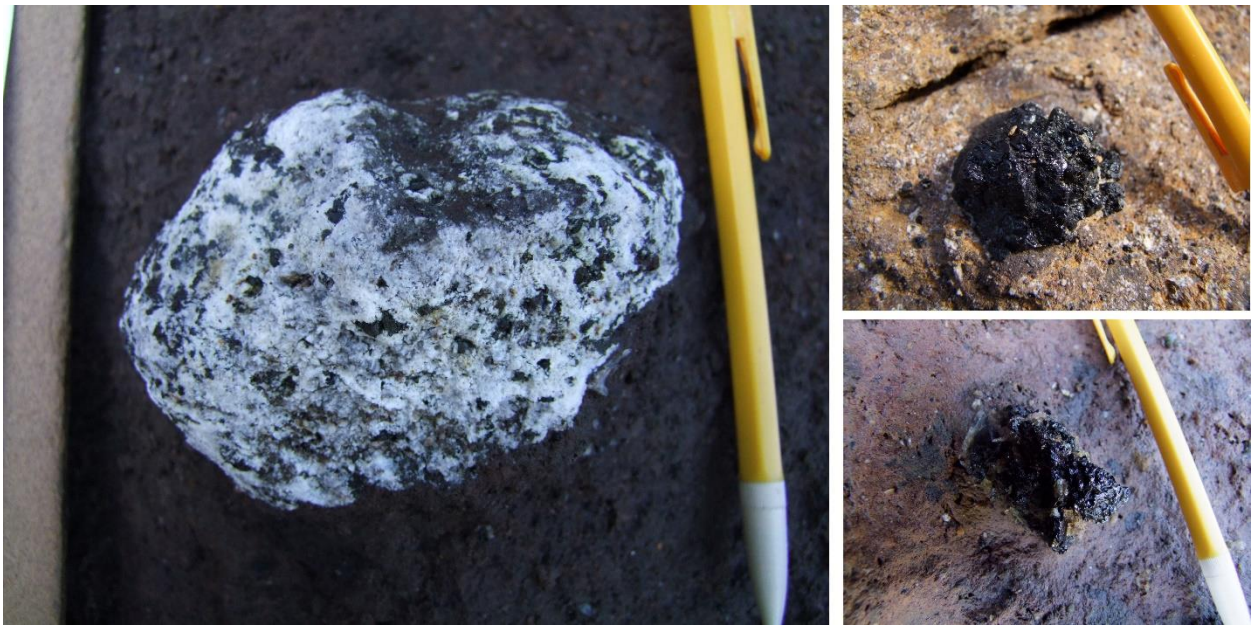

Figure 6.2 Lithics found at Sleepy Bay including pyroxene (with little to some plagioclase) crystal clusters.

Additionally, lithics are continuing to be identified within the other volcanic units of Banks Peninsula. For example, on a guided walk to Camp Bay, Lyttelton Harbour, lithics were found hosted within a trachytic dike on the shore platform. Further lithic-bearing sites found within the Lyttelton Volcanic Complex are at Corsair Bay (Lyttelton Harbour) and Taylors Mistake. In the Diamond Harbour eruptive package at Purau Bay, olivine lithics and pyroxene>olivine>>plagioclase plutonic lithics were also discovered. Identification and sampling of these lithics and associated studies (i.e. this study) will provide insights into the magmatic system of the Lyttelton Volcanic Complex, and the unusual late stage Diamond Harbour Volcanics.

Appendix

Chapter 3 Appendix

Thin sections were prepared for EBSD analysis following Prior (1999). EBSD was conducted on five samples using a Zeiss SEM fitted with Oxford Instruments and Aztec software at a 50 μm step interval. A higher resolution scan at 5.15 μm was conducted on one sample (8B). EBSD was collected under 30 kV accelerating voltage and 100nA current. Wild spikes were removed in Channel 5+ and data was extrapolated to four neighbor pairs to reduce unnecessary noise. Principal plane pole figures were produced with 10° halfwidth contours.

EBSD Settings	GR 8b	GR 8b Fine	GR 7a	GR 9b	GR 10b	GR 11b	GR 14
Resolution (Width):	394 pixels	2458 pixels	1093 pixels	402 pixels	556 pixels	919 pixels	757 pixels
Resolution (Height):	296 pixels	1500 pixels	416 pixels	356 pixels	410 pixels	486 pixels	3128 pixels
Step Size:	50µm	5.15µm	30.2µm	50µm	46.3µm	32.3µm	5.15 µm
Field Width:	19.7mm	12.7mm	33mm	20.1mm	25.7mm	29.7mm	3.9mm
Field Height:	14.8mm	7.72mm	12.6mm	17.8mm	19mm	15.7mm	16.1mm
Number of Points:	116624	3687000	454688	143112	227960	446634	2367896
Hit Rate:	64.10%	70.60%	48.30%	58.80%	49.70%	46.80%	60.39%
Accelerating Voltage:	30.00 kV	30.00 kV	30.00 kV	30.00 kV	30.00 kV	30.00 kV	20.00 kV
Working Distance:	21.7 mm	19.9 mm	25.6 mm	21.9 mm	24.1 mm	23.8 mm	20-25 mm
Detector Insertion Distance:	207.0 mm	207.0 mm	207.0 mm	207.0 mm	207.0 mm	207.0 mm	130 mm
EBSD Camera Binning:	2x2 (320x240 pixels)	2x2	2x2	2x2	2x2	2x2	4x4
EBSD Camera Gain:	15	15	15	15	15	15	15
Frame Averaging:	2 frames	2 frames	2 frames	2 frames	2 frames	2 frames	2 frames
Hough Resolution:	50	50	50	50	50	50	60
Band Detection Mode:	Edges	Edges	Edges	Edges	Edges	Edges	Edges
Number of Bands Detected:	10	10	10	10	10	10	8
Indexing Mode:	Optimized - EBSD	Optimized - EBSD	Optimized - EBSD	Optimized - EBSD	Optimized - EBSD	Optimized - EBSD	Optimized - EBSD

Table 1. EBSD settings. All data collected on a Zeiss SEM with Oxford Instruments at the University of Otago.

Phase	Reference	Reflectors
Anorthite	American Mineralogist (1973), vol. 58, pages 665-675	72
Diopside (CaMgSi2O6)	Aztec Database (HKL phases)	62
Forsterite	Aztec Database (HKL phases)	60
Ilmenite	American Mineralogist (1984), vol. 69, pages 176-185	66
Magnetite	American Mineralogist (1984), vol. 69, pages 754-770	40
Apatite	American Mineralogist (1991), vol. 76, pages 1165-1173	54

Table 2. Phase identification references for all samples.

	Anorthite	Diopside	Forsterite	Ilmenite	Magnetite	Apatite
GR8b	40	13	14	2	1	<1
GR14	47	7	5	<1	<1	<1

Table 3. Phase fraction (excluding zero solutions) for GR8b and GR14. – a lithic not included in this study but that exhibits the same, but weaker CPO as the cumulates presented here. The interstitial phases in both GR14 and the cumulates of this study are clinopyroxene and olivine. Note the decrease in modal abundance of mafic phases with decreasing strength of CPO.

Sample	J Index	M Index
8B Fine	216.354	0.1894
7A	45.3836	0.1537
11B	30.0036	0.1215
9B	16.1206	0.0703
8B	14.1353	0.1368
10B	5.7676	0.0709
14 Fine	6.1095	0.0689

Table 4. J and M indices were calculated using the Matlab package, MTex (Mainprice et al., 2011; Mainprice et al., 2015). Multiple measures were used to account for the dependence of the J index on point count and data resolution while still allowing comparisons to other

plagioclase EBSD data. J and M indices as well as maximum densities within 10º half-width contours are used to describe strength of fabric.

	All Anorthite	>400mu Anorthite
Average aspect ratio	2.37	2.70
Standard deviation	1.26	1.39
Skew	1.75	1.34
Max	8.64	8.64
Min	1.01	1.08

Table 5. Average aspect ratios for all anorthite grains and only the larger fraction in GR8b (EBSD data) with associated statistics.

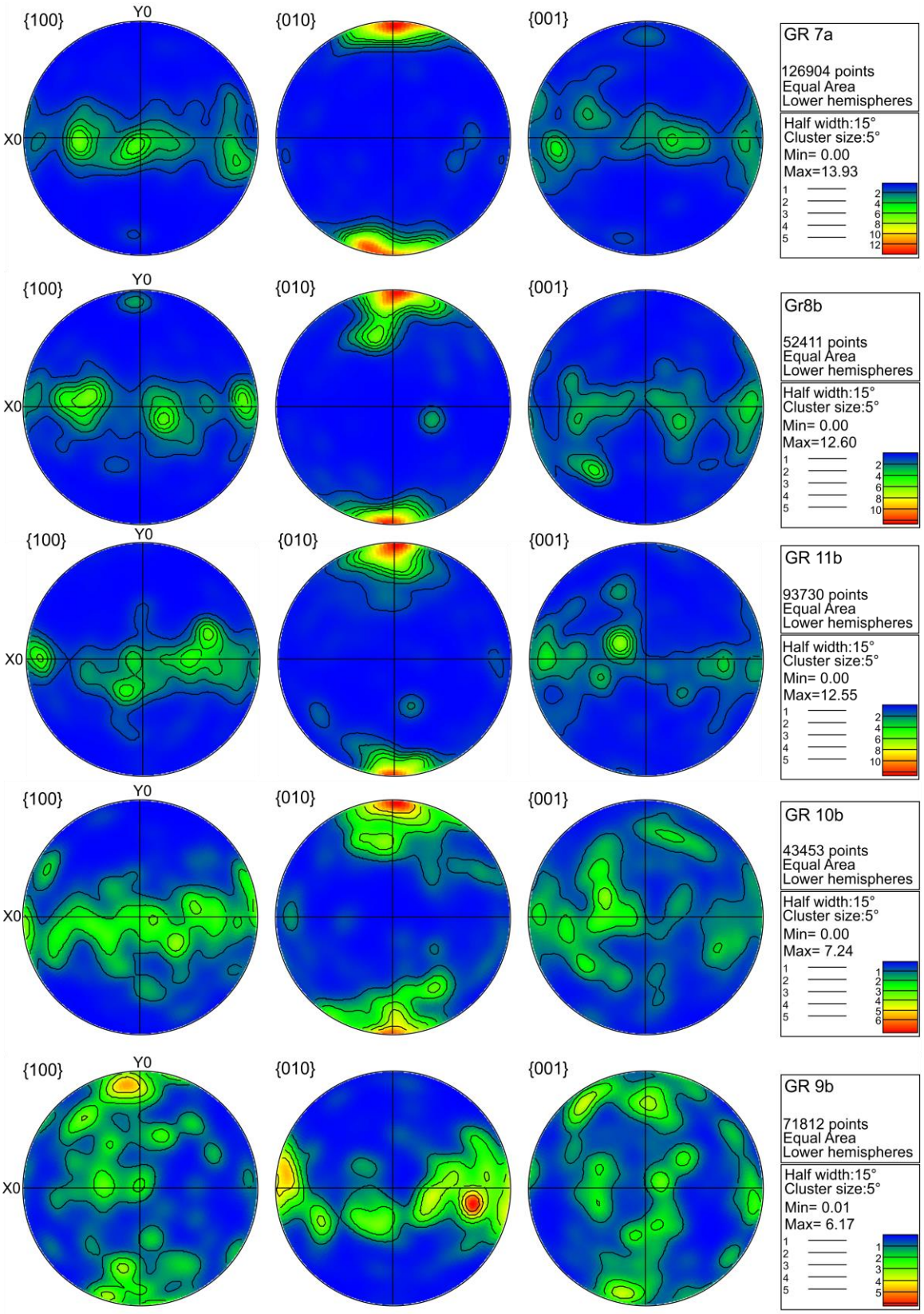

Figure 1. CPOs from the compacted cumulate plutonic lithics analyzed in this study. Lithic CPOs (with the exception of 9b) are characteristic of the organization of plagioclase under

compression with aligned {010} (plagioclase short axis) and {100} and {001} constrained about a great circle. Ordered in decreasing CPO strength.

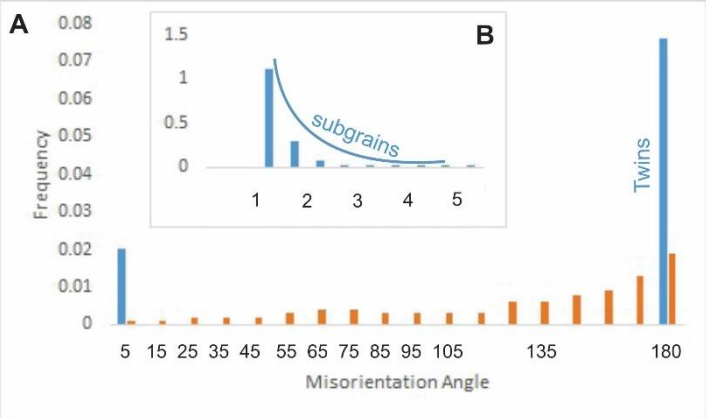

Figure 2. (A) graph of the frequency of a theoretical random-pair (orange) and the sample neighbor-pair (blue) plagioclase misorientation plot of 8B. (B) Zoomed in low angle misorientations from the same plot. The blue line shows the tapering trend of low angle grain boundaries during continuous rotation.

Here, neighbor-pair misorientations are different from those calculated for a theoretical plagioclase fabric with a random CPO, confirming the existence of a plagioclase CPO. Additionally, distinct peaks in neighbor-pair misorientation at angles under 10° (particularly <5°) reflect the presence of subgrains forming under continuous rotation.

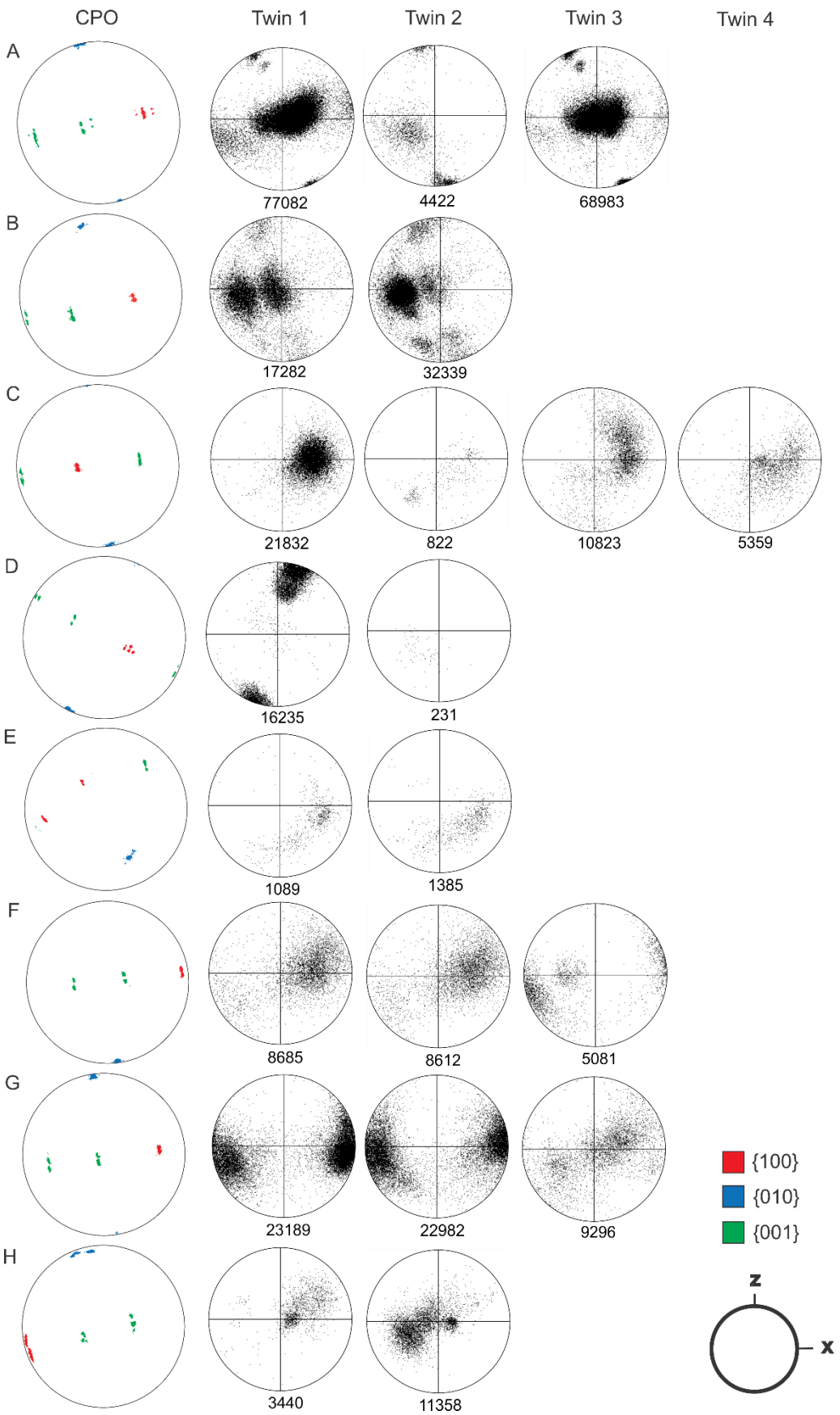
CPO
Twin 1
Twin 2
Twin 3
Twin 4
A
77082
4422
68983
B
17282
32339
C
21832
822
10823
5359
D
16235
231
E
1089
1385
F
8685
8612
5081
G
23189
22982
9296
H
3440
11358
{100}
{010}
{001}
z
x

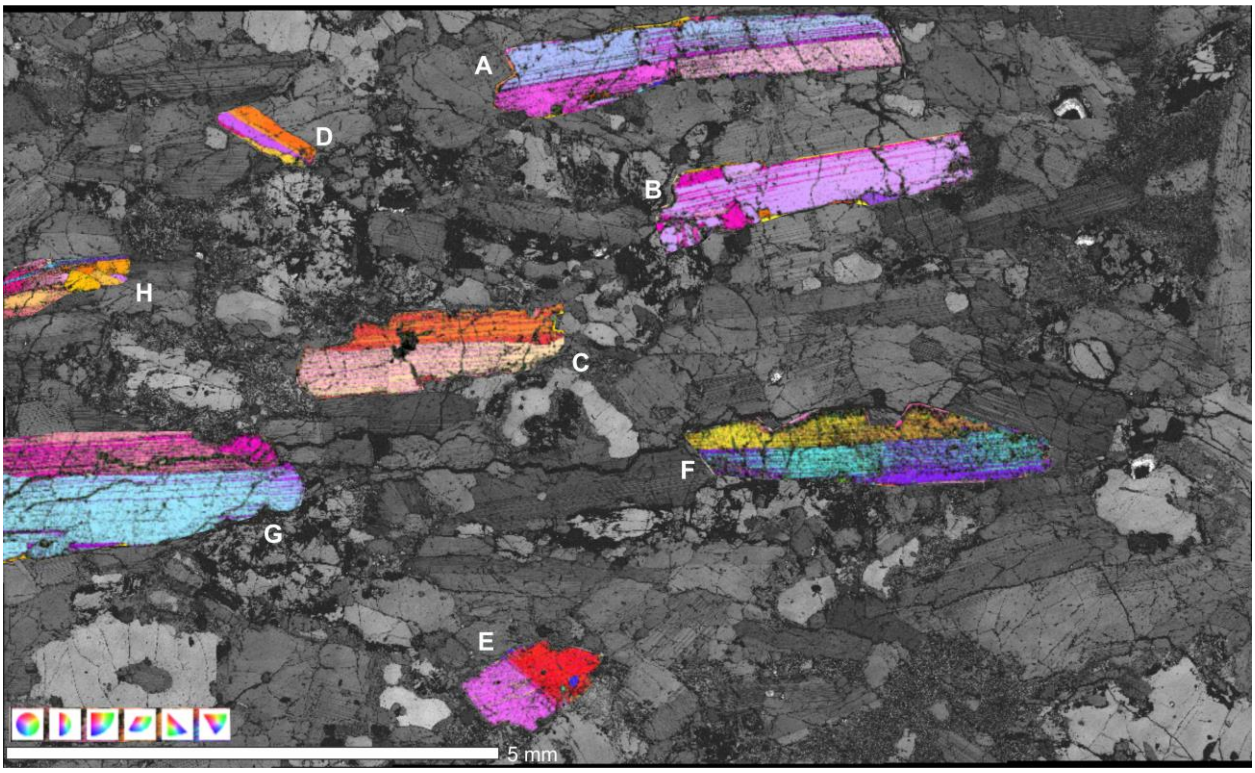

Figure 3. Rotation axis pole figures and map. Rotation axis pole figures in the sample reference frame for the fine resolution scan of GR8B. Eight crystals were selected for analysis and are labeled A-H. Selected crystals are identified in the backscatter electron map by their Euler angle to show their orientation within the sample. Each crystal (A-H) has twin sets, labelled Twin 1-4, and read from left to right. The CPO column indicates the crystallographic orientation of the entire crystal. All directions are plotted together and are indicated by color.

Rotation axes for angles between 3 and 10° were plotted to illustrate the orientation of low angle deformation activated during solid-state deformation. The orientation of the rotation axis of each point in a twin was calculated in Channel 5+, all orientations from a twin-set were exported to Excel and randomly sorted, then imported back to Channel 5+ were they were plotted in pole figures. Numbers under each plot refer to the number of points analyzed. Equal area, lower hemisphere projections with 30° half-width.

The orientation of rotation axes of all crystals and twins, when considered together, show the way that the entire sample deformed. A shared pattern indicates that deformation in the solid-state (*i.e.* a force acting on all crystals in a pile) occurred, confirming petrographic observations of extensive sold-state deformation. GR8b subgrains have a shared pattern of rotation connected by a great circle (Figure 3B), indicating compaction forces present during melt extraction and solid-state deformation.

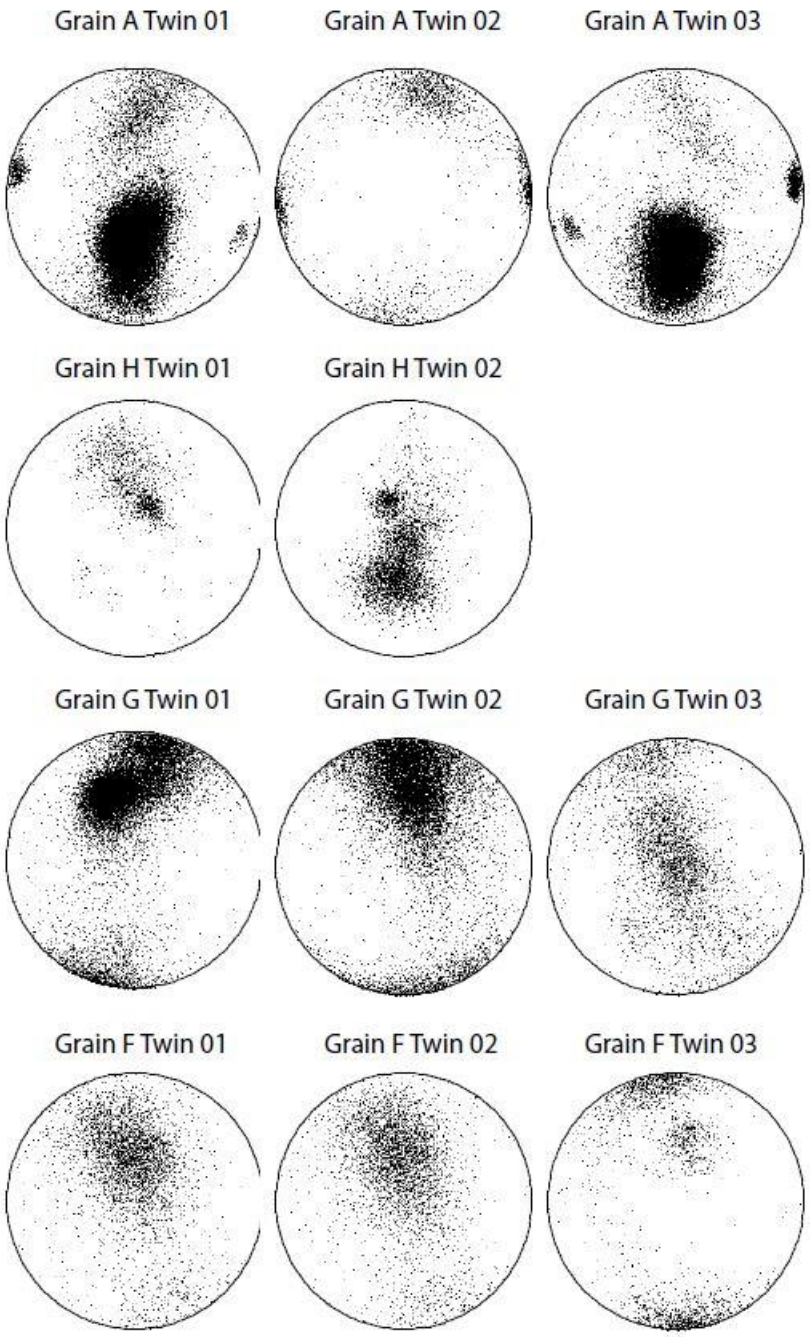

Figure 4. Rotation axis pole figures in the crystal reference frame for a selection of the same grains as plotted in Figure 3. The clustering of points in different locations show that different slip systems operated in different crystals (though all operate in the 010). Note, however, that the same slip system operated in two of the twin sets (as in Grain A) and, to some extent, across different crystals (*e.x.* Grain G and F). This shows that there was both a crystallographic and stress regime control on the deformation of the crystals.

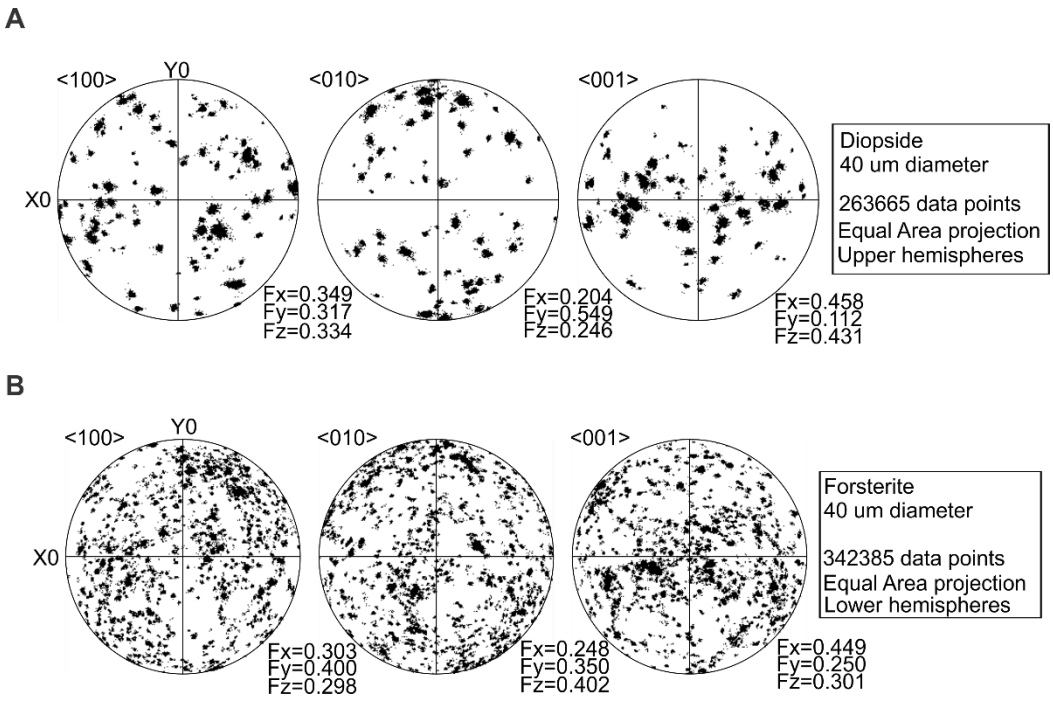

Figure 5. Pole figures of clinopyroxene (a) and olivine (b) in GR8b. Grains greater than 40 μm selected.

References

Mainprice, D., Bachmann, F., Hielscher, R., Schaeben, H., Geologie, M., & Universita, T. (2015). Descriptive tools for the analysis of texture projects with large datasets using MTEX : strength , symmetry and components, *i*, 251–271.

Mainprice, D., Hielscher, R., & Schaeben, H. (2011). Calculating anisotropic physical properties from texture data using the MTEX open-source package. *Geological Society, London, Special Publications*, *360*(1), 175–192.

Prior, D. J., Boyle, A. P., Brenker, F., Cheadle, M. C., Austin, D., Lopez, G., Peruzzo, L., Potts, G., Reddy, S., Spiess, R., Timms, N., Trimby, P., Wheeler, J., Zetterström, L. (1999). The application of electron backscatter diffraction and orientation contrast imaging in the SEM to textural problems in rocks. *American Mineralogist*, *84*(11–12), 1741–1759.

Chapter 4 Appendix

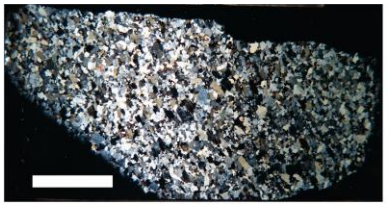

Type A

Equigranular, generally finer-grained with no to some apparent shape preferred alignment

GR14

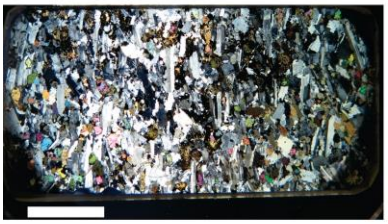

Type B

Relatively high aspect ratio plagioclase defining a moderate fabric

GR20

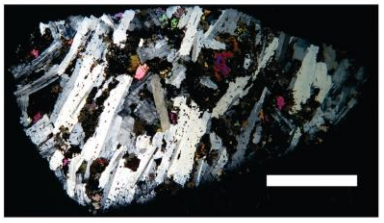

Type C

Very well defined fabric apparent in alignment of high aspect ratio plagioclase crystals

GR04 and GR8b

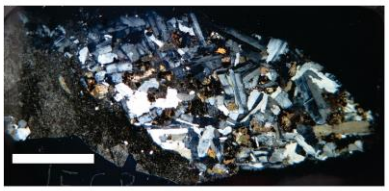

Type D

Random or no apparent fabric

GR22

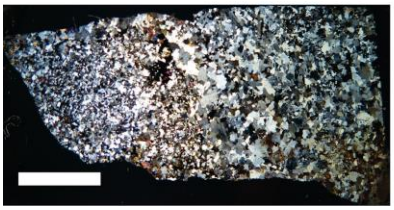

Type E

Variable texture within sample: here as three distinct textural zones

GR26 scale bar 10 mm

Figure 1. Goat Rock plutonic lithic categories defined from field reconnaissance and further qualitative thin section analysis. The representative lithic included in italics. Types A, B, and C are the focus of this contribution and are referred to by their sample names within the text.

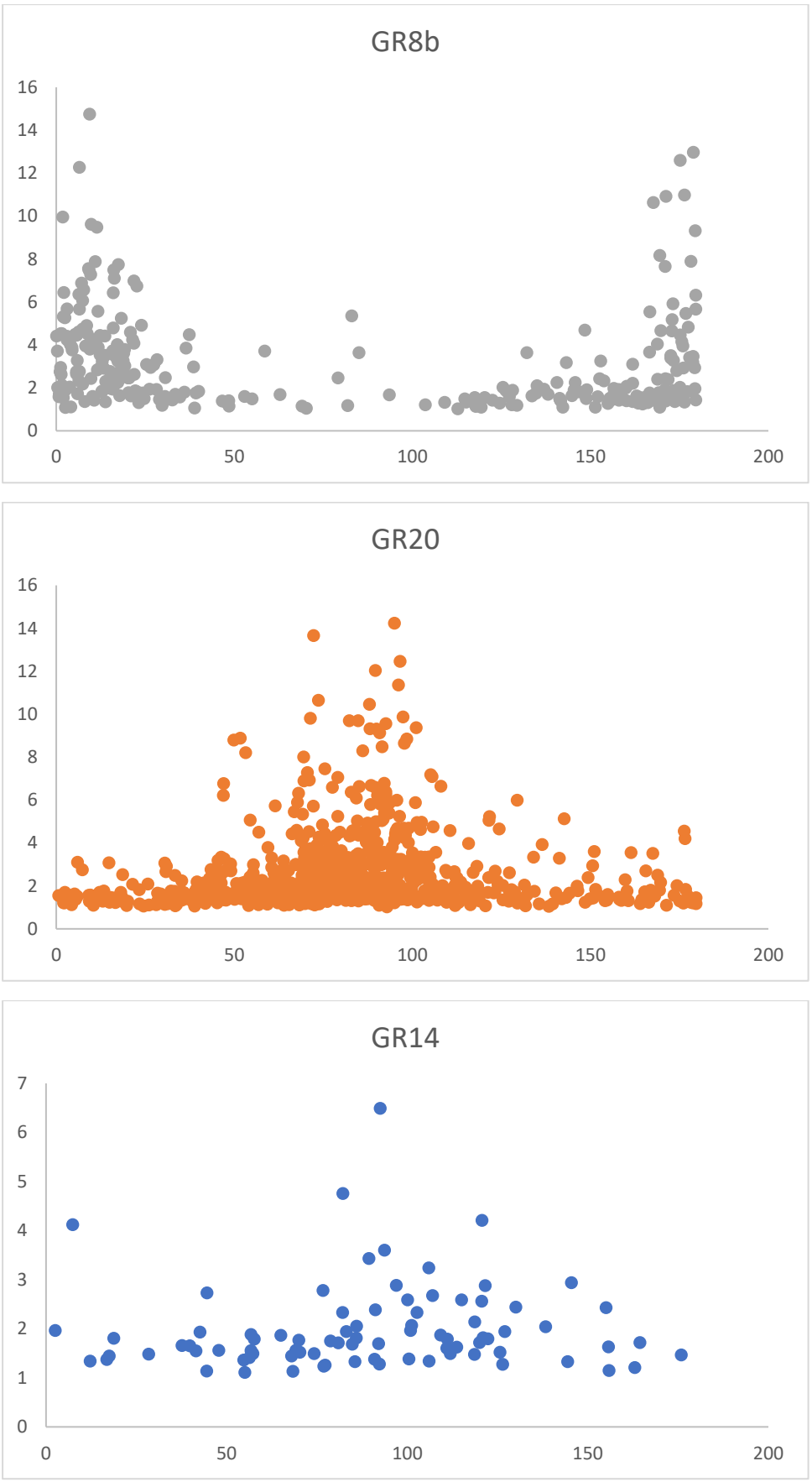

Figure 2. Orientation vs aspect ratio of plagioclase.

Table 1. Twin incidence. Number of twins occurring across a line (1-3) through the thin section with orientation (normal to SPO or not).

	GR8b			
	normal to SPO			
	yes	no	Total	% w/ twins
1	5	0	5	100.0
2	5	1	6	83.3
3	7	1	8	87.5
Average				90.3
	GR20			
	normal to SPO			
	yes	no	Total	% w/ twins
1	14	9	23	60.9
2	11	11	22	50.0
3	12	11	23	52.2
Average				54.3
	GR14			
	normal to SPO			
	yes	no	Total	% w/ twins
1	45	42	87	51.7
2	45	35	80	56.3
3	24	25	49	49.0
Average				52.3

Geochemistry

Table 2. Whole rock data for all lithics and host of this study.

	GR8b*			GR20	GR14	GR Host					
	GR10	GR11	GR04	GR20	GR14	GR17A	GR17B	GR18	GR19	GR24H	GR22H
SiO_2	45.36	47.52	45.64	47.31	54.98	49.85	49.94	50.64	49.17	49.10	48.87
TiO_2	3.58	2.95	3.00	2.80	1.87	2.24	2.24	2.17	2.38	2.38	2.44
Al_2O_3	17.03	16.95	17.41	17.39	21.00	17.08	17.05	17.34	16.81	16.92	16.95
Total Fe	14.59	13.61	14.61	14.68	7.50	12.58	12.56	12.19	12.77	12.83	12.99
MnO	0.25	0.23	0.23	0.23	0.13	0.22	0.22	0.21	0.21	0.22	0.22
MgO	4.42	4.10	3.35	2.99	0.87	3.06	3.05	2.48	3.42	3.36	3.12
CaO	8.08	8.08	8.45	7.25	5.13	6.61	6.60	6.28	7.05	6.91	7.04
Na_2O	4.15	4.52	4.66	4.99	7.08	5.19	5.20	5.48	5.03	5.15	5.25
K_2O	0.66	0.74	0.85	0.98	1.37	1.91	1.89	2.02	1.87	1.86	1.84
P_2O_5	1.89	1.30	1.81	1.38	0.08	1.25	1.25	1.19	1.28	1.25	1.28
LOI	0.09	-0.31	-0.06	-0.41	-0.04	0.13	-0.77	-0.01	0.76	-0.35	-0.45
Total	100.00	100.00	100.00	100.00	100.00	100.00	100.00	100.00	100.00	100.00	100.00

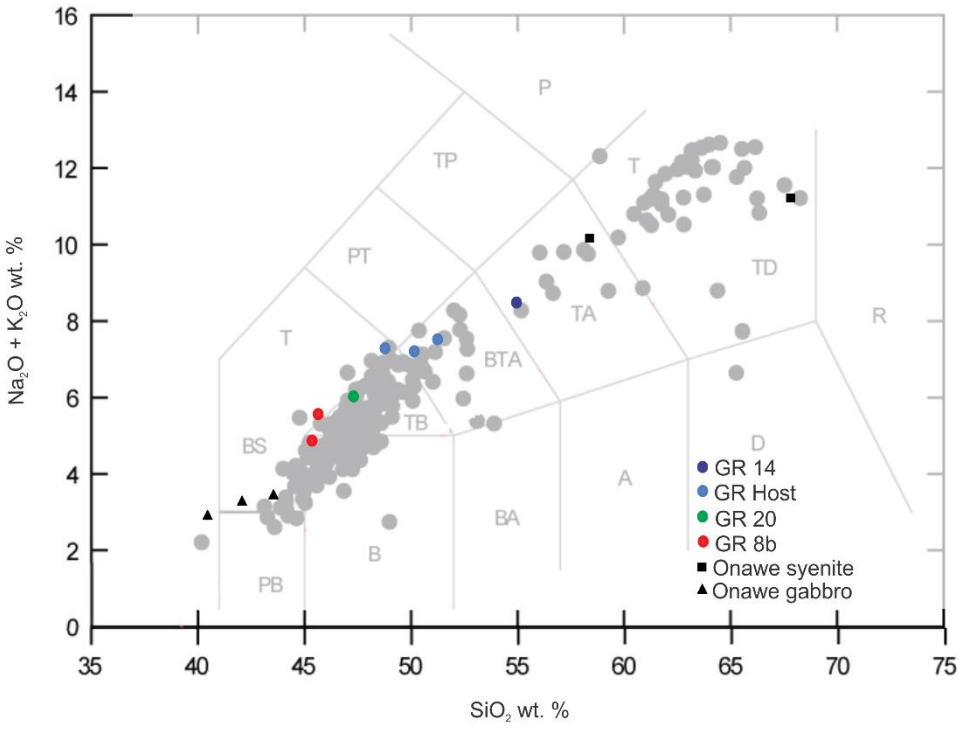

Figure 3. Whole rock plot of silica vs. alkalis for the three lithics of this study and the dome lava (GR Host). All AVC points are in grey (from Hartung et al. 2011).

Table 3. List of standards used on the University of Wisconsin-Madison Microprobe and the microprobe error for each element analyzed in plagioclase samples.

Standards for Microprobe analysis	
Element	**Standard Description**
Na, Al	Monash An49
Ca	Diopside, NY NMNH 11733
Si, Fe	Fayalite syn - CalTech - Rossman
Cr	Cr2O3 synthetic
Mg	Kilbourne Olivine
Ti	TiO2 synthetic
Mn	Rhodonite-Evans - LGM P
Ni	NiO synthetic

Feldspar Error	
Element	**Error**
Na, Ca, Al, Si	<1.5% (An error +/- 0.09)
K, Fe	<15%

Table 4. Plagioclase EMPA chemistries for the three lithics.

Spot	Line.Number	SiO_2	Al_2O_3	FeO_T	CaO	Na_2O	K_2O	Total
GR8B.1.001	532	54.25	28.70	0.38	10.61	5.28	0.40	99.61
GR8B.1.001	533	56.17	27.48	0.40	8.79	6.25	0.51	99.61
GR8B.1.001	534	54.24	28.44	0.37	9.98	5.60	0.48	99.12
GR8B.1.001	535	55.68	28.90	0.35	9.73	5.75	0.44	100.85
GR8B.2.002	536	61.93	24.37	0.25	5.05	7.75	1.79	101.14
GR8B.2.002	537	60.77	24.40	0.37	4.81	7.50	1.92	99.76
GR8B.2.002	538	61.31	24.48	0.24	5.21	7.62	1.63	100.50
GR8B.2.002	539	61.88	24.29	0.22	4.96	7.66	1.97	100.99
GR8B.2.002	540	60.65	24.62	0.29	5.09	7.68	1.73	100.06
GR8B.5	546	61.20	23.76	0.29	5.08	7.76	1.69	99.79
GR8B.5	547	60.89	23.77	0.25	4.79	7.88	1.67	99.25
GR8B.5	548	60.51	24.06	0.17	5.04	7.52	1.66	98.95
GR8B.5	549	60.80	24.62	0.21	5.29	7.67	1.60	100.18
GR8B.5	550	63.19	22.83	0.43	3.09	7.93	3.26	100.72
GR8B.6	551	56.67	27.45	0.16	8.59	6.27	0.63	99.79
GR8B.6	552	56.84	27.95	0.15	8.80	6.40	0.48	100.62
GR8B.6	553	58.32	25.99	0.17	6.97	7.30	0.69	99.44
GR8B.6	554	55.61	27.40	0.12	8.81	6.37	0.52	98.84

GR8B.6	555	56.18	27.17	0.17	8.60	6.38	0.46	98.96
GR8B.7	556	64.90	20.93	0.36	1.30	7.65	5.11	100.25
GR8B.7	557	57.69	27.00	0.15	8.21	6.64	0.51	100.21
GR8B.7	558	56.23	27.36	0.22	8.59	6.52	0.38	99.29
GR8B.7	559	56.24	27.96	0.16	9.08	6.24	0.34	100.02
GR8B.7	560	54.93	28.73	0.15	10.18	5.57	0.35	99.92
GR8B.7	561	57.04	27.15	0.14	8.47	6.62	0.70	100.13
GR8B.7	562	55.94	27.91	0.11	9.13	6.20	0.45	99.74
GR8B.7	563	56.91	28.17	0.23	8.90	6.53	0.43	101.17
GR8B.7	564	56.94	27.32	0.20	8.29	6.57	0.41	99.73
GR8B.7	565	57.31	28.07	0.11	9.15	6.37	0.44	101.45
GR8B.7	566	56.71	27.89	0.17	9.13	6.37	0.53	100.79
GR8B.7	567	56.13	28.13	0.15	9.21	6.27	0.52	100.42
GR8B.8	568	59.73	25.96	0.15	6.69	7.46	1.02	101.00
GR8B.8	569	59.16	25.61	0.17	7.05	7.19	0.92	100.08
GR8B.8	570	58.82	25.94	0.12	7.00	7.31	0.87	100.07
GR8B.8	571	59.23	26.47	0.13	7.14	7.16	0.66	100.78
GR8B.8	572	58.62	26.31	0.13	7.29	7.25	0.64	100.25
GR8B.8.T	573	59.13	25.47	0.14	6.59	7.30	1.05	99.68
GR8B.8.T	574	58.95	25.56	0.18	6.38	7.08	1.00	99.15
GR8B.8.T	575	59.57	25.22	0.14	6.75	7.49	1.06	100.23
GR8B.8.T	577	55.58	28.32	0.13	9.07	6.02	0.51	99.63
GR8B.8.T	578	56.98	27.59	0.18	8.97	6.45	0.50	100.68
GR8B.8.T	579	56.92	27.57	0.17	8.61	6.29	0.53	100.10
GR8B.8.T	580	56.74	27.55	0.20	8.85	6.29	0.54	100.16
GR8B.8.T	581	56.00	27.74	0.15	9.03	6.10	0.52	99.55
GR8B.8.T	582	59.02	25.45	0.19	6.31	7.45	0.92	99.33
GR8B.9.T	583	56.03	27.44	0.16	8.85	6.31	0.60	99.39
GR8B.9.T	584	59.03	26.54	0.14	6.99	7.07	0.87	100.64
GR8B.9.T	585	57.35	27.37	0.18	8.37	6.59	0.51	100.38
GR8B.9.T	586	56.75	27.17	0.10	8.47	6.48	0.39	99.37
GR8B.9.T	587	56.85	27.16	0.15	8.55	6.66	0.47	99.84
GR8B.9.T	588	57.25	27.71	0.14	8.62	6.62	0.58	100.91
GR8B.9.T	589	59.37	26.45	0.18	7.12	7.09	0.94	101.14
GR8B.9.T	590	59.00	25.83	0.27	7.00	7.16	0.71	99.97
GR8B.9.T	591	55.90	28.45	0.18	9.61	5.92	0.38	100.43
GR8B.9.T	592	56.56	27.68	0.19	9.01	6.13	0.38	99.95
GR8B.9.T	593	58.42	26.64	0.15	7.67	7.05	0.49	100.41
GR8B.9.T	595	55.72	28.55	0.16	9.74	5.83	0.32	100.33
GR8B.9.T	596	55.96	28.36	0.15	9.54	5.91	0.35	100.27
GR8B.9.T	597	56.89	28.12	0.19	9.13	6.17	0.47	100.96
GR8B.10.T1	598	58.21	26.01	0.20	7.05	7.13	0.77	99.36
GR8B.10.T1	599	58.45	25.88	0.19	6.89	7.13	0.84	99.39
GR8B.10.T1	600	59.21	25.52	0.16	6.39	7.47	0.88	99.64
GR8B.10.T1	601	60.00	24.83	0.14	6.02	7.73	0.98	99.70
GR8B.10.T1	602	59.13	24.76	0.19	5.68	7.85	0.96	98.57

GR8B.10.T1	604	57.63	26.58	0.14	7.75	6.96	0.68	99.73
GR8B.10.T1	606	57.72	25.27	0.25	6.86	7.11	0.83	98.04
GR8B.10.T1	610	58.50	25.46	0.15	7.02	7.20	0.87	99.19
GR8B.10.T1	611	58.08	25.54	0.17	7.08	7.28	0.70	98.83
GR8B.10.T1	612	56.32	27.48	0.18	8.45	6.53	0.44	99.40
GR8B.10.T1	613	55.44	28.22	0.14	9.54	5.90	0.35	99.59
GR8B.10.T2	616	55.26	27.58	0.18	8.89	6.27	0.42	98.60
GR8B.10.T2	617	56.16	27.03	0.24	8.80	5.97	0.43	98.63
GR8B.10.T2	619	58.73	25.22	0.24	6.48	7.85	0.86	99.38
GR8B.10.T2	620	58.26	25.82	0.18	6.91	7.36	0.83	99.37
GR8B.10.T2	625	58.90	25.32	0.25	6.38	7.73	0.85	99.42
GR8B.10.T2	628	55.49	27.18	0.16	8.65	6.32	0.52	98.32
GR8B.10.T2	629	56.36	26.19	0.22	7.51	7.06	0.65	98.00
GR8B.10.T2	630	57.79	25.42	0.20	6.94	7.26	0.79	98.41
GR8B.10.T2	631	56.10	27.30	0.34	8.69	6.49	0.52	99.43
GR8B.10.T2	633	56.31	26.97	0.18	8.09	6.78	0.71	99.03
GR8B.10.T2	634	55.99	26.87	0.13	8.84	6.44	0.52	98.80
GR8B.10.T3	635	55.60	27.50	0.12	8.86	6.22	0.55	98.85
GR8B.10.T3	637	58.17	26.03	0.19	6.95	7.09	0.91	99.35
GR8B.10.T3	638	58.46	25.42	0.17	6.37	7.59	1.00	99.01
GR8B.10.T3	640	58.65	25.89	0.17	6.71	7.32	0.95	99.70
GR8B.10.T3	641	58.40	25.62	0.20	6.61	7.29	0.85	98.97
GR8B.10.T3	644	58.90	24.80	0.15	6.40	7.48	0.89	98.63
GR8B.10.T3	645	58.87	24.87	0.19	6.10	7.60	1.10	98.73
GR8B.10.T3	646	58.68	25.19	0.22	5.98	7.39	1.19	98.65
GR8B.11.T	656	58.50	25.92	0.15	7.13	7.16	0.89	99.75
GR8B.11.T	657	55.78	27.28	0.16	8.36	6.44	0.56	98.57
GR8B.11.T	667	59.05	25.84	0.21	6.82	7.09	0.66	99.66
GR8B.11.T	668	56.24	26.94	0.31	8.43	6.41	0.43	98.77
GR8B.11.T	672	55.99	27.35	0.16	8.34	6.54	0.34	98.71
GR8B.12.T	686	57.02	26.52	0.14	8.05	6.74	0.68	99.14
GR8B.12.T	687	57.11	26.19	0.16	7.31	7.12	0.76	98.65
GR8B.12.T	688	56.14	26.76	0.14	8.31	6.57	0.50	98.42
GR8B.12.T	689	56.44	26.81	0.12	8.16	6.73	0.52	98.78
GR8B.12.T	690	56.47	26.88	0.14	8.37	6.72	0.45	99.02
GR8B.12.T	694	57.71	26.44	0.10	7.00	7.02	0.83	99.10
GR8B.13.1	695	55.84	27.42	0.14	8.70	6.36	0.58	99.05
GR8B.13.1	696	57.11	27.23	0.15	8.04	6.71	0.55	99.79
GR8B.13.1	697	58.44	25.61	0.20	6.87	7.33	0.74	99.19
GR8B.13.1	698	55.99	27.46	0.15	9.02	6.12	0.34	99.09
GR8B.13.1	699	58.10	26.53	0.19	7.35	6.81	0.82	99.81
GR8B.14	701	56.56	27.03	0.15	8.38	6.53	0.67	99.33
GR8B.14	703	56.79	26.76	0.13	7.86	6.63	0.65	98.82
GR8B.14	705	56.09	26.95	0.14	8.13	6.62	0.63	98.56
GR8B.14	706	57.82	25.71	0.20	7.15	7.09	0.85	98.83
GR8B.14	707	58.04	25.96	0.17	6.69	7.21	0.94	99.02

GR8B.14	708	57.92	25.52	0.16	7.06	7.07	1.03	98.76
GR8B.14	709	59.10	25.06	0.16	5.89	7.46	1.29	98.96
GR8B.14	710	55.73	27.21	0.15	8.57	6.07	0.67	98.40
GR8B.14	711	59.74	24.84	0.20	5.49	7.69	1.30	99.26
GR8B.14	712	59.24	24.88	0.18	5.78	7.56	1.30	98.93
GR8B.19	713	63.79	21.83	0.22	2.52	7.97	3.73	100.05
GR8B.19	714	57.47	26.59	0.18	7.83	6.89	0.69	99.66
GR8B.19	715	56.73	26.84	0.13	8.18	6.63	0.55	99.05
GR8B.19	716	58.63	25.74	0.12	6.80	7.49	0.85	99.63
GR8B.19	717	57.32	27.10	0.18	8.21	6.56	0.66	100.03
GR8B.19	718	63.99	21.86	0.20	2.73	8.27	3.00	100.05
GR8B.20	720	61.30	23.81	0.26	4.65	7.79	1.68	99.50
GR8B.20	721	60.59	24.14	0.21	5.16	7.62	1.69	99.41
GR8B.20	722	59.79	24.24	0.21	5.16	7.63	1.58	98.62
GR8B.21	723	60.47	24.44	0.22	5.27	7.61	1.75	99.76
GR8B.21	725	60.03	24.63	0.16	4.86	7.73	1.92	99.33
GR8B.22	726	60.52	23.61	0.20	4.62	7.71	2.17	98.82
GR8B.22	727	61.25	23.52	0.20	4.43	7.79	2.17	99.35
GR8B.22	728	61.92	23.33	0.29	4.25	7.79	2.15	99.73
GR8B.22	729	61.75	23.18	0.19	4.33	7.91	2.28	99.64
GR8B.22	730	60.75	23.30	0.23	3.93	7.98	2.32	98.51
15GR20.2	1116	61.88	24.71	0.23	5.07	8.12	1.49	101.5
15GR20.3.1	1117	58.33	27.19	0.16	7.99	6.94	0.69	101.29
15GR20.3.1	1118	58.54	27.22	0.16	8.13	6.89	0.71	101.66
15GR20.3.1	1119	58.19	27.06	0.16	7.94	6.82	0.68	100.85
15GR20.3.1	1120	59.07	26.11	0.13	7.44	6.98	0.94	100.66
15GR20.3.1	1123	59.21	24.73	0.33	6.14	7.28	1.15	98.83
15GR20.3.1	1124	60.59	24.49	0.17	5.46	7.75	1.37	99.83
15GR20.3.1	1125	60.91	24.66	0.17	5.66	7.77	1.27	100.45
15GR20.3.2	1126	60.29	25.41	0.21	6.31	7.43	1.22	100.86
15GR20.3.2	1127	60.17	24.65	0.13	6.08	7.74	1.28	100.05
15GR20.3.2	1128	61.93	24.52	0.16	5.43	7.65	1.64	101.33
15GR20.3.2	1130	60.9	24.74	0.2	5.71	7.61	1.46	100.61
15GR20.3.2	1131	59.03	25.86	0.11	7.32	6.67	0.95	99.95
15GR20.3.2	1133	59.38	24.73	0.32	6.22	7.25	1.21	99.1
15GR20.3.2	1135	59.07	26.53	0.19	7.07	7.17	1.01	101.03
15GR20.3.2	1136	59.96	25.6	0.17	6.64	7.46	1.09	100.93
15GR20.3.3	1137	57.69	27.11	0.13	8.24	6.5	0.74	100.42
15GR20.3.3	1138	60.37	25.38	0.19	6.47	7.65	1.18	101.24
15GR20.3.3	1140	60.91	24.67	0.23	5.93	7.43	1.25	100.41
15GR20.3.3	1141	60.49	25.7	0.19	6.36	7.42	1.05	101.21
15GR20.3.3	1142	57.7	26.41	0.24	8.03	6.64	0.72	99.75
15GR20.3.3	1143	58.47	26.62	0.16	7.63	6.91	0.72	100.5
15GR20.3.3	1144	57.99	26.63	0.16	7.54	6.99	0.76	100.06
15GR20.4	1145	58.06	27.57	0.16	8.32	6.62	0.67	101.41
15GR20.4	1146	60.86	25.63	0.17	6.19	7.54	1.03	101.43
15GR20.5	1147	57.9	27.23	0.17	8.07	6.78	0.69	100.84

15GR20.6	1148	59.25	26.59	0.19	6.95	7.32	0.73	101.02
15GR20.6	1149	58.41	27.36	0.22	8.15	6.64	0.6	101.38
15GR20.6	1150	58.67	26.57	0.18	7.71	6.95	0.83	100.9
15GR20.6	1151	61.54	24.77	0.19	5.17	7.72	1.58	100.97
15GR20.6	1152	61.36	24.11	0.2	5.22	7.97	1.62	100.49
15GR20.6	1153	59.22	25.95	0.18	7.41	6.95	0.96	100.67
15GR20.6.1	1154	59.82	25.71	0.18	6.45	7.51	0.98	100.65
15GR20.6.1	1155	60.94	25.53	0.17	6.27	7.55	0.98	101.42
15GR20.6.1	1156	60.68	24.43	0.2	5.07	7.96	1.23	99.55
15GR20.6.1	1157	61.66	24.8	0.2	5.22	7.91	1.19	100.99
15GR20.6.1	1158	62.53	24.19	0.14	5.19	8.03	1.4	101.48
15GR20.6.1	1159	60.98	24.14	0.39	4.91	7.61	1.29	99.32
15GR20.6.2	1161	57.84	27.4	0.12	8.41	6.68	0.62	101.07
15GR20.6.2	1162	58.75	26.41	0.18	7.51	6.98	0.75	100.58
15GR20.6.2	1163	57.91	27.22	0.2	8.38	6.53	0.66	100.91
15GR20.7	1164	61.22	25.04	0.2	5.77	7.73	1.44	101.4
15GR20.7	1165	60.29	24.98	0.15	6.12	7.37	1.1	100.01
15GR20.7	1166	61.16	24.79	0.21	5.39	7.74	1.46	100.75
15GR20.7	1167	61.93	24.37	0.17	5.16	7.83	1.68	101.13
15GR20.7	1168	61.17	24.03	0.21	5.1	7.89	1.75	100.15
15GR20.7	1169	59.66	25.28	0.13	6.31	7.47	1.21	100.06
15GR20.7	1170	59.04	26.71	0.15	7.35	7.02	0.83	101.11
15GR20.7.1	1171	61.64	24.29	0.31	5.36	7.67	1.47	100.73
15GR20.7.1	1172	61.19	24.62	0.16	5.38	7.86	1.47	100.68
15GR20.7.1	1173	59.74	25.8	0.19	6.72	7.34	1.06	100.86
15GR20.7.1	1175	60.51	25.31	0.14	6.3	7.48	1.15	100.88
15GR20.7.1	1176	60.34	25.03	0.16	5.94	7.54	1.21	100.22
15GR20.7.1	1177	62.17	24.01	0.21	4.82	7.98	1.71	100.91
15GR20.7.1	1178	61.01	24.73	0.23	5.19	7.8	1.69	100.65
15GR20.7.1	1180	61.51	24.42	0.18	5.19	7.87	1.7	100.86
15GR20.7.1	1181	60.27	25.11	0.2	6.02	7.37	1.35	100.33
15GR20.7.1	1182	60.65	24.75	0.19	5.12	7.9	1.61	100.23
15GR20.7.1	1183	60.63	25.12	0.17	6.19	7.63	1.34	101.08
15GR20.7.1	1184	59.01	25.87	0.17	6.89	7.1	1.04	100.09
15GR20.7.1	1185	61.55	24.67	0.19	5.47	7.65	1.55	101.08
15GR20.8.1	1186	61.71	24	0.17	4.98	7.82	1.94	100.61
15GR20.8.1	1187	62.41	22.75	0.25	3.74	7.18	3.51	99.83
15GR20.8.1	1188	61.09	24.32	0.16	4.68	7.84	1.87	99.95
15GR20.8.1	1190	61.96	23.83	0.18	4.79	7.56	2.06	100.39
15GR20.8.1	1191	61.7	24.37	0.23	4.82	7.71	1.92	100.74
15GR20.8.1	1192	62.12	23.98	0.17	4.81	7.67	1.91	100.67
15GR20.8.2	1193	61.26	25.36	0.15	5.87	7.56	1.31	101.52
15GR20.8.2	1194	59.84	25.12	0.18	5.84	7.62	1.2	99.8
15GR20.8.2	1195	61.83	24.35	0.2	4.93	7.89	1.41	100.61
15GR20.8.2	1196	61.46	24.22	0.27	5.27	7.86	1.53	100.62
15GR20.8.2	1197	61.52	24.5	0.19	5.35	7.79	1.54	100.91
15GR20.8.3	1198	59.88	24.61	0.19	5.56	7.56	1.65	99.45

15GR20.8.3	1199	61.25	24.89	0.19	5.67	7.59	1.54	101.14
15GR20.8.3	1200	61.25	24.91	0.17	5.52	7.54	1.76	101.15
15GR20.8.3	1203	60.95	24.95	0.18	5.78	7.54	1.59	100.98
15GR20.8.4	1204	61.61	24.97	0.17	5.39	7.58	1.8	101.52
15GR20.8.4	1206	59.93	24.59	0.17	5.82	7.43	1.71	99.65
15GR20.8.4	1207	61.33	25.17	0.13	5.66	7.53	1.66	101.48
15GR20.8.4	1208	61.99	23.1	0.78	4.46	7.31	3.02	100.66
15GR20.8.4	1209	61.3	24.24	0.15	4.8	7.67	1.91	100.07
15GR20.8.4	1210	61.64	24.5	0.18	5.13	7.67	1.67	100.79
15GR20.8.4	1211	61.03	25.21	0.19	5.97	7.45	1.42	101.27
15GR20.10	1212	59.86	25.24	0.21	6.04	7.74	1.01	100.1
15GR20.10	1213	59.75	25.97	0.21	6.65	7.49	0.89	100.96
15GR20.10	1214	59.99	25.69	0.18	6.71	7.33	0.88	100.78
15GR20.10	1215	59.83	26.05	0.19	7.02	7.23	1	101.33
15GR20.10	1216	60.33	25.39	0.24	6.32	7.47	1.23	100.98
15GR20.11	1217	60.48	25.04	0.2	5.81	7.55	1.34	100.41
15GR20.11	1218	57.06	27.42	0.21	8.2	6.57	0.6	100.07
15GR20.11	1219	59.4	25.1	0.16	6.14	7.64	0.95	99.4
15GR20.11	1220	58.16	27.03	0.17	8.44	6.29	0.68	100.77
15GR20.11	1221	60.53	24.14	0.14	5.94	7.77	1.15	99.68
15GR20.11	1222	60.31	24.96	0.18	5.58	7.67	1.59	100.29
15GR20.13	1223	64.19	21.38	0.54	2.3	7.26	4.86	100.53
15GR20.13	1224	57.49	27.06	0.19	8.35	6.6	0.7	100.39
15GR20.13	1225	57.18	26.59	0.2	7.81	6.81	0.72	99.32
15GR20.13	1226	59.91	24.81	0.17	6.21	7.68	1.11	99.89
15GR20.13	1227	59.9	24.94	0.23	6.16	7.54	1.33	100.1
15GR20.13	1228	56.89	26.65	0.12	8.12	6.69	0.66	99.14
15GR20.13.1	1229	56.32	27.05	0.18	8.34	6.48	0.6	98.98
15GR20.13.1	1230	57.7	27.33	0.22	7.95	6.81	0.74	100.75
15GR20.13.1	1231	59.71	24.97	0.19	5.95	7.64	1.23	99.68
15GR20.13.1	1232	59.81	24.61	0.14	5.98	7.72	0.96	99.23
15GR20.13.1	1233	61.22	23.06	0.38	4.17	7.16	3.18	99.17
15GR20.13.1	1234	56.93	27.14	0.15	8.02	6.49	0.74	99.46
15GR20.14.1	1235	58.01	27.32	0.14	8.05	6.54	0.8	100.85
15GR20.14.1	1236	60.5	24.23	0.23	5.61	7.9	1.43	99.9
15GR20.14.1	1238	58.13	27.09	0.2	7.86	6.86	0.7	100.84
15GR20.14.1	1239	57.72	26.38	0.22	7.49	6.87	0.74	99.43
15GR20.14.1	1240	57.83	26.67	0.13	7.85	6.78	0.65	99.92
15GR20.14.1	1241	59.75	25.24	0.18	6.19	7.6	1	99.96
15GR20.14.1	1242	59.96	25.33	0.17	5.75	7.88	1.22	100.31
15GR20.14.1	1243	59.72	24.73	0.18	5.94	7.7	1.26	99.53
15GR20.14.1	1244	61.22	23.73	0.15	4.92	7.87	1.66	99.56
15GR20.14.1	1245	58.6	26.63	0.2	7.39	6.89	0.81	100.52
15GR20.14.1	1246	58.3	25.95	0.19	7.18	7.1	0.82	99.55
15GR20.14.1	1247	56.62	27.4	0.22	8.45	6.39	0.68	99.76
15GR20.14.1	1248	56.66	27.58	0.23	8.47	6.52	0.62	100.08
15GR20.14.1	1249	58.04	26.85	0.16	8.03	6.76	0.68	100.53

15GR20.14.1	1250	58	26.84	0.17	7.49	7.04	0.81	100.35
15GR20.14.1	1251	59.46	25.68	0.21	6.6	7.43	0.98	100.37
15GR20.14.1	1252	58.97	25.77	0.16	6.66	7.25	1.01	99.82
15GR20.14	1255	58.18	25.65	0.17	7.26	7.04	0.9	99.18
15GR20.15.1	1256	59.2	25.58	0.17	6.18	7.34	1.16	99.63
15GR20.15.1	1257	60.57	24.87	0.2	6.19	7.29	1.29	100.4
15GR20.15.1	1258	60.02	25.33	0.2	6.14	7.41	1.37	100.47
15GR20.15.1	1260	60.07	23.1	0.82	6.47	6.59	2.18	99.24
15GR20.15.1	1261	60.93	24.58	0.17	5.65	7.7	1.61	100.64
15GR20.15	1262	60.18	25.6	0.17	6.2	7.39	1.51	101.06
15GR20.15	1263	58.72	25.65	0.22	6.71	7.37	0.82	99.49
15GR20.15	1264	59.65	25.54	0.13	6.88	7.41	0.72	100.34
15GR20.15	1265	59.52	25.53	0.15	6.99	7.37	0.8	100.36
15GR20.16	1267	57.89	26.7	0.15	7.81	6.89	0.73	100.16
15GR20.16	1268	57.95	27.07	0.14	8.08	6.64	0.73	100.62
15GR20.16	1269	56.75	27.32	0.19	8.52	6.56	0.67	100
15GR20.16	1270	57.64	27.07	0.18	8.23	6.58	0.77	100.47
15GR20.16	1271	56.61	26.89	0.22	8.28	6.58	0.72	99.3
15GR20.16	1272	59.06	26.07	0.12	6.95	7.35	0.91	100.46
15GR20.17	1273	56.72	26.71	0.19	8.1	6.53	0.65	98.91
15GR20.17	1275	56.83	26.88	0.34	8.4	6.71	0.62	99.78
15GR20.17	1276	56.06	27.74	0.39	9.12	6.14	0.51	99.96
15GR20.17	1277	56.51	27.08	0.37	8.55	6.44	0.54	99.48
15GR14.2.T	731	61.42	24.09	0.26	4.63	8.29	1.57	100.26
15GR14.2.T	733	60.20	23.88	0.15	5.08	8.05	1.24	98.60
15GR14.2.T	734	60.54	25.21	0.16	5.87	7.73	1.27	100.78
15GR14.2.T	736	61.58	23.88	0.18	4.82	8.07	1.51	100.03
15GR14.2.T	737	61.25	23.70	0.18	4.45	7.90	1.70	99.19
15GR14.2.T	738	60.92	24.50	0.16	5.09	8.10	1.43	100.19
15GR14.2.T	740	60.42	23.83	0.32	4.69	8.14	1.68	99.08
15GR14.2.T	741	61.03	23.74	0.21	4.46	8.07	1.75	99.26
15GR14.2.T	743	62.33	23.30	0.26	4.02	8.05	2.13	100.08
15GR14.2.T	744	60.09	24.27	0.15	5.09	7.96	1.33	98.89
15GR14.2.T	745	60.52	24.30	0.20	5.20	7.89	1.30	99.42
15GR14.2.T	747	60.84	24.51	0.14	5.43	8.04	1.26	100.22
15GR14.2.T2	748	60.51	24.23	0.24	5.72	7.79	1.32	99.81
15GR14.2.T2	749	61.05	23.70	0.16	4.45	7.76	1.67	98.79
15GR14.2.T2	750	62.45	21.79	0.46	3.28	7.81	3.08	98.87
15GR14.2.T2	752	61.96	24.26	0.18	5.12	7.79	1.47	100.79
15GR14.2.T2	753	60.38	24.90	0.19	5.58	7.63	1.30	99.98
15GR14.2.T2	754	62.63	25.63	0.35	5.64	5.88	1.31	101.44
15GR14.2.T2	755	60.28	24.86	0.23	5.48	7.88	1.24	99.98
15GR14.2.T2	757	61.77	23.93	0.18	4.81	8.06	1.56	100.31
15GR14.2.T2	758	60.14	23.79	0.18	5.19	7.74	1.47	98.51
15GR14.2.T2	759	60.67	24.30	0.19	5.19	7.85	1.32	99.52
15GR14.2.T2	760	62.33	23.54	0.24	4.20	8.00	1.74	100.05
15GR14.2.T2	761	61.34	24.32	1.47	5.26	7.31	1.40	101.09

15GR14.2.T2	762	62.42	24.70	0.38	5.05	6.35	1.58	100.47
15GR14.3.T	765	60.67	24.68	0.19	5.25	7.59	1.28	99.66
15GR14.3.T	766	61.18	24.72	0.20	4.96	7.97	1.44	100.47
15GR14.3.T	767	60.55	24.31	0.20	5.02	7.81	1.36	99.26
15GR14.3.T	768	61.18	24.43	0.15	5.11	8.08	1.39	100.35
15GR14.3.T	769	60.92	24.32	0.19	5.49	7.93	1.23	100.08
15GR14.3.T	771	60.27	24.99	0.18	5.58	7.97	1.03	100.02
15GR14.3.T	772	60.91	25.48	0.22	5.86	7.89	0.94	101.30
15GR14.3.T	773	60.98	24.27	0.15	5.14	8.20	1.18	99.91
15GR14.3.T	774	61.63	23.45	0.20	4.82	8.33	1.46	99.89
15GR14.3.T	775	59.61	24.99	0.14	5.61	7.57	1.34	99.26
15GR14.3.T	776	60.56	24.53	0.18	5.17	7.95	1.38	99.77
15GR14.3.T	777	60.12	24.52	0.15	5.38	8.05	1.31	99.53
15GR14.3.T	780	61.27	24.01	0.21	4.93	8.28	1.40	100.10
15GR14.4	781	61.11	24.70	0.26	5.33	7.97	1.38	100.75
15GR14.4	782	60.51	24.78	0.13	5.66	7.85	1.29	100.23
15GR14.4	783	65.26	20.67	0.60	1.18	7.76	5.37	100.84
15GR14.4	784	61.89	23.85	0.18	4.63	8.07	1.64	100.26
15GR14.4	785	60.40	24.66	0.24	5.11	8.11	1.36	99.89
15GR14.5	786	60.55	24.64	0.23	5.28	7.85	1.33	99.90
15GR14.5	787	60.69	24.75	0.22	4.93	7.84	1.51	99.95
15GR14.5	788	60.79	24.14	0.13	5.51	7.97	1.21	99.75
15GR14.5	789	61.18	24.42	0.14	5.25	7.81	1.43	100.23
15GR14.5	790	60.84	25.00	0.12	5.63	7.81	1.18	100.58
15GR14.6T	791	60.43	24.14	0.11	5.37	8.13	1.31	99.48
15GR14.6T	792	60.23	24.29	0.20	5.26	8.02	1.55	99.55
15GR14.6T	793	61.74	23.21	0.12	4.22	8.08	1.69	99.06
15GR14.6T	794	61.49	23.98	0.21	4.79	8.08	1.57	100.11
15GR14.6T	795	60.89	24.14	0.15	5.22	8.10	1.34	99.84
15GR14.6T	796	60.55	24.60	0.18	5.51	7.93	1.26	100.02
15GR14.6T	797	60.23	23.99	0.16	5.28	7.82	1.14	98.62
15GR14.6T	798	62.39	21.97	0.31	3.01	8.38	2.92	98.98
15GR14.6T	799	59.76	24.31	0.23	5.47	7.80	1.21	98.79
15GR14.6T	800	60.95	24.46	0.17	5.32	7.78	1.39	100.08
15GR14.6T	801	61.99	23.49	0.23	4.22	8.27	1.85	100.05
15GR14.6T	802	61.51	24.53	0.17	5.27	7.95	1.30	100.73
15GR14.6T	803	61.17	23.99	0.16	4.99	8.06	1.57	99.93
15GR14.6T	804	61.87	23.73	0.21	4.52	8.22	1.59	100.15
15GR14.6T	805	59.56	23.63	0.22	4.57	7.77	1.55	97.29
15GR14.6T	807	60.61	24.25	0.13	5.21	7.98	1.34	99.52
15GR14.6T	808	59.88	24.32	0.20	5.42	7.84	1.22	98.88
15GR14.6T	809	61.57	24.03	0.19	5.15	8.13	1.23	100.29
15GR14.6T	810	60.48	24.29	0.19	5.18	8.06	1.48	99.68
15GR14.6T	811	60.51	24.43	0.18	5.33	7.93	1.25	99.63
15GR14.6T	812	12.19	3.47	1.14	0.54	0.93	0.37	18.64
15GR14.6T	813	58.50	21.15	0.42	3.23	7.43	2.38	93.11

15GR14.6T	814	61.25	24.47	0.18	5.31	7.85	1.36	100.43
15GR14.6T	816	60.77	24.37	0.20	5.45	7.85	1.32	99.95
15GR14.7	817	60.00	24.41	0.10	5.58	7.80	1.14	99.04
15GR14.7	818	60.36	24.51	0.21	5.33	8.01	1.10	99.51
15GR14.7	819	60.41	24.63	0.18	5.67	7.90	1.18	99.98
15GR14.7	820	64.04	21.32	0.49	2.16	8.23	3.43	99.67
15GR14.7	821	59.36	24.51	0.15	5.44	7.94	1.28	98.68
15GR14.7	822	59.96	24.28	0.17	5.40	8.04	1.29	99.14
15GR14.7	823	60.43	24.64	0.17	5.33	7.80	1.32	99.69
15GR14.7	824	61.38	24.06	0.14	4.77	8.27	1.35	99.97
15GR14.8.T	825	60.84	24.21	0.19	5.22	8.20	1.14	99.81
15GR14.8.T	826	60.80	24.58	0.16	5.41	8.12	1.05	100.12
15GR14.8.T	827	61.06	24.52	0.17	5.45	8.07	1.05	100.32
15GR14.8.T	828	60.47	24.73	0.26	5.66	7.89	1.07	100.08
15GR14.8.T	829	61.05	24.97	0.18	5.39	8.12	1.03	100.73
15GR14.8.T	830	60.49	24.88	0.21	5.76	8.05	0.99	100.39
15GR14.8.T	831	60.77	24.30	0.17	5.15	7.95	1.22	99.56
15GR14.8.T	832	61.42	23.87	0.22	4.66	8.37	1.40	99.94
15GR14.8.T	834	61.29	23.52	0.34	4.51	8.04	1.71	99.40
15GR14.8.T	835	61.01	23.75	0.24	4.67	8.09	1.43	99.19
15GR14.8.T	836	61.44	21.35	1.86	2.51	7.72	3.26	98.14
15GR14.8.T	837	61.62	23.92	0.18	4.58	8.04	1.61	99.96
15GR14.8.T	838	60.86	23.73	0.19	4.51	8.18	1.60	99.07

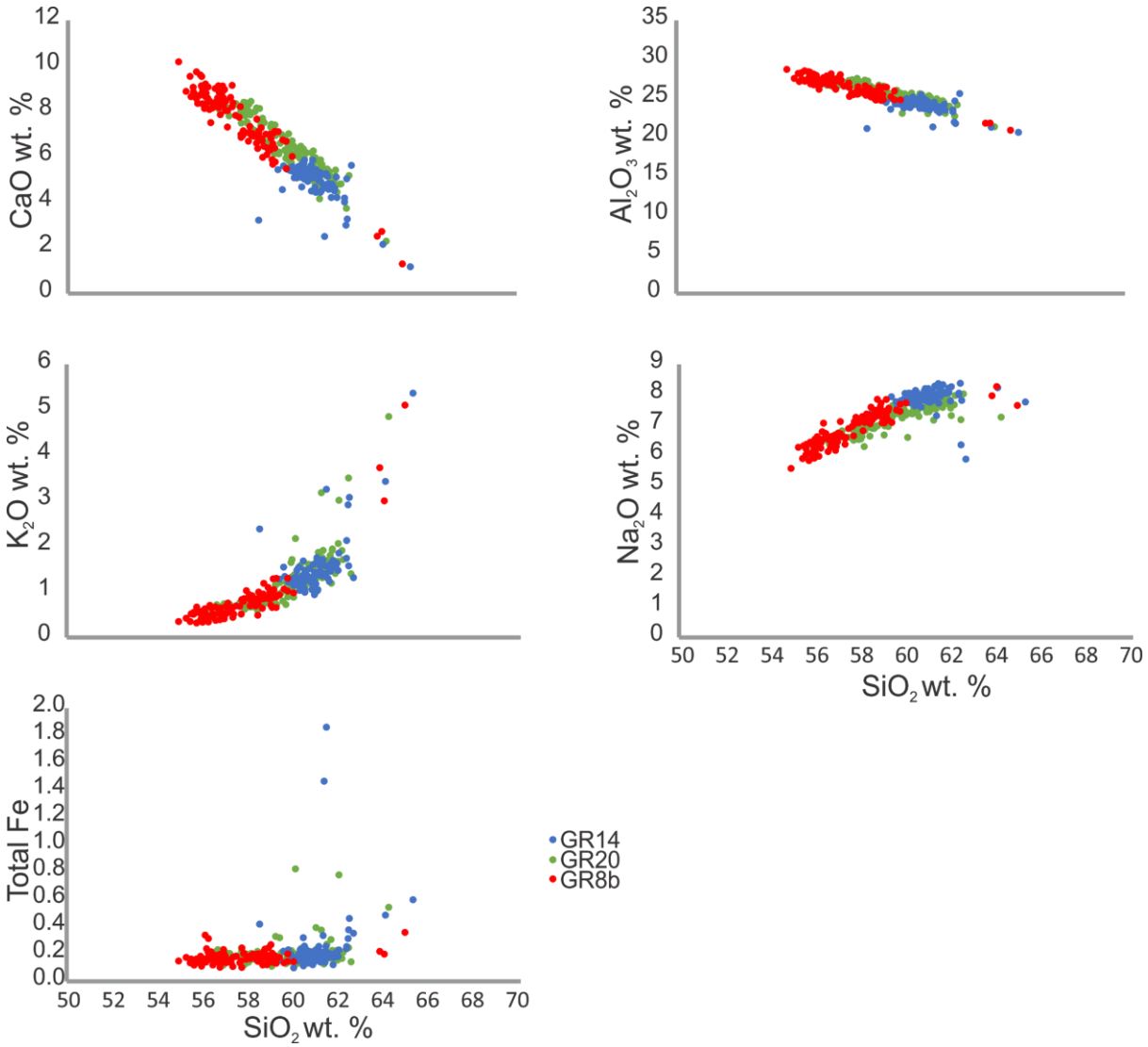

Figure 4. Variation diagrams of silica vs. major oxides for plagioclase in each lithic. Note that high FeO and K_2O points are potentially analyses where interstitial material was analyzed rather than plagioclase.

Color-CL

The CL detector collects photons of certain wavelengths from a mineral. The wavelengths depend on properties of the mineral. Luminescence under electron bombardment can be intrinsic, which depends on characteristics of the lattice structure, or extrinsic (Götze and Kempe, 2009). Extrinsic luminescence results in elements that are quenchers or activators. Certain elements, like titanium and iron are activators and cause minerals to luminesce under the CL detector, while other elements are quenchers and do not luminesce (Götze and Kempe, 2009)

Table 5. Color-CL settings. Data collected on a Tescan VEGA3 LMU SEM with Oxford Instruments at Bowdoin College.

Color CL Settings	**GR 8b**	**GR 20**	**GR 14**
Beam Intensity	18	16	16
Dwell Time	100 µs/pixel	100 µs/pixel	100 µs/pixel
HV	18 kV	18 kV	18 kV
Spot Size	603.361	402.123	490.910
Working Distance	16 mm	16 mm	16 mm

Black Balancing

Find non-luminescing mineral (pyroxene, biotite, etc.) with quenching elements

Using the histogram on this one mineral (zoom in and make a small box), stack the red, green, and blue channels on top of each other by adjusting each brightness

Bring down gamma so that the stacked channels are almost out of the histogram view or so that the mineral truly looks black

Zoom back out and look at the histogram for the entire screen. Bring down max value until it is just cutting off the tail end of the spectra (the spectra won't look stacked anymore because you are looking at minerals that should not appear black). The min value can be adjusted similarly on the lower tail end of the spectra.

Adjust contrast to lighten up the image

If the minerals look too dull, you can go back to the black mineral and brighten up each color individual as long as they remain stacked

Key to this study is the analysis of whole thin sections using colour-CL. Traditional use of CL optimizes acquisition conditions for variations within a single crystal and does not allow for comparison of different grains. Black balancing is a technique that produces data that is more consistent and reproducible across grains and thin sections (DeWet et al., 2016). Black balancing is done by adjusting the brightness, contrast, and gamma on the colour-CL histogram. First, individual red, green, and blue channel peaks are stacked on the histogram by adjusting the brightness of each channel. It is important to do this while only a non-luminescing mineral such as pyroxene is selected with a small box. Once all three channels are stacked, gamma is reduced so that the stacked peaks are very low or the mineral looks truly black. To adjust the lighter end of the spectrum, zoom out of the small box to an area that includes a luminescing mineral and adjust the maximum value of the histogram until the tail of the spectra is just cut off. Contrast may then be adjusted as needed. Black balancing is essential for comparison across thin sections because it optimizes the image for all grains. In this way, luminescence differences between grains are real and can be compared.

EBSD

Table 6. EBSD settings. Data collected on a Zeiss SEM with Oxford Instruments at the University of Otago (GR8b) and a Tescan VEGA3 LMU SEM at Bowdoin College (GR20 and GR14).

EBSD Settings	**GR 8b**	**GR 8b Fine**	**GR 20**	**GR 14**	**GR 14 Fine**
Resolution (Width):	394 pixels	2458 pixels	1134 pixels	721 pixels	757 pixels
Resolution (Height):	296 pixels	1500 pixels	568 pixels	784 pixels	3128 pixels
Step Size:	50µm	5.15µm	40µm	25µm	5.15µm
Field Width:	19.7mm	12.7mm	45.4mm	18mm	3.9mm
Field Height:	14.8mm	7.72mm	22.7mm	19.6mm	16.1mm
Number of Points:	116624	3687000	644112	565264	2367896
Hit Rate:	64.10%	70.60%	56.8%	45.2%	60.39%
Accelerating Voltage:	30.00 kV	30.00 kV	20.00 kV	20.00 kV	20.00 kV
Working Distance:	21.7 mm	19.9 mm	27.0mm	28.3 mm	27.0 mm
Detector Insertion Distance:	207.0 mm	207.0 mm	130mm	130 mm	132 mm
EBSD Camera Binning:	2x2	2x2	4x4	4x4	4x4
EBSD Camera Gain:	15	15	8	8	7
Frame Averaging:	2 frames	2 frames	2 frames	2 frames	2 frames
Hough Resolution:	50	50	60	90	90
Band Detection Mode:	Edges	Edges	Edges	Edges	Edges
Number of Bands Detected:	10	10	8	8	9
Indexing Mode:	Optimized - EBSD	Optimized - EBSD	Optimized -EBSD	Optimized-EBSD	Optimized-EBSD

Table 7. EDS settings. Data collected on a JOEL JSM IT-300 at the University of Canterbury, and Tescan Vega3 LMU at Vanderbilt University and Bowdoin College.

EDS Settings	**GR 8b Interstitial Melt**	**GR 20 Interstitial Melt**	**GR 14 Interstitial Melt**
Resolution (Width):	1024 pixels	1024 pixels	1024 pixels
Resolution (Height):	768 pixels	768 pixels	768 pixels
Field Width:	1.03mm	85.5µm – 642µm	1.03 - 1.51mm
Field Height:	775µm	64.2µm - 481µm	775µm - 1.14mm
Accelerating Voltage:	20.00 kV	20.00 kV	20.00 kV
Working Distance:	15.0mm	11.0mm	14.2 - 15.5mm
Number Completed Frames:	1200	2-867	800 - 1200
Energy Range:	10keV	10 - 20keV	10keV
Number of Channels:	1024	1024	1024
Process Time:	4	2-4	4
Live Time:	9437s	157s - 9437s	6291s – 9437s
Total Counts:	165960523 - 238500939	13908052 - 782210384	128985924 - 202679682

Internal Deformation

Distortion of individual crystals was observed petrographically (visually bent grains, segmented extinction, tapering twins) and further analyzed by calculating the misorientation along a transect of the crystal lattice relative to a starting point (Supplementary Information). Misorientation of the apparent long and short axes were calculated. Each lithic has plagioclase with internal deformation ranging from 2° to >8° misorientation, occasionally along both the crystal's long and short axes. This suggests lithic-wide bending and twisting (rather than local breaking from grain impingement), confirming many of the textural indicators of grain boundary sliding via dislocation creep seen under the microscope. While possible that an oblique cut through a crystal could give the illusion of deformation, the abundance of distorted crystals along the sample scale CPO, the above petrographic observations, and strength of CPOs suggests that the crystal population was modified during compaction and melt extraction (Fiedrich et al., 2017).

Interstitial Material

Table 8. Interstitial material EDS data

Spectrum Label	SiO_2	TiO_2	Al_2O_3	Total Fe	MnO	MgO	CaO	Na_2O	K_2O	P_2O_5	Total
GR8 Site 1											
Spectrum 8	58.08	1.21	21.88	3.78			4.93	7.01	2.01	1.1	100
Spectrum 9	57.79	2.07	21.5	4.83		0.24	3.7	7.02	2.41	0.43	100
Spectrum 10	55.82	1.85	21.08	8.48			3.72	6.74	2.32		100
Spectrum 11	59.09	0.53	19.83	4.86		1.3	5.11	6.14	2.29	0.86	100
Spectrum 12	62.35		20.98	2.37			3.69	7.35	3.26		100
Spectrum 13	60.74	0.56	21.03	3.41			3.29	6.56	3.72	0.68	100
GR8 Site 2											
Spectrum 1	60.51	0.24	23.89	0.74			5.14	7.86	1.62		100
Spectrum 2	58.27	0.23	23.34	0.83			4.69	7.72	1.93		100
Spectrum 3	59.87		24.06	1.43			5.18	7.78	1.68		100
Spectrum 4	60.68		23.76	1.01			4.83	7.83	1.89		100
Spectrum 5	60.42		24.14	0.82			5.61	7.71	1.31		100
Spectrum 6	60.38	0.33	23.71	1.05			4.85	7.57	2.1		100
Spectrum 7	57.32	0.27	23.8	0.66			5.32	7.65	1.5		100
Spectrum 8	59.56	0.56	24.2	0.93			5.5	7.69	1.58		100
Spectrum 9	58.22	0.72	23.82	2.48	0.36		5.09	7.2	2.12		100
Spectrum 10	56.04	1.08	23.16	3.92			4.77	7.3	1.93		100
GR20 Site 10											
Spectrum 37	65.35		34.65								100
Spectrum 38	64.89		35.11								100
Spectrum 40	57.73		25.46	5.97		1.76	5.28	3.03	0.76		100
Spectrum 41	57.64		26.16	5.23		1.55	5.06	3.73	0.62		100
Spectrum 42	58.12		25.95	4.24		1.48	5.71	3.5	1		100
Spectrum 43	57.4		25.8	2.03		0.52	8.1	5.38	0.77		100
Spectrum 44	57.58		25.89	4.1		1.19	6.2	4.05	0.98		100
Spectrum 45	57.12		25.65	1.84		0.63	8.58	4.13	0.91		100

Spectrum 46	58.03		24.64	2.42	0.6	7.34	4.65	0.9	100
Spectrum 47	57.11		26.18	2.08	0.72	8.84	4.03	1.05	100
Spectrum 48	58.23		26.12	1.73	0.51	7.2	5.48	0.72	100
GR20 Site 6									
Spectrum 46	61.54	0.25	22.53	1.14		3.9	7.22	3	99.92
Spectrum 47	62.86		22.21	0.37		3.6	6.49	4.4	100
Spectrum 48	62.88		22.35	0.47		3.69	6.68	3.93	100
Spectrum 49	60.48	0.65	22.62	2.35		3.86	7.32	2.72	100
Spectrum 50	62.09		22.06	1.29		3	5.75	5.82	100
Spectrum 51	63.81		21.3	0.65		2.5	5.87	5.88	100
Spectrum 52	62.62		22.64	0.53		3.74	6.68	3.79	100
Spectrum 53	61.46	0.47	21.7	2.44		3.31	7.08	3.53	100
Spectrum 54	61.67		23.18	0.63		4.48	6.9	3.14	100
Spectrum 59	57.23	0.48	22.85	4.87	0.84	6.53	5.56	1.11	99.47
Spectrum 60	58.52		23.68	4.22	0.94	6.45	4.75	0.94	99.5
Spectrum 61	57.57		23.74	5.57	1.01	5.98	4.74	0.8	99.41
Spectrum 62	59.39		22.52	4.42	1.03	5.04	4.99	1.09	99.45
Spectrum 63	58.69		24.97	2.24	0.75	6.58	5.4	0.97	99.61
Spectrum 64	58.27		24.01	4.35	0.92	5.67	5.41	0.82	99.45
Spectrum 65	59.95		23.14	3.34	0.86	5.24	6.02	1.11	99.65
GR20 Site 7									
Spectrum 70	55.36	2.14	19.25	9.8		2.5	6.06	4.9	100
Spectrum 71	63.73		21.94	0.66		3.03	7.11	3.54	100
Spectrum 72	63.5		22.61			3.53	6.95	3.41	100
Spectrum 73	58.64	1.18	20.75	5.92		2.87	6.08	4.56	100
Spectrum 74	31.45	7.24	13.9	39.49	1.54	2.17	3.09	0.62	99.5
Spectrum 75	49.88	3.3	17.45	16.3		2.44	5.86	4.77	100
GR14 Site 1									
Spectrum 2	63.18		21.4	1.03		2.58	8.53	3.28	100
Spectrum 3	61.59		21.13	2.49		2.45	8.51	3.1	100
Spectrum 4	61.98	0.5	20.91	2.57		2.43	8.58	3.02	100
Spectrum 5	64.31		22.03			2.67	8.06	2.94	100
Spectrum 15	63.42		21.86			2.79	8.76	3.17	100
Spectrum 32	64.29		21.11			2.62	8.3	3.67	100
Spectrum 33	78.18		21.82						100
Spectrum 34	61.89		21.94	2.07		3.38	7.55	3.17	100
Spectrum 35	62.22		22.62	0.83		3.8	8.08	2.45	100
GR14 Site 2									
Spectrum 7	59.5	0.48	22.55	1.23	0.25	3.93	8.29	2.13	100
Spectrum 9	58.74	0.25	25.7	0.45	0.1	6.64	7.35	0.77	100
GR14 Site 3									
Spectrum 18	63.3		21.86			2.86	8.12	3.87	100
Spectrum 19	61.81		23.66			3.75	8.32	2.46	100
Spectrum 20	63.5		21.76			3.25	8.51	2.98	100
Spectrum 21	62.24		20.86	2.22		2.49	8.36	3.84	100
Spectrum 22	64.39		21.2			3.46	7.38	3.57	100
Spectrum 43	63.08		21.55	0.87		3.04	7.64	3.82	100

Spectrum 44	62.21		22.12	0.88	0.55	3.1	7.84	3.29		100
Spectrum 45	60.9		22.41	0.54		3.76	7.77	2.94		100
Spectrum 46	62.53		21.76	1.33		2.8	7.44	4.14		100
Spectrum 47	60.28	0.25	21.45	0.82		3.66	7.53	3.62	0.71	100

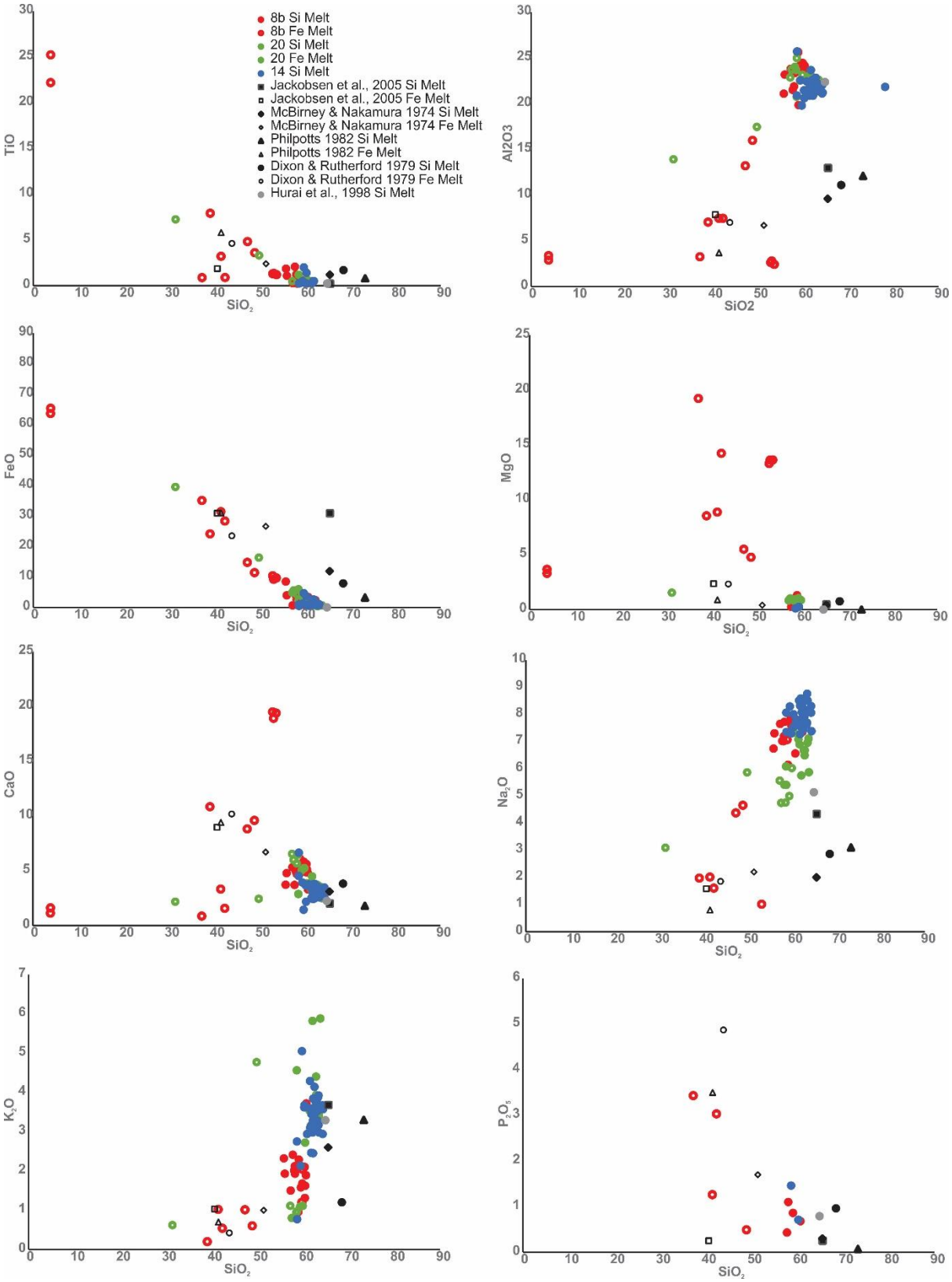

Figure 5. Major element vs. silica variation diagrams for Goat Rock plutonic lithic interstitial material (colored, closed circles) and mafic enriched domains (colored, open circles) compared to Si-rich and Fe-rich immiscible melt end members (from Humphreys, 2011 black shapes and Hurai et al., 1998 grey circle).

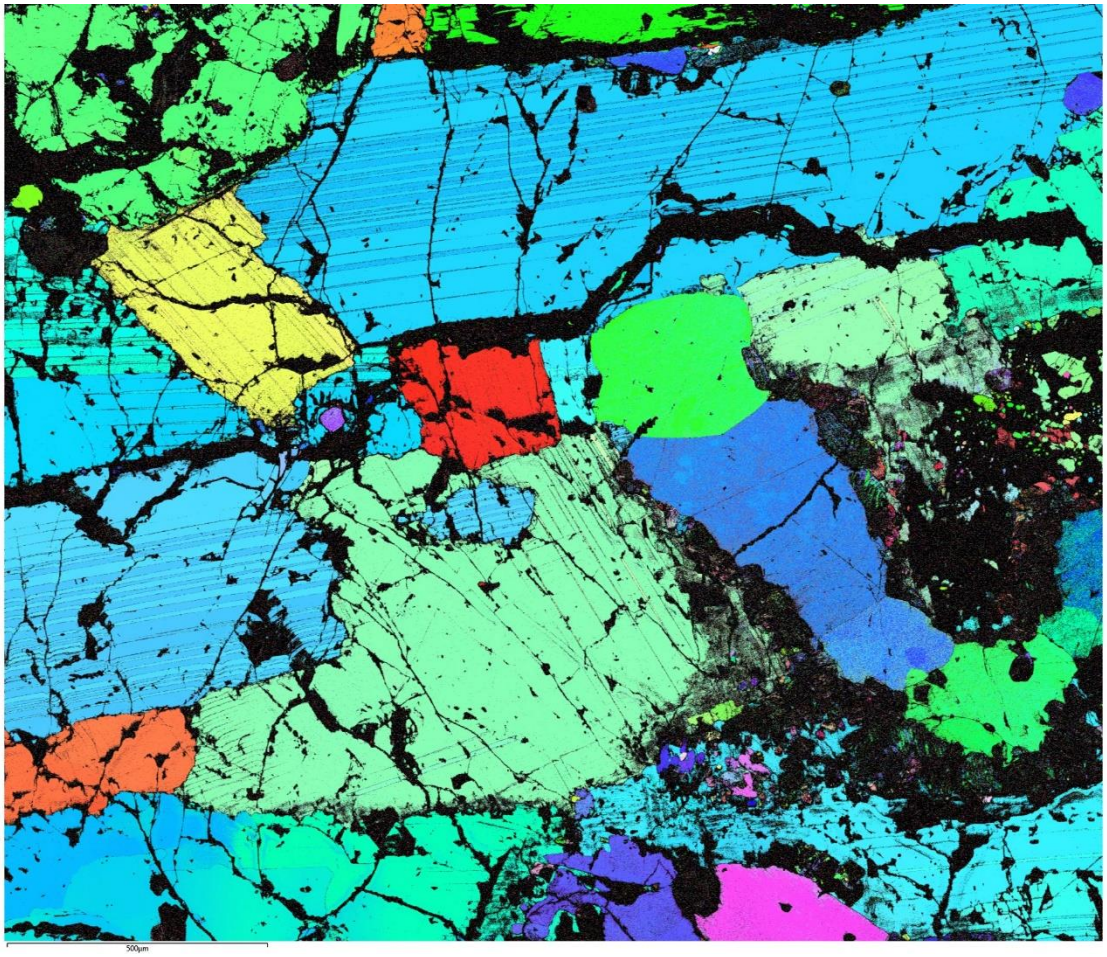

Figure 6. IPF Y EBSD map for GR8b of a mafic enriched domain area (bottom right) surrounding a mafic crystal (blue and green hook, bottom right). Note the areas of black in the area which reflect areas of no indexing. This material is glass with small crystals.

ImageJ Analysis Methods

RGB images were thresholded and manually edited to remove any non-interstitial material. A binary image was created and interstitial material area calculated as a percent of total area. Individual frames for each lithic were processed then averaged (Table 3). While these analyses were conducted from two dimensional images, they offer a robust first order proxy for volume melt fraction just prior to solidification (Chayes, 1957). A limitation of such a method is the small number of individual frames from which interpretations are made. Four frames for each sample were chosen for being representative of interstitial material distribution patterns observed throughout the whole sample. This was most challenging for GR20 which had heterogenous interstitial material distribution. However, the material was found in relative abundance in some parts of the sample and not at all in others, therefore frames that had any interstitial material and those that had none were both used.

References

Chayes, F. (1957). A Provisional Reclassification of Granite. *Geological Magazine*, 94(1), 58-68. doi:10.1017/S001675680006831X

Chapter 5 Appendix

Table 1. Lithic-bearing location and the type of data that exists for each sample, including the study in which it was collected.

Location	Sample	Study	Elevation (m)	Host	Whole Rock Majors	Whole Rock Trace	EBSD	CL Map	Bright CL EDS	Plag Chemistry
Goat Rock	GR10	Bertolett et al., 2019	395	lava dome	x	x	x			
	GR11				x	x	x			
	GR8B						x	x	x	x
	15GR04	Paper 2			x	x	x	x		
	15GR20				x	x	x	x	x	x
	15GR14				x	x	x	x	x	x
	15GR22	this study			x	x	x	x		x
	15GR26				x	x	x	x		x
	15GR01				x	x				
	15GR23				x	x				
	15GR25				x	x				
	15GR17				x	x				
	15GR09				x	x				
	15GR27				x	x				
	GR9						x			
	GR7						x			
	GR17A	Paper 2			x	x				
	GR17B				x	x				
	GR18	this study			x	x				x
	GR19				x	x				
	15GR24H				x	x				
	15GR22H				x	x				
Paua Bay	12PBBP	this study	42	overthickened lava flow			x		x	
	19PBBP						x		x	
	22PBBP				x	x	x		x	x
	23PBBP				x	x				
	20PBBP				x	x	x		x	x
	PBBP24H				x	x				
E. Pigeon Bay	EPB3	this study	131	lava flow	x	x				
	EPB4						x	x	x	
	EPB7				x	x	x	x		
	EPB4H								x	
	EPB6H				x	x				
Flea Bay	FB17A	this study	75	lava flow?	x	x				
Haylocks Bay	HB-RT3	Doresy/Hartung, this study	1.8	lava flow	x	x	x	x	x	x
	HB-RT8				x	x	x	x		
	HBRT2	dorsey/hartung			x	x				x
	HB-RT4				x	x				x
	HB-Rt7				x	x				
	HB-RT5				x	x				
	HB-RT6				x	x				
	3631				x	x				
	3638				x	x				
	3635				x	x				
	3633				x	x				
	3632				x	x				
	3634				x	x				
	3637				x	x				
	3630				x	x				
	3636				x	x				
	13HBBP				x	x				
	14HBBP				x	x				
Pa Bay	PABP3.2	this study	7	scoria cone eruptives	x	x				
	PABP3.3				x	x				
LeBons Bay Peak	LPB1	this study	419	lava dome	x	x	x	x		
	xenolith A	sewell 1993	429		x					
	xenolith B				x					x
	xenolith C				x					x
	LPBH				x					

Data collection and analysis methods for samples part of other studies as indicated in Table 1 can be found in their respective contribution. For Haylocks Bay see Dorsey (1988) and Hartung (2011) and for LeBons Bay Peak see Sewell 1993. Sample preparation, analytical techniques, and SEM acquisitions settings for previously studied Goat Rock samples can be found in the

Appendices for Chapters 3 and 4 of this thesis (i.e. Bertolett et al., 2019 and Bertolett et al., in review). Paua Bay data was collected as part of a senior thesis by Elizabeth Teeter. The analytical methods for those samples are outlined below (modified from Teeter, 2017).

Paua Bay thin sections were polished with colloidal silica for3 hours and then carbon coated with a thickness of 10-11nm for all analyses. Full thin section color-CL and EBSD maps were collected on a TESCAN Vega 3 LMU SEM at Bowdoin College at 16 kV, 16 BI, 8 scan speed, and 16 WD+Z. Full thin section maps took 12-14 hours to complete. Measured EBSD patterns are indexed using known modeled patterns (Prior et al., 1999). Full thin section maps were created for four thin sections. However, while EBSD methods were essential to understanding the formation of Goat Rock lithics, plagioclase is not the fabric forming mineral in the Paua Bay lithics, so EBSD was used primarily to identify mineral percentages.

EDS data was collected on a JEOL JSM IT300LV Variable Pressure Scanning Electron Microscope at the University of Canterbury at 15 kV, and 100x magnification, with 100 pixel dwell time. EDS data was processed using Aztec to create Quant maps to obtain weight percentages and oxide percentages of each mineral.

Samples from previous theses were used to create thin sections for EBSD, CL, and EDS analysis for Haylocks Bay. Field work was undertaken to retrieve newly identified samples from Paua Bay, Eastern Pigeon Bay, and Flea Bay. Samples were also collected from LeBons Bay Peak for microstructural analysis and comparison to Sewell's (1993) analyses.

Whole rock major and trace element data for samples analyzed as part of this study were analyzed either by the University of Canterbury or CRI.

EBSD and color-CL maps for this study's samples were collected at Bowdoin College on a TESCAN Vega 3 LMU SEM. EDS maps and data were collected on on a JEOL JSM IT300LV Variable Pressure Scanning Electron Microscope at the University of Canterbury. Smithsonian standards were analyzed during data collection sessions. External standards are not important for EDS analysis as they only confirm acquisition settings and not the quality of the data. While standards were run, the internal Aztec standards were used for analysis.

Mineral chemistry data was collected as part of Dorsey and Hartung's theses (1988 and 2011) and as part of Bertolett et al. (in review).

Table 2. Average major and trace element composition for lithic and host samples for all locations. See Table 2 for source of data.

	Lithic Whole Rock							Host Whole Rock			
Sample	Goat Rock	Paua Bay	E. Pigeon Bay	Flea Bay	Haylocks Bay	Pa Bay	LeBons Bay	Goat Rock Host	E. Pigeon Host	Haylocks Host	LeBons Host
SiO2	48.09	43.20	46.47	46.59	42.80	50.01	48.92	49.60	47.62	46.39	41.91
TiO2	2.60	3.98	2.31	2.52	4.48	1.75	0.67	2.31	3.15	3.23	2.81
Al2O3	18.78	19.07	21.72	23.61	17.14	17.98	11.74	17.03	16.88	17.06	11.99
Total Fe	13.02	12.66	9.62	7.18	15.31	11.04	8.96	12.65	13.21	13.56	14.36
MnO	0.21	0.11	0.10	0.07	0.15	0.27	0.15	0.22	0.18	0.20	0.18
MgO	2.67	4.99	3.51	3.50	5.65	7.37	19.81	3.08	4.03	4.95	12.47
CaO	7.47	13.31	12.80	12.58	11.08	7.07	8.58	6.75	7.94	8.04	10.58
Na2O	5.07	2.15	2.84	3.60	2.59	3.56	1.63	5.22	4.60	4.38	3.03
K2O	0.94	0.33	0.38	0.28	0.47	0.84	0.47	1.90	1.56	1.42	1.13
P2O5	1.13	0.19	0.25	0.07	0.32	0.12	0.11	1.25	0.83	0.76	0.69
	0.04	0.35	0.47	0.28		3.26	0.32	-0.12	-0.08	-0.02	
Total	100.00	100.35	100.47	100.00		103.26	101.12	100.00	99.92	100.00	99.15
	Lithic Trace Elements							Host Trace Elements			
V	86.2	402.0	216	173.0	337.9	231	189	82.5	145.0	167.0	
Cr	3.5	27.5	<1	<3	83.9	450.5	970	<3	<1	17.4	
Ni	7.8	58.7	25	17.0	62.9	224	205	3.3	12.0	22.3	
Zn	84.7	73.7	60.5	38.0	109.5	81	83	123.8	118.0	114.4	
Ga	24.8	22.0	21.5	20.0	21.1	19	16	23.5	23.0	23.0	
Rb	12.0	8.3	7.5	<1	3.3	8	20	34.7	33.0	24.8	
Sr	1088.5	829.0	1145	1415.7	791.9	556.5	484	808.8	815.0	819.4	
Y	29.1	12.7	13	6.8	15.2	9	10	45.7	36.5	35.6	
Zr	109.8	85.0	80	58.0	81.4	35	57	298.0	301.0	275.2	
Nb	42.2	17.3	15	12.0	20.0	4.5	15	78.2	67.0	73.8	
Ba	458.1	103.0	194	130.0	101.7	266	390	602.8	401.0	410.6	
Pb	2.0	4.0	4.5	<1	3.6	5.5	2	3.0	5.0	1.6	
Th	3.3	1.5	2	<1	1.0	1	1	6.6	6.0	5.0	
La	27.6	10.0	18.5	<5	12.5	9.5	8	45.7	51.0	32.4	
Ce	71.4	12.0	26	13.0	17.1	23	10	99.8	94.0	74.2	
Nd	48.4			12.0	18.8			60.0		49.4	

Table 3. EBSD settings for Haylocks Bay, Eastern Pigeon Bay, and LeBons Bay Peak of this study. See Appendix of Chapter 4 for EBSD settings for Goat Rock samples.

EBSD Settings	**EPB 7**	**HBRT 03**	**LPB 1**
Resolution (Width):	1065 pixels	211-770 pixels	1024 pixels
Resolution (Height):	535 pixels	311-349 pixels	540 pixels
Step Size:	35 µm	35 µm	35 µm
Field Width:	37.3 mm	7.38-27 mm	35.8 mm
Field Height:	18.7 mm	10.9 – 12.2 mm	18.9 mm
Number of Points:	569775	65621 - 268730	552960
Hit Rate:	89.3%	72.2 – 75.5%	82.7%
Accelerating Voltage:	20.00 kV	20.00 kV	20.00 kV
Working Distance:	27 mm	27 mm	27 mm
Detector Insertion Distance:	135 mm	135 mm	135 mm
EBSD Camera Binning:	4x4	4x4	4x4
EBSD Camera Gain:	7	7	7
Frame Averaging:	2 frames	2	2
Hough Resolution:	90	90	90
Band Detection Mode:	Edges	Edges	Edges
Number of Bands Detected:	9	8	9
Indexing Mode:	Optimized - EBSD	Optimized - EBSD	Optimized - EBSD

Table 4. Color-CL settings. Data collected on a Tescan VEGA3 LMU SEM with Oxford Instruments at Bowdoin College. See Appendix of Chapter 4 for Goat Rock color-CL settings.

Color CL Settings	**EPB 4**	**EPB 7**	**HBRT 3**	**HBRT 8**	**LPB 1**	**19 PBBP**	**20 PBBP**	**22 PBBP**
Beam Intensity	16	16	16	16	16	16	16	16
Dwell Time	100 µs/pixel	100 µs/pixel	320 µs/pixel	100 µs/pixel	100 µs/pixel	320 µs/pixel	320 µs/pixel	320 µs/pixel
HV	16 kV	16 kV	16 kV	16 kV	16 kV	16 kV	16 kV	16 kV
Spot Size	411.486	411.486	411.486	411.486	411.486	411.470	411.470	411.486
Working Distance	16	16	16	16	16	16	16	16

Table 5. EDS settings for Haylocks Bay and Eastern Pigeon Bay. See Appendix of Chapter 4 for EDS settings of Goat Rock samples and Teeter's acquisition settings above.

EDS Settings	**HBRT 03**	**EPB 4**
Resolution (Width):	1024 pixels	1024 pixels
Resolution (Height):	768 pixels	768 pixels
Field Width:	642 µm - 1.28 mm	321 µm – 642 µm
Field Height:	481 µm - 962 µm	241 µm – 481 µm
Accelerating Voltage:	20.00 kV	20.00 kV
Working Distance:	11mm	10mm
Magnification:	100 – 200x	200-400x
Number Completed Frames:	100 – 150	167 - 200
Energy Range:	20keV	20keV
Number of Channels:	1024	1024
Process Time:	4	4
Live Time:	1573 – 2359s	2639 – 3146s
Total Counts:	50517540 - 105403342	96292036 - 113264287

Table 6. Whole rock major elements. Red designates host compositions.

Sample	SiO2	TiO2	Al2O3	Fe2O3T	MnO	MgO	CaO	Na2O	K2O	P2O5	LOI	Total	Alkalis
GR10	45.36	3.58	17.03	14.59	0.25	4.42	8.08	4.15	0.66	1.89	0.09	100.00	4.81
GR11	47.52	2.95	16.95	13.61	0.23	4.10	8.08	4.52	0.74	1.30	-0.31	100.00	5.26
15GR04	45.64	3.00	17.41	14.61	0.23	3.35	8.45	4.66	0.85	1.81	-0.06	100.00	5.51
15GR01	47.57	2.72	17.70	15.16	0.23	2.37	6.72	5.16	1.09	1.28	-0.25	100.00	6.25
15GR20	47.31	2.80	17.39	14.68	0.23	2.99	7.25	4.99	0.98	1.38	-0.41	100.00	5.97
15GR23	47.24	2.87	17.26	15.97	0.25	2.54	6.49	5.02	1.09	1.28	-0.21	100.00	6.10
15GR25	46.93	2.98	23.39	8.00	0.10	2.69	11.80	3.66	0.34	0.11	0.36	100.00	4.00
15GR17	46.98	2.38	20.85	11.30	0.19	2.59	8.43	4.91	0.85	1.51	1.14	100.00	5.76
15GR22	51.26	1.85	18.99	12.07	0.24	1.60	5.70	6.22	1.26	0.81	0.24	100.00	7.48
15GR09	48.03	2.23	19.49	11.58	0.20	3.08	8.26	4.80	0.93	1.39	-0.37	100.00	5.74
15GR27	47.47	2.17	17.57	16.57	0.30	2.17	6.12	5.27	1.23	1.13	0.09	100.00	6.50
15GR26	48.84	2.43	19.13	13.67	0.19	2.00	6.64	5.46	0.91	0.72	0.31	100.00	6.37
15GR14	54.98	1.87	21.00	7.50	0.13	0.87	5.13	7.08	1.37	0.08	-0.04	100.00	8.45
GR17A	49.85	2.24	17.08	12.58	0.22	3.06	6.61	5.19	1.91	1.25	0.13	100.00	7.10
GR17B	49.94	2.24	17.05	12.56	0.22	3.05	6.60	5.20	1.89	1.25	-0.77	100.00	7.10
GR18	50.64	2.17	17.34	12.19	0.21	2.48	6.28	5.48	2.02	1.19	-0.01	100.00	7.50
GR19	49.17	2.38	16.81	12.77	0.21	3.42	7.05	5.03	1.87	1.28	0.76	100.00	6.90
15GR24H	49.10	2.38	16.92	12.83	0.22	3.36	6.91	5.15	1.86	1.25	-0.35	100.00	7.01
15GR22H	48.87	2.44	16.95	12.99	0.22	3.12	7.04	5.25	1.84	1.28	-0.45	100.00	7.09
22PBBP	43.16	4.11	18.05	13.56	0.12	5.30	12.86	2.23	0.36	0.26	0.39	100.39	2.59
23PBBP	44.15	4.32	20.90	10.18	0.09	4.11	13.36	2.40	0.33	0.15	0.13	100.13	2.73
20PBBP	42.31	3.50	18.26	14.25	0.12	5.57	13.71	1.82	0.31	0.16	0.53	100.53	2.13
EPB3	45.98	2.63	20.22	11.03	0.11	3.88	12.45	2.86	0.49	0.35	0.36	100.36	3.35
EPB7	46.96	2.00	23.22	8.21	0.09	3.13	13.15	2.82	0.27	0.15	0.57	100.57	3.09
EPB L Av	46.47	2.31	21.72	9.62	0.10	3.51	12.80	2.84	0.38	0.25	0.47	100.47	3.22
EPB6H	48.32	2.86	16.76	13.00	0.19	3.87	7.60	4.78	1.72	0.90	-0.25	99.75	6.49
PBBP24H	46.93	3.44	17.00	13.41	0.17	4.19	8.28	4.41	1.40	0.76	0.08	100.08	5.82

FB17A	46.59	2.52	23.61	7.18	0.07	3.50	12.58	3.60	0.28	0.07	0.28	100.00	3.88

HB-RT3	43.81	4.48	19.01	12.71	0.13	4.54	12.03	2.79	0.34	0.16			3.13
HB-RT4	42.68	5.40	18.08	13.35	0.13	5.07	12.47	2.47	0.27	0.09			2.74
HB-Rt7	39.40	5.21	13.16	19.78	0.17	7.29	12.89	1.86	0.20	0.04			2.06
HB-RT5	45.40	3.66	19.66	12.88	0.15	3.33	10.02	3.88	0.54	0.48			4.42
HB-RT8	38.13	5.64	12.49	21.12	0.16	7.65	12.84	1.62	0.27	0.08			1.89
HB-RT6	40.13	4.33	14.29	21.60	0.23	8.46	7.81	2.45	0.46	0.25			2.91
3631	47.06	2.94	22.24	9.29	0.08	3.03	10.96	3.59	0.58	0.22			4.17
3638	29.88	7.29	7.28	35.26	0.32	11.79	6.92	0.86	0.19	0.22			1.04
3635	43.17	3.88	18.93	13.26	0.18	4.62	11.27	2.88	0.24	1.58			3.12
3633	40.22	6.28	14.38	17.28	0.15	6.65	12.79	1.94	0.24	0.06			2.19
3632	49.03	1.14	21.30	5.12	0.07	5.41	15.08	2.38	0.34	0.13			2.72
3634	46.21	3.70	22.20	9.40	0.12	3.04	11.20	3.44	0.46	0.23			3.89
3637	47.86	3.06	17.82	13.49	0.20	3.95	7.24	3.61	1.76	1.02			5.37
3630	43.93	5.13	18.38	12.71	0.12	4.90	11.57	2.53	0.57	0.15			3.10
3636	45.08	5.04	17.87	12.44	0.11	4.98	11.12	2.63	0.59	0.14			3.22
13HBBP	46.35	3.25	17.04	13.62	0.19	4.98	8.10	4.33	1.40	0.74	-0.17	100.00	5.74
14HBBP	46.43	3.22	17.08	13.50	0.21	4.92	7.99	4.42	1.44	0.78	0.14	100.00	5.86
PABP3.2	52.68	1.29	16.83	11.94	0.44	6.20	6.18	3.43	0.88	0.14	3.43	103.43	4.31
PABP3.3	47.35	2.20	19.12	10.14	0.09	8.55	7.96	3.70	0.79	0.09	3.10	103.10	4.50
LPB1	52.38	0.55	12.69	10.35	0.17	13.03	7.02	2.63	1.03	0.14	0.32	100.32	3.66
xenolith	45.90	0.03	1.35	8.75	0.13	42.69	0.86	0.16	0.11	0.01		100.00	
xenolith	51.78	0.26	23.69	4.86	0.10	7.45	11.25	2.33	0.36	0.05		102.13	
xenolith	45.60	1.86	9.25	11.87	0.18	16.05	15.20	1.41	0.37	0.25		102.03	
host	41.91	2.81	11.99	14.36	0.18	12.47	10.58	3.03	1.13	0.69		99.15	

Table 7. Whole rock trace element

Sample	V	Cr	Ni	Zn	Ga	Rb	Sr	Y	Zr	Nb	Ba	Pb	Th	La	Ce	Nd
GR10	148.00	<3	7.00	86.00	24.00	5.60	1072.14	39.91	103.00	53.00	246.00	<1	3.28	23.00	87.00	62.00
GR11	80.00	<3	4.00	75.00	25.00	6.22	1070.46	35.01	99.00	45.00	292.00	<1	5.60	23.00	83.00	58.00
15GR04	51.00	<3	<3	93.00	22.00	8.53	1144.79	35.57	110.00	35.00	444.00	<1	4.07	33.00	78.00	55.00
15GR01	50.00	<3	<3	89.00	27.00	19.03	1082.44	36.52	120.00	38.00	432.00	1.00	3.66	36.00	95.00	50.00
15GR20	112.00	<3	<3	100.00	26.00	11.79	987.83	36.84	143.00	58.00	451.00	<1	3.12	26.00	93.00	57.00
15GR23	59.00	<3	<3	109.00	25.00	19.13	986.77	37.07	156.00	47.00	449.00	<1	4.41	37.00	93.00	56.00
15GR25	187.00	3.00	13.00	55.00	22.00	<1	1323.09	7.62	110.00	25.00	182.00	<1	2.15	<5	9.00	34.00
15GR17	77.00	<3	<3	71.00	23.00	11.23	1263.62	28.52	102.00	36.00	517.00	<1	1.56	17.00	61.00	46.00
15GR22	24.00	4.00	<3	87.00	25.00	15.74	919.11	27.34	108.00	61.00	610.00	3.00	4.06	35.00	67.00	45.00
15GR09	74.00	<3	<3	79.00	22.00	12.88	1134.56	30.92	123.00	42.00	518.00	<1	2.29	26.00	72.00	62.00
15GR27	34.00	<3	<3	106.00	26.00	16.88	1003.18	35.84	91.00	40.00	694.00	<1	3.34	34.00	110.00	53.00
15GR26	123.00	<3	<3	92.00	27.00	6.51	1050.34	21.02	89.00	33.00	446.00	<1	1.76	14.00	55.00	37.00
15GR14	102.00	<3	7.00	59.00	29.00	10.18	1111.72	6.03	73.00	36.00	674.00	<1	<1	<5	25.00	14.00
GR17A	82.00	<3	4.00	125.00	24.00	33.67	800.93	46.12	304.00	66.00	609.00	1.00	7.72	39.00	105.00	66.00
GR17B	77.00	<3	<3	120.00	24.00	31.56	803.44	46.02	302.00	82.00	612.00	4.00	8.19	51.00	103.00	61.00
GR18	79.00	<3	<3	127.00	24.00	36.74	810.02	46.24	300.00	81.00	672.00	5.00	6.64	50.00	100.00	64.00
GR19	89.00	<3	3.00	119.00	23.00	36.05	813.30	46.30	291.00	79.00	510.00	3.00	6.46	51.00	100.00	61.00
15GR24H	82.00	<3	3.00	123.00	23.00	35.91	811.44	45.42	298.00	81.00	610.00	<1	5.61	39.00	101.00	45.00
15GR22H	86.00	<3	<3	129.00	23.00	34.37	813.39	44.31	293.00	80.00	604.00	2.00	5.25	44.00	90.00	63.00

22PBBP	383.00	<1	30.00	83.00	23.00	10.00	769.00	16.00	94.00	21.00	123.00	3.00	<1	14.00	12.00	
23PBBP	325.00	2.00	10.00	56.00	20.00	7.00	1031.00	9.00	67.00	16.00	95.00	4.00	2.00	8.00	7.00	
20PBBP	498.00	53.00	136.00	82.00	23.00	8.00	687.00	13.00	94.00	15.00	91.00	5.00	1.00	8.00	17.00	

EPB3	241.00	<1	24.00	75.00	22.00	10.00	1070.00	17.00	106.00	22.00	227.00	4.00	2.00	22.00	39.00	
EPB7	191.00	<1	26.00	46.00	21.00	5.00	1220.00	9.00	54.00	8.00	161.00	5.00	<1	15.00	13.00	
EPB L Av	216.00	#DIV/0!	25.00	60.50	21.50	7.50	1145.00	13.00	80.00	15.00	194.00	4.50	2.00	18.50	26.00	#DIV/0!
EPB6H	120.00	<1	<1	119.00	23.00	36.00	810.00	41.00	311.00	70.00	434.00	6.00	6.00	54.00	106.00	
PBBP24H	170.00	<1	12.00	117.00	23.00	30.00	820.00	32.00	291.00	64.00	368.00	4.00	6.00	48.00	82.00	

FB17A	173.00	<3	17.00	38.00	20.00	<1	1415.71	6.75	58.00	12.00	130.00	<1	<1	<5	13.00	12.00

HB-RT3	267.84	28.99	23.21	89.08	20.80	2.63	890.57	13.43	78.27	18.94	151.04	1.00	1.00	5.00	13.40	36.44
HB-RT4	253.56	3.00	31.46	87.73	21.03	1.00	823.20	10.64	83.51	24.16	124.70	1.00	2.26	5.00	5.00	20.58
HB-Rt7	617.07	3.00	68.93	139.99	21.83	1.00	564.03	14.71	71.46	14.53	115.80	1.00	1.00	5.00	5.00	22.28
HB-RT5	187.26	3.00	14.22	113.46	21.87	4.77	1163.14	19.19	100.42	39.36	239.81	1.00	1.00	5.89	21.05	33.77
HB-RT8	509.64	3.00	35.21	137.28	23.84	2.69	385.23	14.96	80.18	14.30	81.04	1.08	1.00	5.00	7.33	20.96
HB-RT6	474.31	251.28	141.82	218.03	21.53	4.05	573.26	23.75	99.53	30.51	208.62	1.00	1.00	9.88	21.18	29.59
3631	147.20	22.70	36.70	63.70	22.00	9.00	1089.00	12.00	102.00	25.50	145.40	4.00	0.00	13.10	26.20	14.30
3638	885.10	507.20	266.60	281.00	22.00	2.00	219.00	21.00	62.00	16.30	130.10	7.00	2.00	22.90	11.50	12.50
3635	256.50	24.10	30.70	135.10	23.00	1.00	1332.00	18.00	50.00	12.30	56.30	6.00	0.00	24.60	39.90	27.00
3633	317.00	24.60	46.70	84.50	19.00	1.00	604.00	17.00	83.00	18.80	0.00	4.00	2.00	17.70	13.00	10.60
3632	149.90	298.80	75.70	25.80	18.00	2.00	781.00	9.00	55.00	6.40	65.00	4.00	0.00	7.60	8.90	11.50
3634	173.60	26.60	31.50	51.20	22.00	3.00	1176.00	10.00	84.00	20.10	90.70	5.00	1.00	17.70	18.80	10.60
3637	370.60	19.90	38.70	83.30	19.00	4.00	529.00	18.00	97.00	19.80	0.00	5.00	2.00	18.00	22.50	11.20
3630	230.50	21.70	51.20	65.50	20.00	5.00	891.00	13.00	86.00	18.40	45.80	6.00	0.00	14.10	20.00	10.60
3636	229.10	20.30	50.70	67.20	20.00	6.00	858.00	13.00	89.00	20.40	71.70	7.00	0.00	15.30	22.30	10.60
13HBBP	170.09	23.25	24.07	113.65	22.67	24.51	815.02	33.22	272.32	73.22	398.31	1.64	5.35	30.87	67.03	52.28
14HBBP	163.83	11.65	20.49	115.07	23.37	25.06	823.73	37.90	278.09	74.38	422.84	<1	4.62	33.99	81.35	46.46

PABP3.2	172.00	69.00	84.00	108.00	21.00	11.00	334.00	13.00	52.00	5.00	397.00	8.00	<1	10.00	23.00
PABP3.3	290.00	832.00	364.00	54.00	17.00	5.00	779.00	5.00	18.00	4.00	135.00	3.00	1.00	9.00	<5

LPB1	189.00	970.00	205.00	83.00	16.00	20.00	484.00	10.00	57.00	15.00	390.00	2.00	1.00	8.00	10.00

Table 8. Ducksfoot lava flow bulk rock major and trace elements

	BRS-01	BRS-02	BRS-03	BRS-04A, 4B	BRS-05	PaB9.2.14.0	PaB9.2.14.33	PaB9.2.14.35
SiO2	52.51	48.12	48.05	46.44	50.34	48.98	51.06	48.05
TiO2	1.49	2.95	2.96	3.53	2.12	2.91	2.40	2.76
Al2O3	17.98	17.96	17.70	16.86	17.99	18.19	18.65	17.01
FeO*	10.98	13.37	13.28	13.91	12.93	12.96	12.87	12.83
MnO	0.21	0.17	0.22	0.19	0.21	0.17	0.17	0.22
MgO	2.05	3.26	3.22	4.75	2.62	3.55	1.73	3.97
CaO	5.51	7.59	7.29	8.30	6.01	6.70	4.68	7.62
Na2O	6.02	3.84	4.37	4.01	4.71	4.10	5.08	4.77
K2O	2.36	1.63	1.73	1.34	1.96	1.79	2.47	1.73
P2O5	0.88	1.11	1.18	0.67	1.12	0.65	0.87	1.05
LOI	-0.36	0.82	0.92	0.81	1.35	1.78	3.15	0.87
Total	100.00	100.00	100.00	100.00	100.00	100.00	100.00	100.00
V	24.01	117.70	135.94	193.28	46.00	124.36	76.52	106.76
Cr	<3	<3	<3	<3	<3	<3	<3	<3
Ni	<3	15.92	6.24	10.28	4.37	13.70	7.14	<3
Zn	133.67	113.03	144.61	99.70	126.23	97.38	137.45	111.91
Zr	421.15	312.01	309.64	250.64	374.19	320.74	360.35	310.13
Nb	116.62	86.78	89.78	64.49	97.95	86.03	99.89	87.22
Ba	648.38	536.00	504.68	416.83	640.93	595.82	813.45	410.14
La	59.72	32.62	35.11	21.48	56.29	46.56	35.02	41.43
Ce	119.06	90.79	96.96	60.96	112.11	80.23	95.77	96.08
Nd	60.14	56.50	45.37	36.52	62.41	49.27	60.79	49.32
Ga	24.20	22.59	23.61	22.42	24.71	23.95	25.03	23.51
Pb	5.36	3.25	4.22	1.42	5.80	<1	3.66	2.01
Rb	58.00	27.21	29.37	21.98	39.10	33.53	51.92	31.83
Sr	788.49	873.47	793.01	796.62	768.70	838.54	688.54	831.19
Th	10.54	6.08	5.11	3.66	5.92	6.43	7.15	4.59
Y	42.14	33.16	42.60	36.01	39.19	33.11	38.67	41.96

Table 9. Plagioclase mineral chemistries.

	SiO2	Al2O3	FeO*	CaO	Na2O	K2O	Total	Alkalis	SrO
Goat Rock									
GR22									
15GR22.1	59.90	26.18	0.16	6.81	7.32	0.80	101.18	8.13	
15GR22.1	64.60	20.87	0.34	1.90	7.56	4.71	99.98	12.27	
15GR22.1	65.75	20.99	0.33	1.78	7.35	5.17	101.38	12.53	
15GR22.1.T1	59.64	25.39	0.20	6.36	7.53	1.03	100.15	8.56	
15GR22.1.T1	60.16	25.43	0.13	6.49	7.57	0.98	100.75	8.55	
15GR22.1.T1	60.66	25.66	0.19	6.27	7.42	1.07	101.28	8.49	
15GR22.1.T1	59.59	25.51	0.16	6.37	7.56	1.12	100.30	8.68	
15GR22.1.T1	59.99	25.63	0.13	6.62	7.60	1.06	101.03	8.66	
15GR22.1.T1	60.73	24.97	0.15	6.18	7.72	1.07	100.81	8.79	
15GR22.1.T1	60.82	24.65	0.18	5.71	7.82	1.19	100.36	9.00	
15GR22.1.T1	60.56	24.52	0.16	5.64	7.92	1.17	99.97	9.08	
15GR22.1.T1	60.97	24.79	0.32	5.39	7.60	1.32	100.39	8.92	
15GR22.1.T1	60.51	24.75	0.30	5.48	7.73	1.33	100.09	9.06	
15GR22.1.T1	61.41	24.62	0.23	5.21	8.03	1.18	100.68	9.21	
15GR22.1.T1	61.68	21.33	0.58	2.67	7.65	3.38	97.29	11.03	
15GR22.1.T1	62.83	23.38	0.26	4.47	8.50	1.74	101.17	10.24	
15GR22.1.T1	61.45	23.79	0.27	4.57	8.05	1.62	99.75	9.67	
15GR22.1.T1	60.56	23.35	0.18	4.70	8.15	1.62	98.56	9.77	
15GR22.1.T1	62.17	23.52	0.22	4.72	8.05	1.52	100.20	9.57	
15GR22.1.T1	61.87	23.96	0.21	4.63	8.12	1.53	100.32	9.65	
15GR22.3	61.24	23.49	0.20	4.43	8.05	2.04	99.45	10.09	
15GR22.3	61.80	23.24	0.14	4.02	8.30	1.58	99.08	9.88	
15GR22.3	62.27	23.97	0.18	4.41	8.13	1.98	100.93	10.11	
15GR22.3	61.20	23.54	0.17	4.39	8.47	1.44	99.22	9.91	
15GR22.3	62.10	22.89	0.17	4.15	8.41	1.67	99.38	10.07	
15GR22.3	62.03	23.73	0.19	4.50	8.29	1.49	100.23	9.78	
15GR22.3.T1	61.31	23.33	0.15	4.20	7.97	2.06	99.01	10.02	
15GR22.3.T1	61.93	22.93	0.18	3.82	7.84	2.50	99.20	10.34	
15GR22.3.T1	61.35	22.72	0.29	3.88	7.76	2.50	98.51	10.27	
15GR22.3.T1	60.47	23.59	0.11	4.64	7.83	1.91	98.56	9.74	
15GR22.3.T1	61.21	23.65	0.34	4.43	8.06	1.79	99.48	9.85	
15GR22.3.T1	61.01	23.50	0.21	4.24	7.99	1.90	98.84	9.89	
15GR22.3.T1	61.24	22.91	0.19	4.15	7.96	2.19	98.64	10.15	
15GR22.3.T1	60.74	23.85	0.16	4.67	7.95	1.72	99.07	9.67	
15GR22.3.T1	61.73	23.24	0.14	4.49	8.04	1.78	99.41	9.82	
15GR22.4	60.66	23.95	0.15	4.87	8.07	1.39	99.09	9.46	
15GR22.4	60.66	23.96	0.12	4.62	7.84	1.82	99.02	9.67	
15GR22.4	63.35	21.66	0.38	2.63	7.92	3.61	99.55	11.53	
15GR22.4	61.00	23.33	0.12	4.53	8.30	1.72	99.01	10.02	
15GR22.4	59.77	25.44	0.16	5.87	7.66	1.19	100.08	8.84	
15GR22.4	61.05	23.29	0.14	4.37	8.46	1.62	98.94	10.08	
15GR22.5	57.65	25.51	0.15	6.94	7.33	0.71	98.28	8.04	
15GR22.5.T1	59.96	24.80	0.16	5.50	8.12	0.95	99.50	9.08	
15GR22.5.T1	59.73	24.15	0.13	5.38	8.17	0.87	98.43	9.04	
15GR22.5.T1	59.12	24.60	0.21	5.77	7.76	0.81	98.28	8.58	
15GR22.5.T1	59.52	25.00	0.22	6.21	7.72	0.76	99.43	8.49	
15GR22.5.T1	60.45	24.36	0.20	5.09	8.22	1.13	99.45	9.35	

15GR22.5.T1	57.37	25.65	0.15	6.82	7.30	0.84	98.14	8.15
15GR22.5.T1	59.68	24.89	0.15	6.12	7.56	0.92	99.32	8.49
15GR22.5.T1	60.28	24.28	0.23	5.00	7.82	1.38	98.98	9.19
15GR22.5.T1	63.96	21.73	0.38	2.42	7.84	3.97	100.29	11.81
15GR22.5.T1	60.11	24.23	0.21	5.04	7.92	1.33	98.84	9.26
15GR22.5.T1	60.35	24.05	0.22	5.32	8.01	1.04	98.99	9.05
15GR22.6.T1	60.68	23.47	0.17	4.37	8.51	1.46	98.66	9.97
15GR22.6.T1	60.47	23.30	0.20	4.54	8.26	1.52	98.27	9.78
15GR22.6.T1	60.42	23.75	0.14	4.49	8.07	1.64	98.50	9.70
15GR22.6.T1	60.88	23.17	0.18	4.39	8.22	1.58	98.42	9.80
15GR22.6.T1	60.08	24.01	0.15	4.87	7.90	1.05	98.06	8.95
15GR22.6.T2	60.71	23.55	0.19	4.64	8.01	1.59	98.69	9.60
15GR22.6.T2	60.94	23.48	0.14	4.63	8.13	1.52	98.84	9.65
15GR22.6.T2	60.28	23.72	0.21	4.12	8.34	1.47	98.14	9.81
15GR22.6.T2	61.03	23.44	0.18	4.39	8.23	1.60	98.86	9.82
15GR22.6.T2	61.52	23.70	0.16	4.34	8.31	1.45	99.48	9.76
15GR22.6.T2	61.30	24.16	0.13	4.75	8.16	1.50	99.99	9.65
15GR22.6.T2	60.69	23.47	0.20	4.52	8.11	1.75	98.75	9.87
15GR22.6.T2	60.57	22.01	0.32	3.60	7.89	2.27	96.65	10.16
15GR22.6.T2	62.15	22.47	0.23	3.34	7.89	3.05	99.13	10.94
15GR22.6.T2	60.36	24.01	0.20	4.92	7.87	1.59	98.95	9.46
15GR22.6.T2	61.09	23.70	0.23	4.66	8.11	1.67	99.46	9.79
15GR22.6.T2	61.03	23.60	0.17	4.54	7.95	1.89	99.19	9.84
15GR22.9	60.98	23.23	0.23	4.41	8.21	1.58	98.64	9.79
15GR22.9	60.67	23.40	0.17	4.65	8.42	1.36	98.66	9.78
15GR22.9.T1	59.79	24.40	0.15	5.49	7.96	0.99	98.78	8.95
15GR22.9.T1	61.45	23.51	0.16	4.22	8.35	1.58	99.25	9.93
15GR22.9.T1	60.21	24.17	0.21	5.10	8.03	1.23	98.95	9.26
15GR22.10.T1	59.22	24.97	0.16	6.26	7.65	0.85	99.11	8.50
15GR22.10.T1	60.93	23.25	0.18	4.31	8.30	1.56	98.53	9.86
15GR22.10.T1	60.62	23.79	0.18	4.98	7.93	1.44	98.93	9.38
15GR22.10.T1	61.45	22.67	0.20	3.62	8.44	1.75	98.13	10.19
15GR22.10.T1	60.26	23.61	0.17	4.21	8.43	1.41	98.10	9.84
15GR22.11.T1	60.16	23.70	0.18	5.01	8.00	1.21	98.26	9.21
15GR22.11.T1	59.94	25.20	0.15	5.63	7.85	0.89	99.66	8.74
15GR22.11.T1	60.63	24.65	0.17	5.41	8.04	0.95	99.85	8.99
15GR22.11.T1	56.02	27.28	0.13	8.59	6.43	0.44	98.89	6.87
15GR22.11.T1	56.20	26.58	0.23	7.70	6.74	0.56	98.01	7.29
15GR22.11.T1	60.37	23.88	0.27	5.05	7.85	1.30	98.72	9.15
15GR22.11.T1	62.22	23.46	0.24	4.62	8.20	1.68	100.42	9.88
15GR22.11.T1	59.81	25.69	0.21	6.09	7.51	0.68	100.00	8.19
15GR22.11.T1	59.58	24.37	0.14	5.71	7.94	0.96	98.69	8.89
15GR22.11.T1	58.47	25.94	0.23	7.47	7.08	0.56	99.74	7.64
15GR22.11.T1	58.80	26.55	0.15	6.78	7.31	0.63	100.23	7.95
15GR22.11.T1	57.51	26.04	0.15	7.47	7.09	0.58	98.85	7.67
15GR22.11.T1	58.58	25.68	0.18	6.79	7.47	0.74	99.43	8.21
15GR22.11.T2	59.99	25.15	0.18	6.05	7.63	1.03	100.02	8.66
15GR22.11.T2	58.00	26.22	0.18	6.76	7.12	0.81	99.09	7.93
15GR22.11.T2	59.19	25.11	0.17	6.59	7.27	0.80	99.13	8.07
15GR22.11.T2	60.00	24.70	0.17	6.04	7.77	0.98	99.66	8.75

15GR22.11.T2	58.29	25.93	0.13	6.70	7.25	0.72	99.02	7.97
15GR22.11.T2	59.78	24.58	0.19	5.78	7.82	1.03	99.18	8.85
15GR22.11.T2	59.30	25.27	0.14	6.23	7.54	1.01	99.48	8.54
15GR22.11.T2	61.17	23.84	0.16	4.74	7.94	1.67	99.52	9.61
15GR22.11.T2	60.27	24.71	0.18	5.79	7.87	1.05	99.87	8.92
15GR22.14.T1	60.63	23.77	0.21	4.92	8.27	1.18	98.99	9.45
15GR22.14.T1	60.16	24.28	0.20	5.08	8.33	1.06	99.11	9.39
15GR22.14.T1	60.01	22.66	0.67	4.06	7.91	1.39	96.70	9.30
15GR22.14.T1	60.08	24.72	0.16	6.01	7.93	1.12	100.02	9.05
15GR22.14.T1	59.97	25.09	0.21	5.75	7.86	1.08	99.95	8.94
15GR22.14.T1	61.21	24.68	0.21	4.93	8.02	1.42	100.47	9.44
15GR22.14.T1	60.83	23.86	0.22	4.83	7.93	1.54	99.21	9.47
15GR22.14.T1	61.28	23.62	0.26	4.33	8.08	2.01	99.58	10.09
15GR22.14	60.95	24.88	0.13	5.36	7.97	1.22	100.52	9.19
15GR22.14	58.89	26.46	0.19	7.07	7.25	0.75	100.61	8.00
15GR22.14	60.85	24.65	0.23	5.30	8.00	1.07	100.11	9.08
GR26								
15GR26.1.1	58.52	25.86	0.23	6.93	7.4	1.07	100	8.47
15GR26.1.1	58.58	26.19	0.24	6.93	7.29	0.95	100.18	8.24
15GR26.1.1	58.35	25.8	0.25	7.2	7.05	0.98	99.63	8.03
15GR26.1.1	58.27	26.08	0.28	7.3	7.08	0.86	99.87	7.94
15GR26.1.1	57.61	26.01	0.53	7.45	6.86	0.88	99.34	7.74
15GR26.1.1	57.85	25.72	0.25	7.25	7.08	0.95	99.09	8.03
15GR26.1.1	57.14	27.1	0.2	8.03	6.65	0.73	99.85	7.38
15GR26.1.1	57.44	26.93	0.2	8.06	6.72	0.82	100.18	7.54
15GR26.1.1	57.19	26.6	0.17	7.95	6.74	0.78	99.43	7.52
15GR26.1.1	57.36	26.78	0.18	7.96	6.84	0.79	99.91	7.63
15GR26.1.1	57.81	26.62	0.2	7.8	6.74	0.92	100.08	7.66
15GR26.1.1	57.8	26.7	0.18	7.8	6.65	0.87	100	7.52
15GR26.1.1	57.79	26.94	0.18	7.72	6.73	0.83	100.19	7.56
15GR26.1.1	57.82	26.46	0.18	7.83	6.84	0.86	99.98	7.7
15GR26.1.1	57.58	26.24	0.17	7.54	6.89	0.92	99.34	7.81
15GR26.1.1	57.9	26.47	0.16	7.85	6.94	0.9	100.23	7.84
15GR26.1	58.32	25.83	0.2	6.82	7.16	0.99	99.31	8.15
15GR26.1	58.33	26.79	0.13	7.35	6.95	0.95	100.5	7.9
15GR26.1	57.67	26.04	0.26	7.19	6.99	1.03	99.17	8.02
15GR26.3.1	59.23	25.63	0.22	6.87	7.07	1.06	100.08	8.13
15GR26.3.1	58.82	25.81	0.23	6.5	7.3	1.17	99.82	8.47
15GR26.3.1	59.04	25.99	0.19	6.79	7.28	1.09	100.38	8.37
15GR26.3.1	61.63	23.52	0.39	4.3	6.76	4.34	100.95	11.1
15GR26.3.1	58.96	25.42	0.24	6.43	7.37	1.16	99.58	8.53
15GR26.3.1	59.4	25.07	0.2	6.23	7.47	1.01	99.39	8.48
15GR26.3.1	59.32	25.69	0.17	6.38	7.44	1.13	100.13	8.57
15GR26.3	57.83	26.54	0.18	7.31	7.06	0.79	99.71	7.85
15GR26.3	58.97	25.79	0.18	6.73	7.19	1.05	99.9	8.24
15GR26.3	58.82	25.72	0.17	6.54	7.5	1.11	99.86	8.61
15GR26.7.1	58.95	25.15	0.2	6.25	7.54	1.23	99.31	8.77

15GR26.7.1	58.7	25.71	0.31	6.6	7.34	1.06	99.72	8.4
15GR26.7.1	59.46	25.34	0.34	6.17	7.47	1.12	99.9	8.59

15GR26.7.1	59.07	25.45	0.83	6.37	7.42	0.88	100.02	8.3
15GR26.7.1	58.8	25.04	0.23	6.66	7.3	1.05	99.08	8.35
15GR26.7.1	59.48	24.91	0.26	6.21	7.78	1.18	99.82	8.96
15GR26.7.1	59.34	25.03	0.2	6.18	7.7	1.22	99.67	8.92
15GR26.7.1	58.29	26.21	0.25	7.14	7.2	0.87	99.95	8.07
15GR26.7.1	59.06	25.46	0.2	6.74	7.49	0.91	99.87	8.4
15GR26.7.1	58.34	26.19	0.17	7.07	7.31	0.84	99.92	8.15
15GR26.7.2	59.57	25.89	0.24	6.45	7.51	1.08	100.74	8.59
15GR26.7.2	58.98	25.59	0.83	6.79	7.21	1.12	100.51	8.33
15GR26.7.2	59.23	25.26	1.11	6.73	7.28	0.75	100.35	8.03
15GR26.7.2	60.45	25.71	0.26	6.4	7.61	1.01	101.44	8.62
15GR26.7.2	60.18	24.5	0.66	5.83	7.53	1.31	100	8.84
15GR26.7.2	59.92	24.39	1.67	5.89	7.1	1.31	100.28	8.41
15GR26.7.3	58.98	24.76	1.92	5.84	7.39	1.18	100.08	8.57
15GR26.7.3	59.69	24.34	1.74	5.83	7.45	1.24	100.29	8.69
15GR26.7.3	59.83	25.65	0.27	6.86	7.34	1.03	100.98	8.37
15GR26.7.3	58.48	24.61	2.27	5.71	7.31	1.15	99.54	8.46
15GR26.7.3	58.83	26.6	0.2	7.5	6.92	0.76	100.82	7.68
15GR26.8.1	60.3	24.77	0.18	5.86	7.71	1.08	99.9	8.79
15GR26.8.1	60.18	24.87	0.2	5.68	7.65	1.27	99.86	8.92
15GR26.8.1	60.81	25.05	0.25	5.85	7.62	1.13	100.71	8.75
15GR26.8.1	60.73	25.14	0.23	5.87	7.66	1.18	100.81	8.84
15GR26.8.1	57.03	23.41	4.11	5.46	7.34	1.21	98.56	8.55
15GR26.8.1	60.83	24.88	0.24	5.92	7.59	1.34	100.8	8.93
15GR26.8.1	60.67	24.91	0.27	5.79	7.65	1.21	100.5	8.86
15GR26.8.1	60.74	25.26	0.33	5.94	7.8	1.14	101.21	8.94
15GR26.8.1	58.48	24.39	1.91	5.76	7.39	1.11	99.04	8.5
15GR26.8.1	60.41	24.52	0.25	6.05	7.54	1.17	99.94	8.71
15GR26.8.1	60.35	25.39	0.21	6.28	7.56	1.12	100.92	8.68
15GR26.8	59.1	25.85	0.23	6.93	7.38	0.85	100.33	8.23
15GR26.8	59.87	24.92	0.18	6.18	7.51	1.12	99.77	8.63
15GR26.8	58.66	25.2	0.26	6.59	7.44	0.88	99.02	8.32
15GR26.8	59.82	25.26	0.17	6.36	7.72	1.11	100.45	8.83
15GR26.10	58.55	25.66	0.28	7.24	7.17	0.83	99.73	8
15GR26.10	60.44	25.12	0.21	5.98	7.32	1.25	100.32	8.57
15GR26.10	58.5	25.85	0.21	7.2	7.07	0.88	99.71	7.95
15GR26.10	59.22	26	0.18	6.93	7.27	0.98	100.58	8.25
15GR26.10	58.52	26.6	0.22	7.75	6.91	0.79	100.8	7.7
15GR26.12.1	60.56	24.82	0.17	5.85	7.67	1.32	100.39	8.99
15GR26.12.1	60.1	25.02	0.22	5.81	7.54	1.32	100.01	8.86
15GR26.12.1	60.23	24.82	0.17	5.8	7.66	1.34	100.02	9
15GR26.12.1	60.18	24.28	0.23	5.99	7.66	1.38	99.72	9.04
15GR26.12.1	60.69	24.68	0.29	5.82	7.58	1.36	100.43	8.94
15GR26.12.1	59.81	24.76	0.3	5.95	7.7	1.24	99.76	8.94
15GR26.12.1	60.72	24.93	0.21	6.01	7.49	1.38	100.72	8.87
15GR26.12.1	59.82	24.88	0.34	5.61	7.6	1.51	99.74	9.11
15GR26.12.1	59.75	24.43	0.19	5.81	7.84	1.38	99.39	9.22
15GR26.12.1	60.78	25.23	0.24	5.68	7.54	1.23	100.7	8.77

15GR26.12.1	59.49	25.15	0.23	6.15	7.55	1.26	99.83	8.81
15GR26.12	58.84	26.2	0.17	7.32	7.08	0.79	100.4	7.87

15GR26.12	60.4	25.1	0.21	6.1	7.59	1.21	100.61	8.8	
15GR26.12	60.97	25.06	0.17	6.13	7.56	1.21	101.1	8.77	
15GR26.13	59.31	25.42	0.15	7.07	7.11	0.96	100.02	8.07	
15GR26.13	60.07	25.15	0.18	6.51	7.57	1.14	100.64	8.71	
15GR26.13	59.13	25.88	0.19	7.15	7.25	0.91	100.51	8.16	
15GR26.13	58.88	26.02	0.19	7.32	7.02	0.91	100.35	7.93	
15GR26.13	58.95	25.68	0.17	6.67	7.39	0.94	99.81	8.33	
15GR26.13	60.58	25.27	0.22	5.98	7.77	1.23	101.06	9	
15GR26.13	60.87	25.21	0.18	5.81	7.69	1.39	101.15	9.08	
15GR26.13	60.33	25.06	0.24	5.72	7.63	1.26	100.24	8.89	
15GR26.13	58.9	24.41	1.55	5.69	7.65	1.24	99.44	8.89	
15GR26.13	60.68	25.37	0.3	5.97	7.7	1.23	101.24	8.93	
15GR26.14	58.59	25.76	0.27	6.93	6.93	0.84	99.33	7.77	
15GR26.14	59.86	25.21	0.24	6.39	7.33	1.22	100.25	8.55	
15GR26.14	58.15	25.57	0.19	6.59	7.32	1.03	98.85	8.35	
15GR26.14	59.5	25.26	0.18	6.18	7.39	1.08	99.59	8.47	
15GR26.15	58.73	25.22	0.24	6.69	7.51	1.06	99.44	8.57	
15GR26.15	60.69	24.77	0.17	5.55	8.11	1.35	100.64	9.46	
15GR26.15	59.61	25.51	0.17	6.6	7.41	1.05	100.35	8.46	
15GR26.15	60.61	26.41	0.18	7.26	6.52	0.83	101.81	7.35	
15GR26.15	57.75	26.51	0.12	7.61	7.02	0.8	99.81	7.82	
15GR26.15	60.34	24.84	0.18	5.83	7.69	1.39	100.26	9.08	
15GR26.15	59.68	25.48	0.18	6.61	7.65	1.02	100.62	8.67	
15GR26.15	59.89	25	0.17	5.96	7.62	1.28	99.92	8.9	
Haylocks Bay									
HBRT 2									
HB-RT-02plag1c	52.58	29.88	0.29	12.36	4.43	0.25	100	4.68	0.22
HB-RT-02plag1r	54.26	28.71	0.35	11.01	5.16	0.31	100	5.47	0.22
HB-RT-02plag3-2	54.01	28.77	0.27	11.38	5.02	0.31	100	5.33	0.25
HB-RT-02plag3-3	56.12	27.29	0.32	9.75	5.87	0.45	100	6.32	0.20
HB-RT-02plag3-4	53.14	29.33	0.32	12.10	4.63	0.28	100	4.91	0.20
HB-RT-02plag3-5	52.94	29.56	0.32	12.15	4.56	0.26	100	4.82	0.20
HB-RT-02plag3c	54.92	28.39	0.32	10.74	5.10	0.31	100	5.41	0.22
HB-RT-02plag6c	54.03	29.00	0.25	11.28	4.92	0.28	100	5.20	0.23
HB-RT-02plag6r	54.76	28.30	0.33	10.69	5.39	0.33	100	5.72	0.22
HB-RT-02plag7c	53.06	29.48	0.29	11.95	4.72	0.26	100	4.98	0.24
HB-RT-02plag7r	55.34	28.00	0.32	10.24	5.50	0.40	100	5.90	0.20
HB-RT-02plag8c	53.38	29.19	0.29	11.83	4.83	0.27	100	5.10	0.21
HB-RT-02plag8r	54.30	28.76	0.39	11.15	4.85	0.31	100	5.16	0.24
HB-RT-02unknown	52.72	30.03	0.32	12.15	4.36	0.23	100	4.59	0.20
HBRT 3									
HB-RT-03plag10ii	53.87	28.84	0.27	11.46	5.05	0.29	100	5.34	0.21
HB-RT-03plag1c	56.73	27.03	0.20	9.13	6.24	0.44	100	6.68	0.23
HB-RT-03plag1r	56.54	27.06	0.20	9.50	5.99	0.47	100	6.46	0.25
HB-RT-03plag2r	56.30	27.14	0.18	9.53	6.15	0.45	100	6.60	0.24
HB-RT-03plag3c	57.33	26.32	0.37	9.11	6.13	0.52	100	6.65	0.22

HB-RT-03plag4c	56.71	26.78	0.19	9.47	6.14	0.44	100	6.58	0.25
HB-RT-03plag4r	56.76	26.92	0.25	9.26	6.11	0.48	100	6.59	0.23

HB-RT-03plag5c	56.64	26.98	0.19	9.37	6.16	0.41	100	6.57	0.24
HB-RT-03plag5r	57.35	26.33	0.21	8.87	6.41	0.57	100	6.98	0.27
HB-RT-03plag6r	55.98	27.00	0.59	10.04	5.73	0.42	100	6.15	0.25
HB-RT-03plag7r	56.53	26.97	0.25	9.47	6.05	0.46	100	6.51	0.25
HB-RT-03plag7rr	56.08	27.66	0.26	9.56	5.79	0.39	100	6.18	0.26
HB-RT-03plag8c	50.42	31.17	0.26	14.42	3.36	0.19	100	3.55	0.18
HB-RT-03plag8r	52.89	29.51	0.27	12.29	4.59	0.26	100	4.85	0.19
HB-RT-03plg.cmarg.1	54.57	28.00	0.72	10.76	5.36	0.40	100	5.76	0.20
HB-RT-03plg.traverse(1)	53.28	29.29	0.38	11.89	4.72	0.24	100	4.96	0.20
HB-RT-03plg.traverse(1)	56.46	27.57	0.34	8.88	6.06	0.46	100	6.52	0.23
HB-RT-03plg.traverse(1)	55.49	27.60	0.33	10.57	5.44	0.36	100	5.80	0.21
HB-RT-03plg.traverse(1)	52.52	29.81	0.28	12.10	4.81	0.28	100	5.09	0.21
HB-RT-03plg.traverse(1)	54.98	28.04	0.26	10.69	5.43	0.37	100	5.80	0.23
HB-RT-03plg.traverse(1)	52.78	29.54	0.29	12.30	4.57	0.29	100	4.86	0.22
HB-RT-03plg.traverse(1)	54.20	28.59	0.31	11.25	5.09	0.33	100	5.42	0.23
HB-RT-03plg.traverse(1)	53.37	29.15	0.28	11.80	4.87	0.29	100	5.16	0.24
HB-RT-03plg.traverse(1)	54.25	28.60	0.29	11.23	5.10	0.32	100	5.42	0.22
HB-RT-03plg.traverse(1)	54.39	28.53	0.27	11.23	5.04	0.29	100	5.33	0.24
HB-RT-03plg.traverse(1)	55.02	28.03	0.31	10.64	5.39	0.39	100	5.78	0.22
HB-RT-03plg.traverse(1)	52.57	29.53	0.29	12.55	4.60	0.26	100	4.86	0.20
HB-RT-03plg.traverse(1)	54.64	28.17	0.30	10.90	5.43	0.37	100	5.80	0.19
HB-RT-03plg.traverse(1)	53.50	29.16	0.29	11.55	4.95	0.30	100	5.25	0.25
HB-RT-03plg.traverse(1)	55.97	27.28	0.37	9.65	6.04	0.46	100	6.50	0.23
HB-RT-03plg.traverse(1)	53.00	29.36	0.28	12.24	4.62	0.30	100	4.92	0.21
HB-RT-03plg.traverse(1)	55.01	27.95	0.33	10.67	5.46	0.38	100	5.84	0.20
HB-RT-03plg.traverse(1)	54.04	28.69	0.31	11.24	5.14	0.34	100	5.48	0.24
HB-RT-03plg.traverse(1)	54.92	28.06	0.33	10.62	5.48	0.37	100	5.85	0.23
HB-RT-03plg.traverse(1)	54.47	28.32	0.35	10.98	5.27	0.36	100	5.63	0.26
HB-RT-03plg.traverse(1)	53.73	28.87	0.29	11.60	4.99	0.32	100	5.31	0.21
HB-RT-03plg.traverse(1)	55.49	27.76	0.34	10.15	5.68	0.35	100	6.03	0.24
HB-RT-03plg.traverse(1)	55.04	27.95	0.30	10.55	5.57	0.38	100	5.95	0.22
HB-RT-03plg.traverse(1)	54.98	27.91	0.27	10.76	5.46	0.39	100	5.85	0.24
HB-RT-03plg.traverse(1)	54.05	28.96	0.29	11.27	4.93	0.33	100	5.26	0.17
HB-RT-03plg.traverse(1)	53.99	28.79	0.28	11.45	4.97	0.33	100	5.30	0.19
HB-RT-03plg.traverse(1)	54.84	28.08	0.30	10.80	5.39	0.36	100	5.75	0.23
HB-RT-03plg.traverse(1)	55.00	28.01	0.29	10.66	5.46	0.33	100	5.79	0.26
HB-RT-03plg.traverse(1)	54.31	28.46	0.33	11.22	5.15	0.31	100	5.46	0.23
HB-RT-03plg.traverse(1)	53.98	28.65	0.29	11.41	5.13	0.32	100	5.45	0.22
HB-RT-03plg.traverse(1)	53.10	29.13	0.33	12.15	4.77	0.29	100	5.06	0.23
HB-RT-03plg.traverse(1)	54.74	28.18	0.30	10.77	5.42	0.38	100	5.80	0.21
HB-RT-03plg.traverse(1)	52.60	29.59	0.29	12.40	4.64	0.23	100	4.87	0.25
HB-RT-03plg.traverse(1)	55.04	27.90	0.34	10.54	5.53	0.41	100	5.94	0.23
HB-RT-03plg.traverse(1)	53.24	29.00	0.32	12.07	4.86	0.29	100	5.15	0.22
HB-RT-03plg.traverse(1)	53.36	28.87	0.31	11.99	4.96	0.30	100	5.26	0.22
HB-RT-03plg.traverse(1)	55.10	27.83	0.32	10.55	5.57	0.42	100	5.99	0.22
HB-RT-03plg.traverse(1)	52.83	29.45	0.32	12.29	4.62	0.26	100	4.88	0.24
HB-RT-03plg.traverse(1)	55.37	27.70	0.32	10.38	5.65	0.36	100	6.01	0.23
HB-RT-03plg.traverse(1)	53.89	28.86	0.29	11.36	5.07	0.33	100	5.40	0.21

HB-RT-03plg.traverse(1)	53.27	29.12	0.29	12.05	4.76	0.27	100	5.03	0.24
HB-RT-03plg.traverse(1)	53.16	29.27	0.28	12.12	4.69	0.27	100	4.96	0.21

HB-RT-03plg.traverse(1)	53.63	29.06	0.27	11.70	4.84	0.28	100	5.12	0.22
HB-RT-03plg.traverse(1)	53.41	29.14	0.25	11.90	4.81	0.28	100	5.09	0.22
HB-RT-03plg.traverse(1)	52.80	29.50	0.27	12.33	4.55	0.29	100	4.84	0.27
HB-RT-03plg.traverse(1)	54.18	28.60	0.28	11.23	5.16	0.32	100	5.48	0.24
HB-RT-03plg.traverse(1)	55.21	27.73	0.26	10.67	5.58	0.34	100	5.92	0.21
HB-RT-03plg.traverse(1)	54.82	27.84	0.32	11.19	5.20	0.39	100	5.59	0.24
HB-RT-03plg.traverse(1)	54.22	28.62	0.29	11.31	5.00	0.30	100	5.30	0.26
HB-RT-03plg.traverse(1)	55.03	27.88	0.23	10.83	5.45	0.37	100	5.82	0.21
HB-RT-03plg.traverse(1)	52.94	29.30	0.31	12.27	4.68	0.26	100	4.94	0.22
HB-RT-03plg.traverse(1)	52.92	29.54	0.30	12.23	4.53	0.25	100	4.78	0.23
HB-RT-03plg.traverse(1)	52.98	29.25	0.31	12.12	4.81	0.29	100	5.10	0.24
HB-RT-03plg.traverse(1)	53.85	28.77	0.32	11.42	5.11	0.30	100	5.41	0.23
HB-RT-03plg.traverse(1)	53.69	28.76	0.35	11.53	5.14	0.28	100	5.42	0.24
HB-RT-03plg.traverse(1)	54.92	28.05	0.32	10.74	5.36	0.37	100	5.73	0.23
HB-RT-03plg.traverse(1)	54.98	28.06	0.30	10.57	5.47	0.40	100	5.87	0.24
HB-RT-03plg.traverse(1)	52.96	29.51	0.28	12.20	4.57	0.28	100	4.85	0.20
HB-RT-03plg.traverse(1)	53.57	28.88	0.29	11.94	4.82	0.29	100	5.11	0.21
HB-RT-03plg.traverse(1)	55.57	27.46	0.36	10.14	5.81	0.45	100	6.26	0.20
HB-RT-03plg.traverse(1)	53.60	28.99	0.30	11.74	4.85	0.28	100	5.13	0.23
HB-RT-03plg.traverse(1)	53.03	29.33	0.29	12.14	4.71	0.28	100	4.99	0.22
HB-RT-03plg.traverse(1)	53.05	29.38	0.29	12.01	4.76	0.29	100	5.05	0.21
HB-RT-03plg.traverse(1)	54.54	28.35	0.35	11.09	5.10	0.35	100	5.45	0.23
HB-RT-03plg.traverse(1)	54.94	27.99	0.31	10.63	5.53	0.39	100	5.92	0.21
HB-RT-03plg.traverse(1)	54.40	28.33	0.33	11.22	5.14	0.35	100	5.49	0.24
HB-RT-03plg.traverse(1)	53.10	29.22	0.29	12.33	4.56	0.26	100	4.82	0.24
HB-RT-03plg.traverse(1)	53.26	29.05	0.28	12.12	4.80	0.29	100	5.09	0.20
HB-RT-03plg.traverse(1)	52.95	29.37	0.30	12.22	4.67	0.28	100	4.95	0.21
HB-RT-03plg.traverse(1)	55.82	27.28	0.38	9.92	5.89	0.45	100	6.34	0.26
HB-RT-03plg.traverse(1)	55.01	28.03	0.29	10.76	5.34	0.37	100	5.71	0.21
HB-RT-03plg.traverse(1)	53.02	29.29	0.32	12.16	4.73	0.28	100	5.01	0.21
HB-RT-03plg.traverse(1)	53.34	29.25	0.28	11.80	4.82	0.30	100	5.12	0.21
HB-RT-03plg.traverse(1)	55.10	27.92	0.37	10.48	5.61	0.30	100	5.91	0.22
HB-RT-03plg.traverse(1)	52.89	29.30	0.29	12.31	4.70	0.28	100	4.98	0.23
HB-RT-03plg.traverse(1)	54.72	28.29	0.30	10.62	5.48	0.34	100	5.82	0.25
HB-RT-03plg.traverse(1)	53.99	28.69	0.39	11.41	4.99	0.32	100	5.31	0.21
HB-RT-03plg.traverse(1)	53.03	29.20	0.30	12.37	4.61	0.27	100	4.88	0.22
HB-RT-03plg.traverse(1)	52.72	29.38	0.25	12.41	4.76	0.29	100	5.05	0.20
HB-RT-03plg.traverse(1)	53.01	29.31	0.27	12.29	4.63	0.26	100	4.89	0.22
HB-RT-03plg.traverse(1)	53.53	29.01	0.30	11.78	4.87	0.27	100	5.14	0.24
HB-RT-03plg.traverse(1)	53.09	29.21	0.36	12.05	4.78	0.29	100	5.07	0.21
HB-RT-03plg.traverse(1)	53.34	29.18	0.31	11.80	4.86	0.29	100	5.15	0.21
HB-RT-03plg.traverse(1)	52.88	29.41	0.31	12.39	4.54	0.26	100	4.80	0.21
HB-RT-03plg.traverse(1)	55.27	27.72	0.29	10.62	5.48	0.40	100	5.88	0.21
HB-RT-03plg.traverse(1)	51.62	30.08	0.51	13.27	4.11	0.25	100	4.36	0.16
HB-RT-03plg.traverse(1)	52.91	29.29	0.32	12.35	4.63	0.29	100	4.92	0.22
HB-RT-03plg.traverse(1)	54.92	28.04	0.35	10.53	5.59	0.33	100	5.92	0.23
HB-RT-03plg.traverse(1)	53.53	28.98	0.34	11.77	4.84	0.30	100	5.14	0.24
HB-RT-03plg.traverse(1)	54.18	28.60	0.30	11.17	5.18	0.33	100	5.51	0.24

HB-RT-03plg.traverse(1)	54.81	28.05	0.32	10.77	5.38	0.44	100	5.82	0.23
HB-RT-03plg.traverse(1)	52.73	29.50	0.32	12.53	4.48	0.24	100	4.72	0.20

HB-RT-03plg.traverse(1)	54.38	28.66	0.31	10.83	5.28	0.35	100	5.63	0.20
HB-RT-03plg.traverse(1)	53.77	28.97	0.31	11.63	4.83	0.29	100	5.12	0.20
HB-RT-03plg.traverse(1)	53.01	29.36	0.28	12.21	4.65	0.25	100	4.90	0.24
HB-RT-03plg.traverse(1)	54.32	28.55	0.31	11.03	5.22	0.33	100	5.55	0.23
HB-RT-03plg.traverse(1)	52.76	29.61	0.27	12.41	4.52	0.24	100	4.76	0.20
HB-RT-03plg.traverse(1)	52.80	29.55	0.33	12.19	4.63	0.27	100	4.90	0.23
HB-RT-03plg.traverse(1)	52.88	29.61	0.32	12.17	4.55	0.27	100	4.82	0.20
HB-RT-03plg.traverse(1)	52.83	29.40	0.30	12.20	4.78	0.25	100	5.03	0.23
HB-RT-03plg.traverse(1)	53.45	29.17	0.27	11.69	4.92	0.30	100	5.22	0.20
HB-RT-03plg.traverse(1)	55.82	27.40	0.36	9.89	5.87	0.45	100	6.32	0.21
HB-RT-03plg.traverse(1)	54.83	28.23	0.29	10.71	5.33	0.39	100	5.72	0.22
HB-RT-03plg.traverse(1)	53.05	29.18	0.28	12.26	4.72	0.29	100	5.01	0.21
HB-RT-03plg.traverse(1)	54.62	28.28	0.33	10.87	5.37	0.31	100	5.68	0.21
HB-RT-03plg.traverse(1)	53.26	29.09	0.34	11.89	4.90	0.30	100	5.20	0.23
HB-RT-03plg.traverse(1)	53.05	29.33	0.33	12.16	4.64	0.27	100	4.91	0.23
HB-RT-03plg.traverse(1)	55.80	27.45	0.35	9.90	5.86	0.41	100	6.27	0.22
HB-RT-03plg.traverse(1)	52.26	29.93	0.34	12.46	4.54	0.25	100	4.79	0.22
HB-RT-03plg.traverse(1)	54.62	28.27	0.35	10.65	5.52	0.36	100	5.88	0.23
HB-RT-03plg.traverse(1)	54.14	28.51	0.29	11.22	5.25	0.38	100	5.63	0.22
HB-RT-03plg.traverse(1)	53.16	29.27	0.31	12.15	4.67	0.22	100	4.89	0.23
HB-RT-03plg.traverse(1)	54.83	28.15	0.35	10.54	5.48	0.42	100	5.90	0.24
HB-RT-03plg.traverse(1)	52.93	29.52	0.29	12.15	4.64	0.26	100	4.90	0.21
HB-RT-03plg.traverse(1)	54.43	28.35	0.30	11.20	5.18	0.32	100	5.50	0.21
HB-RT-03plg.traverse(1)	53.66	28.80	0.29	11.67	5.01	0.31	100	5.32	0.26
HB-RT-03plg.traverse(1)	54.41	28.37	0.33	11.17	5.14	0.30	100	5.44	0.28
HB-RT-03plg.traverse(1)	53.36	29.20	0.29	11.94	4.73	0.27	100	5.00	0.21
HB-RT-03plg.traverse(1)	53.48	28.99	0.30	11.73	5.00	0.29	100	5.29	0.21
HB-RT-03plg.traverse(1)	54.70	28.15	0.34	10.81	5.43	0.35	100	5.78	0.22
HB-RT-03plg.traverse(1)	54.43	28.50	0.29	10.87	5.34	0.36	100	5.70	0.21
HB-RT-03plg.traverse(1)	55.05	27.94	0.34	10.54	5.57	0.35	100	5.92	0.20
HB-RT-03plg.traverse(1)	53.59	28.94	0.33	11.77	4.80	0.34	100	5.14	0.22
HB-RT-03plg.traverse(1)	53.29	29.25	0.27	11.99	4.67	0.28	100	4.95	0.25
HB-RT-03plg.traverse(1)	52.64	29.52	0.33	12.61	4.44	0.24	100	4.68	0.22
HB-RT-03plg.traverse(1)	55.01	28.02	0.26	10.50	5.62	0.39	100	6.01	0.21
HB-RT-03plg.traverse(1)	53.84	28.91	0.31	11.45	4.96	0.29	100	5.25	0.24
HB-RT-03plg.traverse(1)	53.30	29.11	0.31	11.86	4.89	0.27	100	5.16	0.26
HB-RT-03plg.traverse(1)	54.30	28.39	0.26	11.32	5.18	0.32	100	5.50	0.22
HB-RT-03plg.traverse(1)	54.55	28.43	0.24	10.82	5.40	0.33	100	5.73	0.22
HB-RT-03plg.traverse(1)	55.10	27.97	0.34	10.58	5.41	0.40	100	5.81	0.21
HB-RT-03plg.traverse(1)	56.34	27.08	0.34	9.37	6.08	0.56	100	6.64	0.22
HB-RT-03plg.traverse(1)	52.63	29.66	0.28	12.36	4.59	0.25	100	4.84	0.22
HB-RT-03plg.traverse(1)	54.50	28.21	0.34	10.92	5.41	0.40	100	5.81	0.22
HB-RT-03plg.traverse(1)	55.87	27.42	0.37	9.80	5.86	0.46	100	6.32	0.22
HB-RT-03plg.traverse(1)	53.93	28.72	0.39	11.37	4.96	0.39	100	5.35	0.24
HB-RT-03plg.traverse(1)	54.52	28.13	0.42	10.91	5.44	0.36	100	5.80	0.22
HB-RT-03plg.traverse(1)	52.72	29.53	0.32	12.35	4.56	0.28	100	4.84	0.24
HB-RT-03plg.traverse(1)	52.93	29.38	0.30	12.36	4.53	0.28	100	4.81	0.23
HB-RT-03plg.traverse(1)	53.56	28.98	0.32	11.61	4.99	0.33	100	5.32	0.21

HB-RT-03plg.traverse(1)	54.74	28.18	0.30	10.75	5.47	0.34	100	5.81	0.22
HB-RT-03plg.traverse(1)	55.16	27.98	0.36	10.44	5.46	0.37	100	5.83	0.22

HB-RT-03plg.traverse(1)	52.98	29.36	0.35	12.13	4.73	0.25	100	4.98	0.20
HB-RT-03plg.traverse(1)	51.67	29.99	0.54	13.24	4.10	0.29	100	4.39	0.17
HB-RT-03plg.traverse(1)	54.07	28.60	0.26	11.28	5.28	0.30	100	5.58	0.21
HB-RT-03plg.traverse(1)	52.53	29.65	0.30	12.47	4.55	0.28	100	4.83	0.23
HB-RT-03plg.traverse(1)	53.02	29.23	0.30	12.32	4.61	0.31	100	4.92	0.21
HB-RT-03plg.traverse(1)	54.93	28.12	0.28	10.68	5.40	0.38	100	5.78	0.21
HB-RT-03plg.traverse(1)	52.81	29.51	0.28	12.35	4.55	0.26	100	4.81	0.24
HB-RT-03plg.traverse(1)	52.72	29.44	0.32	12.44	4.59	0.27	100	4.86	0.22
HB-RT-03plg.traverse(1)	54.51	28.15	0.37	11.10	5.28	0.36	100	5.64	0.24
HB-RT-03plg11c	53.18	29.43	0.21	11.99	4.78	0.19	100	4.97	0.21
HB-RT-03plg11iii	52.99	29.33	0.27	12.14	4.79	0.24	100	5.03	0.24
HBRT 4									
HB-RT-04plag2	53.00	29.70	0.31	12.08	4.44	0.27	100	4.71	0.20
HB-RT-04plag2r	53.01	29.26	0.38	12.20	4.65	0.32	100	4.97	0.18
HB-RT-04plag3c	50.62	31.19	0.26	14.24	3.32	0.15	100	3.47	0.21
HB-RT-04plag.traverse(2)	51.47	30.73	0.28	13.23	3.90	0.20	100	4.10	0.19
HB-RT-04plag.traverse(2)	51.21	30.63	0.33	13.51	3.95	0.18	100	4.13	0.19
HB-RT-04plag.traverse(2)	51.04	30.80	0.29	13.89	3.59	0.16	100	3.75	0.22
HB-RT-04plag.traverse(2)	51.29	30.70	0.30	13.32	3.94	0.21	100	4.15	0.22
HB-RT-04plag.traverse(2)	52.00	30.18	0.28	13.14	4.02	0.18	100	4.20	0.21
HB-RT-04plag.traverse(2)	52.33	29.94	0.33	12.78	4.15	0.27	100	4.42	0.19
HB-RT-04plag.traverse(2)	52.16	30.26	0.29	12.89	3.98	0.20	100	4.18	0.22
HB-RT-04plag.traverse(2)	52.83	29.75	0.27	12.41	4.26	0.27	100	4.53	0.21
HB-RT-04plag.traverse(2)	51.31	30.65	0.30	13.40	3.95	0.19	100	4.14	0.19
HB-RT-04plag.traverse(2)	51.84	30.47	0.23	13.18	3.83	0.23	100	4.06	0.22
HB-RT-04plag.traverse(2)	51.59	30.26	0.34	13.36	4.05	0.20	100	4.25	0.19
HB-RT-04plag.traverse(2)	52.13	30.09	0.28	13.04	4.07	0.18	100	4.25	0.20
HB-RT-04plag.traverse(2)	52.93	29.71	0.26	12.38	4.28	0.22	100	4.50	0.23
HB-RT-04plag.traverse(2)	52.63	29.84	0.26	12.55	4.25	0.27	100	4.52	0.21
HB-RT-04plag.traverse(2)	51.98	30.21	0.27	13.06	4.04	0.21	100	4.25	0.21
HB-RT-04plag.traverse(2)	52.51	29.95	0.26	12.44	4.41	0.22	100	4.63	0.20
HB-RT-04plag.traverse(2)	53.24	29.44	0.28	12.23	4.38	0.22	100	4.60	0.22
HB-RT-04plag.traverse(2)	51.43	30.63	0.29	13.26	3.99	0.19	100	4.18	0.21
HB-RT-04plag.traverse(2)	51.86	30.21	0.29	13.35	3.88	0.19	100	4.07	0.22
HB-RT-04plag.traverse(2)	53.00	29.38	0.29	12.32	4.49	0.28	100	4.77	0.24
HB-RT-04plag.traverse(2)	51.76	30.39	0.30	13.29	3.89	0.17	100	4.06	0.20
HB-RT-04plag.traverse(2)	51.55	30.71	0.37	12.93	4.05	0.20	100	4.25	0.20
HB-RT-04plag.traverse(2)	51.62	30.49	0.32	13.21	3.95	0.20	100	4.15	0.20
HB-RT-04plag.traverse(2)	51.82	30.28	0.28	13.23	3.97	0.18	100	4.15	0.23
HB-RT-04plag.traverse(2)	51.86	30.17	0.27	12.72	4.54	0.25	100	4.79	0.19
HB-RT-04plag.traverse(2)	50.90	30.91	0.29	13.91	3.62	0.16	100	3.78	0.21
HB-RT-04plag.traverse(2)	50.87	31.11	0.27	13.79	3.57	0.17	100	3.74	0.21
HB-RT-04plag.traverse(2)	52.85	29.71	0.27	12.49	4.26	0.23	100	4.49	0.21
HB-RT-04plag.traverse(2)	52.89	29.67	0.30	12.23	4.42	0.27	100	4.69	0.22
HB-RT-04plag.traverse(2)	51.59	30.49	0.29	13.22	4.01	0.18	100	4.19	0.22
HB-RT-04plag.traverse(2)	51.71	30.37	0.30	13.21	3.96	0.22	100	4.18	0.25
HB-RT-04plag.traverse(2)	51.90	30.37	0.27	13.05	3.98	0.18	100	4.16	0.24

HB-RT-04plag.traverse(2)	50.76	31.19	0.31	13.79	3.60	0.16	100	3.76	0.19
HB-RT-04plag.traverse(2)	52.91	29.58	0.30	12.23	4.46	0.28	100	4.74	0.23

HB-RT-04plag.traverse(2)	53.00	29.64	0.28	12.09	4.53	0.25	100	4.78	0.21
HB-RT-04plag.traverse(2)	53.10	29.58	0.32	12.09	4.45	0.26	100	4.71	0.22
HB-RT-04plag.traverse(2)	51.63	30.57	0.28	13.33	3.79	0.20	100	3.99	0.20
HB-RT-04plag.traverse(2)	52.13	30.31	0.28	12.88	3.96	0.21	100	4.17	0.23
HB-RT-04plag.traverse(2)	50.73	30.97	0.32	13.98	3.63	0.17	100	3.80	0.20
HB-RT-04plag.traverse(2)	52.93	29.57	0.30	12.36	4.35	0.30	100	4.65	0.18
HB-RT-04plag.traverse(2)	51.83	30.41	0.33	13.03	4.02	0.18	100	4.20	0.20
HB-RT-04plag.traverse(2)	52.11	30.13	0.31	13.10	3.93	0.20	100	4.13	0.22
HB-RT-04plag.traverse(2)	51.91	30.16	0.29	13.24	3.97	0.21	100	4.18	0.21
HB-RT-04plag.traverse(2)	51.66	30.53	0.25	13.17	3.99	0.20	100	4.19	0.21
HB-RT-04plag.traverse(2)	51.80	30.33	0.28	13.21	3.99	0.19	100	4.18	0.21
HB-RT-04plag.traverse(2)	52.27	30.01	0.27	12.86	4.11	0.27	100	4.38	0.22
HB-RT-04plag.traverse(2)	51.56	30.48	0.31	13.37	3.88	0.19	100	4.07	0.21
HB-RT-04plag.traverse(2)	51.88	30.24	0.27	13.15	4.02	0.21	100	4.23	0.23
HB-RT-04plag.traverse(2)	51.98	30.23	0.31	13.05	4.03	0.17	100	4.20	0.23
HB-RT-04plag.traverse(2)	52.15	29.99	0.31	13.00	4.14	0.20	100	4.34	0.21
HB-RT-04plag.traverse(2)	50.94	31.06	0.26	13.78	3.58	0.18	100	3.76	0.19
HB-RT-04plag.traverse(2)	51.93	30.43	0.26	12.78	4.13	0.26	100	4.39	0.22
HB-RT-04plag.traverse(2)	51.32	30.70	0.30	13.48	3.84	0.16	100	4.00	0.19
HB-RT-04plag.traverse(2)	52.95	29.59	0.32	12.25	4.38	0.29	100	4.67	0.22
HB-RT-04plag.traverse(2)	52.94	29.45	0.28	12.26	4.56	0.29	100	4.85	0.22
HB-RT-04plag.traverse(2)	53.00	29.70	0.29	12.16	4.38	0.23	100	4.61	0.23
HB-RT-04plag.traverse(2)	51.75	30.42	0.30	13.17	3.96	0.19	100	4.15	0.21
HB-RT-04plag.traverse(2)	53.94	28.78	0.30	11.50	4.88	0.38	100	5.26	0.23
HB-RT-04plag.traverse(2)	52.74	29.62	0.28	12.53	4.40	0.21	100	4.61	0.22
HB-RT-04plag.traverse(2)	52.58	29.67	0.28	12.62	4.36	0.29	100	4.65	0.21
HB-RT-04plag.traverse(2)	51.65	30.35	0.29	13.46	3.85	0.20	100	4.05	0.19
HB-RT-04plag.traverse(2)	51.91	30.32	0.25	13.00	4.11	0.18	100	4.29	0.23
HB-RT-04plag.traverse(2)	52.63	29.80	0.33	12.34	4.43	0.26	100	4.69	0.22
HB-RT-04plag.traverse(2)	52.85	29.50	0.36	12.32	4.44	0.33	100	4.77	0.20
HB-RT-04plag.traverse(2)	52.39	29.96	0.28	12.66	4.27	0.24	100	4.51	0.21
HB-RT-04plag.traverse(2)	52.74	29.79	0.30	12.23	4.46	0.27	100	4.73	0.21
HB-RT-04plag.traverse(2)	50.58	31.18	0.27	14.05	3.56	0.18	100	3.74	0.19
HB-RT-04plag.traverse(2)	52.45	30.07	0.24	12.54	4.26	0.23	100	4.49	0.21
HB-RT-04plag.traverse(2)	52.99	29.58	0.32	12.15	4.47	0.25	100	4.72	0.25
HB-RT-04plag.traverse(2)	53.00	29.45	0.35	12.32	4.39	0.30	100	4.69	0.19
HB-RT-04plag.traverse(2)	51.94	30.23	0.26	13.05	4.12	0.18	100	4.30	0.21
HB-RT-04plag.traverse(2)	52.66	29.68	0.30	12.40	4.48	0.27	100	4.75	0.20
HB-RT-04plag.traverse(2)	52.16	30.22	0.28	12.83	4.15	0.22	100	4.37	0.15
HB-RT-04plag.traverse(2)	51.72	30.42	0.26	13.21	4.02	0.19	100	4.21	0.20
HB-RT-04plag.traverse(2)	52.53	29.88	0.22	12.68	4.30	0.21	100	4.51	0.19
HB-RT-04plag.traverse(2)	52.52	29.89	0.26	12.64	4.29	0.20	100	4.49	0.20
HB-RT-04plag.traverse(2)	53.26	29.45	0.29	12.06	4.46	0.27	100	4.73	0.20
HB-RT-04plag.traverse(2)	51.66	30.46	0.29	13.29	3.91	0.17	100	4.08	0.22
HB-RT-04plag.traverse(2)	51.01	30.87	0.31	13.89	3.55	0.16	100	3.71	0.22
HB-RT-04plag.traverse(2)	52.07	30.10	0.28	13.01	4.09	0.23	100	4.32	0.22
HB-RT-04plag.traverse(2)	51.61	30.41	0.30	13.26	3.99	0.21	100	4.20	0.22
HB-RT-04plag.traverse(2)	52.10	30.16	0.32	12.77	4.23	0.25	100	4.48	0.16

HB-RT-04plag.traverse(2)	51.01	31.01	0.29	13.80	3.53	0.15	100	3.68	0.19
HB-RT-04plag.traverse(2)	52.00	30.22	0.29	13.15	3.92	0.20	100	4.12	0.22

HB-RT-04plag.traverse(2)	52.67	29.72	0.34	12.33	4.45	0.30	100	4.75	0.19
HB-RT-04plag.traverse(2)	51.25	30.82	0.30	13.45	3.76	0.22	100	3.98	0.21
HB-RT-04plag.traverse(2)	51.57	30.51	0.28	13.53	3.74	0.16	100	3.90	0.21
HB-RT-04plag.traverse(2)	52.90	29.54	0.32	12.35	4.37	0.31	100	4.68	0.21
HB-RT-04plag.traverse(2)	51.44	30.61	0.29	13.52	3.76	0.18	100	3.94	0.20
HB-RT-04plag.traverse(2)	53.16	29.53	0.27	12.11	4.50	0.24	100	4.74	0.19
HB-RT-04plag.traverse(2)	52.59	29.81	0.28	12.65	4.22	0.25	100	4.47	0.21
HB-RT-04plag.traverse(2)	52.89	29.61	0.29	12.52	4.22	0.24	100	4.46	0.22
HB-RT-04plag.traverse(2)	52.36	29.87	0.32	12.69	4.31	0.24	100	4.55	0.21
HB-RT-04plag.traverse(2)	52.48	29.97	0.28	12.66	4.15	0.24	100	4.39	0.22
HB-RT-04plag.traverse(2)	52.89	29.61	0.29	12.20	4.52	0.27	100	4.79	0.23
HB-RT-04plag.traverse(2)	52.65	29.99	0.29	12.40	4.23	0.25	100	4.48	0.20
HB-RT-04plag.traverse(2)	50.88	31.01	0.26	13.89	3.57	0.18	100	3.75	0.21
HB-RT-04plag.traverse(2)	53.34	29.47	0.25	12.04	4.46	0.24	100	4.70	0.20
HB-RT-04plag.traverse(2)	52.95	29.59	0.28	12.28	4.46	0.22	100	4.68	0.22
HB-RT-04plag.traverse(2)	51.65	30.57	0.31	13.14	3.95	0.18	100	4.13	0.19
HB-RT-04plag.traverse(2)	52.59	29.88	0.25	12.65	4.19	0.24	100	4.43	0.20
HB-RT-04plag.traverse(2)	51.88	30.29	0.32	13.00	4.09	0.19	100	4.28	0.23
HB-RT-04plag.traverse(2)	52.77	29.74	0.28	12.43	4.32	0.22	100	4.54	0.24
HB-RT-04plag.traverse(2)	51.69	30.41	0.24	13.21	4.06	0.20	100	4.26	0.20
HB-RT-04plag.traverse(2)	52.66	29.66	0.31	12.44	4.41	0.29	100	4.70	0.22
HB-RT-04plag.traverse(2)	52.22	30.17	0.25	12.78	4.10	0.25	100	4.35	0.22
HB-RT-04plag.traverse(2)	52.47	29.85	0.28	12.58	4.32	0.29	100	4.61	0.20
HB-RT-04plag.traverse(2)	53.02	29.56	0.26	12.16	4.51	0.24	100	4.75	0.25
HB-RT-04plag.traverse(2)	53.33	29.48	0.31	11.73	4.61	0.33	100	4.94	0.21
HB-RT-04plag.traverse(2)	52.95	29.68	0.31	12.21	4.34	0.30	100	4.64	0.20
HB-RT-04plag.traverse(2)	52.33	30.09	0.30	12.68	4.15	0.24	100	4.39	0.20
HB-RT-04plag.traverse(2)	52.01	30.24	0.32	13.15	3.89	0.20	100	4.09	0.21
HB-RT-04plag.traverse(2)	52.99	29.33	0.28	12.29	4.52	0.35	100	4.87	0.24
HB-RT-04plag.traverse(2)	52.62	29.80	0.25	12.54	4.28	0.29	100	4.57	0.23
HB-RT-04plag.traverse(2)	54.16	28.61	0.36	12.24	4.13	0.28	100	4.41	0.21
HB-RT-04plag.traverse(2)	50.97	30.87	0.27	13.85	3.68	0.15	100	3.83	0.21
HB-RT-04plag.traverse(2)	53.01	29.56	0.27	12.17	4.54	0.24	100	4.78	0.21
HB-RT-04plag.traverse(2)	53.05	29.61	0.29	12.14	4.43	0.23	100	4.66	0.24
HB-RT-04plag5ccc	49.92	31.42	0.31	14.84	3.21	0.13	100	3.34	0.17
HB-RT-04plag5ii	49.91	31.68	0.25	14.62	3.25	0.11	100	3.36	0.17
HB-RT-04plag5iii	52.30	29.82	0.27	12.86	4.30	0.22	100	4.52	0.21
HB-RT-04plag5r	50.47	31.08	0.28	14.48	3.40	0.12	100	3.52	0.18
HB-RT-04plag5vi	51.67	30.10	0.34	13.43	3.99	0.26	100	4.25	0.22
Paua Bay									
12PRBP	52.5	30.31	0	12.95	3.91	0.33	100	4.24	
	51.68	30.87	0.38	12.94	3.81	0.31	100	4.12	
	51.16	30.32	1.76	12.83	3.62	0.31	100	3.93	
	51.82	30.64	0.79	12.89	3.61	0.25	100	3.86	
	50.86	31.23	0.49	13.79	3.43	0.2	100	3.63	
19PRBP	52.14	30.24	0.32	12.85	4.14	0.32	100	4.46	
	52.66	29.93	0.34	12.59	4.26	0.23	100	4.49	

57.85	27.63	2.96	0.95	1.94	6.5	100	8.44
51.63	30.49	0.55	13.1	3.96	0.27	100	4.23

	52.73	29.87	0.46	12.68	3.98	0.29	100	4.27
20PRBP	49.57	32.36	0.56	14.29	2.87	0.25	100	3.12
	49.85	32.25	0.58	14.22	2.87	0.23	100	3.1
	52.06	30.47	0.4	13.1	3.58	0.39	100	3.97
	51.28	30.63	0.47	13.64	3.69	0.29	100	3.98
22PRBP	51.72	31.54	0.38	12.84	3.22	0.3	100	3.52
	51.22	29.88	1.75	11.97	4.21	0.41	100	4.62
	53.29	29.62	0.31	12.05	4.35	0.39	100	4.74
	51.01	30.99	0.39	13.64	3.69	0.29	100	3.98
Goat Rock Host								
GR18								0.00
GR18	56.83	26.88	0.34	8.40	6.71	0.62	99.78	7.33
GR18	56.06	27.74	0.39	9.12	6.14	0.51	99.96	6.65
GR18	56.51	27.08	0.37	8.55	6.44	0.54	99.48	6.97
GR18								0.00
GR18	57.17	26.82	0.24	8.14	6.59	0.69	99.63	7.27
GR18	57.92	26.54	0.24	7.40	6.77	0.82	99.69	7.59
GR18	58.33	25.74	0.18	7.11	7.14	0.90	99.40	8.03
GR18	58.22	25.66	0.24	6.72	7.26	0.98	99.08	8.24
GR18	59.75	25.71	0.23	6.56	7.35	1.14	100.74	8.49
GR18								0.00
GR18	62.58	22.77	0.21	3.64	8.09	2.69	99.97	10.78
GR18	60.31	25.11	0.25	5.70	7.69	1.20	100.26	8.89
GR18	62.68	22.97	0.21	3.58	8.13	2.76	100.32	10.89
GR18	62.16	22.86	0.16	3.85	7.95	2.56	99.54	10.50
GR18	62.42	23.03	0.23	3.70	7.97	3.00	100.34	10.97
GR18	60.77	24.40	0.19	5.37	7.82	1.43	99.98	9.25
GR18	62.52	22.79	0.20	3.72	7.88	2.67	99.77	10.54
GR18	60.78	24.33	0.25	5.39	7.68	1.48	99.91	9.16
GR18	61.13	24.37	0.22	5.38	7.84	1.49	100.43	9.33
GR18								0.00
GR18	61.41	24.29	0.25	4.96	7.88	1.63	100.42	9.51
GR18	64.13	21.42	0.42	2.13	7.56	4.61	100.26	12.16
GR18	61.01	24.19	0.20	5.12	7.77	1.65	99.94	9.42
GR18	61.46	24.04	0.20	4.95	7.94	1.43	100.03	9.37
GR18	61.07	23.96	0.16	4.97	7.80	1.64	99.60	9.44
GR18	57.82	25.52	0.38	6.99	6.98	1.31	99.00	8.29
GR18	55.37	27.93	0.48	9.22	6.15	0.51	99.66	6.67
GR18								0.00
GR18	57.56	26.29	0.23	8.13	6.75	0.78	99.74	7.53
GR18	59.26	25.62	0.18	6.55	7.25	1.03	99.89	8.28
GR18	60.83	24.51	0.25	5.26	7.71	1.44	100.00	9.15
GR18	60.12	25.48	0.21	5.98	7.49	1.32	100.60	8.82
GR18								0.00
GR18	57.22	26.37	0.23	7.98	6.69	0.80	99.30	7.49
GR18	57.48	26.62	0.29	7.81	6.66	0.76	99.61	7.43
GR18	58.42	26.44	0.22	7.51	6.70	0.85	100.15	7.55

GR18	57.78	26.89	0.20	8.12	6.46	0.69	100.14	7.15
GR18	57.18	27.31	0.16	9.11	6.31	0.61	100.67	6.91

GR18	57.14	27.34	0.21	8.71	6.52	0.73	100.63	7.24
GR18	60.03	23.68	0.37	4.51	6.52	3.42	98.53	9.94
GR18	59.29	25.48	0.31	6.30	7.13	1.46	99.97	8.59
GR18								0.00
GR18	60.45	24.47	0.24	5.52	7.76	1.31	99.73	9.06
GR18	59.49	25.64	0.17	7.01	7.24	0.98	100.53	8.22
GR18	57.20	27.32	0.22	8.64	6.41	0.64	100.42	7.05
GR18	56.78	27.69	0.21	8.92	6.17	0.68	100.45	6.85
GR18	56.66	27.47	0.25	8.50	6.30	0.62	99.81	6.92
GR18	56.41	27.46	0.30	8.78	6.04	0.62	99.61	6.66
GR18	63.14	21.09	0.70	2.36	7.05	4.97	99.32	12.02
GR18	58.91	25.17	0.24	6.54	7.36	1.07	99.29	8.43
GR18								0.00
GR18	60.81	24.48	0.23	5.30	7.79	1.48	100.10	9.27
GR18	61.01	24.73	0.22	5.38	7.56	1.38	100.28	8.94
GR18	60.73	24.51	0.21	5.04	7.56	1.66	99.70	9.22
GR18	61.27	24.82	0.24	5.51	7.92	1.38	101.14	9.30
GR18	61.07	24.77	0.18	4.92	7.78	1.87	100.58	9.65
GR18	60.39	24.51	0.18	5.35	7.67	1.38	99.47	9.05
GR18	61.01	24.39	0.24	5.18	7.86	1.49	100.17	9.35
GR18								0.00
GR18	60.88	24.96	0.30	5.45	7.68	1.45	100.72	9.13
GR18	60.79	24.24	0.37	5.40	7.80	1.39	99.99	9.19
GR18								0.00
GR18	59.37	24.72	0.24	6.52	7.52	1.14	99.50	8.66
GR18	62.40	23.84	0.23	4.53	8.23	1.64	100.87	9.87
GR18	55.49	27.79	0.38	9.73	5.89	0.42	99.71	6.31
GR18	55.52	27.90	0.37	9.52	5.87	0.52	99.71	6.40
GR18	56.26	27.28	0.54	9.11	6.21	0.49	99.88	6.70
GR18	59.13	25.13	0.25	6.05	7.67	0.97	99.21	8.65
GR18	58.49	25.34	0.22	6.80	7.30	0.91	99.07	8.22
GR18	59.21	25.38	0.26	6.18	7.45	1.17	99.66	8.62
GR18								0.00
GR18	62.22	23.61	0.18	4.39	8.04	1.97	100.41	10.01
GR18	62.67	23.43	0.22	4.25	7.95	2.15	100.67	10.09
GR18	60.91	24.39	0.30	5.67	7.76	1.23	100.26	8.99
GR18	60.10	24.50	0.23	5.25	7.78	1.56	99.42	9.34
GR18	61.38	23.97	0.14	4.93	7.80	1.43	99.65	9.23
GR18	61.58	23.23	0.20	4.21	7.93	1.97	99.12	9.90
GR18								0.00
GR18	56.06	27.05	0.19	8.17	6.40	0.76	98.63	7.16
GR18	56.75	27.12	0.21	8.23	6.55	0.78	99.64	7.33
GR18	59.81	24.11	0.27	5.21	7.18	2.63	99.21	9.80
GR18	57.34	26.31	0.21	7.88	6.76	0.86	99.36	7.62
GR18	57.10	27.11	0.22	8.59	6.44	0.70	100.16	7.15
GR18	56.61	26.84	0.21	8.18	6.41	0.69	98.94	7.10
GR18	61.36	23.60	0.16	4.16	7.91	1.87	99.07	9.78
GR18	61.99	23.60	0.16	4.30	8.07	1.77	99.89	9.83

GR18	61.02	23.72	0.20	4.68	8.11	1.69	99.42	9.80
GR18								0.00

GR18	66.05	19.17	0.16	0.29	6.36	8.05	100.08	14.42
GR18	64.98	19.61	0.15	0.69	6.61	7.70	99.74	14.31
GR18	65.00	19.06	0.13	0.31	6.25	7.94	98.68	14.19
GR18	65.31	18.98	0.20	0.31	6.19	7.71	98.69	13.89
GR18								0.00
GR18	65.63	19.57	0.17	0.27	6.17	8.21	100.01	14.38
GR18	65.44	19.12	0.13	0.33	6.39	7.94	99.35	14.33
GR18	66.11	19.15	0.13	0.31	6.21	8.23	100.15	14.45
GR18	65.64	18.85	0.11	0.25	6.13	8.26	99.26	14.39
GR18								0.00
GR18	61.09	23.39	0.22	4.12	7.89	2.13	98.83	10.02
GR18	60.17	24.23	0.42	5.25	7.82	1.53	99.42	9.35
GR18	60.12	24.38	0.17	5.57	7.67	1.30	99.21	8.96
GR18	60.30	25.15	0.26	5.41	7.66	1.25	100.03	8.91
GR18								0.00
GR18	59.84	25.01	0.19	5.87	7.63	1.31	99.85	8.93
GR18	54.87	27.98	0.16	9.35	5.70	0.55	98.60	6.24
GR18	59.92	24.60	0.19	5.80	7.66	1.29	99.46	8.95
GR18								0.00
GR18	58.42	25.16	0.17	6.57	7.15	1.07	98.54	8.22
GR18	58.38	25.87	0.26	6.83	7.42	1.05	99.81	8.47
GR18	58.52	25.29	0.24	6.76	7.32	1.02	99.15	8.33
GR18								0.00
GR18	59.20	24.48	0.21	6.30	7.50	1.14	98.83	8.65
GR18	58.58	25.21	0.25	6.34	7.44	1.12	98.94	8.56
GR18	60.05	25.17	0.20	6.46	7.41	1.10	100.38	8.51
DucksFoot Bay								
PAB33								0.00
PAB33	53.69	28.54	0.51	10.40	5.38	0.35	98.86	5.73
PAB33								0.00
PAB33	53.97	28.52	0.35	10.75	5.23	0.37	99.19	5.60
PAB33	54.01	28.04	0.41	10.35	5.42	0.34	98.57	5.76
PAB33	54.14	28.61	0.41	10.73	5.30	0.38	99.57	5.69
PAB33	52.22	29.45	0.37	11.43	4.86	0.35	98.69	5.21
PAB33	53.97	28.65	0.38	10.16	5.58	0.36	99.11	5.95
PAB33								0.00
PAB33	53.58	28.39	0.48	10.40	5.23	0.39	98.47	5.62
PAB33	54.14	28.00	0.34	9.81	5.91	0.37	98.57	6.28
PAB33	54.59	28.14	0.39	9.76	5.67	0.38	98.94	6.06
PAB33	53.77	28.75	0.60	10.29	5.20	0.39	99.00	5.59
PAB33								0.00
PAB33	56.84	26.81	0.30	8.34	6.52	0.45	99.26	6.97
PAB33	54.19	27.96	0.54	10.32	5.36	0.44	98.81	5.80
PAB33								0.00
PAB33	53.96	28.93	0.54	10.42	5.38	0.38	99.61	5.77
PAB33								0.00
PAB33	54.28	28.03	0.39	10.24	5.21	0.35	98.50	5.56

PAB33	53.47	28.72	0.45	10.54	5.22	0.33	98.73	5.55
PAB33	52.67	29.18	0.52	11.02	5.12	0.31	98.81	5.42

PAB33								0.00
PAB33	54.08	28.22	0.47	10.19	5.33	0.41	98.70	5.74
PAB33	54.31	28.12	0.55	10.53	5.51	0.41	99.43	5.92
PAB33	54.61	28.11	0.50	10.18	5.37	0.31	99.08	5.68
PAB33								0.00
PAB33	53.71	27.98	0.44	10.62	5.52	0.40	98.67	5.92
PAB33	54.35	28.04	0.52	10.00	5.55	0.46	98.91	6.01

Table 10. Bright CL chemistries

Spectrum Label	Si	Ti	Al	Fe	Mg	Ca	Na	K	P	W	S	Mn	Ge	Rb	Sb	Mo	Ir	Te	Total	Alkalis
Haylocks Lithics																				
HBRT 3																				
Spectrum 5	10.36	9.55	5.21	70.25	4.63														100	
Spectrum 6	7.23	10.23	4.06	71.2	6.26	1.02													100	
Spectrum 7	12.52	9.48	4.59	65.7	5.71	1.99													100	
Spectrum 8	11.9	7.56	4.01	70.71	4	1.82													100	
Goat Rock Lithics																				
GR8 Site 1																				
Spectrum 8	58.08	1.21	21.88	3.78		4.93	7.01	2.01	1.1										100	9.02
Spectrum 9	57.79	2.07	21.5	4.83	0.24	3.7	7.02	2.41	0.43										100	9.43
Spectrum 10	55.82	1.85	21.08	8.48		3.72	6.74	2.32											100	9.06
Spectrum 11	59.09	0.53	19.83	4.86	1.3	5.11	6.14	2.29	0.86										100	8.43
Spectrum 12	62.35		20.98	2.37		3.69	7.35	3.26											100	10.61
Spectrum 13	60.74	0.56	21.03	3.41		3.29	6.56	3.72	0.68										100	10.28
GR8 Site 2																				
Spectrum 1	60.51	0.24	23.89	0.74		5.14	7.86	1.62											100	9.48
Spectrum 2	58.27	0.23	23.34	0.83		4.69	7.72	1.93				3							100	9.65
Spectrum 3	59.87		24.06	1.43		5.18	7.78	1.68											100	9.46
Spectrum 4	60.68		23.76	1.01		4.83	7.83	1.89											100	9.72
Spectrum 5	60.42		24.14	0.82		5.61	7.71	1.31											100	9.02
Spectrum 6	60.38	0.33	23.71	1.05		4.85	7.57	2.1											100	9.67
Spectrum 7	57.32	0.27	23.8	0.66		5.32	7.65	1.5				3.48							100	9.15
Spectrum 8	59.56	0.56	24.2	0.93		5.5	7.69	1.58											100	9.27
Spectrum 9	58.22	0.72	23.82	2.48		5.09	7.2	2.12	0.36										100	9.32
Spectrum 10	56.04	1.08	23.16	3.92		4.77	7.3	1.93				1.8							100	9.23
GR20 S10																				
Spectrum 37	65.35		34.65																100	0
Spectrum 38	64.89		35.11																100	0
Spectrum 39	100																		100	0
Spectrum 40	57.73		25.46	5.97	1.76	5.28	3.03	0.76											100	3.79

Spectrum 41	57.64		26.16	5.23	1.55	5.06	3.73	0.62					100	4.35
Spectrum 42	58.12		25.95	4.24	1.48	5.71	3.5	1					100	4.5
Spectrum 43	57.4		25.8	2.03	0.52	8.1	5.38	0.77					100	6.15
Spectrum 44	57.58		25.89	4.1	1.19	6.2	4.05	0.98					100	5.03
Spectrum 45	57.12		25.65	1.84	0.63	8.58	4.13	0.91	0.4			0.75	100	5.04
Spectrum 46	58.03		24.64	2.42	0.6	7.34	4.65	0.9			1.41		100	5.55
Spectrum 47	57.11		26.18	2.08	0.72	8.84	4.03	1.05					100	5.08
Spectrum 48	58.23		26.12	1.73	0.51	7.2	5.48	0.72					100	6.2
GR20 S6														
Spectrum 46	61.54	0.25	22.53	1.14		3.9	7.22	3			0.26	0.08	99.92	10.22
Spectrum 47	62.86		22.21	0.37		3.6	6.49	4.4				0.07	100	10.89
Spectrum 48	62.88		22.35	0.47		3.69	6.68	3.93					100	10.61
Spectrum 49	60.48	0.65	22.62	2.35		3.86	7.32	2.72				0	100	10.04
Spectrum 50	62.09		22.06	1.29		3	5.75	5.82				0	100	11.57
Spectrum 51	63.81		21.3	0.65		2.5	5.87	5.88					100	11.75
Spectrum 52	62.62		22.64	0.53		3.74	6.68	3.79					100	10.47
Spectrum 53	61.46	0.47	21.7	2.44		3.31	7.08	3.53					100	10.61
Spectrum 54	61.67		23.18	0.63		4.48	6.9	3.14				0	100	10.04
Spectrum 59	57.23	0.48	22.85	4.87	0.84	6.53	5.56	1.11					99.47	6.67
Spectrum 60	58.52		23.68	4.22	0.94	6.45	4.75	0.94					99.5	5.69
Spectrum 61	57.57		23.74	5.57	1.01	5.98	4.74	0.8					99.41	5.54
Spectrum 62	59.39		22.52	4.42	1.03	5.04	4.99	1.09	0.96				99.45	6.08
Spectrum 63	58.69		24.97	2.24	0.75	6.58	5.4	0.97					99.61	6.37
Spectrum 64	58.27		24.01	4.35	0.92	5.67	5.41	0.82					99.45	6.23
Spectrum 65	59.95		23.14	3.34	0.86	5.24	6.02	1.11					99.65	7.13
GR20 S7														
Spectrum 70	55.36	2.14	19.25	9.8		2.5	6.06	4.9					100	10.96
Spectrum 71	63.73		21.94	0.66		3.03	7.11	3.54					100	10.65
Spectrum 72	63.5		22.61			3.53	6.95	3.41					100	10.36
Spectrum 73	58.64	1.18	20.75	5.92		2.87	6.08	4.56					100	10.64
Spectrum 74	31.45	7.24	13.9	39.49	1.54	2.17	3.09	0.62					99.5	3.71
Spectrum 75	49.88	3.3	17.45	16.3		2.44	5.86	4.77					100	10.63
GR20 S8														

Spectrum 41	62.82	0.1	22.34	0.48		3.65	7.09	3.52						100	10.61
Spectrum 42	62.16	0.16	23.01	0.5		4.12	7.37	2.67						100	10.04
Spectrum 43	62.66	0.12	22.44	0.38		3.65	6.98	3.77						100	10.75
Spectrum 44	57.65	1.82	19.71	6.9		2.06	6.64	5.07			0.09			99.93	11.71
Spectrum 45	4.12	19.64	3.41	69.06	0.37	0.39	1.06	0.08	0.22		1.28	0.37		100	1.14
GR14 S1															
Spectrum 2	63.18		21.4	1.03		2.58	8.53	3.28						100	11.81
Spectrum 3	61.59		21.13	2.49		2.45	8.51	3.1					0.73	100	11.61
Spectrum 4	61.98	0.5	20.91	2.57		2.43	8.58	3.02						100	11.6
Spectrum 5	64.31		22.03			2.67	8.06	2.94						100	11
Spectrum 15	63.42		21.86			2.79	8.76	3.17						100	11.93
Spectrum 32	64.29		21.11			2.62	8.3	3.67						100	11.97
Spectrum 33	78.18		21.82											100	0
Spectrum 34	61.89		21.94	2.07		3.38	7.55	3.17						100	10.72
Spectrum 35	62.22		22.62	0.83		3.8	8.08	2.45						100	10.53
GR14 S2															
Spectrum 7	59.5	0.48	22.55	1.23	0.25	3.93	8.29	2.13			1.62			100	10.42
Spectrum 8		15.98	6.8	77.11	0	0.04	0.04	0.03						100	0.07
Spectrum 9	58.74	0.25	25.7	0.45	0.1	6.64	7.35	0.77						100	8.12
Spectrum 6			62.86		22.82		7.65	2.97					3.7	100	10.62
Spectrum 36			63.02	0.84	21.82		8.15	3.04					3.14	100	11.19
Spectrum 37			63.3	0.8	21.88		7.62	2.87					3.53	100	10.49
Spectrum 38		0.87	61.83	1.1	22.03	0.5	7.27	2.96					3.45	100	10.23
Spectrum 39			62.58		22.58		7.77	3.62					3.45	100	11.39
Spectrum 40			59.78	4.66	19.79	2	7.29	1.43					5.05	100	8.72
Spectrum 41			63.4		22.15		7.69	2.84					3.92	100	10.53
Spectrum 42			61.51	1.84	22.09		7.6	3.37					3.59	100	10.97
Spectrum 48			62.71	0.6	22.14		8.19	3.26					3.11	100	11.45
Spectrum 49		0.17	60.34	3.67	20.59	1.4	8	2.17					3.67	100	10.17
Spectrum 50	1.46		58.7	0.93	20.89	0.24	8.06	4.52			2.44		2.75	100	12.58
Spectrum 51			61.54	0.74	20.86	0.27	7.62	2.52			2.16		4.29	100	10.14
Spectrum 52			62.96		22.27		8.02	3.52					3.24	100	11.54
Spectrum 53			62.15	1.22	22.42		7.79	3.43					2.98	100	11.22

Spectrum 54			62.78		22.26		7.92	3.48							3.57		100	11.4
GR14 S3																		
Spectrum 18	63.3		21.86			2.86	8.12	3.87									100	11.99
Spectrum 19	61.81		23.66			3.75	8.32	2.46									100	10.78
Spectrum 20	63.5		21.76			3.25	8.51	2.98									100	11.49
Spectrum 21	62.24		20.86	2.22		2.49	8.36	3.84									100	12.2
Spectrum 22	64.39		21.2			3.46	7.38	3.57									100	10.95
Spectrum 43	63.08		21.55	0.87		3.04	7.64	3.82									100	11.46
Spectrum 44	62.21		22.12	0.88		3.1	7.84	3.29						0.55			100	11.13
Spectrum 45	60.9		22.41	0.54		3.76	7.77	2.94							1.68		100	10.71
Spectrum 46	62.53		21.76	1.33		2.8	7.44	4.14									100	11.58
Spectrum 47	60.28	0.25	21.45	0.82		3.66	7.53	3.62							1.68	0.71	100	11.15
GR8b Host S2																		
Spectrum 35	57.85		27.14	0.58		6.74	7.11	0.57									100	7.68
Spectrum 36	54.05	1.04	4.12	8.01	13.68	18.23	0.88										100	0.88
Spectrum 37	3.27	21.71	4.55	65.87	3.55					1.06							100	0
Spectrum 38	8.92	3.73	3.92	7.11		38.76		1.57	36								100	1.57
Spectrum 39	58.34	2.34	18.24	5.58		3.13	2.93	9.44									100	12.37
Spectrum 40	61.34		21.07			4.91	8.09	4.59									100	12.68
Spectrum 41	61.79		23.7	0.54		3.57	9.03	1.38									100	10.41
E. Pigeon Bay																		
EPB4 Lithic S1																		
Spectrum 1	7.15	20.42	4.91	60.81	3.08	1.45				2.17							100	0
Spectrum 2	35.12		15.89	45.19		3.5		0.3									100	0.3
Spectrum 3	39.44		20.04	30.88	1.53	6.97	1.15										100	1.15
Spectrum 4	39.54	0.3	1.71	31.63	25.85	0.85		0.12									100	0.12
Spectrum 5	47.22	2.25	8.37	9.07	11.14	21.42	0.54										100	0.54
Spectrum 6	49.75	1.92	14.39	5.41	7.47	18.11	1.27						1.67				100	1.27
Spectrum 7	49.23	1.46	6.24	7.16	11.22	21.39	0.53				0.09	2.68					100	0.53
Spectrum 8	51.68	1.38	6.07	7.08	12.4	20.83	0.57										100	0.57
Spectrum 9	47.38	2.17	6.95	7.69	10.62	19.91						5.29					100	0

Spectrum 10	50.01	2.37	6.17	7.13	10.59	19.74	0.68					3.31		100	0.68
Spectrum 11	51.06	2.46	7.7	8.21	10.25	18.3	0.76						1.28	100	0.76
Spectrum 12	59.12		22.49	6.2		6.83	4.61	0.74		0				100	5.35
Spectrum 13	51.59		22.65	7.99	6.1	7.44	3.86	0.37		0				100	4.23
Spectrum 14	55.39	0.61	24.41	3.56	1.9	9.29	4.43	0.4						100	4.83
Spectrum 15	58.77		25.28	1.11		8.99	5.04	0.6		0.22				100	5.64
Spectrum 16	56.07		26.16	1.2		10.62	5.26	0.51		0.17				100	5.77
Spectrum 17	61.97		22.95	1.87	0.94	7.68	3.16	1.44						100	4.6
Spectrum 18	55.41		23.08	6.12	0.73	6.45	5.73	1.05	1.44					100	6.78
Spectrum 19	62.39		21.93	2.7	1.12	6.74	3.29	1.83		0				100	5.12
Spectrum 20	62.36		21.35	1.66		6.17	4.89	3.5		0.09				100	8.39
Spectrum 21	59.86		24.77	1.04		7.29	4.73	2.19		0.12				100	6.92
Spectrum 22	63.96	2.67	16.21	5.4	1.39	3.53	2.11	4.72		0				100	6.83
Spectrum 23	56.1		27.13	1.53		9.79	4.69	0.75						100	5.44
EPB 4 Host															
Spectrum 31	62.83		21.42	1.65		3.12	6.74	4.23						100	10.97
Spectrum 32	62.88	0.44	21.93	0.9		3.36	7.26	3.22		0				100	10.48
Spectrum 33	56.97	0.79	19.44	7.49	2.17	3.6	5.95	2.97	0.48	0.14				100	8.92
Spectrum 34	63.53		21.76	0.74		2.61	6.8	4.51		0.05				100	11.31
Spectrum 35	62.53		22.12	1.29		3.93	6.84	3.29						100	10.13
Spectrum 36	63.13		21.06	1		2.82	6.13	5.85						100	11.98
Spectrum 37	63.31		21.39	1.07		3.68	6.45	4.11						100	10.56
Spectrum 38	61.75		20.54	2.4	0.58	3.8	6.43	3.77	0.73					100	10.2
Spectrum 39	63.34	0.22	21.6	0.65		3.12	6.85	4.22						100	11.07
Spectrum 40	63.4	0.2	22.06	0.71		3.23	7.34	3.05		0				100	10.39
Spectrum 41	59.77	0.47	21.75	2.01	0.51	4.87	7.5	2	1.13	0				100	9.5
Spectrum 42	61.19		23.29	0.62		5.5	6.69	2.71						100	9.4
Spectrum 43	61.33		22.24	1.84		4.48	6.96	3.15						100	10.11
Paua Bay											0.02			100	8.53
12PRBP	58.07	26.45	1.18	2.99	1.73	1.04	1.6	6.93			0			100	11.13

	61.31	24.4	0.52	1.56	1.76	0.74	2.21	7.49	0	100	9.7
	61.37	22.89	0.55	1.85	2.48	1.41	2.22	7.24	0	100	9.46
											0
19PRBP	51.22	21.09	2.43	8.12	2.84	8.57	4.03	1.67	0.04	100	5.7
	57.85	27.63	1.15	2.96	1.02	0.95	1.94	6.5	0	100	8.44
	59.05	24.53	1.2	3.21	0.86	0.73	2.75	7.67	0	100	10.42
	41.32	14.34	6.75	11.75	10.83	13.7	1	0.17	0.12	100	1.17
	51.38	21	2.56	6.94	3.49	9.37	3.12	2.03	0.11	100	5.15
											0
20PRBP	39.42	13.03	6.78	14.85	11.29	12.48	1.94	0.11	0.1	100	2.05
	40.71	14.85	6.05	12.96	10.65	12.37	1.16	1.19	0.07	100	2.35
	44.71	18.44	3.59	12.47	6.75	10.26	3.41	0.23	0.13	100	3.64
											0
22PRBP	62.03	20.27	1.12	2.65	1.58	1.28	3.2	7.88	0	100	11.08
	43.26	16.79	5.45	16.35	6.63	7.61	3.32	0.6	0	100	3.92
	60.22	22.44	1.04	3.43	2.24	0.89	2.3	7.45	0	100	9.75
	40.16	15.64	7.38	21.45	4.7	7.5	3.17	0	0	100	3.17